Electromagnetic Fast-transients in LV Networks with Ubiquitous Small-scale Embedded Generation

David A. Clark

Thesis submitted to Cardiff University
for the degree of Doctor of Philosophy

30^{th} March , 2012

Abstract

Small-scale embedded generation projects rated below 16A per phase are being integrated into low-voltage distribution networks in ever increasing numbers. Seen from the network operator's perspective as little more than negative load, the commissioning of such generators is subject to compliance with the *Fit and Forget* connection requirements of ENA Engineering Recommendation G83/1. This thesis has sought to quantify the electromagnetic switching transient implications of integrating very large volumes of embedded generation into the UK's low-voltage supply networks.

Laboratory testing of a converter-interfaced PV source has been undertaken to characterise typical switching transient waveshapes, and equivalent representative source models have been constructed in EMTP-ATP. A detailed frequency-dependent travelling wave equivalent of the DNO-approved Generic UK LV Distribution network model has been developed and, by means of extensive statistical simulation studies, used to quantify the cumulative impact of geographically localised generators switching in response to common network conditions.

It is found that the magnitude of generator-induced voltage and current transients is dependent on the number of concurrently switched generators, and on their relative locations within the network. A theoretical maximum overvoltage of 1.72pu is predicted at customer nodes remote from the LV transformer terminals, for a scenario in which all households have installed embedded generation. Latent diversity in switch pole closing and inrush inception times is found to reduce predicted peak transient voltages to around 25-40% of their theoretical maxima.

Acknowledgements

This work was carried out within the High-Voltage Energy Systems (HIVES) Research Group, Institute of Energy, Cardiff School of Engineering between October 2007 and March 2012.

Thanks are due first and foremost to Prof. Manu Haddad and Dr. Huw Griffiths for their supervision and guidance, without which this work would not have been possible. Sincere thanks are also due to Prof. Noel Schulz for her invaluable input while on sabbatical from Mississippi State University.

Experimental work was undertaken in the Cardiff University Solar Energy Laboratory under the guidance of Dr. Anthony Giles and with assistance of the school's technical staff, principally Mr. Paul Farrugia, Mr. Steve Mead, Mr. Mike Baynton, Mr. Alan Jauncey, Mr. Denley Slade, Mr. Richard Rogers and Mr. David Glinn. With regard to supporting EMTP simulation work, the author would like to acknowledge the invaluable expertise of his colleagues Dr. Maurizio Albano, Mrs. Haziah Abdul Hamid, Mr. Stephen Robson and Mr. Fabian Moore.

Thanks are also due to Prof. Nicholas Jenkins, Dr. Noureddine Harid, Dr. Dongsheng Guo, Dr. Liana Cipcigan, Dr. Jun Liang, Dr. Bieshoy Awad, Mr. Steve Watts, Mr. Alexander Bogias and Mr. Ahmed El-Mghairbi for their advice and input throughout this project.

Finally, I would like to thank my family for their patience and encouragement throughout my time at Cardiff.

List of Publications

Conference

D. Clark, A. Haddad, and H. Grffiths,"Switching transient analysis of small distributed generators in low voltage network", *CIRED 2009. 20th International Conference and Exhibition on Electricity Distribution* - Prague, Czech Republic, June 2009.

D. Clark, A. Haddad, H. Griffiths, and N. N. Schulz, "Analysis of switching transients in domestic installations with grid-tied microgeneration", *North American Power Symposium (NAPS)* - Starkville, MS, October 2009.

Journal

D. Clark, A. Haddad, H. Griffiths, "A laboratory test facility for the evaluation switching transients in small-scale embedded generators", *In progress, expected submission for review: Autumn 2012*

D. Clark, A. Haddad, H. Griffiths, "A generic model for determining electromagnetic transient propagation in low voltage supply networks", *In progress, expected submission for review: Autumn 2012*

Contents

List of Figures

List of Tables

List of Abbreviations

Abbreviation	Expansion
ABC	Aerial Bundled Conductor
AC	Alternating Current
ADC	Analogue to Digital Converter
ARMA	Auto-Regressive Moving Average (Function)
BI	Benefit Index
BIS	Department of Business, Innovation and Skills
BSi	British Standards Institution
CFL	Compact Fluorescent Lamp
CHP	Combined Heat and Power
CNE	Combined Neutral and Earth
CONSAC	Concentric Sheath Aluminium Conductor(s)
CP	Cable Pipe
CSA	Cross-Sectional Area
CSH	Code for Sustainable Homes
DAQ	Data Acquisition
DC	Direct Current
DCG	EMTP Development Coordination Group
DECC	Department of Energy and Climate Change
DEP	Double Exponential Pulse
DNO	Distribution Network Operator
DOW	Damped Oscillatory Wave
DTi	Department of Trade and Industry (now BIS)
EEUG	European EMTP Users Group
EIRI	Environmental Impact Reduction Index
EMC	Electromagnetic Compatibility
EMTP	Electromangetic Transients Program
ENA	Energy Networks Association
EPRI	Electric Power Research Institute
ER	Engineering Recommendation
EU	European Union
FDNE	Frequency-Dependent Network Equivalent
FEM	Finite Element Method
FFO (VFFO)	(Very) Fast Front Overvoltage

Abbreviation	Expansion
FIT	Feed-in Tariff
FPSE	Free-Piston Stirling Engine
GaN	Gallium Nitride
GPIB	General Purpose Interface Bus
GUI	Graphical User Interface
HAWT	Horizontal Axis Wind Turbine
LCC	Line and Cable Constants
LLRI	Line-Loss Reduction Index
LoM	Loss of Mains
LV	Low-Voltage ($\leq$1kV)
MCB	Miniature Circuit Breaker
MOV	Metal Oxide Varistor
MPPT	Maximum Power Point Tracking
MTBF	Mean Time Between Failures
MV	Medium Voltage ($\leq$33kV)
NI	National Instruments
OHL	Overhead Line
PLC	Power Line Communication
PMSG	Permanent Magnet Synchronous Generator
PV	Photovoltaic
PVC	Poly-Vinyl Chloride
PWM	Pulse-Width Modulation
pu	Per-Unit
RCBO	Residual Current Circuit Breaker with Overload Protection
RCD	Residual Current Device
RHI	Renewable Heat Incentive
SiC	Silicone Carbide
SMPS	Switch-Mode Power Supply
SPD	Surge-Protective Device
SSEG	Small-Scale Embedded Generation
STP	Symmetrical Trapezoidal Pulse
TACS	Transient Analysis of Control Systems
%THD	Percentage Total Harmonic Distortion
TNA	Transient Network Analyser
TOV	Temporary Overvoltage
VAWT	Vertical Axis Wind Turbine
VICP	Versatile Instrument Control Protocol
VISA	Virtual Instrument Software Architecture
VPII	Voltage Profile Improvement Index
WG	Welsh Government
XLPE	Cross-Linked Polyethylene
ZnO	Zinc Oxide

List of Mathematical Symbols

Symbol	Definition
$A(\omega)$	Propagation Matrix of a Frequency-Dependent Line
A_D	Amplitude of a Damped Oscillatory Wave
A_S	Amplitude of a Symmetrical Trapezoidal Pulse
$\alpha(\omega)$	Attenuation Constant of a Frequency-Dependent Line
B_g	Branch Count of a Generator Block (ATPDraw)
B_l	Branch Count of a Load Block (ATPDraw)
B_m	Branch Count of a Measurement Block (ATPDraw)
$\beta(\omega)$	Phase Constant of a Frequency-Dependent Line
c	Velocity of Light in a Vacuum ($3 \times 10^8\ ms^{-1}$)
C	Capacitance
$C'(\omega)$	Shunt Capacitance of a Frequency-Dependent Transmission Line
C_i	Effective Inrush Capacitance of a Grid Inverter
C_{ss}	Steady-state Capacitance of a Grid Inverter
d_C	Conductor Diameter
Δt	Simulation Time-step
ΔI	Transient Component of a Current Waveform
ΔV	Transient Component of a Voltage Waveform
f	Frequency
f_N	Nyquist Frequency
G	Conductance
$G'(\omega)$	Shunt Conductance of a Frequency-Dependent Line
$[G]$	System Conductance Matrix (EMTP)
$[G_A]$	Conductance Submatrix of Uncoupled System A
$[G_B]$	Conductance Submatrix of Uncoupled System B
$\gamma(\omega)$	Propagation Constant of a Frequency-Dependent Line
γ_{mode}	Mode Propagation Constant of a JMarti Line
$i(t)$	Current - Continuous Time
$i[t]$	Current - Discrete Time
I_{hist}	Historic Current Term in EMTP Solution
I_{pk}	Largest Peak of Measured Current Waveform
I_{max}	Positive Peak of Measured Current Waveform
I_{min}	Negative Peak of Measured Current Waveform
I_{mpp}	Maximum Power Point Current of a PV Cell/Array
I_{sc}	Short-Circuit Current of a PV Cell/Array

Symbol	Definition
k_B	Correction Factor in Total Branch Count Approximation
k_N	Correction Factor in Total Node Count Approximation
k_p	Parallel Damping Factor
k_s	Series Damping Factor
L	Inductance
$L'(\omega)$	Self and Mutual Inductance of a Frequency-Dependent Line
λ	Transformer Core Flux
λ_{sat}	Transformer Core Saturation Flux
λ_{mode}	Modal Eigenvalue (JMarti)
$[\Lambda]$	Matrix of Modal Eigenvalues (JMarti)
$n_{c1\phi}$	Total Number of Single-Phase Cable Segments (ATPDraw)
$n_{c3\phi}$	Total Number of Three-Phase Cable Segments (ATPDraw)
n_f	Total Number of Feeder Subgroups (ATPDraw)
n_g	Number of Generator Blocks per Feeder (ATPDraw)
n_l	Number of Load Blocks per Feeder (ATPDraw)
n_m	Total Number of Measurement Blocks (ATPDraw)
n_{branch}	Total Branch Count (ATPDraw)
n_{group}	Total Compressed Group Count (ATPDraw)
n_{obj}	Total Object Count (ATPDraw)
n_{node}	Total Node/Bus Count (ATPDraw)
N_g	Node/Bus Count of a Generator Block (ATPDraw)
N_l	Node/Bus Count of a Load Block (ATPDraw)
N_m	Node/Bus Count of a Measurement Block (ATPDraw)
ω	Angular Frequency
R	Resistance
R_{DC}	Direct-Current Resistance
R_{eff}	Effective Resistance of RLC Branch by Dommel's Method
$R'(\omega)$	Self and Mutual Resistance of a Frequency-Dependent Line
ρ_g	Penetration of SSEG (% of Capacity *or* per Feeder Phase)
ρ_{eff}	Effective SSEG Penetration Accounting for Switch Diversity
s	Operator Variable in the Laplace Domain
$\overline{s}$	Mean Separation Between Conductor Centres
S_g	Switch Count of a Generator Block (ATPDraw)
S_i	Current Transient Energy Measure
S_v	Voltage Transient Energy Measure
σ	Standard Deviation of Statistical Data Set
t	time
t_a	Rise/Fall Time of a Symmetrical Trapezoidal Pulse
t_h	Half-Magnitude Interval of an STP
τ	Time Constant

Symbol	Definition
τ_{km}	Wavefront Propagation Time from node k to m
τ_{max}	Propagation Time of the Slowest Mode (JMarti)
τ_{min}	Propagation Time of the Fastest Mode (JMarti)
τ_R	Rising Time Constant of a Double-Exponential Pulse
τ_D	Decay Time Constant of a Double-Exponential Pulse
τ_{sw}	Inter-pole Switching Delay
τ_i	Delay Between Switch Closing and Inrush Inception
$[T_i]$	Current Transformation Matrix (JMarti)
$[T_v]$	Voltage Transformation Matrix (JMarti)
T_{sim}	Simulation Time Window
T_1	Rise Time of a Fast Front Transient (IEC71)
T_2	Tail Time of a Fast/Slow Front Transient (IEC71)
T_p	Rise Time of a Slow Front Transient (IEC71)
$T_{rise[20-80\%]}$	Transient Wavefront Rise Time between 20 and 80% of Magnitude
$T_{rise[10-90\%]}$	Transient Wavefront Rise Time between 10 and 90% of Magnitude
$T_{rise[30-90\%]}$	Transient Wavefront Rise Time between 30 and 90% of Magnitude
$T_{fall[80-20\%]}$	Transient Wavefront Fall Time between 80 and 20% of Magnitude
$T_{fall[90-10\%]}$	Transient Wavefront Fall Time between 90 and 10% of Magnitude
$T_{fall[50\%]}$	Transient Wavefront Fall Time from Peak to Half Magnitude
θ_1	Angle of First Switch Pole Closing Relative to Voltage Zero
θ_2	Angle of Second Switch Pole Closing Relative to Voltage Zero
θ_i	Angle of Inrush Inception Relative to Voltage Zero
u_m	Amplitude of a Synthesised Test Waveform
$v(t)$	Voltage - Continuous Time
$v[t]$	Voltage - Discrete Time
v_p	Phase Velocity of an Electromagnetic Wave
V_{mpp}	Maximum Power Point Voltage (PV Cell/Array)
V_{oc}	Open Circuit Voltage (PV Cell/Array)
V_{pk}	Largest Peak of Measured Voltage Waveform
V_{max}	Positive Peak of Measured Voltage Waveform
V_{min}	Negative Peak of Measured Voltage Waveform
W	Energy Content of a Transient Waveform
x_g	Generator Position on a Radial Feeder
$Y'(\omega)$	Shunt Admittance of a Frequency-Dependent Line
y_p	Proximity Effect Factor
y_s	Skin Effect Factor
z	Operator Variable in the Z-Domain
$Z'(\omega)$	Series Impedance of a Frequency-Dependent Line
$Z_C(\omega)$	Characteristic Impedance of a Frequency Dependent Line
$[Z_{mode}]$	Modal Domain Impedance Matrix (JMarti)
$[Z_{phase}]$	Phase Domain Impedance Matrix (JMarti)

Hypothesis

Wide-scale integration of small power generators, energy storage devices and electric vehicles into low-voltage distribution networks shall give rise to potentially disruptive transient effects due to strict disconnection requirements, the frequency and severity of such events being dependent on localised device concentration

Introduction

With mounting concern over energy security, growing public opposition to conventional power generation on environmental grounds and increasingly uncertain economics and politics of fossil fuel supply, there are set to be major changes in the way in which our electrical energy is generated, distributed and utilised. The traditional radial supply model of the power system, with electrical energy flowing from central plant to end consumer, is becoming less familiar and there is an increasing role for embedded generation feeding directly into low- and medium-voltage distribution networks.

With ambitious energy efficiency and primary fuel sustainability targets for 2020 fast approaching, the UK's networks need to adapt in order to accommodate the vast amounts of distributed energy sources, storage devices and electric vehicles required (see Figures 1 and 2). At the demand side, small scale generators rated below 16A per phase may make a significant contribution to meeting these targets, with a realistic projection of some 2-3 million installed units by 2020 [1].

To date, numerous studies have been published on energy yield maximisation and ancillary service provision capability of low capacity or intermittent sources, either through the use of sophisticated interface and storage devices, or by a variety of aggregation techniques. Little attention, however, has yet been given to electromagnetic switching transient phenomena associated with connecting large numbers of such sources into public supply networks. On the customer side of the meter, such transients may lead to increased insulation degradation and damage to electronic components of equipment and appliances, while in small industrial premises other problems such as nuisance tripping of variable speed drives may occur [4]. From the DNO's perspective,

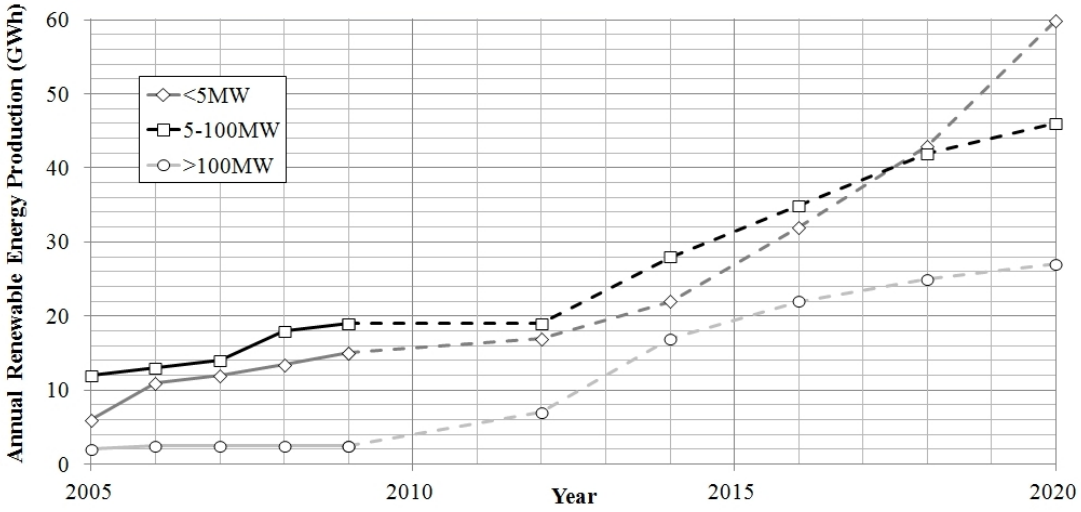

Figure 1: Historic and Projected Renewable Energy Production to 2020 by Scale [2]

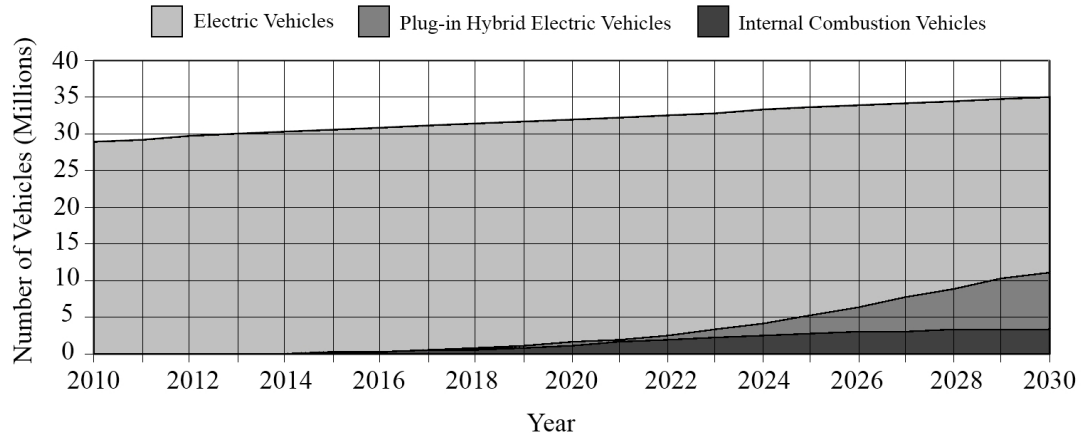

Figure 2: Projected Electric Vehicle Uptake in UK to 2030 (BERR *High* Scenario) [3]

there is the risk of damage to distribution hardware and a general degradation of power quality.

In the UK and across Europe, commercial Small-scale Embedded Generation (SSEG) equipment for photovoltaic, micro CHP, small wind and hydro generation may undergo a type-testing procedure in order to minimise the duration and complexity of the commissioning process. Such generators may then be installed under a *Fit and Forget* policy, in which the source is viewed from the network as variable negative load, and no ongoing ancillary service provision is required.

One of the conditions of this policy is that grid-connected generators must disconnect from the public supply when significant voltage or frequency deviations occur, reconnecting again following a pre-defined delay. The conditions for these switching operations, defined in the UK Energy Networks Association Engineering Recommendation G83/1 [5] and its equivalent British Standard BS EN 50438 [6], are summarised below.

Table 1: Recommended Disconnect Times for Generators Rated Below 16A/phase [5,6]

Protection Setting	Max. Clearance Time (s)	Max. Trip Setting
Overvoltage (stage 1)	1.5	264V (+15%)
Undervoltage (stage 1)	1.5	207V (-10%)
Overfrequency	0.5	50.5Hz (+1%)
Underfrequency	0.5	47Hz (-6%)
Loss of Mains	0.5	-

By a combination of laboratory measurement and extensive simulation studies, this thesis seeks to predict the degree to which such disconnection requirements, when applied to increasing penetrations of localised SSEG capacity, give rise to electromagnetic switching transients within LV supply networks, and how such transients might be mitigated should they become a concern.

Contributions of Thesis

The following is a summary of significant contributions presented in this thesis:

- Detailed analysis of EMTP simulation software capabilities in application to LV network modelling, with a view to developing a suite of generic travelling-wave

network models critical to the analysis of electromagnetic transients in public supply networks.

- Design and construction of a laboratory rig, consisting of photovoltaic array, solar inverter and grid connection for the purpose of switching transient characterisation.
- Determination and statistical analyses of generator switching transient characteristics necessary for the development of representative EMTP source models.
- Translation of the test arrangement into an EMTP model for verification of the laboratory test regime.
- Using established steady-state and dynamic network models as reference, developed detailed travelling-wave simulation models for the representation of generic LV networks and feeders under fast-front transient conditions - this aspect may be regarded as the principal novelty of the work.
- Extensive simulation of SSEG penetration scenarios in urban and rural networks, to determine the cumulative effect of increasing localised source penetration on expected voltage/current transient magnitudes.

Chapter Summaries

Chapter 1 (p7) is a review of literature underpinning research work presented in this thesis. Given the relative novelty of electromagnetic transient studies at low voltages, particularly those relating to embedded generation, the number of immediately relevant research papers is quite small. This work does, however, draw upon published papers, standards and guidelines pertaining to related areas, such as insulation coordination at high voltage and electromagnetic compatibility. A fairly broad range of review topics has therefore been covered.

Chapter 2 (p45) is concerned with the numerical solution of electrical circuits in the time-domain, with a view to performing computational transient analyses on LV networks. Underlying theory of Dommel's trapezoidal integration method is discussed, and its potential limitations when applied to low-voltage circuits identified. Solutions are proposed for the treatment of network models with short cable/line travel times, small circuit time constants, non-circular cable geometries and marginal satisfaction of

the assumptions of Carson's equations due to proximity effects.

Chapter 3 (p71) details the specification and construction of a laboratory test bed for the acquisition of generator switching transient data. A complete photovoltaic installation was designed and installed in the Cardiff University Solar Energy Laboratory, and a semi-automated data-acquisition system constructed using NI LabVIEW. A range of appropriate synthesisable waveshapes is proposed for the emulation of typical waveforms in subsequent time-domain simulation studies and laboratory tests.

Chapter 4 (p100) presents and discusses the results obtained using the laboratory rig of chapter 3. Statistical data on voltage and current magnitudes, ramp rates, energy measures and switch timing analyses are presented, and standardised synthetic test waveforms fitted to typical and worst-case results. Transient front timing data is analysed for the purpose of developing a distributed statistical switching model in EMTP.

Chapter 5 (p135) is the first of two chapters concerning the specification and results of transient simulation studies in EMTP. Generator switching models are developed and compared with results of chapter 4, and a suite of simulation studies performed to evaluate expected switching transient magnitudes due to individual generators feeding simplified urban and rural network models.

Chapter 6 (p165) then expands upon this simulation work to assess the cumulative impact of many generators switching in response to a single common stimulus. A detailed travelling wave equivalent of the DNO approved Generic UK LV Network model is developed, and extensive statistical simulation performed to assess typical and theoretical worst-case scenarios for different levels of feeder SSEG penetration up to 100% (One unit per customer). The self-mitigating effect of switch pole and inrush time-dispersion is investigated, and possible solutions for the prevention of simultaneous switching proposed.

Finally, a conclusions chapter (p204) summarises the key findings of this work and a number of topics are identified for ongoing study.

Chapter 1

Literature Review

The focus of this thesis, by its nature, necessitates that a variety of existing research areas be considered. Analysis of electromagnetic transient phenomena in Low-Voltage networks with regard to embedded generation, though a somewhat unknown quantity in itself, is underpinned by existing research in the fields of high-speed electrical power measurement, time-domain circuit simulation techniques and generator technology.

Given the consumer-led nature of microgeneration adoption, it is also important to consider aspects of government energy strategy, existing and future financial incentives and established predictive adoption studies in order that representative future scenarios may be developed. Assessment of each of these aspects shall help to establish the context for this work.

The following chapter is split by topic into five sections; Section 1.1 gives an overview of current policy, energy strategy and scenario assessments relating to the roll-out of Small-scale Embedded Generation (SSEG) technologies in the UK. The various SSEG technologies currently and soon to be commercially available are then discussed in section 1.2, together with a review of system impact assessments. Section 1.3 then moves on to the topic of LV Network transients, their measurement and classification.

Section 1.4 is concerned with the development of simulation models, and a review of established and novel techniques is performed. This section gives an overview of the small number of scientific papers concerned with research problems closely related to

this thesis. Finally, section 1.5 is reserved for a summary of standards, engineering recommendations and guidelines pertinent to studies presented in later chapters.

1.1 UK Microgeneration Prospects

One of the key factors in guaranteeing the success of the European SmartGrid vision [7, 8] is the need to integrate increasing amounts of distributed and renewable energy sources with existing energy networks. In addition to the UK's commitment to long-term emissions reduction targets, there are major concerns for the future availability of primary fuels, planning barriers and public opposition to new centralised plant and network expansion, and an ongoing requirement to maintain secure and reliable energy supplies. All drivers point to a need for greater diversity in the UK energy mix, with an increasing role for renewable generation over the next few decades.

Within such a dispersed energy structure, there is scope for a significant proportion of overall energy demand to be satisfied using distributed generation (DG) embedded within Medium- and Low-Voltage networks. At the level of the domestic and small commercial customer, *Microgeneration* technologies such as Combined Heat and Power (μCHP), Small Wind and Solar Photovoltaics (PV) have the potential to contribute a great deal of this distributed energy requirement at the point of end use, making the energy consumer an increasingly active participant in the developing energy supply structure [9].

In 2008, the Welsh Government (WG) published its Renewable Energy Routemap [10], a detailed appraisal of Wales's sustainable energy resource and distributed generation targets for 2025. This document followed the publication the previous year of the Microgeneration Action Plan for Wales [11], calling for the installation of 200,000 electrical generator units (mostly below $3kW_e$ [12]) by 2020.

Wider UK government targets were established in 2011 with the publication of the Department of Energy and Climate Change (DECC) Microgeneration Strategy [13] and the Microgeneration Government-Industry Contact Group Action Plan [14]. These documents provide an outline of incentives to accelerate the adoption of microgeneration in the UK, including the Feed-in Tariff (FIT) established in 2010, and the Renewable

Heat Incentive (RHI) now deferred until 2013. In comparison to the WG publications, however, projected and target uptake figures are somewhat absent.

Despite the recent introduction of consumer market incentives, there remain a number of technical, economic and political barriers to the wide scale adoption of microgeneration in the UK [15]. Considerable progress will be required over the coming decade in order to close the gap between the UK and those European countries with established microgeneration support schemes such as Denmark and Germany [16]. There is at present no explicit policy framework at European level to incentivise the adoption of microgeneration technologies, and EU member states are left some freedom to respond to market directives in a manner of their choosing. These aspects, together with varying network regulation approaches as discussed in [17], have contributed to an inhomogeneous uptake of microgeneration across Europe.

1.1.1 Small-scale Embedded Generation - A Definition

Legally defined in the Energy Act 2004 [18] as electrical generation rated below $50kW_e$ (or thermal generation below $45kW_{th}$), Microgeneration represents the smallest capacity subset of DG technologies. From the perspective of the Distribution Network Operators (DNOs), this definition is overly broad, and such classified generators are further subdivided according to capacity and type of grid interface in order that appropriate connection requirements and guidelines may be standardised.

All electrical generators connecting to the public supply must comply with regulation 22 of the Electrical Safety, Quality and Continuity Regulations 2002 [19, 20], but some acceleration of the compliance process has been achieved with the introduction of the following engineering recommendations: Generators rated below 16A per phase, with power electronic converter interfaces typical of domestic installations, are subject to the connection requirements outlined in Engineering Recommendation (ER) G83/1 and its equivalent draft standard [5, 6]. Higher Capacity generator connections to the public electricity supply rated up to an above $50kW_e$ are governed by ER G59/1 [21].

Those generators falling under the remit of G83/1 are the primary focus of this thesis, and in the interest of clarity and to distinguish these from larger Microgeneration technologies, the term *Small-scale Embedded Generation* (SSEG) has been adopted from

this point onwards. This convention is in line with related studies presented in [22–25], discussed later in this chapter.

1.1.2 Adoption Scenarios

A wide range of SSEG adoption scenarios have been proposed for the UK over the past decade. Possibly the most widely cited is the 2004 report of the DTi (now BIS) and Ofgem's Distributed Generation Programme [26], in which three adoption scenarios to 2020 are presented. Total capacities and expected annual energy yields are summarised in Table 1.1

Table 1.1: SSEG Adoption Scenarios of 2004 DTi Report [26]

Scenario	**2010**		**2015**		**2020**	
	GW	**TWh/yr.**	**GW**	**TWh/yr.**	**GW**	**TWh/yr.**
Low	0.37	0.96	1.19	3.07	2.23	5.65
Mid	1.23	3.22	4.06	10.36	7.92	19.41
High	2.48	6.48	8.26	21.15	15.78	39.22

Late adoption of feed-in tariffs in the UK resulted in slow market growth initially, with an estimated $22MW_e$ of microgeneration capacity installed by the end of 2008 [27]. By December 2010, nine months following the introduction of the tariff, cumulative FIT applications had reached approximately $72MW_e$, consisting primarily of PV (67%), Small Wind (20%) and Hydro (12%) [28, 29]. Total capacity at the end of 2010 stood at approximately 100MWe, well short of the DTi *low* adoption scenario of Table 1.1, though growth to the end of 2011 was encouraging. It remains to be seen how uncertainty over feed-in tariff rates in 2012 will impact this growth rate.

The targets presented under the Microgeneration Action Plan for Wales are similarly ambitious, with cumulative domestic installed capacity in Wales alone reaching $500MW_e$ by 2020 (assuming a mean installation size of 2.5kW [29]). This corresponds to an installation in approximately one in eight of all Welsh households at current growth rates.

Other adoption scenarios include the RWE nPower Microgeneration Market Adoption Model (MMAM) [30], which projects roughly 30% market growth rates to 2020 under

the influence of the current FIT and introduction of the Code for Sustainable Homes (CSH) level 6 in around 2016. Growth is then curtailed from 2020 onwards as government incentives expire and the now established industries revert to natural growth models based on economies of scale. Figure 1.1 illustrates this projected growth, and figures for the year 2020 are comparable to the *Mid* adoption model of the DTi report [26].

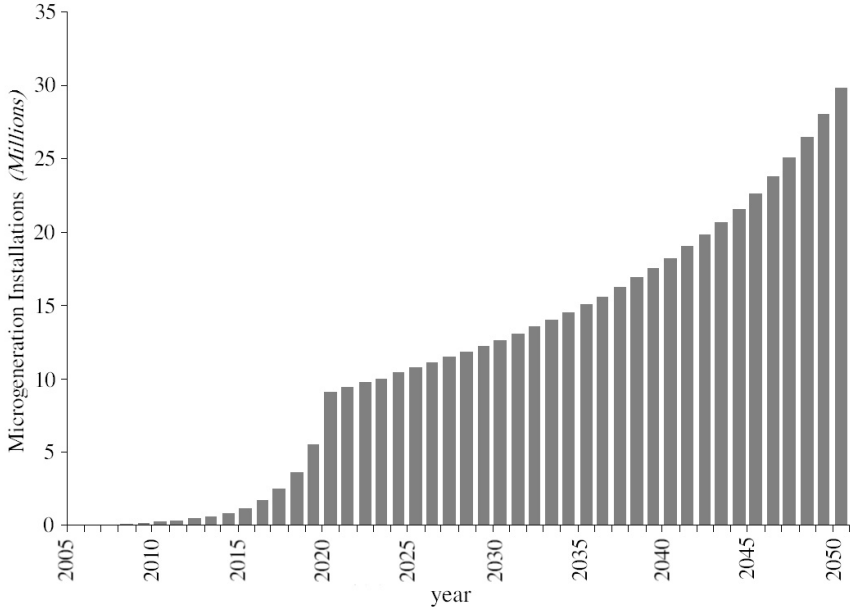

Figure 1.1: MMAM: Projected Microgeneration Adoption to 2025 [30]

Some of the adoption models studied are technology-centric, such as the UK market projections for μCHP presented in [31] and [32]. These are of somewhat less use for the purposes of developing future network models as there is invariably an inherent bias in favour of a particular generating technology, at the possible expense of another. Where only a single immature technology is considered, there is also the increased potential for overestimation in projections, should an unforeseen hindrance to progress occur in its development or commercialisation. μCHP adoption in the UK is a good example of this delayed adoption, but remains a promising technology and is discussed in section 1.5.

The final class of microgeneration adoption scenarios considered were those relating to specific impact studies and generic network models, such as those presented in [23, 25, 33]. Here, microgeneration penetrations are typically treated as fractions of network capacity rather than absolute quantities, and the weighting and characteristics

of individual technologies are of secondary importance. The models presented in later chapters draw heavily from this type of generic model, but are greatly informed by the market-oriented projections of [26] and [30].

1.2 Embedded Generation Technologies and Their Impact on System Performance

1.2.1 Source Types

The following is a breakdown of the types of SSEG technologies currently available and eligible for UK FIT, or otherwise nearing commercialisation. The technologies presented are those projected to make significant contribution to total DG capacity in 2020 and beyond.

1.2.1.1 Photovoltaics

The SSEG technology with the largest market share in the UK is currently solar PV, with considerable growth in the 18 months since introduction of the FIT. By the end of March 2011, approximately $77.3MW_e$ of PV capacity had been registered at 28,375 individual installations [34]. A typical installation will involve a parallel array of N module strings, each of M modules, connected to a common DC bus as shown in Figure 1.2 [35]. Each module shall itself consist of a series arrangement of mono- or poly-crystalline Silicon cells, so connected as to generate a rated voltage of between 12 and 240V dependent on design. Advertised module efficiencies under standard test conditions as per [36, 37] are summarised in Table 1.2 [38].

Table 1.2: Typical Module Efficiency of Comercial PV Technologies [38]

Technology	**Module Efficiency η (%)**
Monocrystalline Si	14-19
Polycrystalline Si	7.5-15
Thin-Film	6-8

Polycrystalline modules are the current favoured technology of installers due to typically lower capital costs and reduced exposure to the price volatility of the high-grade silicon market. Thin-film technologies allow a minimisation of material requirements

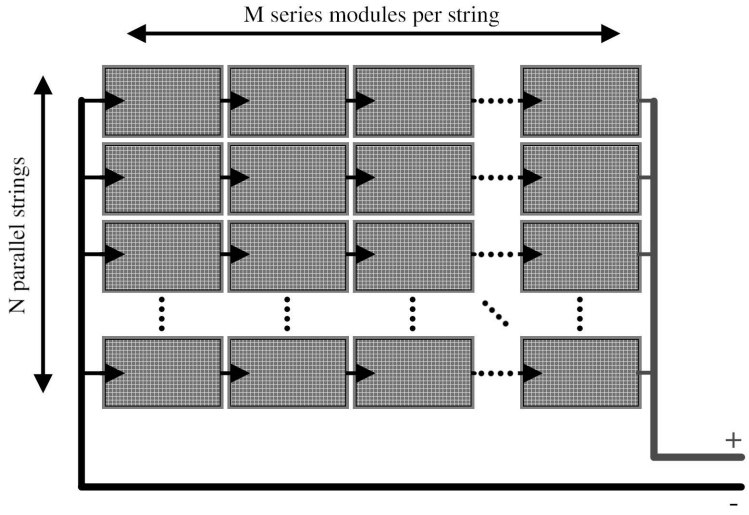

Figure 1.2: $N \times M$ PV Module Array

for cell manufacture, and are expected to play a key role in driving down the total cost of future PV installations. Thin-film cells also benefit from increased performance at low-light levels, but present typical conversion efficiencies are lower than that of Polycrystalline Silicon, as can be seen from Table 1.2 [38].

Two primary measures are used to quantify the annual performance of a photovoltaic installation:

1. Availability Factor (A_{pv}): The ratio of actual operating hours to the number of hours during which irradiation was sufficient to operate.

2. Capacity Factor (C_{pv}): The ratio of kWh generated to the number of kWh that would be produced if output was constant at its peak [39].

In reality, the availability factor of a typical small-scale photovoltaic installation is expected to be near to 100%, due to good reliability and infrequent service requirements. Capacity factors for small PV systems are low, however, with 9.7% being the UK average [34]. This is because of the daily and seasonal variation of incident radiation, and economic non-viability of position tracking systems for small arrays [40]. The efficiency of a fixed roof-mounted installation is maximised only for variable light conditions using a Maximum Power Point Tracking (MPPT) system, integrated into the converter interface. Figure 1.3 illustrates seasonal variation in the output profile of a typical installation, and maximum power point shifting due to a change in global irradiance.

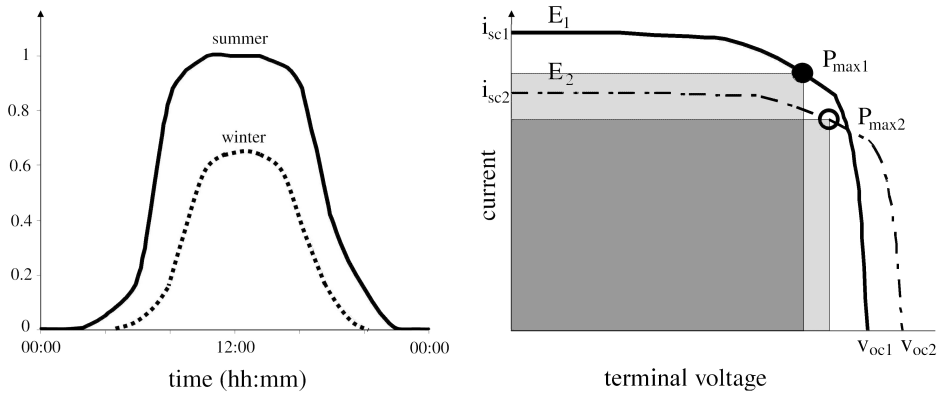

Figure 1.3: Output Profile Shift and MPPT in a Typical PV Installation

1.2.1.2 Wind

Demand for small-scale wind installations has also increased following introduction of the FIT in March 2010. The third quarterly report on the AEA UK Microgeneration Index estimates total capacity of wind generators rated below $50kW_e$ as $4.73MW_e$, split across 736 individual installations. This puts the average installation size of small wind turbines at around $6.4kW_e$, reflecting the efficiency and capacity factor increases attainable with larger systems [41].

The Energy Saving Trust defines a small wind-powered electricity generating system as having an output between $500W_e$ and $25kW_e$ [42], but a wide variety of manufacturers' designs exist within this definition [43]. Turbine designs are subdivided into horizontal-axis (HAWT) and vertical-axis (VAWT) configurations, with ground-anchoring being the preferred installation option for systems larger than about $2kW_e$. An overview of roof-mounted designs rated below $2kW_e$ can be found in the Mid-Wales Energy Agency document [44], though reduced wind-speeds and turbulence at low hub heights will typically render this size of turbine less economically viable.

Similar to the PV technologies discussed in the previous section, the installed performance of a given turbine installation can be defined in terms of its availability and capacity factors (A_w, C_w). As with PV systems, the availability of a typical small wind installation is very high (normally in excess of 95%), but capacity factors vary widely according to size and location, ranging from less than 5% for small systems in urban areas [45] up to 15% or more for installations of $20kW_e$ [46].

The larger capacity factors for higher rated turbines is primarily due to increased wind speeds and reduced turbulence at elevated hub-heights, the mechanical power output being determined by Equation (1.1) where ρ is the air density, S the blade cross-section and V_w the wind speed at the hub height. C_p is a coefficient of performance which is itself highly sensitive to variation in wind speed [43] as shown in Figure 1.4. This sensitivity is most pronounced in the case of VAWTs, and MPPT systems are necessary to maximise the output of all installed systems.

$$P = \frac{C_p \rho S V_w^3}{2} \tag{1.1}$$

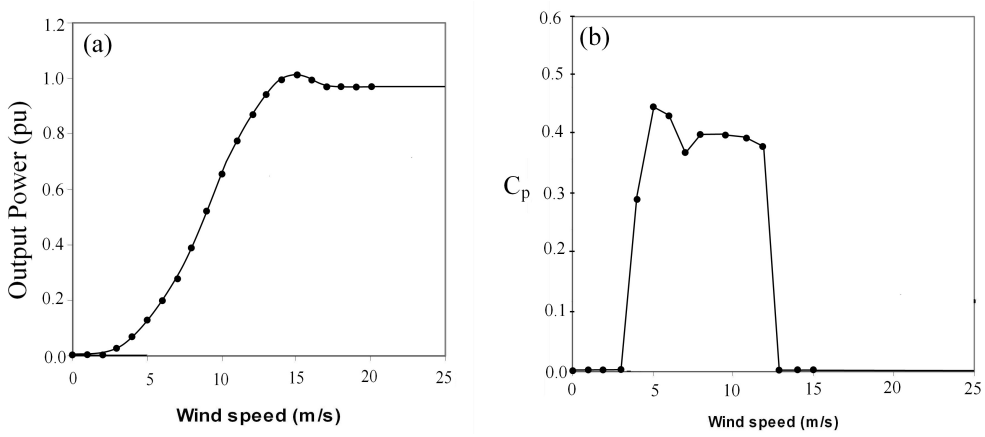

Figure 1.4: (a) Design Power Curve of a 2.5kW Micro Wind Turbine (3 blade, HAWT) [47], (b) Measured Sensitivity of kW-scale Turbine Performance Coefficient to Wind Speed [48]

It is reasonable to assume that due to the poor performance of very small turbines, new installations will typically have a capacity in excess of $5kW_e$, and shall be mainly connected to rural networks or small commercial building supplies [9]. Small wind generation is unlikely to impact urban and suburban distribution networks due to considerations of space availability, air turbulence and noise. A thorough performance comparison is complicated, however, by the ongoing lack of dedicated standardised test specifications for small turbines [49].

As a general rule, the mechanical energy harvested by a small turbine shall be converted to electrical energy by means of a permanent magnet synchronous generator (PMSG), with its variable frequency output being rectified and inverted back to 50Hz for export to the grid. Systems larger than $15kW_e$ shall normally be geared to increase

the PMSG shaft speed, but a power electronic interface remains preferable to the small direct connected induction machine for systems up to $25kW_e$. Seen from the utility's perspective, beyond temporal variation in output profiles, the electrical characteristics of small wind and PV systems are thus quite similar.

1.2.1.3 Small Hydro

Small Hydroelectric generation commissioning during the first 12 months of the FIT totalled $9.72MW_e$ across 203 installations, for an average plant rating of $48kW_e$ [34]. This puts a typical small hydro system rating well above that of the largest SSEG, taken as the 3-phase limit from [5] of 11kW, though low-head run of river projects may be rated as low as $1kW_e$. It is recognised that the availability of sites suitable for such projects is limited, and like small wind turbine installations shall predominantly be confined to rural networks.

Unlike PV and small wind, there is an array of established hydro generator designs available and the choice of technology shall depend on the characteristics of the location. Primary factors in determining the rating of a small hydro system are the head (vertical displacement of inlet and outlet less frictional effects) and expected flow rate. Turbine types and typical applications are summarised in Table 1.3

Table 1.3: Small-hydro Turbine Types and Capacities [50]

Turbine	Head (m)	Discharge (m^3/s)	System Sizing
Pelton (impulse)	> 50	< 1	$> 20kW$
Turgo (impulse)	> 10	< 1	$> 5kW$
Crossflow (impulse)	< 50	< 5	$1 \rightarrow 500kW$
Propeller (reaction)	< 5	> 1	$1 \rightarrow 500kW$

As with PV and wind systems, interfacing of smaller systems with the public LV supply shall be achieved by means of an inverter, and thus the electrical characteristics of equivalently sized systems should remain similar regardless of the energy source employed.

1.2.1.4 MicroCHP

A promising SSEG technology better suited to suburban domestic application is that of MicroCHP, with ongoing development of kilowatt-scale internal-combustion, fuel-cell and Stirling engines [51,52]. Large-scale CHP is well established technology, particularly in Scandinavia and Germany, but the siting of high capacity plant is economically dependent on the availability of a sufficiently large local heat demand [53].

At the domestic level, highly efficient μCHP units rated at around $1kW_e$ are a promising alternative for the UK, with heat-led systems directly replacing the common household boiler being the generally favoured approach. Such devices utilise a highly efficient condensing boiler integrated with an external combustion (Stirling) engine designed to convert a portion (approximately 10%) of the heat of combustion to electrical energy. μCHP is projected to make by far the most significant contribution to 2020 SSEG adoption targets [1], but at the time of writing only one such system (Baxi) has reached commercial launch in the UK [54], with three others (E.On-Whispergen, Bosch and Inspirit) due on the market in 2012 [55].

The operation of a Stirling engine relies on the change in volume of a fixed mass of working fluid (typically Nitrogen or Helium), as it is alternately heated and cooled within an hermetically sealed casing, to drive the pistons. This motion can be used to drive a rotating machine in the case of α- and β-type Kinematic Sterling Engines, or a linear alternator in the case of the simpler Free-Piston Stirling Engine (FPSE) - see Figure 1.5. A detailed comparison of μCHP technologies can be found in the paper by Harrison [32], who identify a number devices either in development or undergoing performance trials. Economic viability analyses estimate the payback period on marginal unit cost (the additional cost of opting for a μCHP unit over like-for-like replacement of a domestic boiler) to be in the region of 3-4 years.

Since the energy dissipated in the cold sink of the Stirling engine is returned to the domestic hot water system via a heat recovery process, overall fuel efficiencies can be extremely high. In the case of the β-type engine, the most efficient of the three configurations, electrical efficiencies are in the region of 10-15%, while the high thermal efficiency of the boiler raises the nominal primary fuel efficiency to above 90%.

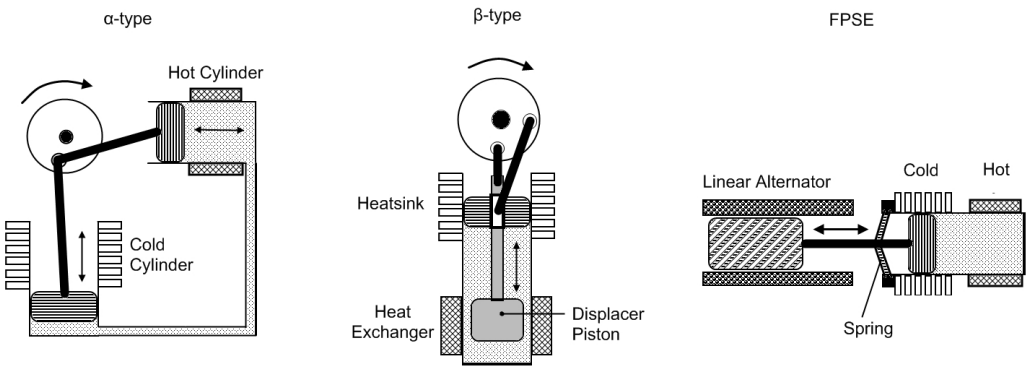

Figure 1.5: Stirling Engine Configurations for μCHP applications [50]

For a grid-connected device, having two useful energy outputs theoretically allows for two different modes of operation:

1. Thermally-Led, in which the heating demand of the home determines the electrical generating pattern of the μCHP unit, and;

2. Electrically or Grid-Led, in which the thermal inertia of the home is exploited to allow instantaneous network demand to determine the generator output profile.

It is evident that a grid-led operating mode would be of greatest use to a DNO, by making available a degree of controllable localised generation at times of peak demand, thus helping to smooth network load profiles. These operating modes have been investigated in the paper by Pielke et al. [56], who concluded that grid-led operation could be implemented with no noticeable effect on user comfort, but that the unbundling of the distribution networks from generation at present means that no added value exists in implementing such a system.

With regard to the economics of μCHP, Jablko et al. [57] found that heat engine based units were among the most cost-effective options, but that the lifetime cost of any CHP option is extremely sensitive to a number of factors, including gas and electricity prices, feed-in payments and the cost of initial investment. It is unclear as yet what rate of uptake can be expected for the first generation commercial μCHP units, given recent volatility of gas and electricity prices. Initial FIT rates for μCHP were low at 10p per generated kWh, with a further 3p for exports for the first 30,000 installations [34]. With tariffs expected to rise to 15p/kWh and a lifting of the installation cap [58], it

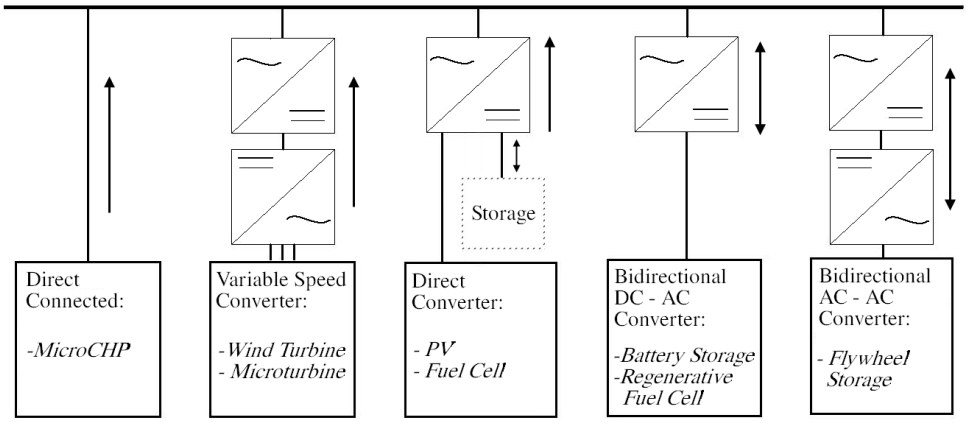

Figure 1.6: Interface Configurations for the Integration of SSEG in LV Networks

is anticipated that marginal payback periods will reduce and uptake of this technology shall increase significantly.

1.2.1.5 Developing Technologies

The generator technologies discussed previously are those commercially available and sufficiently mature to be eligible for subsidy under the FIT. It is likely that these shall constitute the vast majority of new SSEG installations over the next 10-20 years, and as such other less mature technologies such as microturbines, hydrogen fuel cells and regenerative fuel cells have been omitted from the studies presented here. With the possible exception of μCHP, however, all SSEG shall be grid-connected via a power-electronic interface, and thus future developments in the exploitation of small-scale distributed energy sources should have little impact on the overall findings of this thesis.

1.2.2 Interfaces

As discussed in the previous section, low voltage networks with high penetrations of SSEG shall predominantly interface with those devices by means of power electronic converters. The various interface topologies available are summarised in Figure 1.6.

Advances in photovoltaic converter technology were reviewed by Mallwitz et al. [59] in which general trends in inverter cost, efficiency and mean time between failures (MTBF) were observed, as summarised in Table 1.4. The authors determine the integration level of an inverter module as being characterised by its specific power per unit weight (P_W) and specific power per unit volume (P_V), both of which are

negatively affected by increases in device complexity and protection class as increased power handling capabilities are sought. A range of future developments are identified, including new semiconductor materials based on SiC and GaN to reduce switching losses, and increased switching frequencies requiring advanced magnetic materials and components.

Table 1.4: Trends in Solar Inverter Development [59]

Year	**1990**	**2009**	**2015**
Cost	£0.9/W	£0.3/W	£0.2/W
Efficiency	90%	96 - 98%	97 - 99%
MTBF	0.1M hrs	0.5M hrs	1M hrs

A similar review of converter topologies for small wind applications can be found in the paper by Baroudi et al. [60], in which the main PMSG diode rectifier - converter configurations are compared in terms of cost, complexity and control requirements. It is found that the combination of a simple diode bridge rectifier, dc boost circuit and hard-switching inverter typical of commercially available converter modules offers a good mix of low cost and flexibility, though controllability is somewhat limited by the passive nature of the rectifier stage.

Finally, the paper by Emhemed et al. [61] gives an overview of the performance of direct-connected single phase induction generators typical of those used in μCHP systems. Particular attention is paid to the transient stability of low-rated machines in response to faults on the 400V and 11kV networks. It is found that for LV networks with high penetrations of small induction machines, fault ride-through is of concern due to the lack of speed control in grid-connected mode. It is noted that the use of static VAR compensation to mitigate voltage dips on such a network shall improve the stability margin of all adjacent machines, and recommends an aggregated approach to such remedial measures based on considerations of cost and complexity.

1.2.3 Impact on Grid Operation

Regardless of the particular technologies employed, mass-integration of SSEG into low-voltage power networks will increasingly impact upon the operations of the DNOs. A number of authors have identified symptoms associated with increasing SSEG penetration

levels [25, 62–66], and impact studies of the following are numerous in the literature:

- Network power flows.
- Voltage regulation, rise and unbalance.
- Distribution system losses.
- System fault levels.
- Harmonic and DC current injection.
- Reliability and outage probability.

The above effects may be variously beneficial or detrimental to operation of the distribution networks, dependent primarily on the percentage penetration of SSEG relative to feeder capacity. Studies of these phenomena are reviewed in the following subsection.

1.2.3.1 Power Flows

In the paper by Thomson and Infield [67], the authors present a developed load-flow analysis tool for the evaluation of time-varying power flows on LV networks with high penetrations of grid-connected PV and μCHP systems. This tool is used to simulate mean voltage and network losses on a real 11/0.4kV network in Leicester, in order to determine feasible penetration levels of SSEG according to the 10-minute mean voltage range allowance BS EN 50160 [68]. It is found that a combined penetration of PV (28% of customers) and μCHP (23% of customers) marginally satisfies the requirements of BS EN 50160 without the need for network alterations. It is noted that increasing capacity beyond these limits by adjustment of LV transformer taps is not necessarily the best course of action as minimum winter voltages remain largely unchanged, particularly in the case of high PV penetration. A system of distributed automatic voltage control (DAVC), in which SSEG inverter interfaces supply or consume reactive power as a means of network voltage improvement, is proposed.

A feature of high SSEG penetration is a reduction in mean net feeder demand. Due to source variability, however, predictability of instantaneous power flows on the network will be reduced in relation to a more traditional demand model. In cases where peak generation is coincident with times of minimum demand, power flows across the

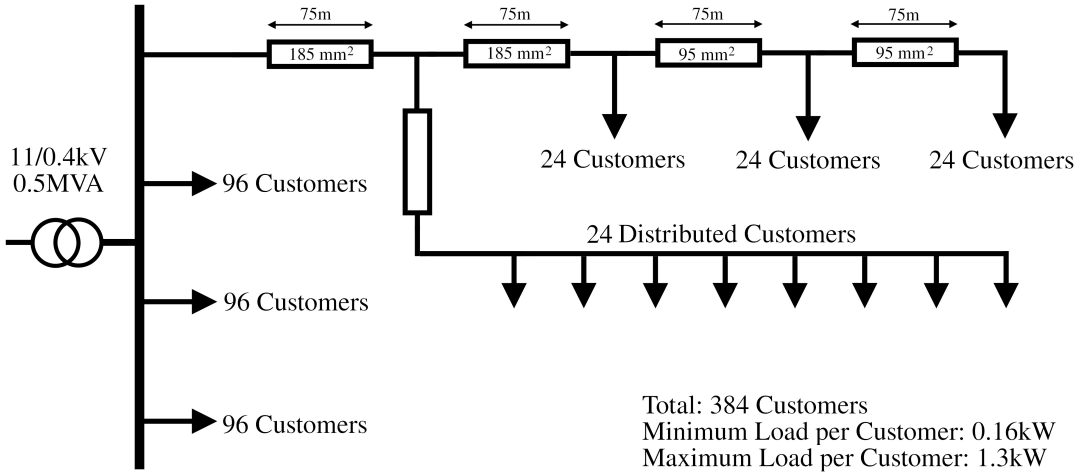

Figure 1.7: Generic UK LV Distribution Network as Presented in [23, 25, 33]

11/0.4kV and primary transformers may be reversed. This aspect has been investigated by Cipcigan and Taylor [23] with regard to the penetration of small wind turbines, using a PSCAD model of the UK generic LV network illustrated in Figure 1.7.

The authors found that with a minimum average customer demand of 0.16kW and accounting for diversity of generator output, reverse power flow across the 11/0.4kV transformer occurred at a penetration threshold of only 10% of primary transformer capacity. Reverse flows across the primary transformer itself were observed at penetration in excess of 82.5%, with typical transformer power handling capability being exceeded for a 100% penetration scenario, in which a $1.1kW_e$ source is installed in the home of each individual customer.

Trichakis et al. [25] also make use of the UK generic LV network to evaluate the maximum allowable penetration of SSEG on a single 0.5kVA LV feeder, supplying an average 384 customers. Based solely on cable and transformer thermal limits, and an even radial distribution of generator infeed, a maximum allowable penetration of $610kW_e$ was determined for generators operating at unity power factor. This allowance is reduced to 585 and $550kW_e$ for 0.95 leading and 0.95 lagging power factors respectively, reflecting the narrow operating range of a typical grid inverter.

Conti et al. [69] investigate allowable penetration levels of SSEG in the context of transformer and cable thermal constraints, and attempt to evaluate the maximum

current injection achievable without violating thermal limits. The authors found that allowable penetration of SSEG decreases with an increase in radial distance from the LV transformer bus to the point of current injection. A critical voltage rise Δu_C is also defined as the voltage increase above nominal at which thermal constraints, rather than voltage rise, determine the current injection limits of the network. It is determined that if the existing supply voltage limit Δu_{max} lies above the critical value, there is no technical benefit in further increasing that limit to accommodate additional generating capacity. The effect of injection distance z' and capacity plateaus due to Δu_C are both visible in Figure 1.8, with currents normalised to the thermal limiting value at the most remote node of the network ($I_{L'max}$).

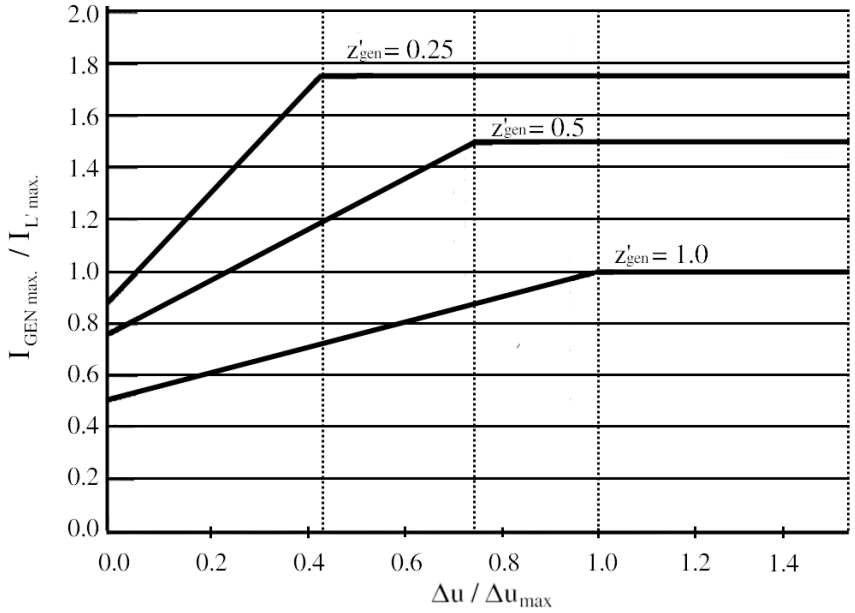

Figure 1.8: Maximum Permissible Current Injection as Function of Voltage Rise, Equipment Thermal Limits and Radial Feeder Position [69]

Finally, Bärwaldt and Kurrat [70] investigate the potential for using distributed energy storage as a means of reducing peak power flows across the 11/0.4kV transformer due to temporal fluctuations in the output of PV systems. Such an approach would have the benefit of increasing the allowable penetration of SSEG beyond that defined by thermal limits in [69]. The authors present laboratory and simulation results of an 0.8kW PV array with on-site battery storage overseen by an energy management system. An overall long-term efficiency of 67.5% is recorded, highlighting one of the many economic barriers to mass adoption of distributed storage.

1.2.3.2 Voltage Control

Lyons et al. [33] and Trichakis et al. [22, 25] present studies of voltage regulation, voltage rise and phase imbalance on LV networks due to the integration of SSEG, using the generic LV network model of Figure 1.7. Voltage *rise* was found by the authors to be the limiting factor above all others determining the maximum volume of SSEG within a given LV network. In the case of the generic UK network, with four feeders downstream of the 11/0.4kV transformer and assuming a uniform distribution of generation, a limit of $185kW_e$ of SSEG capacity at unity power factor was determined, equivalent to approximately $0.48kW_e$ per customer. The power factor of the generators impacts greatly upon the total allowable SSEG volumes, as can be seen from Table 1.5.

Table 1.5: Penetration Limits (kW) Downstream of the 11/0.4kV Transformer due to Voltage Rise, Regulation and Unbalance (Generic UK Network) [25]

Condition	Voltage Rise	Regulation	Unbalance (per feeder)
Unity PF	185	770	47.8/ph.
0.95 Leading	380	860	49.5/ph.
0.95 Lagging	123	615	46.1/ph.
2x Line Impedance	92	385	29.0/ph.

The limiting value of SSEG penetration due to Voltage Regulation is considerably higher at approximately $2kW_e$ per customer, exceeding the maximum value imposed my the thermal rating of the transformer. The authors identify Voltage Unbalance as the secondary limiting factor, assuming that the problems associated with voltage rise can be overcome. Voltage unbalance, defined as the maximum deviation of each individual phase value from the average of the three-phase voltages or currents, may be represented using the Voltage Unbalance Factor (%VUF) defined in [22] as:

$$\%VUF = \frac{Negative\ Sequence\ Component\ V_2}{Positive\ Sequence\ Component\ V_1} \times 100 \tag{1.2}$$

The %VUF is subject to a UK statutory limit of 1.3% (2% for short term deviations of less than 1 minute). Based on this criterion, the authors have determined the maximum phase bias of SSEG allowable on a single LV feeder (assuming an extreme condition with all generators connected to one phase), which are summarised in the third column of Table 1.5. SSEG capacity limits based on voltage unbalance are far less sensitive to deviation in generator power factor than those based on voltage rise.

Indeed, at unity power factor, the capacity limits are equivalent given that each 0.5MVA transformer supplies four identical feeders. The effect of the cable impedance is far greater, with a doubling of Z reducing allowable SSEG volumes by around 40%.

Chiradeja and Ramakumar [62,63], in their work on quantifying the system benefits of distributed generation have proposed an indexing system for comparison of different embedded generation scenarios. Three indices are defined for the evaluation of voltage profile improvement (VPII), line-loss reduction (LLRI) and environmental impact reduction (EIRI), with an overall benefit index (BI) calculated as a weighted sum according to the priorities of the DNO.

The VPII is defined as the ratio of the voltage profile measure VP in cases with and without distributed generation. VP itself is calculated using Equation (1.4), where N is the total number of network load buses, V_i is the p.u. voltage at bus i, S_i is p.u. load at i, and k_i is a weighting factor reflecting the criticality of a given load. In all cases, k_i must satisfy Equation (1.5).

$$VPII = \frac{VP_{with\ SSEG}}{VP_{without\ SSEG}} \tag{1.3}$$

$$VP = \sum_{i=1}^{N} V_i S_i k_i \tag{1.4}$$

$$\sum_{i=1}^{N} k_i = 1 \tag{1.5}$$

Simulations are performed to evaluate each index, together with weighting-factor sensitivity analyses, for a 12-bus 33kV network. Such a benefit indexing method could conceivably be applied at low-voltage for the assessment of SSEG integration scenarios.

Another paper by Conti et al. [71] concerns the development of analytical methods to evaluate the impact of SSEG on network voltage profiles, and thus the maximum allowable volume of embedded generation that may be connected to a single feeder without the need for relaxation of statutory supply voltage limits. For a single feeder of unit length, the maximum permissible current injection at any position z'_{gen} is presented in Figure 1.9 for a range of normalised load distribution factors λ_{LN}.

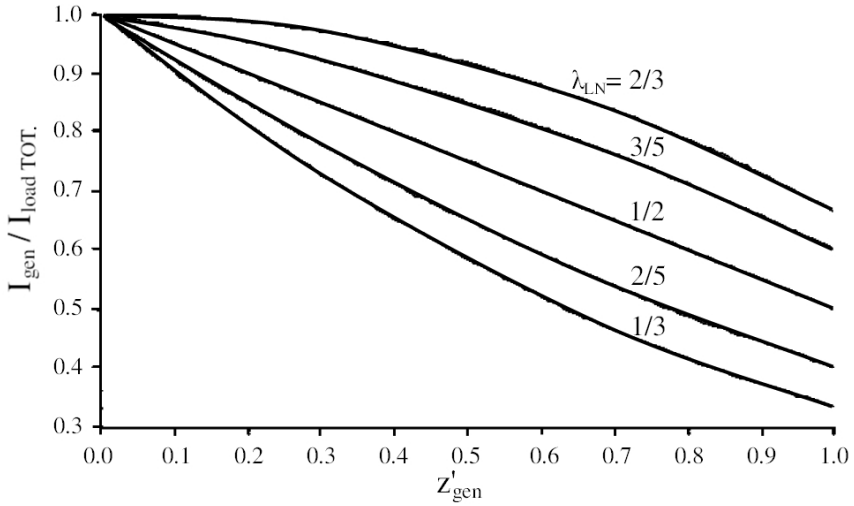

Figure 1.9: Allowable SSEG Current Injection at Radial Position z'_{gen} for Different Load Distributions λ_{LN} [71]

The factor λ_{LN} is a measure of the uniformity of load distribution on the feeder. It is the equivalent normalised radial distance from the transformer bus of a single lumped element representation of the distributed load profile of the feeder. It is calculated using (1.6), where z' is the normalised radial distance and i_L is the distributed load current as a function of z'.

$$\lambda_{LN} = \frac{\int_0^1 z' \cdot i_L(z')dz'}{\int_0^1 i_L(z')dz'} \tag{1.6}$$

With reference to Figure 1.10, a uniformly distributed feeder load has $\lambda_{LN} = \frac{1}{2}$, while a triangularly descending load profile gives $\lambda_{LN} = \frac{1}{3}$. Thus, from Figure 1.9, a feeder load bias toward the remote end of the line increases the scope for voltage improvement, raising the headroom for generator current injection i_{gen} as $z' \to 1$.

Fletcher et al. [72] investigated the potential for voltage support in rural feeders using distributed grid-tied PV. The authors noted significant voltage profile improvement in networks with near unity load power factors, as illustrated in Figure 1.11. For lagging power factors below 0.7, the inability of a small grid inverter to provide reactive compensation means that only minimal gains in line capacity can be made using SSEGs.

The presence of SSEG may be beneficial in maintaining statutory voltage limits

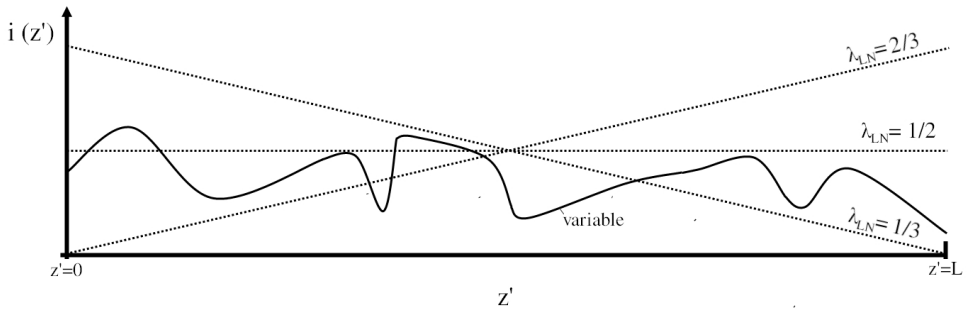

Figure 1.10: Uniform and Triangular LV Feeder Load Profiles [71]

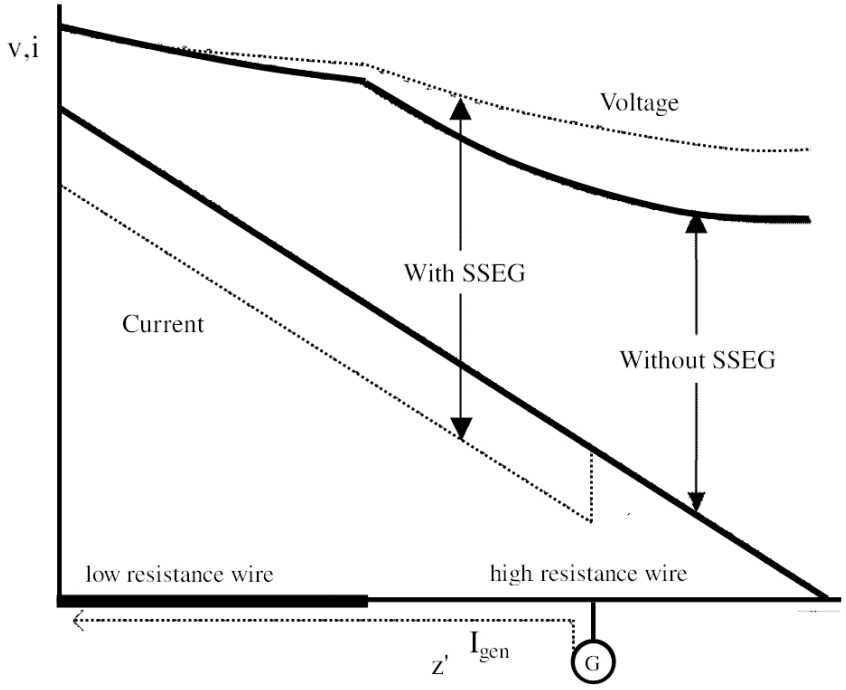

Figure 1.11: Voltage Profile Improvement and Reduced Line Capacity Usage on a Rural LV Feeder with SSEG and Near-Unity Power Factor Load [72]

during system voltage dips. Renders et al. [73] attempt to evaluate, and propose improvements to, the system voltage dip immunity of voltage source converter based SSEG interfaces. It is of note that generators rated below 16A per phase must disconnect from the grid within 1 second in response to prolonged voltage dips below 90% of nominal [5,6]. It is important that the response time of the disconnector is sufficient to distinguish between short duration dips of the order of 1 or 2 cycles, and the prolonged dips specified in ER G83/1. The authors note that high penetrations of SSEG with overly sensitive voltage dip detection, rather than supporting the voltage may lead to more severe voltage dip conditions as generating capacity is removed from the network.

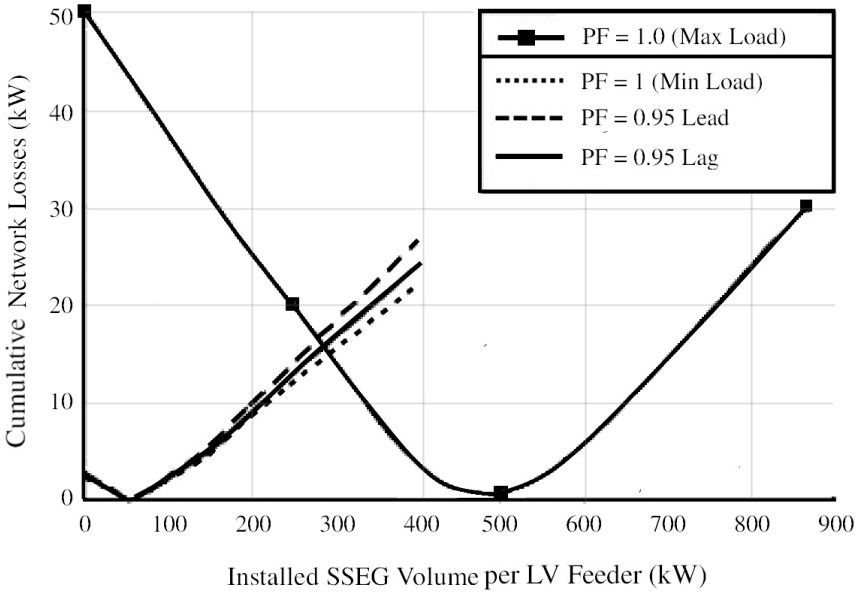

Figure 1.12: Impact of SSEG on Networks Losses [25]

1.2.3.3 Losses

One of the potential benefits of SSEG from a network operator's perspective, as identified by a number of authors, is a reduction in I^2R losses as transmission and distribution capacity is freed up. As a best-case indication of loss reduction, one might assume the output of a given SSEG or cluster of SSEGs to coincide with the time of peak demand, thus curtailing the maximum current flows on the network. In reality, however, as with any detailed system impact study, the variability of PV and CHP and locally stochastic output profile of wind generation must all be accounted for.

In addition to their work on voltage rise, reverse power flow and thermal limit considerations, Trichakis et al. [25] investigate the impact of SSEG on network losses downstream of an 11/0.4kV transformer using the generic UK distribution network model (Figure 1.7). Instantaneous network losses are evaluated downstream of the 11kV bus under average customer maximum load ($1.3kW_e$) and minimum load ($0.16kW_e$) conditions, for a range of SSEG infeed volumes. The observed characteristics are illustrated in Figure 1.12.

As one might expect, losses on the network are minimised in instances where local generation matches local demand. Due to the variability of both load and source, however, optimal loss minimisation scenarios will rarely occur in practice without

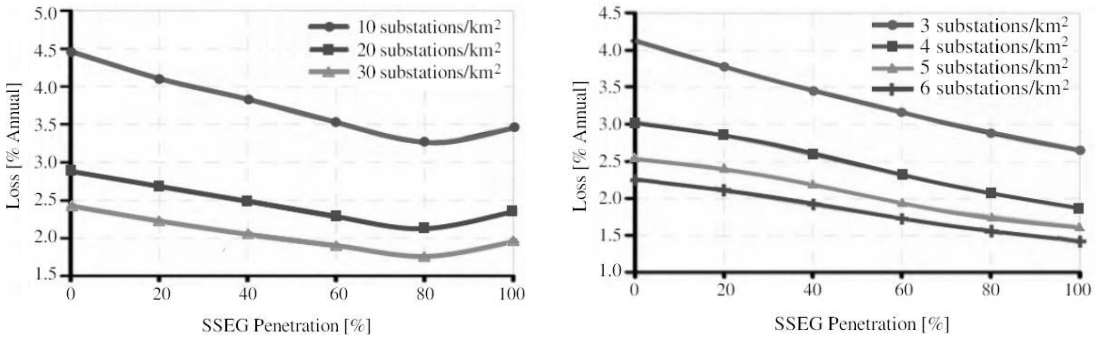

(a) Suburban (b) Rural

Figure 1.13: Annual Network Loss Reduction with Increasing SSEG Penetration [66]

additional load control. Figure 1.12 does highlight one important consideration - the coincidence of high SSEG availability and low local load may inadvertently lead to an increase in network losses. There will, therefore, be an optimal SSEG penetration for loss reduction on a given feeder loading profile. It should also be noted that both load and generation are assumed to be uniformly distributed along the line.

While extreme operating scenarios offer an insight into network loss reduction with SSEG, a more thorough evaluation requires the investigator to take a long-term perspective. Such an approach might account for hourly or half-hourly load/generation variability in order to compare cumulative energy losses over the course of a year.

Silva and Strbac [66] take a more detailed approach to the evaluation of network losses with different penetrations of PV and μCHP. The authors' models, based on real distribution network topologies, account for the hourly and seasonal variability of customer demand and SSEG output in order to evaluate losses as a percentage of annual energy demand. Figure 1.13 illustrates the impact of each SSEG technology on the losses in suburban and rural networks with different substation densities.

Percentage penetration here is defined as the proportion of customers with either a $1.1kW_e$ rated μCHP or $1kW$ PV installed. It can be seen that despite reverse power flow losses at peak generation with minimum load as predicted in [25], the net annual energy loss is consistently reduced by an increase in SSEG penetration.

Finally, Chiradeja and Ramakumar [63, 74, 75] in their work on benefit indexing

of SSEG in LV networks have proposed a Line-Loss Reduction Index (LLRI) for the comparison of different penetration scenarios. In a similar manner to their voltage-profile improvement index, the LLRI is determined by comparison of the total line losses (LL) before and after addition of SSEG to an LV feeder as given in Equation (1.7).

$$LLRI = \frac{LL_{with\ SSEG}}{LL_{without\ SSEG}} \tag{1.7}$$

$$LL = \sum_{i=1}^{M} I_i^2 R_i D_i \tag{1.8}$$

The quantity LL is the sum of losses in each section of cable or overhead line, as calculated in (1.8), where I_i is the current flowing in the i^{th} line, R_i is the resistance per unit length of conductor i, D_i is the length of the i^{th} conductor and M is the total number of constituent line segments. Using this definition, the LLRI is in fact the per-unit power loss as related to the 11/0.4kV transformer rating, which can be straightforwardly calculated if all power flows into and out of the network are known. Otherwise, current probes must be inserted into, and R_i evaluated for, each line segment. The authors demonstrate the use of the LLRI by application to a 33kV meshed network with distributed generation, but it can similarly be applied at Low-Voltage.

1.2.3.4 Additional Considerations

Other technical considerations relating to the connection of SSEG to utility networks are summarised by O'Gorman and Redfern [65]. In addition to the impact studies already discussed, the authors are primarily concerned with the behaviour of LV networks under fault conditions, where a portion of fault current is supplied by embedded generation. It is noted that fault current contribution from a remote end of a feeder may result in maloperation or delayed operation of protection systems, and that low inertia sources with power electronic interfaces can easily lose synchronism during a fault.

High speed disconnection of SSEGs under fault conditions as specified in ER G83/1 [5] is therefore required, but this has the detrimental effect that unfaulted generators are unavailable during the post-fault system recovery. The improvement of SSEG fault ride-through capability is of course key to the successful development of islandable microgrid system models, but such scenarios are beyond the scope of this thesis. We

consider all SSEG in later chapters to act only as a switched negative load, as currently treated by all UK DNOs.

Schwaegerl et al. [76] present an indexing system to evaluate the impact of distributed generation on LV network reliability. Reliability indices based on a number of measures are developed, as summarised in Table 1.6.

Table 1.6: LV Network Reliability Indices as per [76]

	Index	Unit
F_i	Supply Interruption Frequency	*per-annum*
D_i	Mean Duration of Interruption	*hrs* or *mins*
Q_i	Annual Unavailability	*mins/yr*
P_i	Cumulative Interrupted Power	*MVA/yr*
E_i	Cumulative Energy Not Supplied	*MVAh/yr*
C_i	Cumulative Interruption Cost	*£/yr*

By application of this indexing system to a representative residential 20/0.4kV distribution system in Germany, it is demonstrated that a minimum reliability cost exists at the equivalence point of interruption and investment costs. Though DNO operating costs have little bearing on this work, a similar evaluation system might be employed to determine the likelihood of encountering a given SSEG network penetration scenario. The associated overall reliability index can also be used as an indicator of the number of SSEG disconnection events that may be encountered in any one year.

Finally, a number of impact studies relating to power quality in LV netwotks have been performed. Good examples include work by Bhowmik et al. [77] on allowable SSEG penetration in accordance with supply harmonic limits, and the work of Gertmar et al. [78] on DC current injection with non-isolated grid inverters.

Supply harmonic limits provide an additional criterion for determining SSEG capacity scenarios, but are assumed to be less severe than the voltage rise limits presented in [25]. DC injection meanwhile has been largely eliminated from the studies presented in later chapters by use of isolating toroidal step-up transformers between the power electronics and output filter stage as in Figure 1.14 (typical of manufacturers' single phase inverter designs), but transformer-less configurations could be included if required.

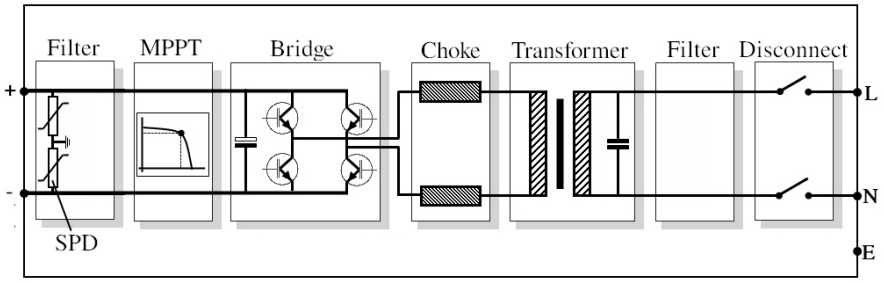

Figure 1.14: Typical PV Grid Inverter Configuration [79]

1.3 Transients in Low-Voltage Systems

As noted earlier in this chapter, the treatment of switching transients arising within LV networks as a direct result of SSEG integration has received little or no attention in the literature to date. There are, however, a number of more general transient measurement, surge propagation and power quality assessments which may be used as a benchmark for results comparison.

1.3.1 Transient Measurement Studies

Two classic measurement studies of short duration transients in LV networks are of note. Bull and Nethercot [80] present results of a project that gathered some 36,000 event records over a period of approximately three months, at 19 locations in and around the Electrical Research Association (now ERA Technology) headquarters at Leatherhead in Surrey. Measurement locations were split among domestic premises, small industrial supplies and local Area Board substations. In a similar fashion, Goedbloed [81] presents an analysis of 28,000 transients logged at 40 domestic, business and industrial locations in Eindhoven, the Netherlands, collected over a total of 3,400 measurement hours.

At the service cable entries of domestic premises, both papers report a high incidence of transient activity in the magnitude range 50-100V, with a roughly ten-fold decrease in incidence frequency for each doubling of the magnitude. Incidence rates presented in both papers are summarised in Figure 1.15.

Neither author has reported measured transient voltage peaks in excess of 500V (1.5pu) at the domestic customer supply point. This contrasts sharply with business and industrial customers who may experience transient voltages in excess of 1000V. To

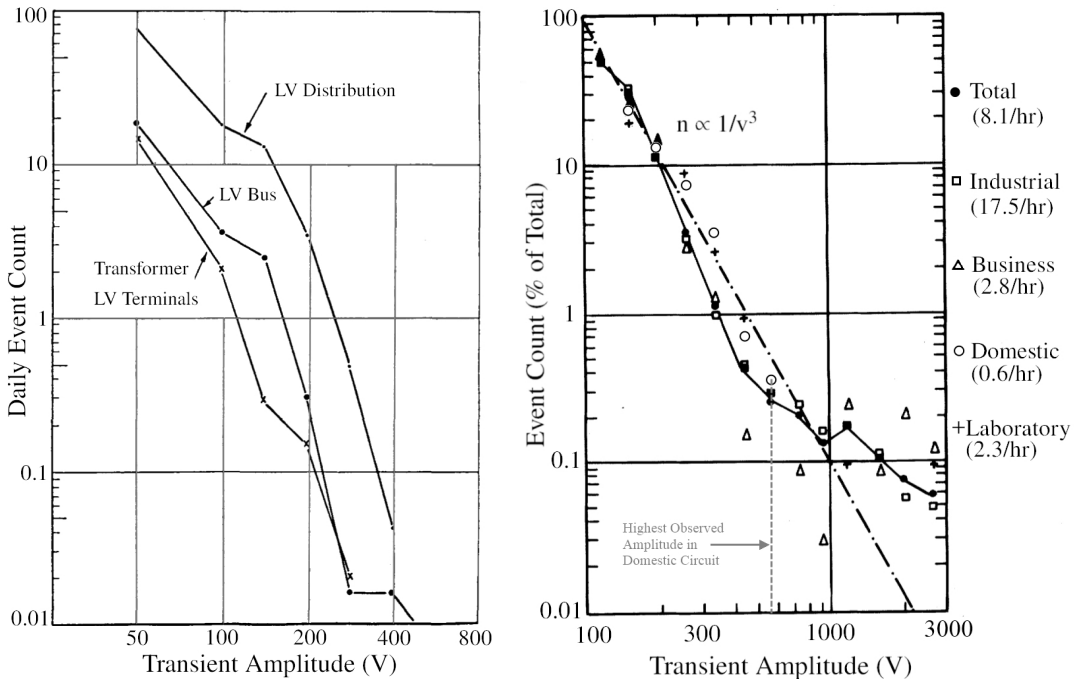

(a) Daily Event Counts [80]

(b) Event Frequency by Location [81]

Figure 1.15: Magnitudes and Incidence of Transients in LV Supply Networks

be of concern from a protection standpoint, phenomena investigated within this thesis would need to cause some alteration in the measured incidence characteristics. However the origin of a transient, be it due to atmospheric effect, network switching operation or occurring within the home itself, is also important.

Bull and Nethercot also note that the incidence rate of transients of a given magnitude is reduced by a factor of ten at the 11/0.4kV transformer terminals in comparison to the customer supply point, as may also be seen from Figure 1.15. A modified form of the filter design presented in [80] is used for the capture of low magnitude transients presented in Chapter 4, together with a post-process analysis technique based on equivalent EMC pulse waveshapes, similar to that presented in [81].

Other papers used for reference and guidance on measurement techniques were an analysis of low-voltage main transient designs by Rhoades [82]; Measurement of transients at the customer bus due to load energisation (Tjäder and Daadler [83]), the operation of utility switched capacitors (McGranaghan et al. [4]); and an analysis of ultra wide band (UWB) transient propagation in single-phase 230V domestic cabling by Månsson et al. [84, 85].

1.3.2 Surge Propagation and LV Transient Suppression

Simulation studies of transient conduction into and propagation through LV networks have been performed by Ametani et al. [86], Pazos et al. [87] and Metwally and Heidler [88]). Further detailed discussion is presented in section 1.4.

Devices for the suppression of transient overvoltages at LV are typically geared toward minimising the effect of conducted and induced lightning strokes in overhead distribution lines. Osmokrovic et al. [89] describe a test methodology to determine the volt-ampere and volt-ohm characteristics of an LV surge protective device (SPD). A useful review of LV surge overvoltage protection devices and terminology can be found in [90].

The protective levels and distances of LV SPDs are evaluated for different cable types and earthing arrangements by Fiamingo et al. [91]. The authors conclude that for systems equipped with protective earth conductors, the protection distance covered by an SPD may reduce to less than 1m, making protection of an entire domestic installation very costly. A preventative rather than curative approach has, therefore, been proposed in the simulation scenarios of Chapter 6.

1.3.3 Power Quality Implications of SSEG

Harmonic current injection from SSEG inverters and low magnitude voltage spiking due to frequent switching of disconnectors must both be considered from the perspective of power quality. The former have been investigated by Silva et al. [92] on an example network with an uneven penetration of inverter interfaced SSEG equivalent to 25% of the transformer rating. In the case of an urban network, three load scenarios (25%, 50% and 75%), of which a fixed proportion of 80% are non-linear, has been considered. The authors observed the most significant increases in total harmonic distortion (%THD) and neutral rms voltage rise for the low load case, but in none of the scenarios encountered were statutory limits imposed by the standards exceeded. A line diagram of the simulated urban network and key results are depicted in Figure 1.16. Higher penetration scenarios were not considered by the authors.

Tse et al. [93] present a fluctuation detection algorithm based on Continuous

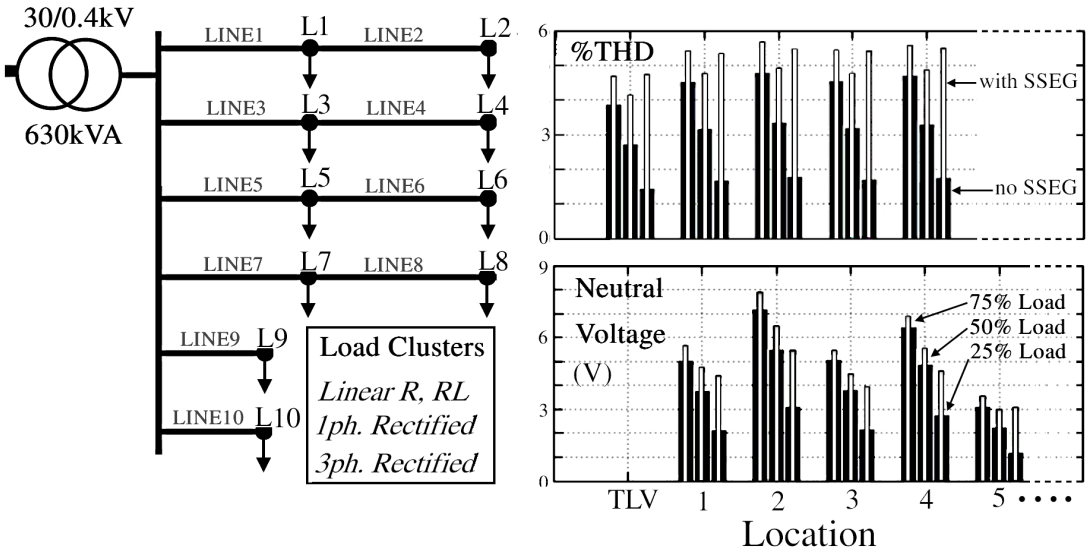

Figure 1.16: Effect of Inverter Based SSEG on %THD and Neutral Voltage Rise in the Simulated Network of [92]

Wavelet Transforms that, in addition to evaluating the harmonic content in a given voltage waveform, is capable of determining the magnitude and frequency of a single superimposed oscillatory transient. This method may be applied to simultaneous power quality and transient analysis without the requirement for separate measurement systems.

Finally, Pezos and Navarro [94] discuss field experience of power frequency overvoltages in networks with wide scale adoption of PV systems. The overvoltages reported occur in the time window between grid isolation of one or more inverters due to operation of upstream circuit breakers, and the subsequent disconnection of the sources in response to their local Loss of Mains (LoM) protection, as depicted in Figure 1.17 for a $25kW_e$ three phase device. Peak phase-neutral overvoltages in excess of 3.5pu have been measured by the authors, and damage to revenue meters and other low voltage equipment attributed to these phenomena.

1.4 Time-Domain LV Network Simulation

The final topic of this review concerns the application of digital simulation to the solution of low-voltage transient problems, with particular reference to the modelling of LV cables and overhead lines, distribution transformers, switches and sources.

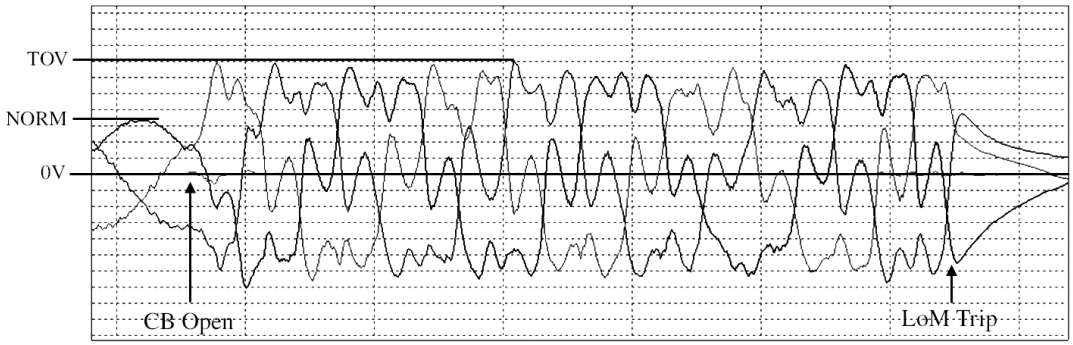

Figure 1.17: Temporary Overvoltages on Upstream Isolation of PV Inverter (25kW,3ϕ) [94]

1.4.1 General

The primary simulation software employed in this work is a widely used royalty-free distribution of Bonneville Power Administration's *Electromagnetic Transients Program* (EMTP). The Alternative Transient Program (EMTP-ATP), which was developed following attempts to commercialise the previously public domain EMTP in the early 1980s [95], is together with a number of pre/post-processing tools distributed free of charge for academic and non-commercial use under authority of the European EMTP User Group (EEUG).

The basic time-domain digital solution method of the EMTP-ATP is based on the algorithm presented in the 1969 paper by Dommel [96]. Many additional tools have since been incorporated in order to expand software capability. These include frequency dependent travelling wave line models (J. Marti, Noda . . .) [97,98], nonlinear components for representing varistor characteristics and transformer core saturation [99] and supplementary tools for including and analysing control systems [100].

Specifics of the literature relating to formulation of network components and their application in time domain simulation are discussed in the succeeding sub-sections. General guidance on simulation component parameter estimation is given by the series of papers by Martinez et al. [101–107], which have been used extensively in the construction of the network models presented in Chapters 5 and 6.

1.4.2 Cable and Line Modelling

Many of the considerations facing the researcher studying travelling wave propagation in low-voltage networks apply equally to the field of power-line communication (PLC). Existing research in the modelling of PLC systems is of great use as an indicator of good quality line and cable modelling at 11kV and 230/400V. An introductory comparison of the different line/cable models and their characteristics is provided by Hevia [108], ranging from the simplest lumped element equivalent PI model to the more advanced modal and phase domain frequency dependent models of Martí and Noda respectively.

It is noted that the PI approximation, used extensively in early incarnations of the developed network models, is far from the best choice of line representation whenever accurate broad-band frequency response is required. This is due (a) to the fact that the model components are evaluated at a single frequency, with degradations in accuracy appearing with deviation from the specified solver frequency; (b) the lumped approximation may result in spurious damped oscillation in the results which do not appear in practice; and (c) the cascaded PI lumped approximation approach results in a network model with many more solver nodes than there are physical system nodes, imposing limits on the complexity and efficiency of the final simulation [108].

The solution is to employ a frequency-dependent line model, defined by its characteristic admittance and propagation 'constant' which themselves are rational functions of frequency. Options are primarily limited to the indirect modal domain model of J. Martí, and the direct phase domain model of T. Noda, the benefits and drawbacks of each model being discussed in Chapter 2.

The paper by Tran-Anh et al. [109] discusses the use of a J. Martí frequency dependent transmission line for modelling medium and low voltage cabling for PLC applications. The MV cable model developed uses three single phase sheathed cables in a triangular arrangement, like that in Figure 1.18; a geometry that is simple to implement in the Line and Cable Constants (LCC)routine, but ignores any outer structure such as bedding, wire screens and external insulation. The authors accordingly claim reasonable results with this method.

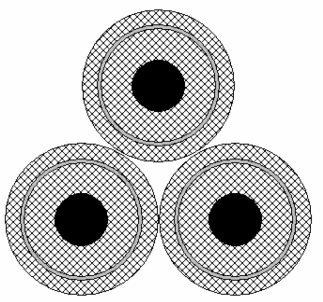

Figure 1.18: Cross-section of MV Cable Model as in [109]

Of greater interest in this particular study, however, is the modelling of the LV distribution trunk and service cables, details of which the authors do not divulge in their paper. The modelling of LV cables is greatly complicated by complex geometry and proximity effects, neither of which are particularly well handled by the LCC routine and parameter determination subroutines in EMTP [110]. A typical sectored 3-phase trunk cable with concentric neutral is depicted in Figure 1.19.

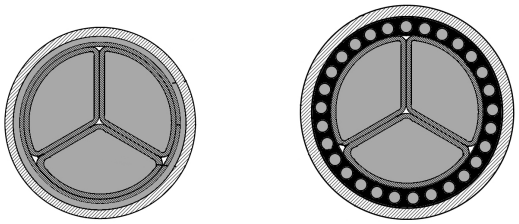

Figure 1.19: Cross-section of a Typical LV Distribution Cable [111]

Arguably, the best approach to the problem of modelling concentric neutrals is to make use of the LCC Cable Pipe (CP) model. The alternative methods available for determining CP model parameters are compared in the paper by da Silva et al. [112]. Along with two of their own proposed methods, the authors discuss and compare results for the simplified method of Ametani, neglecting proximity effects and assuming infinite pipe thickness, and the more detailed method of Kane, which accounts for conductor proximity and for which a finite pipe thickness may be specified.

At frequencies approaching 50Hz, the authors note that with respect to Kane's method, the assumption of infinite thickness in non-magnetic pipes introduces significant error in both self- and mutual- components of the line impedance matrix. These errors diminish at higher frequencies as the effect of the skin depth in the pipe begins to

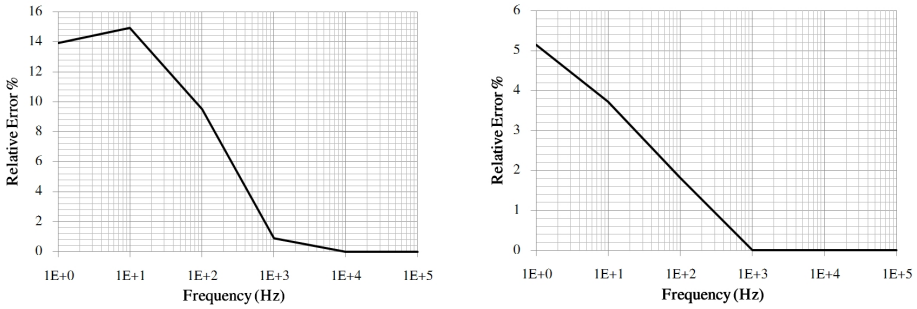

(a) Self Resistance R_{nn} (b) Self Inductance L_{nn}

(c) Mutual Resistance R_{nm} (d) Mutual Inductance L_{nm}

Figure 1.20: % Error in Self- and Mutual-Impedance Components of a 2-Phase Cable Pipe (*Infinite* Pipe Thickness, Proximity Effect *Included*) [112]

dominate, as may be seen from the plot in Figure 1.20.

By contrast, neglecting proximity effects in a cable was found to increase errors in the resistive components of $[Z]$ at high frequencies, particularly in the case of the mutual resistance R_{nm} as shown in Figure 1.21. For good accuracy at both 50/60Hz and at high frequency, cable pipe models should ideally incorporate both proximity effects and assume a finite pipe thickness. Parameter sensitivity analysis of the various cable models employed may be found in Appendix D.

High-frequency modelling of indoor single-phase cabling for PLC applications has been performed by Andreou et al. [113,114]. The authors compare series resistance and inductance values obtained with the EMTP-ATP CABLE CONSTANTS/PARAMETERS routine with those obtained by a finite element method (FEM), for $2.5mm^2$ PVC insulated copper conductors in both flat and circular arrangements as illustrated in Figure 1.22.

It is noted that for cable models in which the earth is neglected, the series resistance

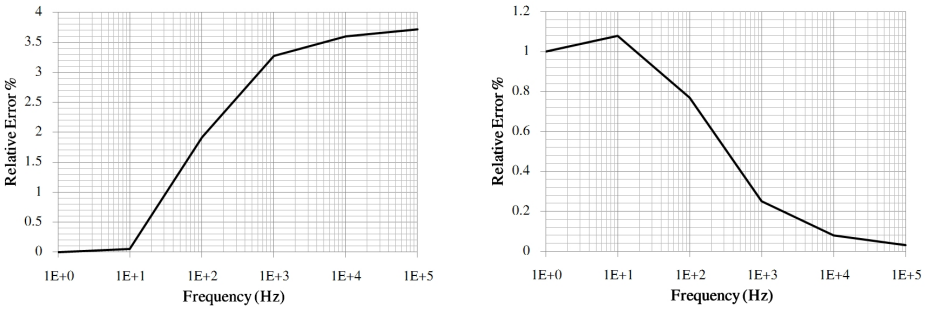

(a) Self Resistance R_{nn}

(b) Self Inductance L_{nn}

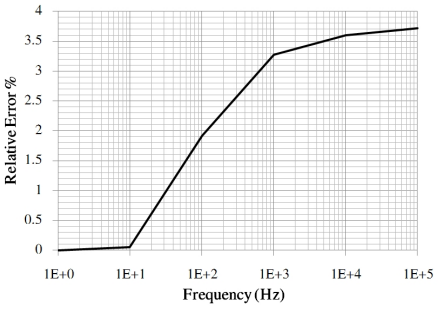

(c) Mutual Resistance R_{nm}

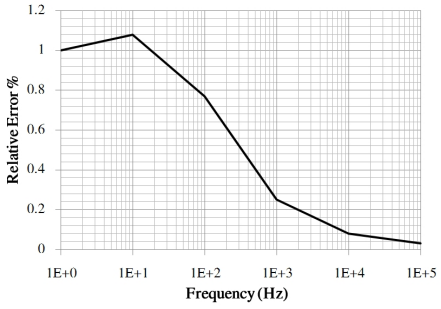

(d) Mutual Inductance L_{nm}

Figure 1.21: % Error in Self- and Mutual-Impedance Components of a 2-Phase Cable Pipe (*Finite* Pipe Thickness, Proximity Effect *Ignored*) [112]

(R_{11}) calculated by the EMTP and FEM methods agree to within a margin of 5% over the frequency range 50Hz to 1MHz. The self inductance (L_{11}), however, is subject to a fixed error of approximately 25%. If the earth is not neglected, the error in L_{11} at 50Hz remains large (approximately 20%), but reduces to below 5% at frequencies above 10kHz. Of concern is the significant error introduced in the calculation of R_{11} over the range 0.5-500kHz, peaking at 34% at approximately 10kHz. The authors suggest marginal conformity to assumptions of Carson's equation/correction terms as the source of observed errors.

By contrast, the modelling of for rural overhead cables is relatively straightforward due to the simple geometry of the problem. Detailed studies in EMTP of LV and MV overhead distribution lines may be found in [115] and [116] respectively, the latter being used to determine the attenuation of high frequency signals for different customer load types.

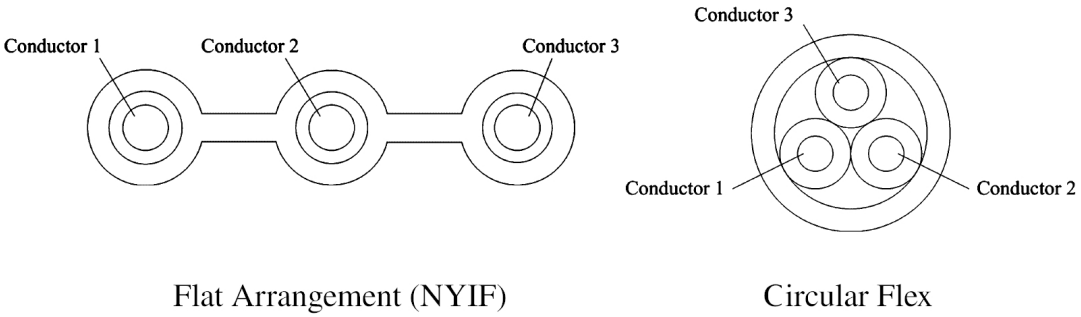

Figure 1.22: Illustrative Domestic Cable Cross-sections Used in [113, 114]

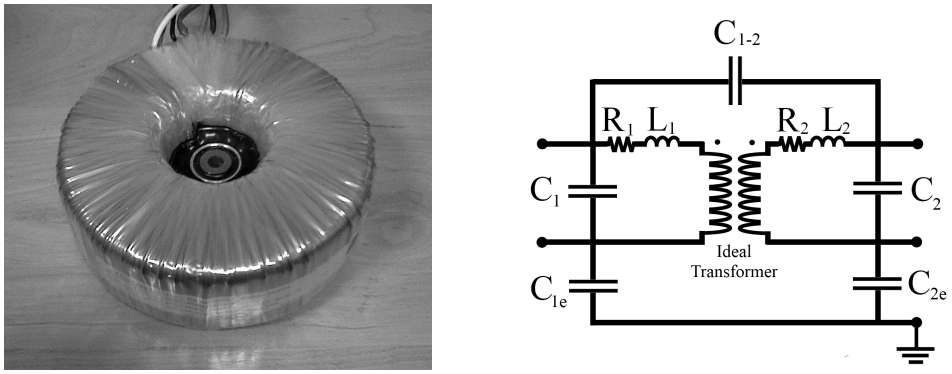

(a) 700VA Inverter Transformer (b) Equivalent Circuit

Figure 1.23: Toroidal Transformer Representation for Fast-Transient Study [104, 120]

1.4.3 Transformers

Modelling of the LV distribution transformer for fast-front overvoltage studies has been performed by Mikropoulos et al. [117]. The most common transformer configuration encountered in this work however is the single-phase toroidal transformer, common to the vast majority of converter interfaces. Models of such transformer configurations are non-existent in the literature. High frequency components of the transformer required manual derivation from laboratory test results by reference to [104, 118, 119].

The final iteration of the toroidal transformer model consists of a linearised magnetic circuit with lumped capacitances to represent primary, secondary and inter-winding stray effects, as shown in figure 1.23. Detailed discussion of the transformer models and other network components can be found in Chapter 5.

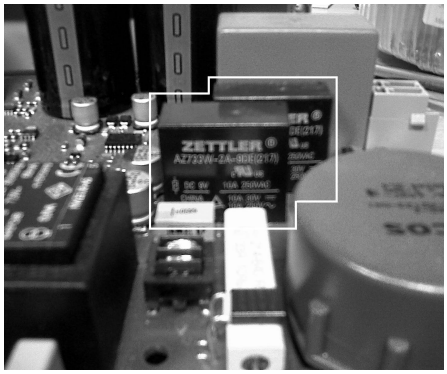

(a) Typical Protection Relays

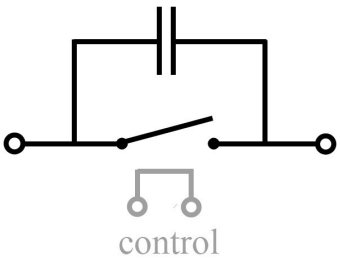

(b) Equivalent Circuit

Figure 1.24: Representation of Inverter Interface Relays in EMTP Simulation [121,123]

1.4.4 Relays and Circuit Breakers

As switching transient analyses shall constitute the vast majority of computational studies in this work, the correct modelling of low-voltage circuit breakers is of importance. Switching models vary widely in scope and complexity, from the most simple ideal open/short circuit [121] through to elaborate nonlinear representations of switching arc dynamics for the analysis of re-strike phenomena [122]. Due to the high recovery voltage withstand capability of typical 230V electromechanical relays, coupled with need to represent tens or even hundreds of independently specified switching operations, a simplistic approach was adopted for the of modelling these devices.

Relays have been here modelled as ideal switches in parallel with an open position contact capacitance obtained from the relevant relay datasheet. Series impedance in the closed position may be ignored as it is negligible in comparison with that of both the incoming circuit and the device being isolated. An example of this representation is given in Figure 1.24. Further detail may be found in in Chapter 2

1.4.5 Pertinent Studies

Electromagnetic transient phenomena arising due to small-scale embedded generators connecting to and disconnecting from low voltage distribution networks have not, to the author's knowledge, been the prime focus of any existing research to date. The somewhat broad nature of this review is testament to this assertion.

Of relevance is the study by Cipcigan et al. [124], of voltage control in LV networks with high SSEG penetrations and the effects on voltage quality of disconnecting and reconnecting small induction generators. The authors noted switching transient voltages of the order of 3pu and significant inrush currents at the generator terminals, resulting in temporary supply voltage sags. These are identified as issues of concern for scenarios involving large numbers of generators switching in response to common stimuli.

1.5 Relevant Standards

The following pertinent standards have been identified as relevant to this work, and are referenced at various points throughout the text.

Number	Part(s)	Description
BS EN 50438	-	Requirements for the Connection of Micro-generators in Parallel with the Public Low-voltage Distribution Network
BS EN 60071	1,2,4	Insulation Coordination.
BS EN 60664	1,2	Insulation coordination for equipment within low-voltage systems.
BS EN 60060	1	High-voltage test techniques.
BS EN 50160	-	Voltage characteristics of electricity supplied by public distribution networks.
BS 6662	-	Guide to methods of measurement of short duration transients on low voltage power and signal lines.
BS EN 50525	1,2	Electric cables. Low voltage energy cables of rated voltages up to and including 450/750V.
BS 6004	-	Electric cables: PVC insulated, non-armoured cables for voltages up to and including 450/750V.
BS EN 7870	1,3,5	LV and MV polymeric insulated cables for use by distribution and generation utilities.
BS EN 50182	-	Conductors for overhead lines. Round wire concentric lay stranded conductors.
BS 7671	-	Requirements for Electrical Installations IEE Wiring Regulations 17th Edition.
BS EN 60904	3	Photovoltaic devices. Measurement principles for terrestrial photovoltaic (PV) solar devices with reference spectral irradiance data.

1.6 Chapter Summary

In this chapter, a review of literature on the topics of embedded generation technology, low-voltage transient measurements and time-domain circuit simulation techniques has been presented. Given the relative novelty of electromagnetic transient studies at low voltages, particularly those relating to embedded generation, the number of immediately relevant research papers was found to be few. Accordingly, a fairly broad range of review topics has been included, covering published papers, standards and guidelines in the aforementioned areas. In the next chapter, suitability of electromagnetic transient simulation tools for low-voltage application is assessed.

Chapter 2

Time-Domain Simulation Suitable for Low-Voltage Systems

In this chapter, aspects of electromagnetic transient simulation pertaining to the modelling of low-voltage networks are discussed. Consideration is given to the modelling of individual network components and appropriate simulation setup criteria, with the ultimate goal of developing representative LV network, embedded source and load models in EMTP-ATP.

2.1 Overview of Time-Domain Simulation

Simulation of electrical networks is an essential process in the design and engineering of modern power systems. Where an existing system configuration is to be altered by some action, by addition or removal of generation, bulk load or transmission capacity, good simulation methods are necessary in order to predict and manage any associated changes in performance.

Steady-state simulations are used to approximate the power flows and voltage profiles across complex power systems under a given set of time-invariant conditions. Iterative computational methods, such as the Gauss-Seidel and Newton-Raphson algorithms [125], are widely employed in order to determine the power flow solution where the size and complexity of a network prohibits an efficient method of determining an exact analytical solution.

When the network configuration changes over time, or is subject to disturbance, a power system may be considered to occupy a transient state [126], and steady-state methods alone are no longer capable of computing the associated time-variant quantities. Thus, time-domain analyses become necessary to determine the dynamic performance of a large electrical network. This type of simulation constitutes a diverse range of possible system studies, broadly categorised in terms of their duration and constituent frequency components. These criteria in turn determine the time-step resolution necessary in order to observe and analyse a given phenomenon:

- Load and Generation Profiling [127]; Allow minute by minute or hourly assessment of load flow variations on a power system by computation of a sequence of steady-state snapshots ($1s < \Delta t < hours$).

- System Dynamic Simulations; Take account of the electromechanical and control characteristics of generators and loads in order to assess the system stability in response to a sudden change in configuration e.g. dynamic fault studies and assessment of power-frequency temporary over-voltages (TOV) due to switching, line/transformer energisation or resonance in networks with large LC components ($\Delta t \approx 1ms$).

- Slow-front Transient Analysis [120]; Typically associated with over-voltages arising due to the switching of system components, e.g. line energisation, fault clearing and the making and breaking of capacitive or inductive loads. These techniques typically require numerical solution of the time-domain differential equations governing the electrical network in question. ($\Delta t \leq 10\mu s$).

- Fast-front Transient Analysis; Mainly concerned with the impact of lightning strokes to and in the vicinity of electrical power lines and installations, but also applicable to certain switching operations. Travelling wave phenomena are important in all but the shortest line sections ($\Delta t \leq 100ns$).

- Very-fast-front Transients; Usually observed in flashover of gas-insualted switchgear (GIS), though similar analysis techniques have application in close proximity (undamped) lightning studies and switching in lower voltage systems. Such studies require knowledge of the power system response at very high frequencies (up to 100MHz) and model components accordingly share few similarities with their 50Hz counterparts ($\Delta t \leq 1ns$)

For a fixed real time window, the computation time and memory requirement of a simulation increase in inverse proportion to the size of the required time step Δt. Consequently, the extent both in time and space of a solution will be largely dictated by the frequency components of the phenomenon of interest; any over-specification in the simulation set-up will result in wasted computing resource. It is not uncommon to find steady state load flow models representing entire national transmission networks, but a sufficiently comprehensive lightning fast-front over-voltage (FFO) study might only consider a single substation and its proximate overhead lines and cables. Very-fast-front over-voltage (VFFO) studies may even be confined to an individual substation bus section and remain suitably representative of real phenomena.

Such considerations will be addressed in this chapter with a view towards high resolution time-domain simulation of low voltage networks. This will allow comprehensive studies of electromagnetic transients in such networks to be undertaken, with particular relevance to the impact of ubiquitous small-scale embedded generation (SSEG).

2.2 Numerical Solution of Electromagnetic Transients

Numerical integrator substitution is a method for the time-domain computation of variables in physical systems. The method was developed in the late 1960s for application in digital simulation of electrical networks, as a more flexible and powerful alternative to the analogue Transient Network Analyser (TNA). It forms the basis of Dommel's Electromagnetic Transient Program (EMTP) [96,123], a widely used and accepted tool for the simulation of electromagnetic phenomena in power systems.

2.2.1 The Trapezoidal Rule and Linear Circuits

For the purposes of digital simulation, continuous systems must be converted to discrete time equivalents, either as a z-domain transfer function or a set of branch difference equations. This is most commonly achieved using the closed first order Newton-Cotes numerical integration method, commonly known as trapezoidal integration, and is the method employed in the EMTP-ATP simulation package due to its simplicity, stability and accuracy in the majority of cases [123].

The solution method works by discretising all components of a given linear network

to branch difference equations by numerical integration, followed by formation of the network branch conductance matrix $[G]$. The circuit may then be solved for each successive discrete time step using the nodal equation:

$$[G]\,\mathbf{v}(t) = \mathbf{i}(t) + \mathbf{I}_{old} \tag{2.1}$$

where $\mathbf{v}(t)$ is the vector of nodal voltages, $\mathbf{i}(t)$ is the vector of present external current sources, and $\mathbf{I}_{old}$ the vector of current sources which represents the state of system at the previous time step.

This section aims to highlight the potential pitfalls in using trapezoidal integration methods for the solution of low-voltage circuits, namely solution accuracy and stability, and considerations of matrix conditioning. For a general summary of trapezoidal integration and its application to linear circuit elements, please refer to Appendix A.

2.2.1.1 Accuracy of Solution

It can be easily shown that the branch difference equation, generated by Dommel's method for a given arrangement of linear components, is equivalent to a first-order approximate Taylor series expansion of the exponential function:

$$e^{-x} = \frac{e^{-\frac{x}{2}}}{e^{\frac{x}{2}}} \simeq \frac{1 - \dfrac{x}{2}}{1 + \dfrac{x}{2}} \tag{2.2}$$

where $x = \dfrac{\Delta t R}{L}$ for an RL branch or $\dfrac{\Delta t}{RC}$ for an RC branch. Since the exact circuit response is exponential in nature, this approximation results in a truncation error dependent on the ratio of solution timestep and branch time constant. Δt must, therefore, be carefully chosen to account for the shortest time constants and highest frequency components in the system. It is preferable to select a value no greater than one third of the shortest time constant of the circuit [128] (τ_{min}) in order that erroneous simulated circuit behaviour be avoided.

It is possible to minimise such errors through the use of exponential functions in the system difference equations, thereby better approximating an analytical solution. This method is known as the Root Matching (Euler) approach, in that it exactly maps the roots of the frequency domain equivalent admittance matrix from the s- to the

z-domain, eliminating the truncation error described above. For further details, see Appendix A

2.2.1.2 Stability

For the purpose of converting a continuous system to a discrete one, the trapezoidal integrator is equivalent to bilinear transformation. An important consequence of this equivalence is that if the continuous time transfer function of the network being modelled is stable, the resulting discrete system will itself be stable [123]. This is one of the reasons that the EMTP (employing Dommel's method) is the favoured solution method in this work.

It must be emphasised, however, that the stability of a solution does not imply its exactness, nor indeed vice versa. Certain circuit configurations involving minimally damped RLC branches or short τ values are susceptible to marginal numerical stability when the trapezoidal rule is employed in its differential form. The result is a node voltage or branch current that oscillates about the exact solution, reversing in polarity with each successive time step. This fictitious circuit behaviour is known as numerical oscillation [123]. For a discussion of causes, effects and mitigation of this phenomenon, see Appendix A

2.2.1.3 Conditioning

As a general observation on the limiting factors of the EMTP solution method, the conditioning of the system steady-state admittance matrix [$\mathbf{Y}$] and the time-domain conductance matrix [$\mathbf{G}$] must be considered. As a general rule, it is advised that the use of extremely small branch resistances and inductances in a simulation be avoided. This is because the formation of network the Y- and G-matrices generates very large values which tend to obscure the behaviour of other components connected to the same node. A similar limitation applies to very large capacitances, though values large enough to cause ill-conditioning of the conductance matrix are unlikely to be encountered in any practical scenario. Equations (2.3) to (2.5) summarise the admittance and effective conductance components in the EMTP solution.

for a Resistor, we have $$Y = \frac{1}{R}, \qquad G = \frac{1}{R} \tag{2.3}$$

for an Inductor, we get $$Y = \frac{1}{\omega L}, \qquad G_{eff} = \frac{\Delta t}{2L} \tag{2.4}$$

and in the case of a Capacitor $$Y = \omega C, \qquad G_{eff} = \frac{2C}{\Delta t} \tag{2.5}$$

Conversely, very large resistances and inductances or very small capacitances will produce very small Y- and G-matrix components, effectively removing them from the solution altogether. This is of far lesser concern as it has little or no effect on the final results. Ill-conditioning of the network conductance matrix is a prime cause of solution inaccuracies and should be actively avoided in all simulations [110, 123].

Due to small circuit time constants and line travel times, electromagnetic transient simulation of Low-Voltage networks will generally require very short simulation time steps. This requirement will tend to counteract the conditioning problems caused by small inductances as the effective conductance is proportional to Δt. The effective conductance of a capacitive branch, however, is inversely proportional to Δt, so a requirement for high resolution will effectively reduce the threshold defining a *very large* capacitance. It is still unlikely that sufficiently large values of C will be encountered, but conditioning errors may be ruled out if consistent results can be demonstrated for a range of simulation step sizes.

2.2.2 Non-linear Components

A brief general analysis of non-linear component representation in EMTP is given here in order to highlight some important features.

The solution methods discussed in section A.1 are ideally suited to the accurate analysis of linear circuits in the time domain. The modelling of non-linear components, such as metal oxide varistors (MOV) and saturable transformer cores, can by contrast be very accurately modelled by the use of non-linear techniques. Unfortunately, it is not possible to combine these techniques in solving a single circuit consisting of both linear and non-linear components, and thus a single technique must be made to work

for all components. Non-linear circuit analysis techniques involving representations of *all* component characteristics by continuous analytical functions can be employed, but present a wasteful computational burden when only a small proportion of circuit components are non-linear. Far more efficient linear methods are, therefore, modified in order to approximate a particular device performance [110].

2.2.2.1 Non-linear Inductors

Piecewise linear inductances, defined by a given flux-current characteristic, are implemented in the EMTP using the "switched" component representation shown in Figure 2.1. For values of λ below λ_{sat}, the switch remains open, but closes once λ_{sat} is exceeded. The result is the two-slope characteristic presented.

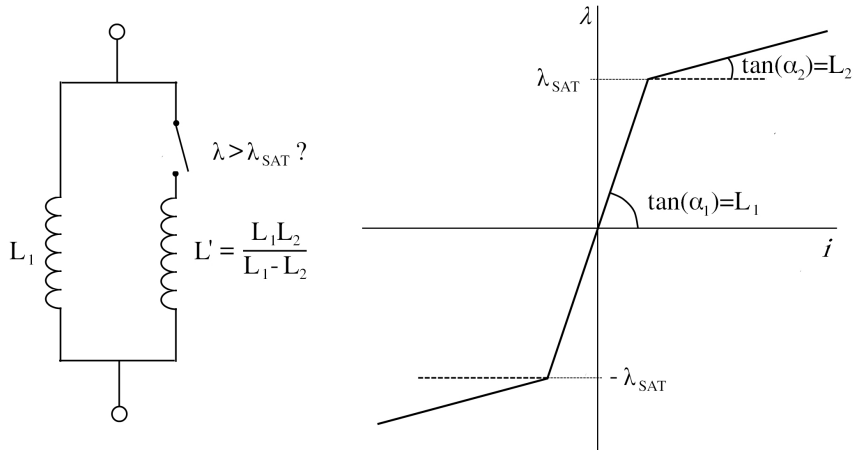

Figure 2.1: Two-slope Non-linear Inductor Representation

In reality, no switch exists in the circuit, and the branch inductance value is simply changed directly within the conductance matrix [**G**] at the first time step following the knee-point crossing. This transition is essentially analogous to a discontinuity in the inductor current, and as such presents similar potential for numerical oscillation as discussed in the previous section. The inclusion of representative core loss resistance in a model will generally negate this problem.

In making the transition from slope L_1 to L_2 in the discrete time domain, there will always be some degree of overshoot error if the exact crossing instant occurs between time steps. The reconfigured circuit only applies from the first time step following the

knee-point transit. This error is reduced internally by the use of a non-recursive form of the inductive branch difference Equation ((2.6) and (2.7)) which, for the first time step following discontinuity, recalculates the present state current with the old slope L_1, using a history term I_{hist} calculated using the new slope L_2 [110]. Errors can be further reduced manually by a shortening of the simulation time step.

$$i\,[t] = \frac{\Delta t}{2L_1} \cdot v\,[t] + I_{hist}\,[t - \Delta t] \tag{2.6}$$

$$I_{hist}\,[t - \Delta t] = i\,[t - \Delta t] + \frac{\Delta t}{2L_2} \cdot v\,[t - \Delta t] \tag{2.7}$$

The use of the pseudo-nonlinear inductance model for transformer saturation in EMTP is not limited to two-slope representation. The saturation characteristic can be represented using a practically unlimited number of linear elements, assuming that a suitable flux-current characteristic can be obtained for the device. If implemented in the form of the saturable transformer component [97], the subroutine SATURA will generate a point-wise flux-current characteristic from open circuit $v - i$ test data [129]. Care must be taken however to ensure that Δt is sufficiently small for the solver to track the characteristic accurately.

2.2.2.2 Hysteresis Modelling

Problems involving transformer inrush usually demand that the effects of magnetic hysteresis be included, achieved here by use of the type 96 non-linear hysteretic reactor component in EMTP [99]. This model allows residual flux in the core to be defined as an initial condition [110], which is an extremely useful feature where simulation times are too short for circuit variables to settle (typically where T_{max} is less than the power frequency period). Residual flux modelling and piecewise hysteresis characteristic are illustrated in Figure 2.2.

2.2.2.3 Non-linear Resistance

The type 92 exponential current-dependent resistance [99] in EMTP is used for the modelling of overvoltage protection devices, such as source side DC bus varistors in photovoltaic grid converters. The MOV Type 92 block in ATPDraw builds on the basic Type 92 model, allowing a variety of devices (ZnO, SiC) to be modelled directly

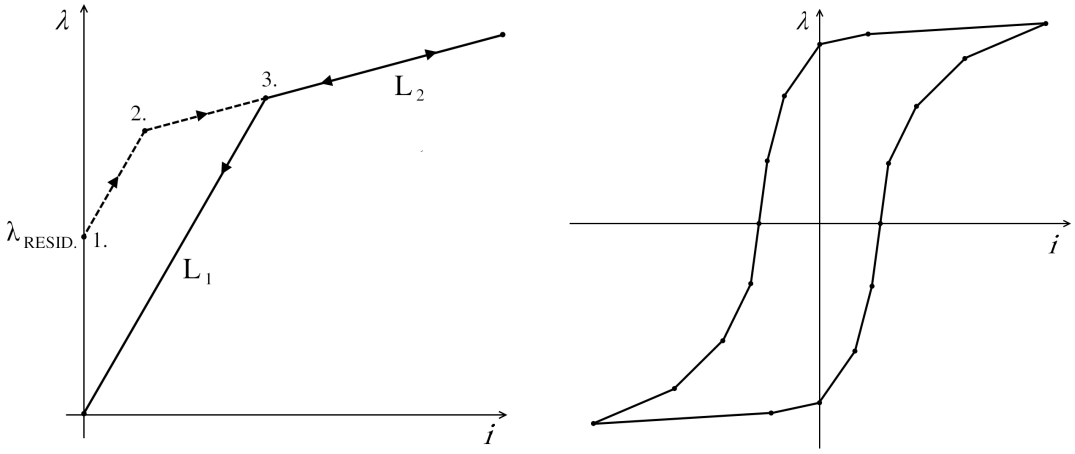

(a) Residual Flux (b) Piecewise Hysteresis Loop

Figure 2.2: Non-linear Hysteresis Modelling in EMTP

from the device manufacturers' data. A least squares method is used to fit the entered data points to the exponential formulation in (2.8) to within a defined tolerance.

$$i = p \cdot \left(\frac{v}{V_{ref}} \right)^q \tag{2.8}$$

2.2.3 Transmission Lines

This section provides a general discussion of the transmission line model selection process, and the merits and limitations of the available representations.

As a general rule, if a length of cable or overhead line to be modelled has a travel time τ less than the solution time step Δt, a nominal PI model with mutual coupling of conductors, as illustrated in Figure 2.3, is considered sufficient [123]. Where $\tau > \Delta t$, travelling wave models should always be used in order that the distributed line parameters and propagation delays be correctly represented.

A number of travelling wave models are available, ranging in complexity from the constant frequency lossless Bergeron model with lumped resistance approximation, through to the frequency dependent JMarti and Noda models. If geometric and material data for the line in question is available, it is preferred that a frequency dependent model be used [123]. This preference becomes a requirement in cases where broad frequency spectra are to be observed, in unbalanced problems where the zero sequence current

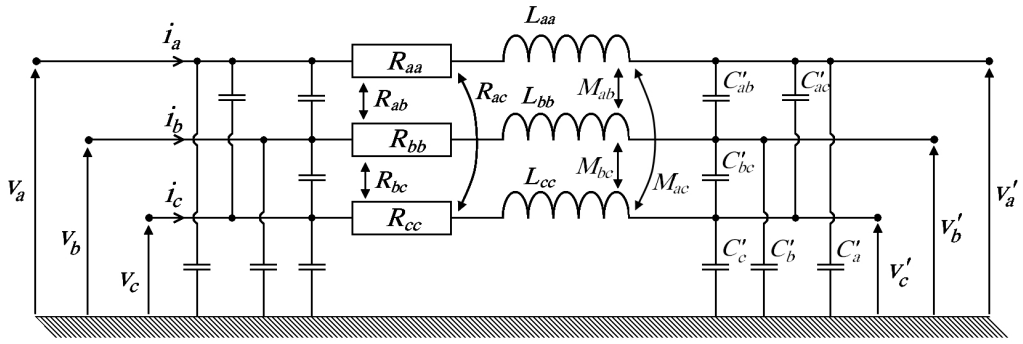

Figure 2.3: Nominal PI Line Representation

plays a significant role, or in high frequency solutions of overhead lines taking account of eddy current induction in the earth [110].

A benefit of the use of transmission lines from the perspective of computational requirements is that the present voltages and currents at one end of the line are completely independent of the present states at the other. Therefore, mutual coupling in the equivalent conductance matrix of two subsystems A and B linked by a transmission line is eliminated, allowing the subsystems to be represented as diagonal sub-matrices in [**G**] (2.9):

$$[\mathbf{G}] = \begin{bmatrix} [G_A] & \\ & [G_B] \end{bmatrix} \tag{2.9}$$

The increased sparsity of the conductance matrix that arises from using transmission line sections can greatly reduce the computational burden in simulating extensive meshed networks. It is preferable to use a transmission line model in all cases, except those in which it would itself impose prohibitively short Δt requirements.

2.2.3.1 Frequency Dependent Transmission Lines

A discussion of the general aspects of frequency-dependent line representation may be found in Appendix A.

The treatment of frequency-dependent lines and cables in the EMTP software may be achieved by the use of a variety of models. Two such models are compared here - one employing modal decomposition (JMarti), the other applied directly in the phase

domain (Noda).

2.2.3.2 Modal Domain Model (*J. Martí*)

This model employs a process of modal decomposition, simplifying any M-phase coupled line into M decoupled single phase lines. Voltages and currents along the line are determined in the phase domain by Equations (2.10) and (2.11).

$$\left[\frac{d^2V_{phase}}{dx^2}\right] = \left[Z'_{phase}\right] \cdot \left[Y'_{phase}\right] \cdot \left[V_{phase}\right] \tag{2.10}$$

$$\left[\frac{d^2I_{phase}}{dx^2}\right] = \left[Y'_{phase}\right] \cdot \left[Z'_{phase}\right] \cdot \left[I_{phase}\right] \tag{2.11}$$

where the products $[Z'][Y']$ and $[Y'][Z']$ are distinct except in the case where the matrices are balanced and a lossless high-frequency approximation is assumed [110]. Modal decomposition of the phase voltage and current vectors is achieved by the use of an appropriate transformation matrix (2.12).

$$[V_{mode}] = [T_V]^{-1} \cdot [V_{phase}] \qquad [I_{mode}] = [T_I]^{-1} \cdot [I_{phase}] \tag{2.12}$$

Thus, in the modal domain:

$$\left[\frac{d^2V_{mode}}{dx^2}\right] = [T_V]^{-1}\left[Z'_{phase}\right]\left[Y'_{phase}\right][T_V][V_{mode}] = [\Lambda][V_{mode}] \tag{2.13}$$

$$\left[\frac{d^2I_{mode}}{dx^2}\right] = [T_I]^{-1}\left[Y'_{phase}\right]\left[Z'_{phase}\right][T_I][I_{mode}] = [\Lambda][I_{mode}] \tag{2.14}$$

$$\tag{2.15}$$

where the matrix $[\Lambda]$ contains the modal eigenvalues λ_{mode} of the matrix products ZY and YZ. The transformation matrices $[T_V]$ and $[T_I]$ are the eigenvector matrices, and because $[Z][Y] \neq [Y][Z]$ they are different, in contrast to their eigenvalues which are always identical. However, only one of transformation matrices need be determined, as they are related to each other by (2.16) [110].

$$[T_I] = [T_V^t]^{-1} \tag{2.16}$$

The modal Impedance and Admittance matrices are then given by (2.17).

$$[Z'_{mode}] = [T_I^t][Z'_{phase}][T_I] \qquad [Y'_{mode}] = [T_V^t][Y'_{phase}][T_V] \tag{2.17}$$

and the characteristic impedance of a given mode k is

$$Z_{C\ mode\ k} = \frac{\gamma_{mode\ k}}{Y_{mode\ k}} \qquad \left(\gamma_{mode\ k} = \sqrt{\lambda_{mode\ k}}\right) \tag{2.18}$$

From this point, it is a straightforward process to fit rational functions to the modal characteristic admittances and propagation constants. These are then transformed back into the phase domain by the use of the eigenvector matrices $[T_V]$ and $[T_I]$, and the time domain equivalent of Figure A.6 generated by computing the receiving end history term by recursive convolution.

$$i_{k\ hist\ propagation} = -\int_{\tau_{min}}^{\tau_{max}} i_{m\ tot}(t-u)a(u)du \tag{2.19}$$
$$i_{m\ tot} = y_C(t) * v_m(t-\tau_{min}) - i_m(t-\tau_{min})$$

where τ_{min} and τ_{max} are the shortest and longest modal travel times respectively, and y_C and a are the inverse Fourier transformations of the Admittance and Propagation matrices (see Appendix A) [110, 123].

Of the frequency dependent line representations available to the EMTP user, Martí's model is by far the most widely used. There are, however a number of considerations which limit its applicability to the modelling of Low-voltage networks. The primary drawback of the modal-domain approach is that while the matrices $[Y_{C\ mode}]$ and $[\gamma_{mode}]$ are themselves frequency dependent, the transformation matrices $[T_V]$ and $[T_I]$ are only defined at a single frequency specified in the model set-up and thus remain constant across the frequency range of interest [108]. This limitation impacts the modelling of cable networks more than overhead lines, and results in errors when applied to untransposed conductors. As such, its appropriateness for the representation of low-voltage distribution networks in urban areas is questionable.

The fitting of the rational function to the frequency dependent modal characteristic admittances produces an inherent instability at very low frequencies, as the functions

will all pass through zero if the mode shunt conductance $G(\omega)$ is omitted. Since trapped charge investigation is not required in the studies presented in this work, this is of little concern except in the event of dc-current injection from an embedded generator. Most problems can be overcome by starting the function fitting from a very low frequency (typically 10^{-4}Hz is considered adequate [108]).

2.2.3.3 Phase Domain Model (*Noda*)

In order to avoid the accuracy problems caused by the mode-phase transition in the Martí line model, it has become increasingly desirable to do away altogether with modal transformation, and treat the fitting of frequency-dependent characteristics directly in the phase domain [108]. Because the phase domain solution is inherently a coupled problem, a greater number of frequency dependent components are necessary as the off-diagonal components of the Y-matrix are non-zero. This is a minor trade-off in favour of improved accuracy over a broad frequency range, and is more than justified in the author's opinion.

One of the problems associated with phase domain representation of lines is that conversion back to the time domain by recursive convolution generates discontinuities whenever the *modal* propagation times differ [98]. The solution to this problem, as implemented in the Noda model, is to fit a rational function in the z-domain to the frequency dependent data output by the LINE CONSTANTS and CABLE PARAMETERS subroutines. This function fitting is performed by the external routine ARMAFIT, which outputs auto-regressive moving average (ARMA) functions for the line parameters of the form shown in (2.20).

$$G(z) = \frac{a_0 + a_1 z^{-1} + a_2 z^{-2} + \cdots + a_N z^{-N}}{1 + b_1 z^{-1} + b_2 z^{-2} + \cdots b_N z^{-N}} \tag{2.20}$$

When converted to the time domain, these simply produce expressions for the present value of a variable at one terminal of the line as a sum of weighted delay terms at the other, which is the discrete time equivalent of the recursive convolution method required for the s-domain fitting.

$$y[t] = a_0 x[t] + a_1 x[t - \Delta t] + a_2 x[t - 2\Delta t] + \cdots + a_N x[t - N\Delta t] \quad (2.21)$$

$$- b_1 y[t - \Delta t] - b_2 y[t - 2\Delta t] - \cdots - b_N [t - N\Delta t] \quad (2.22)$$

This discrete-time function can be used directly in the EMTP simulation, making it far more efficient than recursive convolution, and overcomes discontinuity representation problems caused by differences in modal phase velocities. One limitation of note is that the phase-domain line or cable model must be generated using the same time-step Δt as used in the simulation itself [130]. A change of solver resolution will, therefore, require all phase domain models to be recalculated prior to simulation, but this is only a minor inconvenience. The frequency response of a Noda model computed at a new Δt should always be compared with its predecessor to ensure that a correct re-fitting has taken place.

2.3 Special Considerations in LV Networks

This section highlights a number of considerations pertaining to the modelling of low-voltage systems in EMTP.

2.3.1 Distance and Time

Discrete time-domain simulation of electrical networks requires selection of a solution time step and duration that is appropriate for the problem being investigated. In general, low voltage network models will impose stringent limits on the time step because of the short lengths of LV cables and overhead lines (compared to MV and HV circuits), and the need to account for very fast-front transients generated close to the customer.

The correct representation of travelling wave transmission line models requires that the time step be no greater than half the travel time τ of the fastest propagation mode [120]. This criterion does not, however, guarantee solution accuracy as travel times that are a non-integer multiple of Δt shall be subject to linear interpolation errors [110,123]. It is desirable that τ_{mode} for each propagation mode be equal to $n \cdot \Delta t$, where n is an integer. This requirement is in practice very difficult to fulfil, but simulation errors

may be minimised by ensuring that

$$\Delta t \leq \frac{\tau_{mode\ min}}{5} \tag{2.23}$$

Clearly, the reproduction of high frequency phenomena is absolutely limited by the Nyquist sampling criterion. The maximum theoretical frequency component that can be observed in a simulation with time-step Δt is

$$f_N = \frac{1}{2\Delta t} Hz \tag{2.24}$$

though such data would be meaningless, being indistinguishable from spurious numerical oscillation. The inclusion of damping networks to combat numerical oscillation problems would similarly damp the high frequency components of interest, and as such further limits the maximum frequency reproducible at a given time step. For the steepest expected transient voltage or current front, a minimum of 10 data points are required in order to correctly evaluate the peak value and rate of rise [120], but a more liberal approach has been taken here to leave sufficient headroom for the damping of numerical problems. For a specified upper frequency bound f_{max}, a time step is chosen such that

$$\Delta t \leq \frac{1}{50 f_{max}} \tag{2.25}$$

For the simulation of locally generated transients, involving only a single timed switch operation, a time-step of 1ns was chosen following multiple test executions, to allow domestic cabling to be represented as short transmission line sections. The modelling of multiple sources in distribution networks implies a far greater number of solution nodes, with computational burden increasing in proportion to n^2. However, the time step requirement here can be relaxed given that minimum travel times in distribution line and cable sections are increased, and that greater attenuation of high frequency components with distance can be assumed. Table 2.1 summarises the impact of selected time steps on minimum mode propagation times and maximum frequency representation according to the criteria in (2.23) and (2.25). The minimum allowable length of transmission line section $L_{min\ TL}$ is determined assuming a worst-case mode propagation velocity equal to the speed of light in vacuo.

Table 2.1: Limiting Criteria as Determined by Choice of Solution Time-step

	Detailed Models	LV Network Models	
	(Domestic)	Urban	Rural
Δt	5ns	20ns	40ns
$L_{min\ TL}$	3m	12m	24m
f_{max}	4MHz	1MHz	0.5MHz
$T_{rise\ min}$	50ns	200ns	400ns

The establishment of a single Δt for comparison studies is beneficial where phase domain transmission line models are used, as the ARMA function can only be specified at the exact solution time-step. In all cases, the total simulation real time window T_{sim} must at least be wide enough to pick up any travelling wave reflection from the most remote node of the model [120].

2.3.2 Conductor Geometry

The use of established overhead line and underground cable models for the representation of low-voltage systems is not widely documented, and the assumptions made in the development of these models must be accounted for in order to ensure that the circuits implemented in EMTP-ATP are a true representation of real equipment. A significant feature of LV circuits is the low X/R ratio at 50Hz, due to the small cross-sectional area (CSA) of conductors. The attenuation *constant* $\alpha(\omega)$ of a low voltage line is far higher than that of an equivalent length of 400kV conductor and, therefore, the geographic area of interest covered by propagating transients is very localised.

A second feature of the small CSA is that the skin depth becomes significant at a much higher frequency than in a high voltage conductor bundle. This is illustrated in Figure 2.4 with reference to a range of conductor stranded cross-sections. Current is assumed to be evenly distributed among the strands of the conductors, and the frequency-dependent resistance is normalised to the DC value. This flatter response aids in the fitting of rational functions to the cable parameters and line constants in the frequency domain. An estimate of the skin effect in LV 3-phase conductors at a

given temperature θ is given by

$$R(f) = R_{DC} \cdot (1 + y_s + y_p) \tag{2.26}$$

with the DC resistance R_{DC}, and skin and proximity effect factors y_s and y_p defined [131] as

$$R_{DC} = R_O \cdot [1 + \alpha_{20}(\theta - 20)] \tag{2.27}$$

$$y_s = \frac{x_s^4}{192 + 0.8x_s^4} \tag{2.28}$$

$$y_p = \frac{x_p^4}{192 + 0.8x_p^4} \left(\frac{d_C}{\overline{s}}\right)^2 \cdot \left[0.312 \left(\frac{d_C}{\overline{s}}\right)^2 + \frac{1.18}{\frac{x_p^4}{192 + 0.8x_p^4} + 0.27}\right] \tag{2.29}$$

$$\text{where} \qquad x_s^2 = \frac{8\pi f k_s}{R_{DC}} \cdot 10^{-7} \qquad x_p^2 = \frac{8\pi f k_p}{R_{DC}} \cdot 10^{-7}$$

where R_O is the dc resistance at 20°C, α_{20} is the temperature coefficient of resistance of the conductor material evaluated at 20°C, f is the frequency in Hz, d_C is the conductor diameter in mm, and $\overline{s}$ the mean separation between conductor axes in mm. The coefficients k_s and k_p are both equal to 1 for circular stranded conductors [131]. The skin- and proximity-effect factors are multiplied by 1.5 in equivalent pipe-type cables.

An alternative method for the calculation of internal resistance is to use Kelvin functions (modified Bessel functions) as presented in [132]. This is a more exact solution for simple conductor geometries, and is used for the evaluation of skin effect in EMTP line and cable models. The principal limitation of this method is that proximity effects are unaccounted for. Resistance at high frequency is calculated by Equation (2.30), where r is the conductor radius, ω the frequency in $rad\,s^{-1}$ and ρ is the conductor resistivity.

$$\frac{R}{R_{DC}} = \frac{\kappa}{2} \frac{Ber(\kappa)Bei'(\kappa) - Bei(\kappa)Ber'(\kappa)}{Ber'^2(\kappa) + Bei'^2(\kappa)} \qquad \left(\kappa = r \cdot \sqrt{\frac{\omega\mu_0}{\rho}}\right) \tag{2.30}$$

Geometric models computed under LINE CONSTANTS and CABLE PARAMETERS subroutines must conform to the underlying assumptions of the equations on which they are based. All bare-conductor overhead line models used in the simulations conform

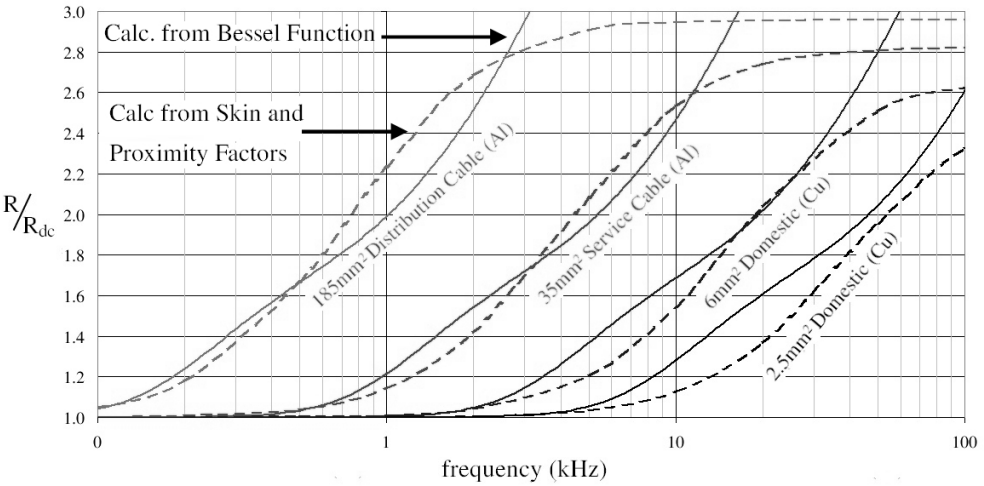

Figure 2.4: Skin Effect in Stranded Conductors (Circular Cross-Section) [131, 132]

to the assumptions of Carson's formula for homogeneous earth [110]. Parabolic sag is assumed in sections shorter than 500m, and the following criteria are satisfied:

1. Conductors may be assumed to be horizontal with sag accounted for by average height approximation, and long enough for end-effects to be ignored.

2. The air surrounding the conductors is lossless and homogeneous with permittivity and permeability equal to that of free space.

3. The earth is also homogeneous ($\varepsilon = \varepsilon_0$, $\mu = \mu_0$), with uniform resistivity ρ. Electrical behaviour is that of a conductor ($\omega\rho\varepsilon_0 << 1$), which for a critical frequency of 4 *MHz* as determined in Table 2.1, places an upper limit on ρ of 4.5 $k\Omega m$. A nominal value of 100 Ωm was specified for all rural overhead lines in this research investigation.

4. Conductor *spacing* $\geq 10\times$ *diameter*, allowing proximity effects to be ignored.

The suitability of geometric cable models is less clear as there exists no unified solution equivalent to Carson's equations for OHLs [123]. Distribution cable geometries with circular conductors and symmetric co-axial sheath construction can be modelled quite easily using an insulated cable-pipe representation. Armoured four-conductor cables, where a smaller neutral conductor is bundled with the three phases, are a lot harder to represent as the individual conductors are non-circular and of varying sizes, and the overall symmetry of the cable cross-section is lost. Indoor cabling is also difficult to model due to the very small features involved, and the variety of environments

encountered makes an evaluation of a singular earth resistivity almost impossible. The exact choice of models in this work is discussed in sections 2.4.2, 2.4.3 and 2.5.1.

2.3.3 Insulation Materials

Insulation and sheathing materials considered in the simulations were Cross-linked Polyethylene (XLPE) for 3-phase distribution mains [133] and Extruded Poly-Vinyl Chloride (PVC) for both indoor wiring [134] and distribution service cables [135, 136]. At present, there is no method for the inclusion of frequency-dependent dielectric permittivity and loss factors in the insulation and sheathing of cable models. This is of little concern as the dielectric properties of PVC and XLPE are essentially constant over the frequency range of interest, and thus a single valued ε_r is considered sufficient.

2.3.4 Insulation Coordination

Insulation Coordination in low voltage systems is covered by *BS EN 60664* [137], but reference has also been made to high voltage insulation coordination standards *BS EN 60071* [138] in the classification of transient wave shapes. Reference to these standards is made throughout this document in relation to specific test and simulation criteria.

2.4 LV Distribution Network Components

This section briefly summarises the specification of distribution network components in ATPDraw, the graphical preprocessor to EMTP-ATP.

2.4.1 Basis in Generic Models

Because of the wide variation in LV distribution network topologies, it would be impossible to simulate scenarios covering all possible combinations of feeder capacity, local loading and penetration of small-scale embedded generators (SSEG). Instead, generic network models have been developed based on the dynamic benchmark models employed in [23, 24, 33]. The models themselves are discussed in detail in Chapter 6

2.4.2 Cables

A variety of 415/240V cable models [111] have been constructed in ATP-EMTP for the analysis of transient propagation in LV grids. The two categories of cable models; 3-phase mains and single-phase service cables, are summarised in Figure 2.5.

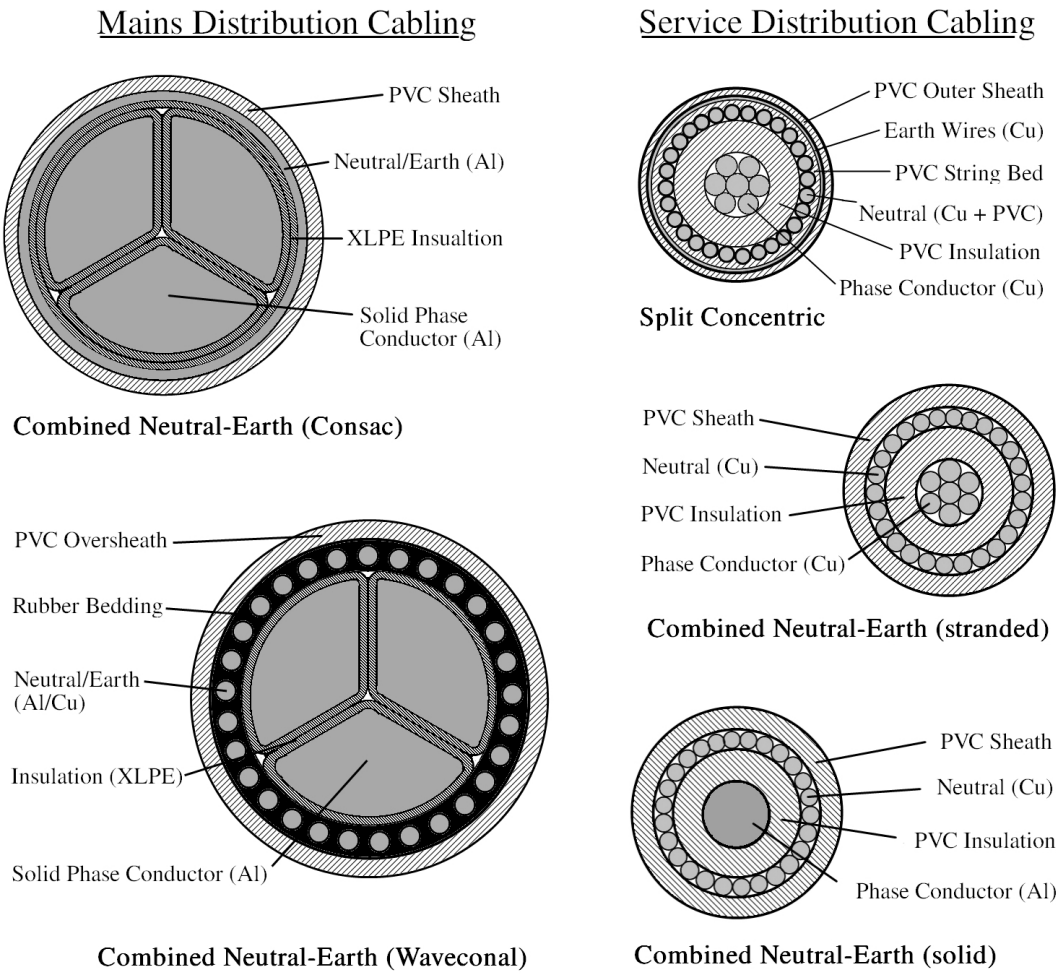

Figure 2.5: 415/240V Distribution Cable Geometries [111]

Concentric single phase service cables are straightforward to model in ATP-EMTP as sheathed single core cables, assuming the stranded conductors to be solid tubular sections of equal Cross-Section Area (CSA). Split concentric constructions can also be accommodated by the use of an additional armour conductor for the earth wires. Cable data used in this work as per [135, 136] are provided in Appendix D

The modelling of 3-phase cables with concentric combined Neutral-Earth conductors is considerably more difficult, mainly due to the sector geometry of the phase conductor cross-section. As a rule, cable models in electromagnetic transients simulation software pre-processors accept conductors of circular or tubular cross-section only, in order that an analytical solution for the cable parameters may be easily obtained. A geometric cable model accepting conductors of arbitrary shape and orientation would require an intermediate finite element modelling stage in order to achieve similar results, adding significant computational requirements to a given simulation. At present, no such function is available to any of the ATP pre-processors, and an approximation to circular conductor cross-section has been made where necessary.

2.4.3 Overhead Lines

The modelling of wood pole mounted bare-conductor overhead lines for rural distribution networks is comparatively straightforward as the assumptions of carson's equations are easily satisfied. Aerial bundled conductor (ABC) lines common to rural 230/400V circuits are somewhat less straightforward due to the effects of proximity between phases.

Single and three-phase ABC conductors may be modelled using the LCC routine in EMTP as unsheathed single sore cables in a close bundle as depicted by the cross-sections of Figure 2.6 [139].

2.4.4 Transformers

All models used in this thesis consider the distribution network in detail up to the 11kV transformer. As such, the 415V winding of the transformer should be rendered in detail, taking account of its winding impedances and stray capacitance, and also including the inter-winding capacitive coupling to the 11kV primary.

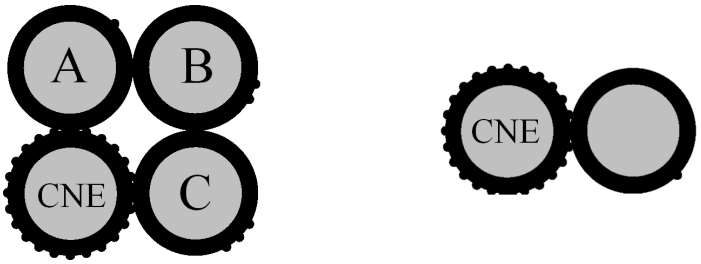

(a) 3 Phase + Neutral (b) Single Phase

Figure 2.6: Aerial Bundled Conductor Cross-Sections

2.4.5 Switchgear

Switchgear in the LV supply such as circuit breakers and isolators play no role in the studies presented here, and are represented as short connections in all cases. Only generator protection relays as depicted in Figure 2.7 are modelled in any detail as these are the active switching devices of interest.

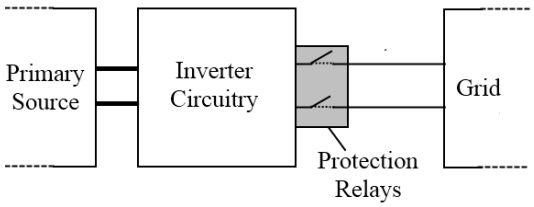

Figure 2.7: Switching Devices to be Modelled in Detail

2.4.6 System Equivalent Impedance

For the representation of the system upstream of the 11kV transformer, a voltage source behind an equivalent circuit consisting of the power-frequency short-circuit impedance in parallel with the characteristic impedance of the line is normally recommended for simulations in high voltage circuits [120]. For 11kV distribution circuits, the frequency dependence of the line surge impedance plays a small role, and thus $Z_C(\omega)$ may be better represented as a rational ARMA function in the z-domain. Such a representation is referred to as a frequency-dependent network equivalent (FDNE).

The problem with this approach is that the frequency-domain data necessary for the formation of such a model is not collected by Distribution Network Operators (DNOs). The closest approximation that one can obtain in this case is achieved by running a frequency scan on a good quality frequency-dependent geometric model of a length

or mesh of 11kV cable or OHL. Figure 2.8 illustrates the process of extracting the frequency domain self- and mutual-impedance scan, to which rational functions $Z(z)$ may be fitted by linearised least-squares approximation as per [140, 141].

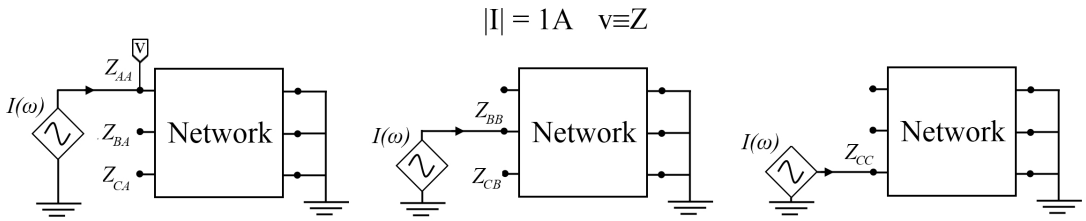

Figure 2.8: Formation of an FDNE by Line Frequency Scan

2.5 Domestic/Commercial Wiring Installations

There follows a discussion of requirements for the modelling of cabling and load conditions, for scenarios in which additional detail downstream of the customer supply point is needed.

2.5.1 Cables and Distribution Boards

Early domestic cable models consisted of lumped equivalent PI sections, providing reasonable results in simulations with time steps greater than 10ns. The drawback with this approach is that the discrete components have to be evaluated individually for each length and cross-section of cable, and are only correct at a single frequency. A frequency dependent transmission line is therefore preferred, but given the prohibitively short travel times between cable terminals, a different time step has been chosen for the more detailed studies (see Table 2.1).

Assuming a propagation velocity equal to that of free space ($\nu_p = c$), a travelling wave line model at a solution time-step of 5ns can theoretically represent section lengths as short as 3m. This reduces to approximately 1.6m if one assumes that all propagation modes occur within the PVC insulation/sheath. Minimisation of interpolation errors then dictates a practical lower limit of 8m for a single line section, which is considered ample for the representation of typical domestic wiring circuits.

A library of flat and circular flex cable geometries, as depicted in Figure 2.9 has been constructed using both modal- and phase- domain frequency dependent line models,

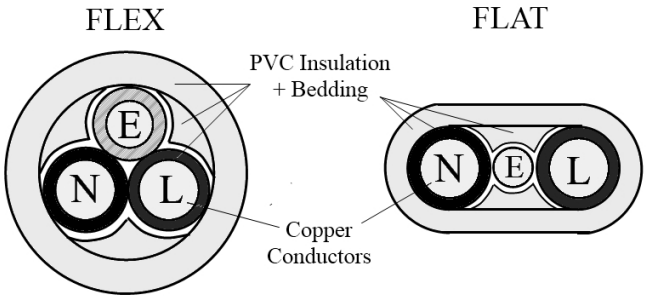

Figure 2.9: Domestic Cable Geometries

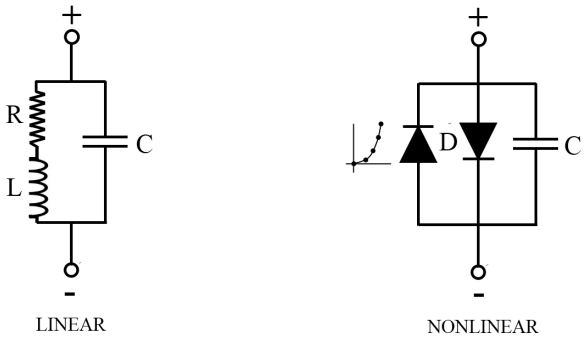

Figure 2.10: Linear and Non-Linear Load Representation

yielding very similar results.

2.5.2 Loads

Localised customer load is represented to varying degrees of detail as dictated by the required time-step resolution of a given model. High resolution domestic circuit circuit models in which mains cable runs are represented explicitly as travelling-wave models (section 2.5.1) require that loads appearing on different mains and spurs be modelled separately. A selection of linear and pseudo-nonlinear branches are used to represent typical localised loads for different household occupancy scenarios.

Nonlinear load is modelled as an antiparallel arrangement of empirically defined Shockley diode elements as depicted in Figure 2.10. Linear loads are supplemented with shunt capacitance of 10-40pF, representing stray effects in adapters and power supply circuitry. Nonlinear loads by contrast are assumed to possess significant input capacitance allowing stray effects to be neglected.

In lower resolution models incorporating many customer nodes dispersed across multiple LV feeders, the modelling of circuits downstream of the consumer unit becomes

impractical. Individual customer load must, therefore, be aggregated into a single linear branch. Stray effects are still included, though supplemented with an additional capacitance in place of the omitted cable spurs.

2.6 Small-scale Embedded Generation

2.6.1 Direct Connection

Direct-connected induction machine type sources, being limited to certain μCHP and micro-wind designs, are taken to constitute only a small proportion of future installed SSEG capacity. The specific characteristics of such generators have for this reason been omitted from study, an exclusive adoption of converter-based devices being assumed.

2.6.2 Converter Interfaces

The necessary level of detail in modelling converter topologies is largely dictated by its required degree of flexibility in application. A range of device equivalent circuits have been developed, ranging from a simplistic representation of output filters and capacitive inrush to complex explicit representation of power electronic circuits and toroidal transformer saturation characteristics. A detailed discussion of each topology and its applicability to the simulation of transient phenomena can be found in Chapter 5.

2.6.3 Switches and Disconnects

Main inverter disconnect relays are represented as ideal switches in parallel with their nominal open-state stray capacitances, with contact resistance neglected. Power-electronic switches are treated in a similar fashion, with the addition of on-state series resistance, snubber circuitry and antiparallel diode branch as depicted in Figure 2.11. Discussion of relay pole adaptation to statistical or systematic switches for the purpose of large-scale repeat simulations is given in Chapter 6.

2.7 Chapter Conclusions

In this chapter, Dommel's trapezoidal integration method for time-domain computation of electromagnetic transients has been discussed. The merits and drawbacks of this solution method have been evaluated, with particular consideration of solution accuracy,

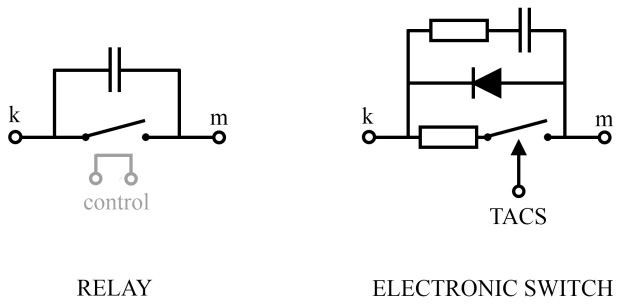

Figure 2.11: Switch Representation by Type

stability and conditioning of the network conductance matrix. It was determined that a discretisation based on trapezoidal integration, despite a propensity for giving rise to numerical oscillation, was the best initial choice due to the inherent stability of the resulting discrete system model.

Particular consideration has been given to difficulties in the modelling of low-voltage network components, as distinct from those relating to MV and HV systems. Principal considerations are time-step constraints due to propagation times in very short (of the order of 10m) cables and lines and the handling of small circuit time constants; non-circular cable geometries; and marginal satisfaction of the assumptions of Carson's equations due to the neglect of proximity effects.

In the light of such considerations, with the aid of laboratory test and manufacturers' data, a library of low-voltage system components has been generated using the EMTP-ATP graphical preprocessor *ATPDraw*. Transient characteristics of small distributed generators, however, remain an unknown, necessitating the design and construction of a generator test bed as discussed in the next chapter.

Chapter 3

Laboratory Rig for the Evaluation of Microgeneration Transient Phenomena

The development of good predictive simulation models is heavily dependent on the availability of field and laboratory test data. In the case of LV networks and associated embedded generation technologies, the available data are somewhat limited, with little or no data relating to electromagnetic transient phenomena. This chapter details the design and construction of a laboratory test bed for the acquisition of the necessary simulation model data.

3.1 Overview

The principal aim of the laboratory work undertaken was to study voltage and current transients at the device terminals and consumer bus, arising due to switching of an integrated protection relay as required by ENA ER G83-1 [5]. The chosen source technology for this investigation was a solar photovoltaic energy system, as depicted in Figure 3.1, which was constructed and tested within the Cardiff University Solar Energy Laboratory.

The chosen solar inverter, as with all off-the-shelf SSEG grid interfaces, has an integrated electromechanical protection relay and control system to facilitate disconnection of the source from (and delayed reconnection to) the grid in response to voltage rise/dip, frequency deviation and loss-of-mains scenarios as defined in G83-1. It is the operation of this relay and any associated electrical transients that shall be of primary interest

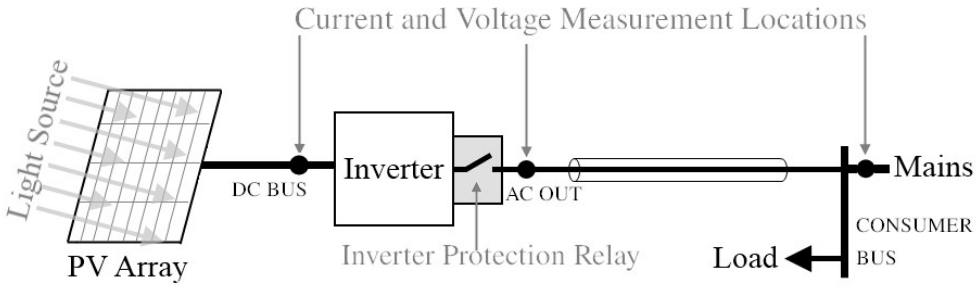

Figure 3.1: Basic Test Layout of Rig Indicating the Switching Device of Interest

in this chapter. The laboratory rig design would therefore need to incorporate the following components:

- A means of triggering inverter grid protection in a user-determinable manner;
- Steady-state measurement apparatus to record pre- and post-switch conditions;
- Transient measurement system capable of capturing and processing a wide range of voltage and current waveform data, consisting of one or more transient peaks;
- Data acquisition system for the automated logging of large quantities of steady-state and transient data.

3.2 Test and Equipment Specification

This section describes the specified laboratory test regimes, together with a breakdown of key measurement criteria as derived from insulation coordination and electromagnetic compatibility standards. Requirements of the test equipment, such as measurement resolution and data handling capability, are then discussed.

3.2.1 Time-Domain I-V Measurement

In order to correctly characterise the transient behaviour of each switching event, a comprehensive set of measurement criteria was established. These criteria serve to maximise the data yield of a given test, thereby minimising the need for repetition and allowing statistical methods to be applied. Using the standardised wave-shapes from Insulation Coordination and EMC standards [137, 138, 142, 143] (Table 3.1) and commonly used electromagnetic susceptibility test wave-shapes as in [81] (Table 3.2) as reference, it was determined that the following data should be acquired for each switching event:

- Peak transient voltages and currents $(V_{max}, V_{min}, I_{max}, I_{min})$ at the generator terminals and consumer unit bus,
- Rate of rise of voltage and current fronts $\left(\frac{dV_{rise}}{dt}, \frac{dI_{rise}}{dt}\right)$ for both positive- and negative-going transients,
- 50% values of voltage and current tails and rates of roll-off $\left(\frac{dV_{fall}}{dt}, \frac{dI_{fall}}{dt}\right)$,
- Switching delays (τ_{sw}) in operation of live and neutral relay poles, and any subsequent transients due to inrush (τ_i),
- Instantaneous terminal voltage and timing of switching instants with respect to the supply voltage sinusoid $(t_{sw1},\ t_{sw2})$.

A sequence of transient events may be observed for each switching operation, due to independent pole closing delays and the possible occurrence of capacitive inrush. A sufficiently large time window would therefore be necessary to capture all of the relevant data for each event. A suitable window was found experimentally to be around 20ms. It was anticipated that while relay pole operation might give rise to the fastest transients, worst case current and voltage magnitudes would be associated with the subsequent inrush. It was important, therefore, to quantify the magnitudes and relative frequency of occurrence of any and all inrush events as these shall represent the most onerous conditions with regard to insulation degradation, thermal overload and damage to electronic components by induced effects.

The components of the electromagnetic immunity test waveshapes can be calculated from acquired data using the relations in Table 3.2, where u_m is the peak value of the transient, $\frac{du}{dt}$ the initial rate of rise and S the energy measure of the wave:

$$S = \int_0^\infty u^2(t)dt \tag{3.1}$$

These measurements may either be interrogated in hardware at the time of test, or sufficient waveform data should be stored such that the required values may be extracted by post-processing. Figure 3.2 illustrates the measurement points of interest on a generic waveform, with reference to one cycle of the 50Hz supply voltage.

Given the lack of pre-existing transient data, and the fact that electrical time constants in an LV network are typically much shorter than those at medium and

Table 3.1: Transient Classes and Standard Test Waveshapes According to Insulation Coordination Standard BS EN 60071 [138]

Class	Slow-Front	Fast-Front	Very-Fast-Front
Typical Waveshapes	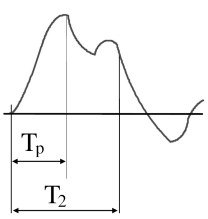	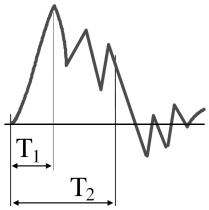	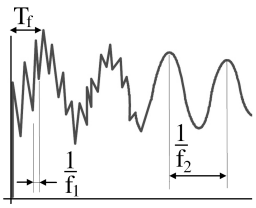
Range of Waveshapes	$20\mu s < T_P \leq 5ms$ $T_2 < 20ms$	$0.1\mu s < T_1 \leq 20\mu s$ $T_2 < 300\mu s$	$T_f < 100ns$ 0.3MHz $< f_1 <$ 100MHz 30kHz $< f_2 <$ 300kHz
Standard Waveshapes	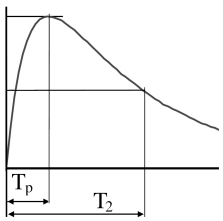	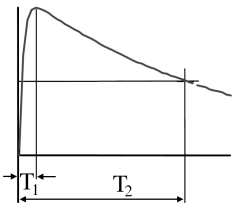	-
Standard Values	$T_P = 250\mu s$ $T_2 = 2\,500\mu s$	$T_1 = 1.2\mu s$ $T_2 = 50\mu s$	-
Standard Test	Switching Impulse Test	Lightning Impulse Test	-

Table 3.2: Common Electromagnetic Susceptibility Test Waveshapes [81]

Symmetric Trapezoidal Pulse (STP)	Double Exponential Pulse (DEP)	Damped Oscillatory Wave (DOW)
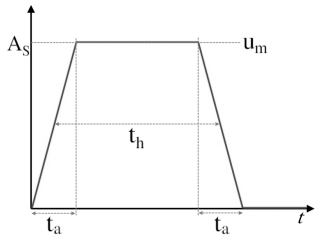	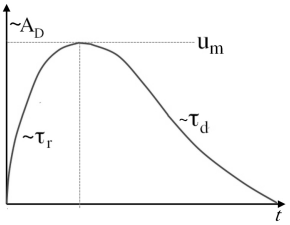	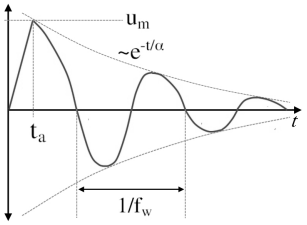
-	$u(t) = A_D\left(e^{-\frac{t}{\tau_d}} - e^{-\frac{t}{\tau_r}}\right)$	$u(t) = \dfrac{u_m}{t_a}t \quad [0 \le t \le t_a]$
-	-	$u = u_m e^{-\alpha(t-t_a)}\cos\left(\omega(t-t_a)\right)$ $[t > t_a]$
$u_m = A_S$	$u_m = A_D \cdot \dfrac{r-1}{r}e^{-\frac{ln(r)}{r-1}}$	-
$\dfrac{du}{dt} = \dfrac{A_S}{t_a}$	$\dfrac{du}{dt} = \dfrac{r-1}{\tau_d}A_D$	-
$S = \left(t_h - \dfrac{t_a}{3}\right)A_S^2$	$S = \dfrac{\tau(r-1)^2}{2(r+1)}A_d^2$	$S = \left(\dfrac{t_a}{3} + \dfrac{2\alpha^2+\omega^2}{4\alpha(\alpha^2+\omega^2)}\right)u_m^2$
-	$\left(r = \dfrac{\tau_d}{\tau_r}\right)$	$(\omega = 2\pi f_w)$

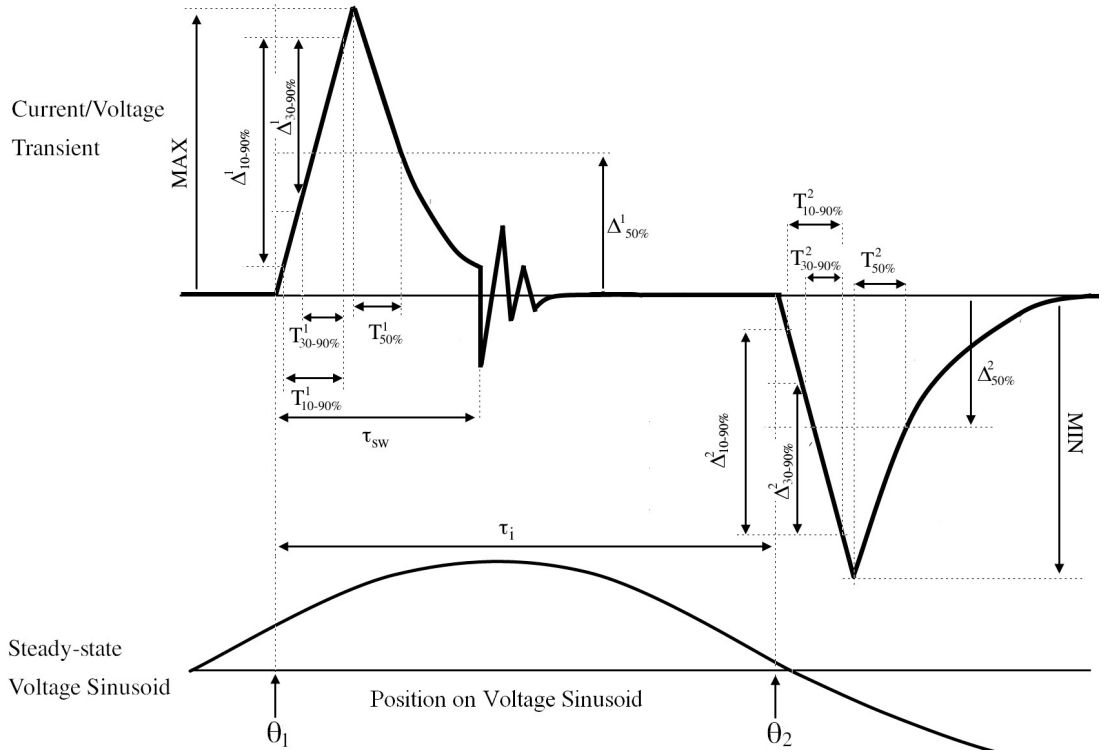

Figure 3.2: Key Data Extraction from a Generic Event Record

high-voltage, the data acquisition equipment was specified to achieve the maximum possible bandwidth. Post-processing of very large data files was deemed undesirable, and a direct extraction of characteristic values in hardware preferred wherever feasible.

3.2.2 Test Scenarios

A primary requirement of the laboratory study was to quantify the dependence of transient currents and voltages on instantaneous local loading, and on distance of the connection point from the 11kV transformer. As such, the test rig was designed to include a variable local dump load, and a range of possible fault levels at the consumer bus. In addition, all tests were specified to perform switch timing and delay analyses on the acquired data. Three principal test configurations were specified in order to quantify the following:

- Transient voltages and currents generated on disconnection of the inverter from the mains supply.
- Transient voltages and currents generated on reconnection to the supply.
- The effect of supply impedance on the magnitudes of these transients.

Details of the rig components and equipment capabilities are given in sections 3.4 and 3.5. The specifics of each testing configuration are covered in detail in Chapter 4

3.2.3 Statistical Analyses

Simulations of individual timed switching events provide useful pointers to the transient phenomena of interest, but the information that these simulations provide is minimal, and in many cases represents a worst-case scenario which itself may occur too infrequently to be of any concern. Far more useful information can be obtained by performing a sequence of simulations in which the operation of switches in successive re-runs is governed by a statistical distribution in time. This is of particular use when multiple devices are operating on a single network in response to a common stimulus, each with their own pole operation delay.

In order to inform such simulations, sufficient statistical data must be obtained by laboratory test under repeatable conditions. A large number of events must be recorded in order that the statistical distributions governing the switch pole operation may be extracted, and minimisation of total lab time requires that all test scenarios be specified to generate this timing data. Being confined to a single test rig and lacking any external source of additional data, the amount of statistical information that could be extracted was somewhat limited due to the time-consuming nature of the acquisition process.

3.2.4 Repeatability

It was determined that all testing and data acquisition be performed on a complete system rather than using a representative source behind a grid inverter, so as to be able to fully mimic source-device interaction in subsequent simulations. Given the present drive towards expansion in small grid-tied photovoltaic systems in the UK, this form of generation was deemed most appropriate for study, and a small test rig constructed (section 3.4). In order to collect useful laboratory data on a systematic basis, external variables such as temperature, irradiance and airflow had to remain as constant as possible for the duration of a test, allowing electrical phenomena to be observed in isolation. Outdoor testing was deemed unfavourable in the short-term due to variability of conditions, and it was decided that all testing be undertaken within the School of Engineering's Solar Energy Laboratory.

3.3 The Solar Energy Laboratory

The Solar Energy Laboratory at Cardiff University is a dedicated environment for the evaluation and testing of full-scale solar thermal and photovoltaic systems in situ, under repeatable controlled conditions. The laboratory's main feature is a manoeuvrable array of 36 parabolic Compact Iodide Daylight (CID) lamps, shown in operation in Figure 3.3. The lamps are arranged in a square array, measuring 2.85m x 2.85m between corner beam centers, and at a distance of 5.2m from target illuminates an area of approximately $10m^2$ at a spectral intensity in excess of $400W/m^2$.

Figure 3.3: CID Lamp Array in the Solar Energy Laboratory

The use of narrow beam angles results in considerable hot-spot formation, and peak intensities at the center of the target area are typically above $700W/m^2$. A number of broadband irradiance tests were performed using a pyranometer placed at 25 evenly spaced points in a plane perpendicular to the angle of incidence. The results of these tests were used to determine the optimal size and position of a test rig, and the radiation flux density at the surface of the chosen configuration is shown in Figure 3.4.

3.3.1 Lamps

The lamps used are $1000W$ Cold-restrike narrow-spot CIDs with 8-inch parabolic reflectors. These produce a spectrum comparable to that of direct solar radiation,

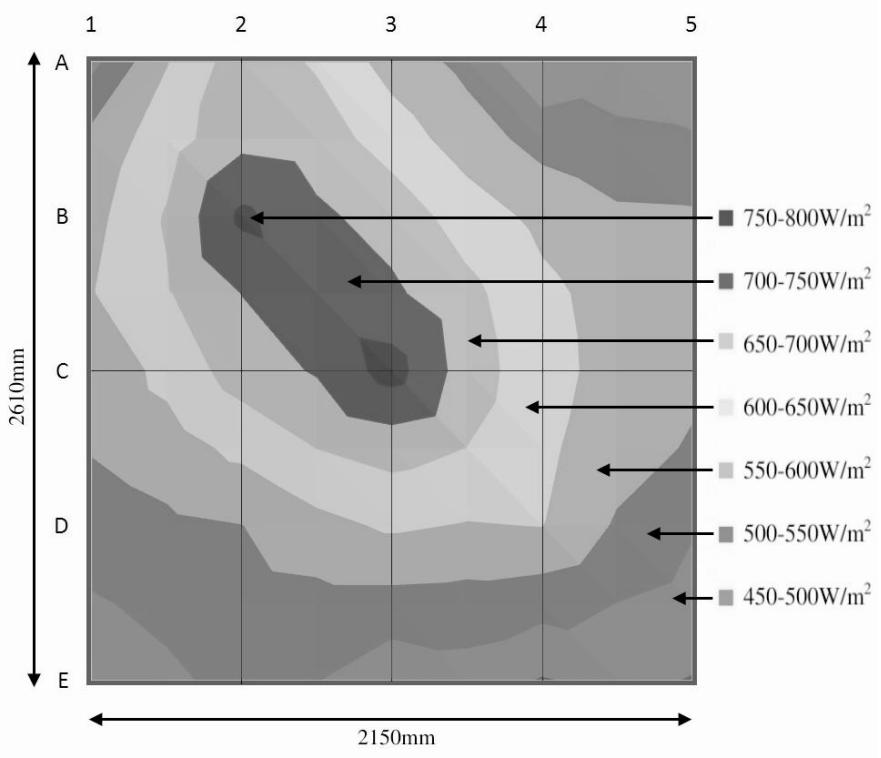

Figure 3.4: Cumulative Irradiance in the Plane with an Angle of Incidence of 90° and Range to Target of 5.2m

and spectra measured in the laboratory using a spectral radiometer calibrated to a reference source are shown in Figures 3.5 and 3.6 with *AM1.5* standard reference light source [144] for comparison.

Two features are of note in relation to the spectral irradiance curves: The measured curve of the lamp array has a number of sharp peaks coinciding with the emission spectra of the mercury vapour, the spectrum being spread by the vaporised sodium-iodide amalgam. Also, the spectral intensity is reduced below 400nm in comparison with the reference source, due to the dual-layer ultraviolet filter build into the lamp glass. Otherwise, the spectra are very similar, and the normalised cumulative irradiance spectrum (Figure 3.6) of the lamps up to $800nm$ is shifted only very slightly towards the infra-red.

It was decided that cumulative intensity over the absorption frequency range of a solar cell was of more importance than the individual weighting of component frequencies, due to the generally flat response of polycrystalline silicon over the emission range of the lamps. Thus, the existing CID array was deemed suitable for use with a photovoltaic

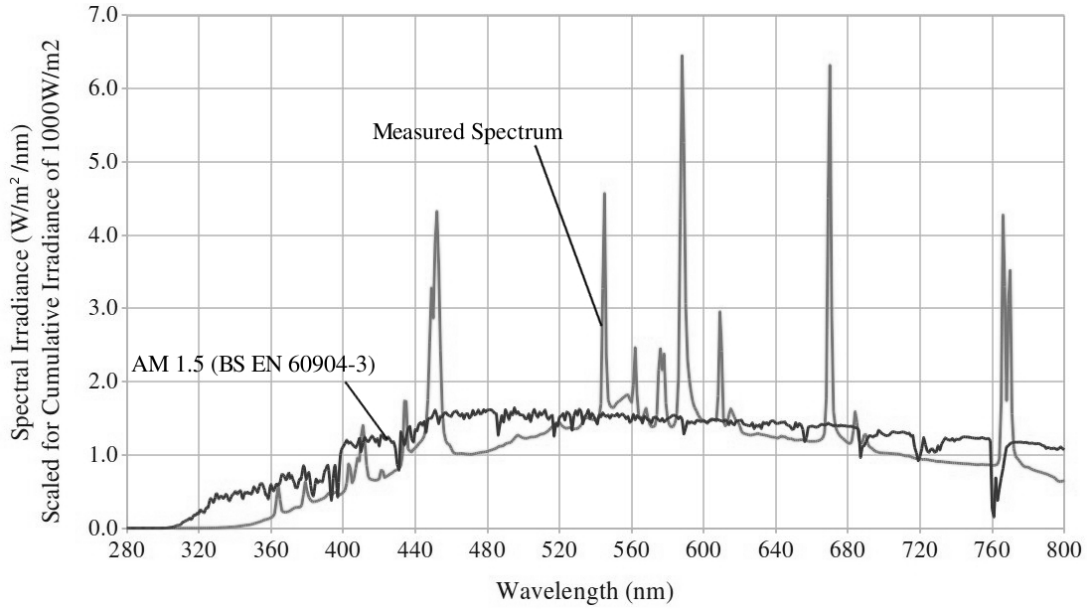

Figure 3.5: Spectral Irradiance of Lamp Array, Scaled for a Cumulative Total of $1000Wm^{-2}$ (AM1.5 Spectrum [144] for Comparison)

rig, with the condition that the rig be placed far enough from the lamps to avoid cell damage due to hot-spot formation.

3.3.2 Ignition and Control

The intensity and lifetime of metal-halide discharge lamps are sensitive to deviation of terminal voltage from their rating. To minimise the effect of the high supply voltage (typically in excess of $420V$, 3-phase), as well as more short-term variability, the lamp-ballast and ignition circuits are fed from a stabilised supply configured to supply the lamps at their rated voltage. In addition, single phase variacs are provided downstream of the stabilisers, to provide a degree of individual lamp brightness control.

Because the lamps have a very limited dimming capability, the usefulness of individual control variacs is limited. It was not possible to repeat experiments for a range of irradiance levels, and small adjustments were made only periodically in order to counteract the natural dulling that occurs with with lamp ageing.

Finally, lamp ignition is performed by individual 12kV igniters housed at the rear of each lamp assembly. Lamps are fired in groups of three from ignition switches mounted on the wall of the laboratory, and once ignited are subject to a 30-minute power cycle before re-ignition. This condition was found to be the principal cause of

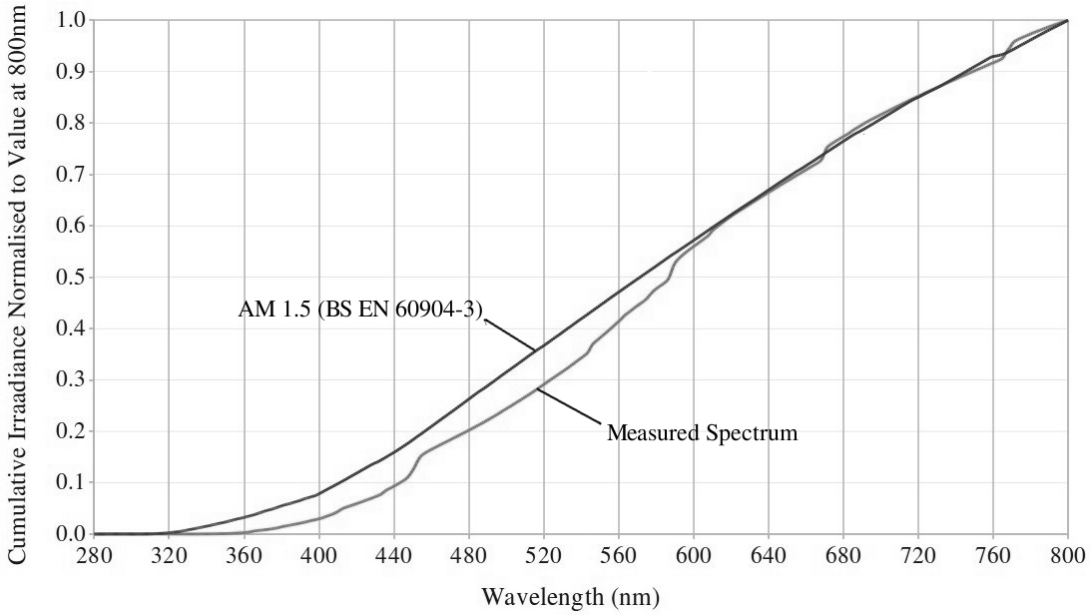

Figure 3.6: Normalised Cumulative Irradiance of Lamp Array from $280nm$ to $800nm$ (AM1.5 [144] for Comparison)

delay in extended test regimes, as a misfired lamp requires those already lit to be fully cycled before a second attempt can be made. A proposal was drafted by the author for conversion of the CID array to equivalently rated parabolic halogens utilising a stage lighting system, which would eliminate time-consuming power cycling requirements and allow for dynamic variation in light intensity during future tests (see Appendix E).

3.3.3 Orientation and Manoeuvrability

Positioning of the lamp array is achieved by use of two travelling crane hoists running on I-beams in the ceiling space of the laboratory. Once in position, the array must be anchored by means of fixed load-bearing chains so as not to statically load the crane clutch. Verical and Horizontal manoeuvring of the array during test is therefore not possible, and a suitable fixed position of the tilt axis was determined for all tests. The tilt angle and lamp rotation were then adjusted in order to align with the test object.

In order to maximise the beam spread, and thereby minimise hotspot formation, the full length of the laboratory was utilised. A tilt angle of 36° was found to satisfy this condition, and kept fixed for the duration of testing. Thus a fixed tilt angle could also be specified for the photovoltaic array, discussed in the next section. The laboratory configuration is shown diagrammatically in Figure 3.7

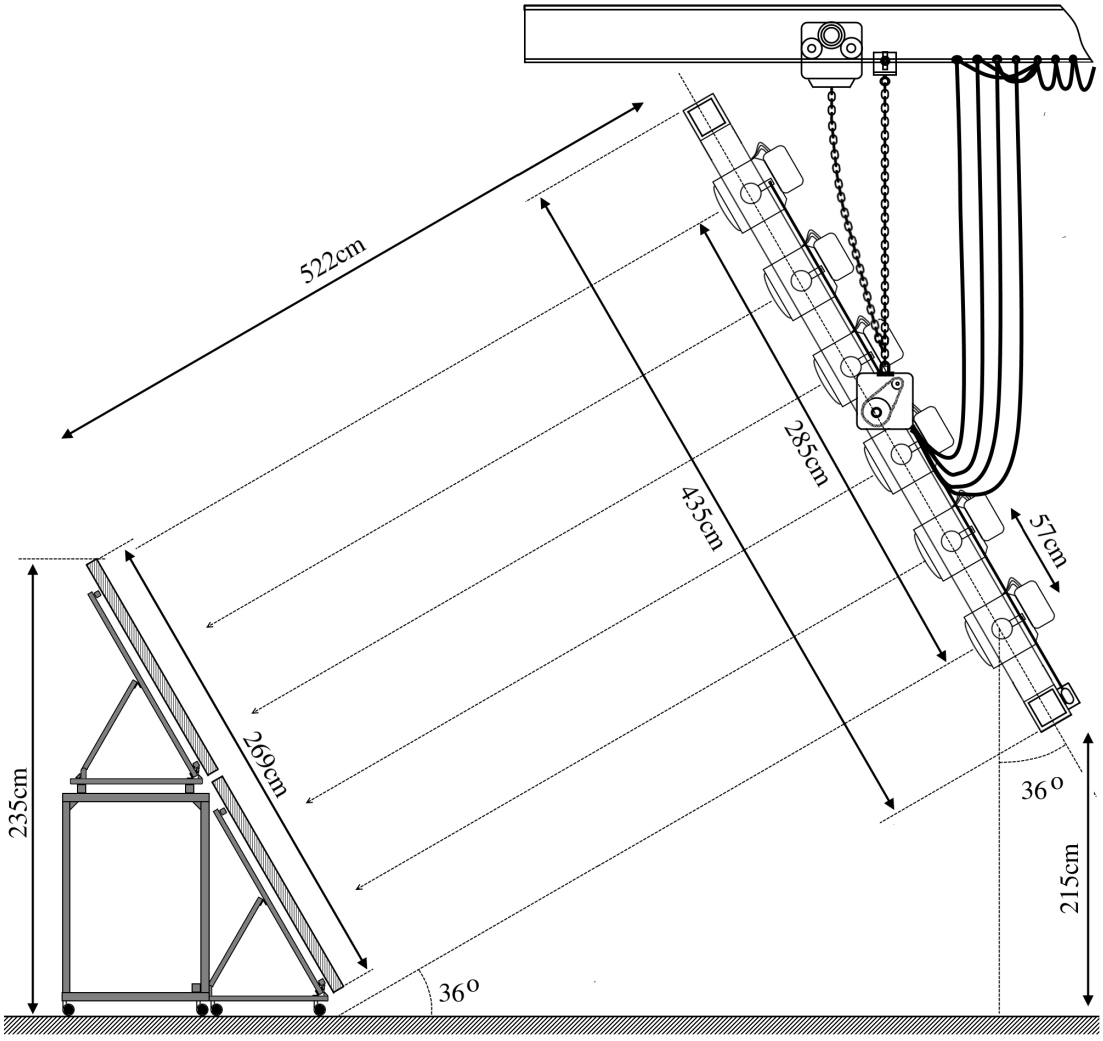

Figure 3.7: Position and Orientation of CID Array and Target

3.4 Photovoltaic Array Test Rig

3.4.1 Panels

Economical use of the illuminable area was made using an array of BP Solar 380J multi-crystalline silicon-nitride PV panels [145]. The panels were arranged in a 4×2 array, measuring 2150mm by 2690mm with a total cell surface area of $4.80m^2$. These were mounted on a lightweight frame constructed from 30×30mm and 45×45mm modular aluminium section, as shown in Figure 3.8. Manoeuvrability was achieved by mounting on antistatic castors, and a sliding hinged frame construction was chosen to allow minor adjustment of the tilt angle ($36^\circ \pm 5^\circ$).

Figure 3.8: Photovoltaic Array and Mounting

The panels were string-connected to form an array with a nominal rating of 640W under standard test conditions ($1000W/m^2$ AM1.5 spectrum, $20°C$ air temperature). Due to a reduced and uneven distribution of radiation emitted by the lamps, and an elevated air temperature typically around $25°C$, the peak output power was reduced to approximately 350W as shown in the array I-V curve of Figure 3.9. Operation at the maximum power point (MPP) at an air-temperature of $25°C$ generated a current of 2.83A at a terminal voltage of 123.3V DC. System open circuit voltage was approximately 151.1V, while short-circuit current was measured at 4.64A, slightly above its nominal value of 4.55A.

3.4.2 Inverter

Output current from the array was fed to an SMA SunnyBoy^{TM} 700 Grid Inverter, mounted on a moveable trolley as shown in Figure 3.10. The inverter input MPP voltage range was set to 100-160V for a peak theoretical efficiency of 93.3%. The AC terminals were connected through a 16A miniature circuit breaker (MCB) to a 16m

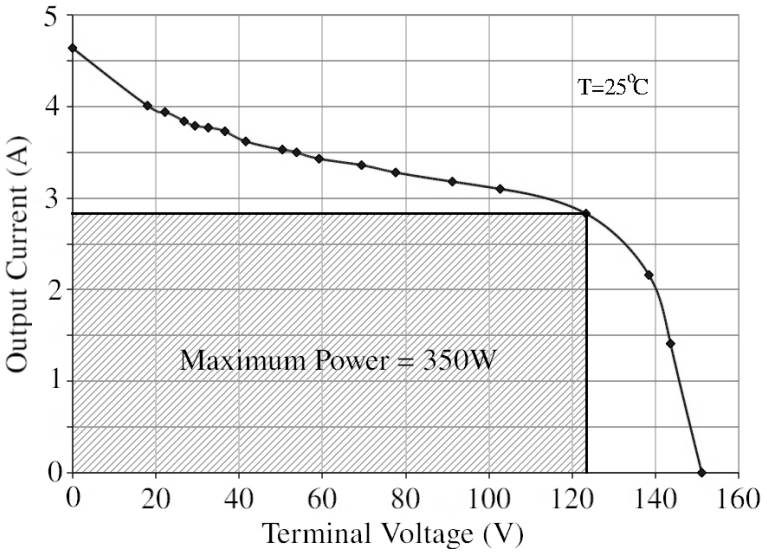

Figure 3.9: Photovoltaic Array V-I Characteristic at $25°C$ with a Mean Surface Irradiance of $500W/m^2$

length of flat twin and earth PVC insulated cable, routed around the laboratory to a dedicated mains supply fed from a Residual Current Circuit Breaker with Overload protection (RCBO). Test and measurement equipment was supplied from a separate circuit to avoid possible nuisance tripping. A switched resistive dump load was also added at the end of the cable run to mimic different local loading scenarios.

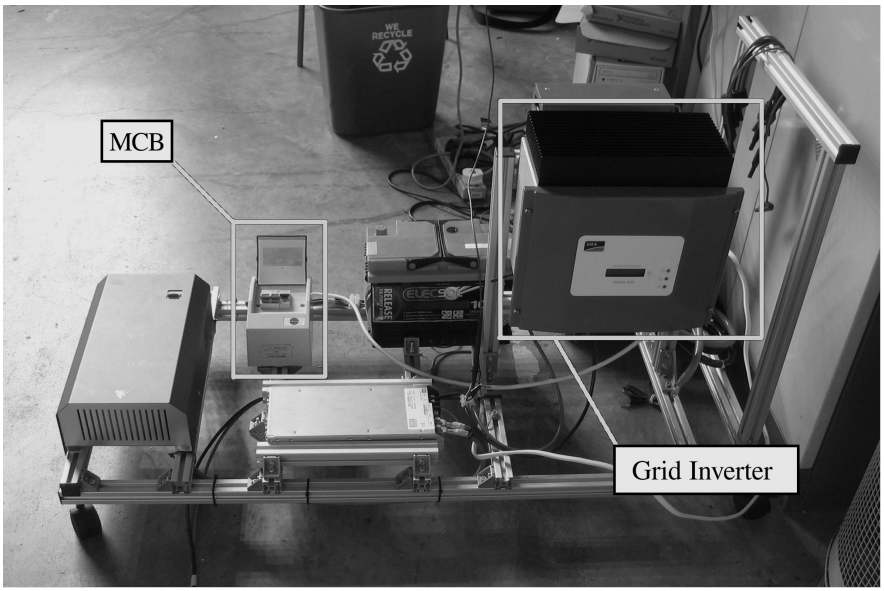

Figure 3.10: Grid Inverter Trolley

In order that typical behaviour of an installed SSEG be properly mimicked, no alterations to the control or protection arrangements of the solar inverter were undertaken.

The integrated protection was permitted to disconnect the device from the supply in response to voltage deviations and loss-of-mains, in the same manner as would occur in a normal domestic installation. Controlled disconnection was achieved indirectly by manipulation of the incoming mains supply voltage, rather than by direct manual operation of the protection relays. The pre-set delay in the relay open/close cycle was also preserved to allow realistic settling time for the DC bus capacitance post-disconnect.

3.5 Test and Measurement Equipment

The following section briefly discusses the measurement equipment specifications for the laboratory, and provides a breakdown of devices used and their key features. Detailed equipment information can be found in Appendix B. Equipment may be broadly split into two categories according to resolution; one for steady state applications (monitoring) and the other for high speed transient data capture.

3.5.1 Steady-State Monitoring

Continuous monitoring of the voltages and currents in the test system is necessary in order that switching operations may be repeated from the same initial state, and to allow relation of transient measurements to prior steady-state conditions.

3.5.1.1 Probes and Meters

Voltage and current measurements on the array DC bus were made using LeCroy SI-9000 200:1 differential voltage and LEM PR20 20kHz multimeter AC/DC current probes. A second, identical pair of probes were used for monitoring of the AC voltage and current at the inverter terminals. Steady-state voltage and current measurement at the load was performed by a Keithley 2000 Multimeter and a third LEM PR20 current probe.

The current and voltage probes were connected in differential mode to analogue input channels 0 to 4 of a USB data-acquisition board, while the multimeter was connected to the PC via a National Instruments^{TM} GPIB-USB converter. The set-up is illustrated in Figure 3.11.

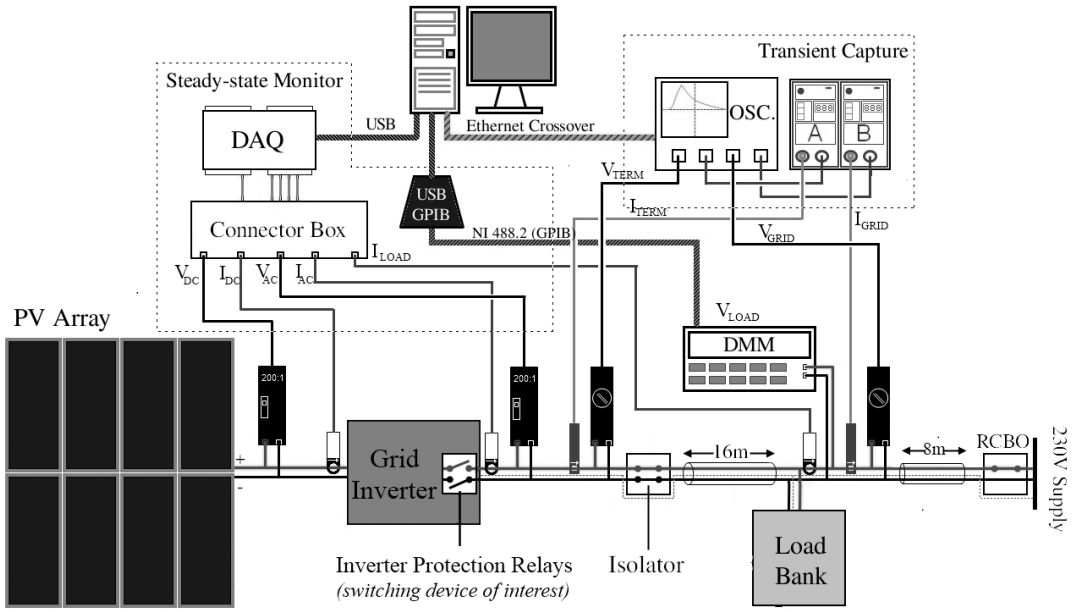

Figure 3.11: Complete Laboratory Equipment Set-up, Indicating the Switching Operation of Interest

3.5.1.2 Data-acquisition Board

An NI USB-6212 400kS/s multifunction data-acquisition (DAQ) board with 16-bit input ADC was used for the collection of steady-state system data. All probes were connected to the DAQ via a connector box and short lengths of 0.23mm^2 foil-shielded twisted pair cable. The signal lines were terminated in differential mode with $100k\Omega$ resistor pairs between each channel and the earth reference of the DAQ.

3.5.2 Fast Transient Measurement

A second set of measurement equipment was specified for the high-frequency measurement of transients, as can also be seen in Figure 3.11.

3.5.2.1 Voltage Probes

Voltage transients were measured at the inverter AC terminals and consumer unit bus using a pair of Pintek DP-25 differential probes. These probes have a low input capacitance (1.2pF differential, 3.7pF common), and a -3dB bandwidth of 25MHz at an attenuation setting of 200:1.

3.5.2.2 Current Probes

Current measurement at the same positions was made using two Tektronix A6302 current probes, each connected to an AM503 probe amplifier. The current probes have a 50MHz bandwidth and continuous current-handling capacity of 20A (100A peak), and attenuation ratios are adjustable via the amplifier controls. A ratio of 200mA/10mV scope division (20:1) was fixed for all tests.

3.5.2.3 Scope

Fast-transient data was captured and processed using a 4-channel LeCroy Waverunner 64-Xi 600MHz scope. This model was chosen for its flexible triggering rules, on-board data processing capability and straightforward integration in LabVIEW^{TM} via the NI Virtual Instrument Software Architecture (VISA). The scope itself was connected to the PC via an RJ45 cat5e crossover, and device communication facilitated by LeCroy's Versatile Instrument Control Protocol (VICP) plug-in for NI-VISA.

Operating as a four-channel device, the scope has a maximum sampling rate of 5GS/s per channel providing sufficient bandwidth in excess of that of both the voltage and current probes for high frequency data acquisition. A sampling interval of 50ns (20MS/s per channel) was chosen for the shortest acquisition window, allowing capture of transient front times down to 0.5μs, while remaining within the operating frequency range of the differential voltage probes.

For switch/inrush timing analyses requiring a 20ms acquisition window, the sampling interval specification was relaxed to make handling and post-processing of output data more manageable. The sampling interval was increased to $1\mu s$ producing 20,000 data points per channel per event.

The next section details the extraction, processing and display of measured steady-state and transient data using a LabVIEW virtual instrument (vi).

3.6 Data Acquisition

Due to the large number measurements and volume of information associated with each transient event capture, a supervisory system was required in order to coordinate

the triggering and data-extraction processes. A transient logger was constructed using LabVIEW for the processing and storage of steady-state and transient data extracted via the DAQ and Oscilloscope.

3.6.1 Requirements

It was decided that the transient logger should perform the following broad functions:

1. Steady-state monitoring of array and inverter currents, voltages and power flows for the full duration of a test.
2. Display captured transient waveforms on an event-by-event basis.
3. Provide visual indication of measurement system status and prompt for action following triggering events.
4. Allow remote re-arming of all triggers from inside the execution loop.
5. Facilitate the extraction and storage of data, either by generating new files or appending to an existing dataset.

3.6.2 Program Overview

The transient logger *vi* consists of a tabbed display, with controls and indicators assigned to pages by function. The tabs are broken down as follows:

- *Inputs*: For the specification of measurement equipment set-up parameters prior to test.
- *Execution*: Provides rolling display of steady-state measurements and trigger event feedback during the test.
- *Error Handling*: Gathers error log information at key stages of the program execution loop.

3.6.2.1 Inputs

The *Inputs* panel is shown in Figure 3.12. This screen allows the user to enter information such as the attenuation settings of voltage and current probes, the desired scope set-up parameters (time-base, vertical scale, sample size, trigger levels) and DAQ card set-up (sampling rates, scaling, number of cycles recorded per sweep). The number of events

to be recorded in a test session may be specified, as well as the location to which output data is to be saved (either to a new file, or appended to an existing data set).

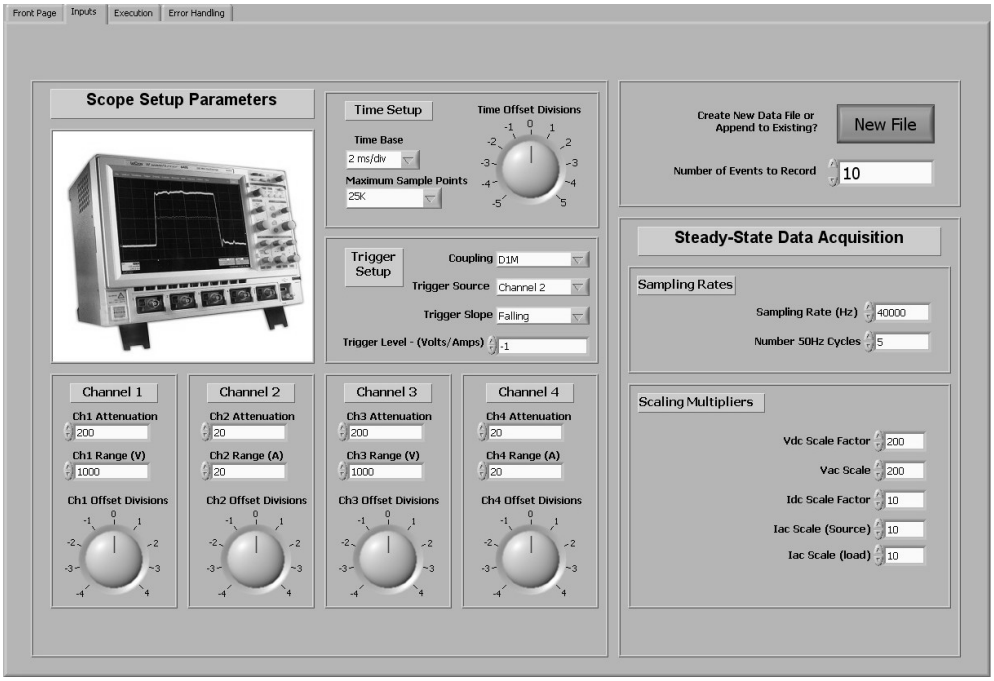

Figure 3.12: Input Pane

3.6.2.2 Execution

The *Execution* panel is shown in Figure 3.13. When a test is being performed, this pane provides a continuously updating display of the steady state operation of the system, allowing the user to ensure switching of the generator disconnect only after steady state operation has been reached. Steady state monitoring is performed with the visual aid of the left-hand charts, while the right-hand side displays transient waveforms from the previous event as a visual review.

The DC power output of the PV array, AC real power output of the inverter and load power are calculated internally using the *power analyser* module and displayed, together with converter efficiency and export power factor. An indicator is provided to inform the user when the system is fully grid-connected and exporting power. Only under such conditions should a new fault event be initiated, so this feature helps to minimise the duration of a test. Similarly, indication is provided when the trigger state

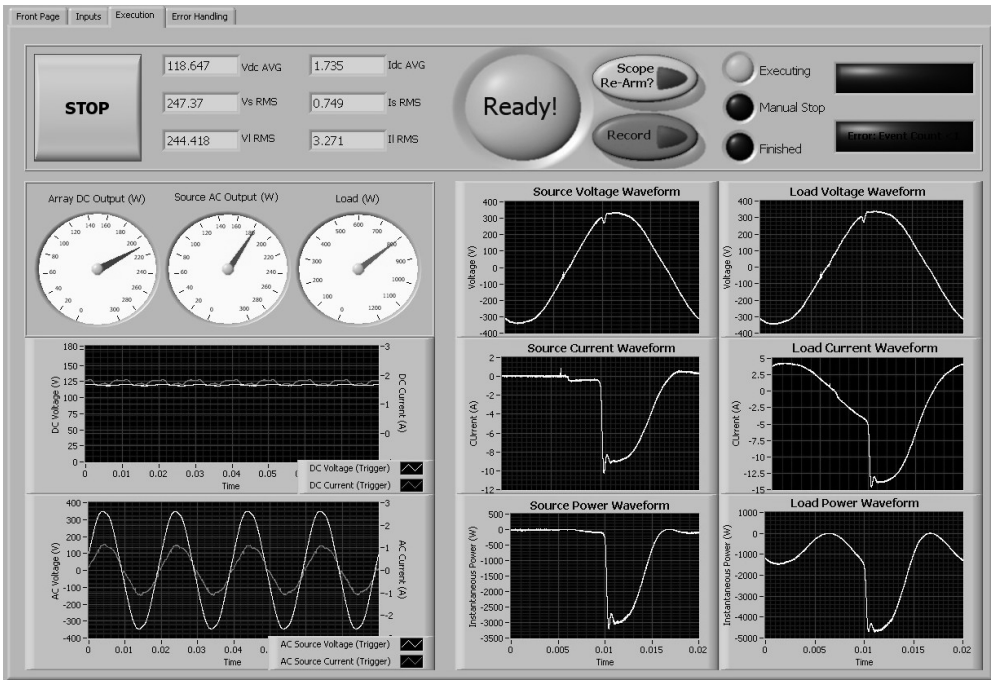

Figure 3.13: Execution Pane

of the scope changes, allowing the user to verify captured data before it is stored.

After testing numerous versions of the *vi* during its development stage, it was decided that a manual approval mechanism for the storage of event data was the most robust approach, even if initially it is time-consuming. The sensitive trigger requirements of certain tests gave rise to a significant number of nuisance events, while others were missed entirely due to ill-defined glitch trigger set-up. No optimal triggering regime could be identified such that only useful data was produced, limiting the applicability of a fully automated data logging system. This was only of minor inconvenience, as user input was still necessary to initiate successive transients.

3.6.3 DAQ Program Execution Structure

Figure 3.14 summarises the execution structure of the transient data logger *vi*. Once initial set-up parameters have been specified by the user, a run command will initialise the scope and DAQ card before dropping in to a loop in which steady-state monitoring data is collected and refreshed. On closing the MCB, the inverter will remain disconnected for three minutes as a safety precaution. This is followed by a short period of grid monitoring (typically around 20s) before the GridGuard^{TM} disconnectors close.

Triggering of the scope due to this switching operation is flagged to the user, who must verify that correct triggering has occurred. If so, the program execution breaks out of the steady-state loop and continues to the data extraction stage, otherwise the scope is manually re-armed from the *execution* panel and the program continues to wait for an event.

The data extraction stage involves interrogation of the waveforms within the scope software to retrieve the following measurements:

- Peak currents and voltages: $V_{max},\ V_{min},\ I_{max},\ I_{min}$
- Rise time of the front: $T_{r\ 20-80\%},\ T_{r\ 10-90\%},\ T_{r\ 30-90\%}$
- Fall time of the tail: $T_{f\ 80-20\%},\ T_{f\ 90-10\%},\ T_{f\ 90-30\%}$
- Maximum rate of change: $\left.\frac{dV}{dt}\right|_{max},\ \left.\frac{dI}{dt}\right|_{max}$
- Energy content of the transient: $W \approx \int_0^T (v \cdot i)\ dt$
- Energy measure of the transient: $S_v \approx \int_0^T v^2(t)\,dt, \quad S_i \approx \int_0^T i^2(t)\,dt$

On the first recorded event, the user is either prompted for a new measurement file name, or to identify an existing file to append, and measurements of subsequent events are automatically appended to the same file. The raw waveforms are also time-stamped and saved to auxiliary data files, with descriptive file names generated from that of the parent measurement file.

Once the transfer to the data logging PC is complete, the event count is incremented and if the requested number has been reached, the program exits with a visual indicator signifying successful completion. Otherwise, the scope is re-armed and the program returns to the steady-state monitoring loop to await the next trigger event. The program may be halted manually at any point if necessary.

3.6.4 Data Files

Measurement and Raw Data files are saved as comma-separated variable (csv) files for simple post-processing in Matlab or Excel. If a new file is to be created, the first storage

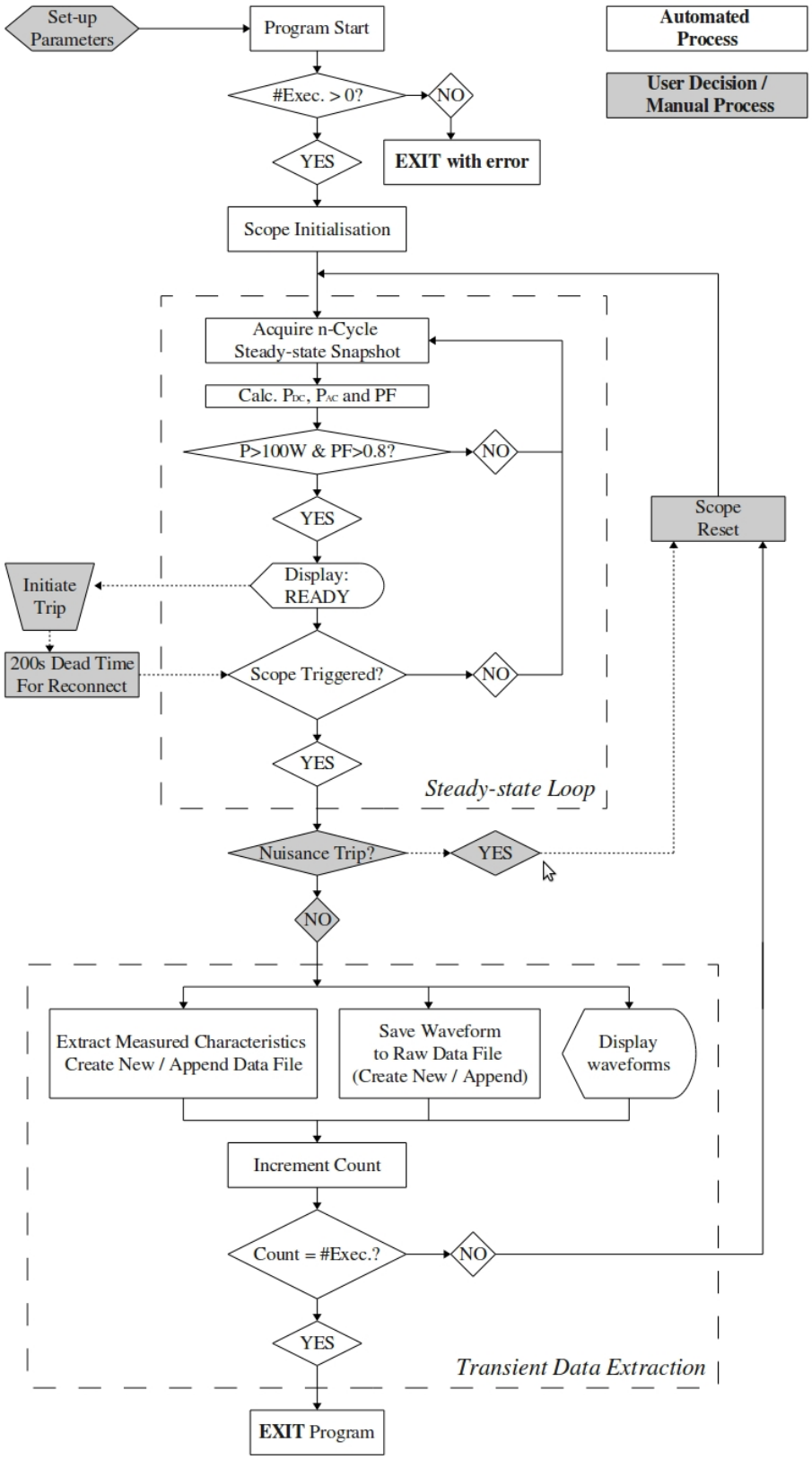

Figure 3.14: Execution Structure of the LabVIEW Data Acquisition *vi*

request will prompt for a file name for the measurement file. The program will then create a set of raw data files by appending a descriptive string to this file name, and saving these to the same folder. For example, a measurement file name `"file1.csv"` will generate auxiliary files `"file1_Vsource.csv"`, `"file1_Vload.csv"`... for each of the transient data acquisition channels.

3.7 Data Post-processing

Fast transient waveforms captured using the scope fall into one of two categories:

1. Single-peak snapshots for determining peak values and rates of change at high precision.

2. Dual-peak capture for switch timing analysis, determination of switch pole delay and transformer current inrush measurement.

Interrogation of single-peak waveforms, such as that shown in Figure 3.15, is a simple process, and the measurements identified on page section 3.6.3 can all be extracted in the scope hardware before the data is transferred to the PC for storage. A sub-vi within the data-acquisition program was written in order to perform this interrogation procedure, thus minimising the amount of post-processing of raw data required.

For the identification of timing of transient fronts with respect to the supply voltage sinusoid, a longer capture window of 20ms is necessary. Within this window, a pair of transients of opposing polarity are normally observed as shown in Figure 3.16, from which the required timing information can be extracted. Due to the variation in switch pole delay τ_{sw} and inrush delay τ_i between successive tests, evaluation of these quantities using scope hardware was found to be unreliable. Determining the amplitudes and rise/fall-times of the secondary peak was thus inconsistent, and as such, all waveform captures with multiple peaks required further post-processing to complete the measurement data set.

This section details the post-processing operations undertaken in order to generate measurement sets from raw waveforms.

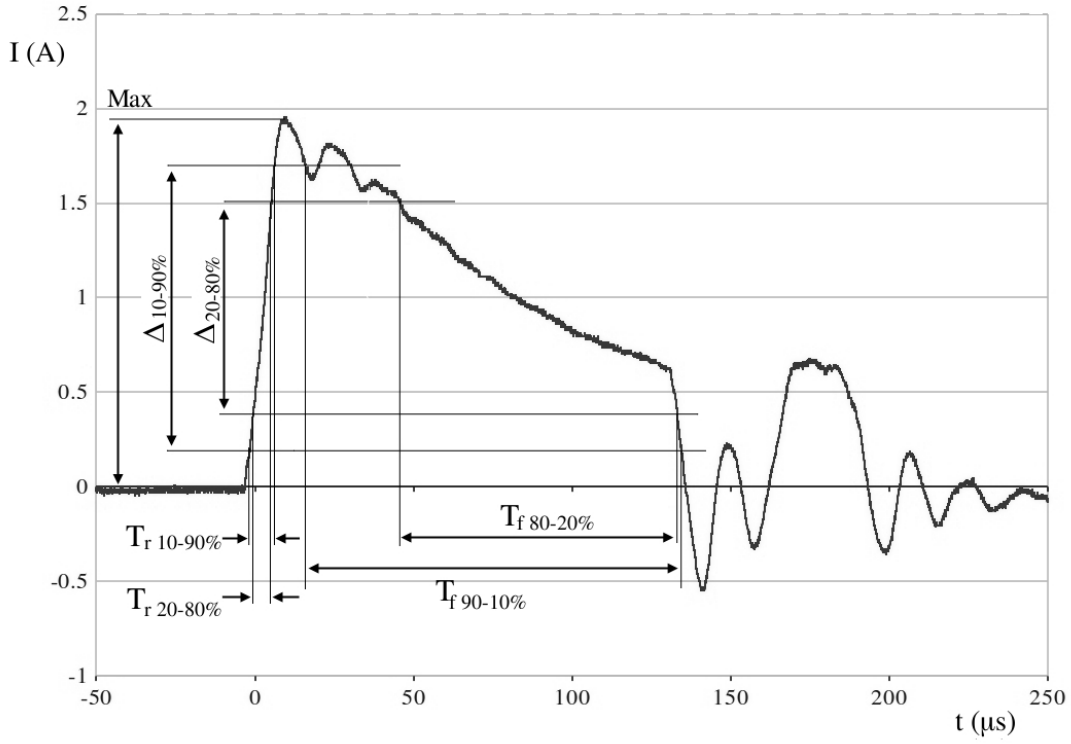

Figure 3.15: Single Transient Capture and Direct Data Extraction (at inverter AC terminals)

3.7.1 Rising Edge

The rates of rise $\frac{dV_{rise}}{dt}$ and $\frac{dI_{rise}}{dt}$ of both transients are determined from the 10-90% and 20-80% intervals, as with the direct measurements performed in the scope hardware. Peak values are first obtained, from which the 10, 20, 30, 80 and 90% levels are calculated. The first sample time at which the voltage or current exceeds each level is then identified to give a crude estimate of rise times. For very fast rising edges, the accuracy of this first approximation is unacceptable, introducing an error of up to ±10% for a slope defined by only 10 discrete measurement points.

Improved accuracy is achieved by a second step, comparing the calculated level with measured values immediately above and below it, and using linear interpolation to determine an intermediate time instant more closely approximating its true value. This process is illustrated in Figure 3.17.

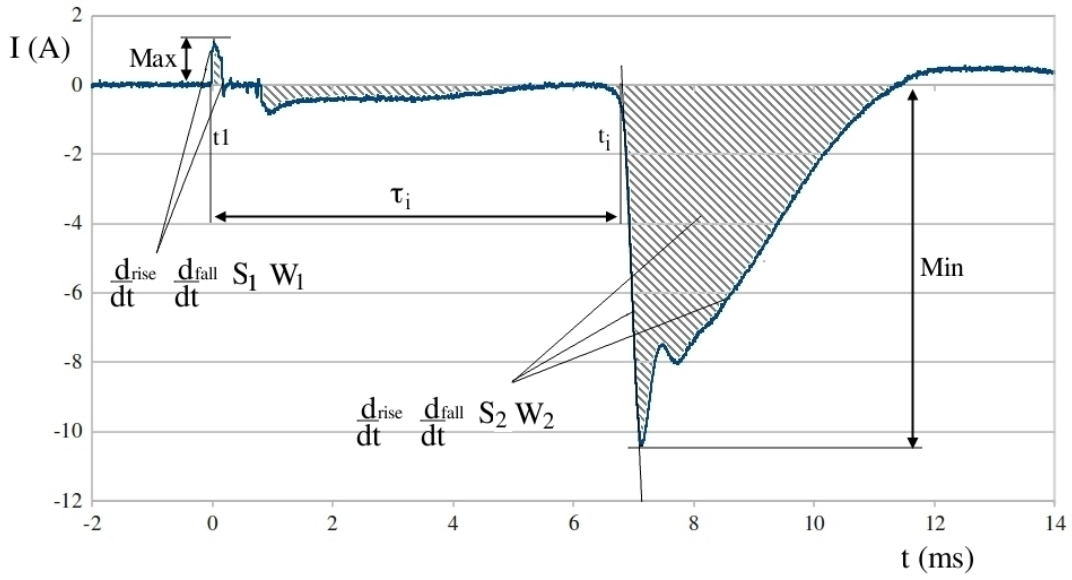

Figure 3.16: Measurements on a Typical Dual-peak Current Waveform (at inverter AC terminals)

3.7.2 Falling Edge

Measurements on the falling edge were performed in a similar manner, except that the scan is started from the data point corresponding to the peak value. The first discrete instant in time at which the variable drops *below* each threshold level is then tabulated. The time at which the variable drops to 50% of its peak value is also recorded for comparison with the standard lightning test waveform of Table 3.1. Since the steepness of tail roll-off is much less than that of the initial rising edge, the percentage error introduced by approximating the timings in this way is significantly reduced, making further interpolation unnecessary.

The tail time T_2 from Table 3.1 is found by linearly extrapolating the rising edge slope back to zero, and subtracting the corresponding time t_0 from that of the tail half-magnitude point $t_{50\%}$. This is illustrated in Figure 3.18.

3.7.3 Energy Measure

The energy measure of a given voltage or current waveform is necessary for the derivation of equivalent standard test waveforms. It is determined by trapezoidal integration of the square of the measured data between instant t_0 and a later point at which the tail has effectively rolled off to zero, a window of $5 \times T_2$ deemed sufficient in most cases.

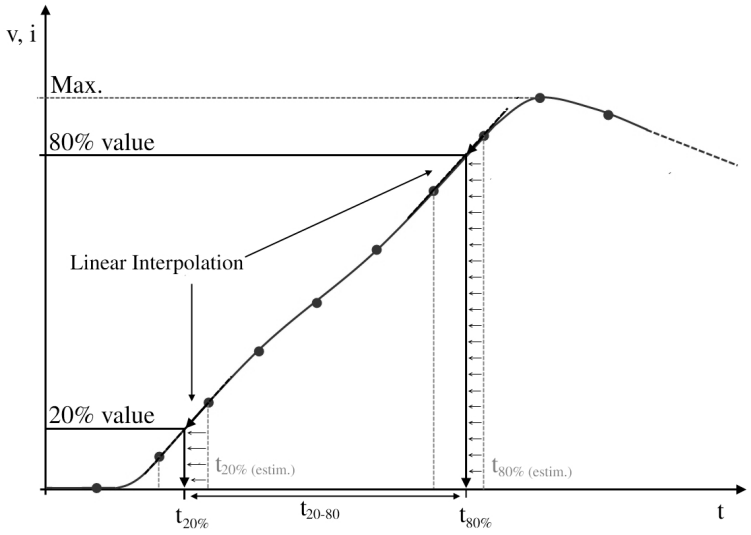

Figure 3.17: Linear Interpolation Process for Determining Slope and Rise Time of Fast-front Transients

The integration in Equation (3.2) was performed for both transients in each captured waveform, where Δt represents the sampling interval of the oscilloscope. The process is illustrated in Figure 3.19.

$$S_v = \int_{t_0}^{t_0+5\cdot T_2} v^2(t)\,dt = \sum_{n=1}^{\frac{5\cdot T_2}{\Delta t}} \left\{ \frac{v^2[(n-1)\Delta t + t_0] + v^2[n\Delta t + t_0]}{2} \right\} \cdot \Delta t \tag{3.2}$$

3.7.4 Energy Content

The energy content W is determined in a similar manner, except that it is calculated from a third waveform $p(t)$, which is simply the product of the coincident instantaneous values of $v(t)$ and $i(t)$. This waveform is then numerically integrated over the same time window as used for the energy measure S.

$$W = \int_{t_0}^{t_0+5\cdot T_2} p(t)\,dt = \sum_{n=1}^{\frac{5\cdot T_2}{\Delta t}} \left\{ \frac{p[(n-1)\Delta t + t_0] + p[n\Delta t + t_0]}{2} \right\} \cdot \Delta t \tag{3.3}$$

3.7.5 Switch/Inrush Timing and Delay

The timing of switch operation and inrush inception relative to the zero-crossing of the grid reference sinusoid can be determined by interrogation of the inverter terminal current and voltage waveforms. No point-on-wave control of the relay closing operation

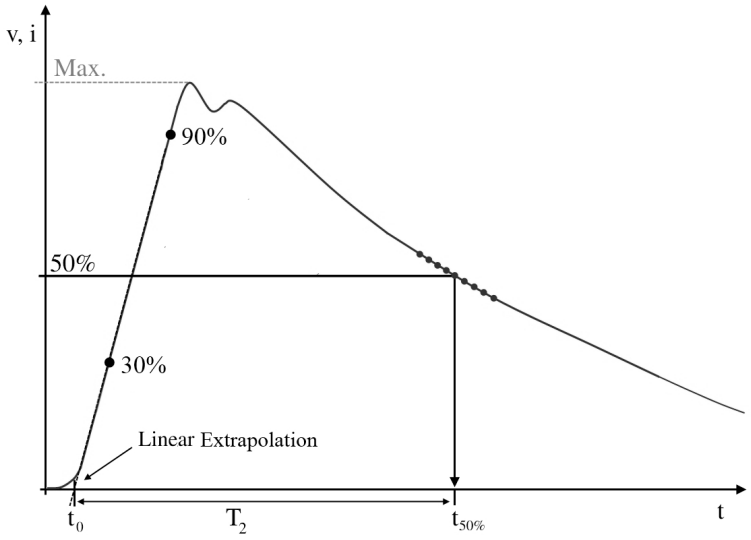

Figure 3.18: Falling Edge Measurement from Raw Waveforms

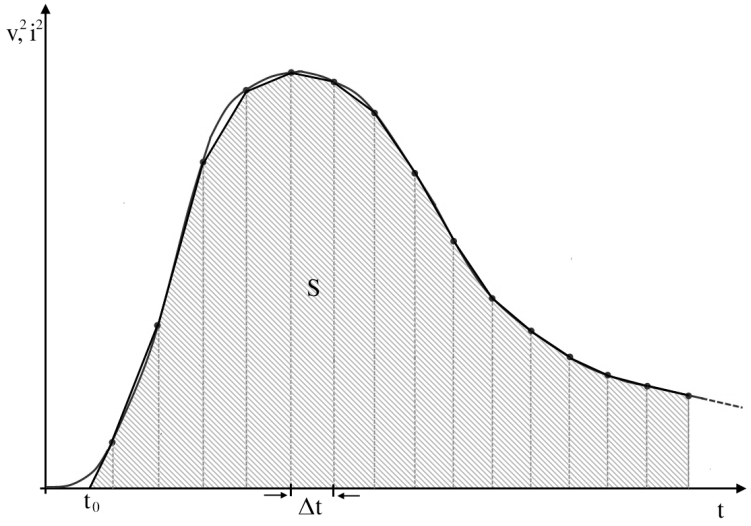

Figure 3.19: Determination of the Wave Energy Measure S by Trapezoidal Integration

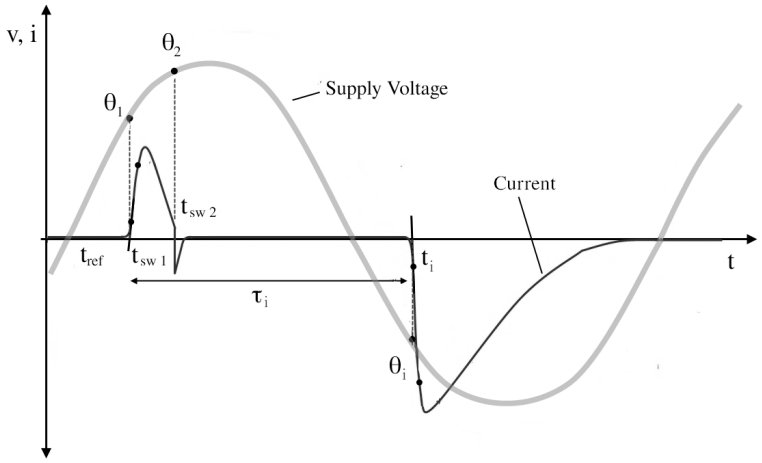

Figure 3.20: Switch Timing and Pole Delay Measurements

is assumed, and a window of one cycle (20ms) following the initial trigger instant is specified to capture any subsequent inrush transient. Switching instants are obtained from the current waveform by linear extrapolation of the line passing through both 20 and 80% magnitude points.

The zero-crossing reference time t_{ref} is then determined from the voltage waveform. As with determination of the rising edge timings, identifying the first data point greater (or less) than a threshold value is not necessarily the most accurate means of identifying the instant of crossover, this time due to the presence of small amounts of noise in the signal. A best fit line is, therefore, applied to the 50 data points either side of the estimate reference time, and the crossover instant of this fitting taken as the true value of t_{ref} (see Figure 3.20).

Switching angles are calculated by Equations (3.4) - (3.6). Similarly, delay terms are determined from Equations (3.7) and (3.8)

$$\theta_1 = \frac{t_{sw\ 1} - t_{ref}}{20ms} \cdot 360^\circ \tag{3.4}$$

$$\theta_2 = \frac{t_{sw\ 2} - t_{ref}}{20ms} \cdot 360^\circ \tag{3.5}$$

$$\theta_i = \frac{t_i - t_{ref}}{20ms} \cdot 360^\circ \tag{3.6}$$

$$\tau_{sw} = t_{sw\ 2} - t_{sw\ 1} \tag{3.7}$$

$$\tau_i = t_i - t_{sw\ 1} \tag{3.8}$$

3.8 Chapter Conclusions

Characterisation of switching transients associated with SSEG disconnect and reconnect operations is vital to the development of good simulation models. Details of a laboratory test bed for the acquisition and analysis of switching transient magnitude, waveshape and energy content under repeatable conditions and according to existing Insulation Coordination standards have been presented. A complete photovoltaic installation was designed and installed in the Cardiff University Solar Energy Laboratory, and a semi-automated data-logging system constructed using NI LabVIEW for the acquisition of generator transient data.

A variety of appropriate synthetic waveshapes has been proposed for the emulation of typical waveforms in future time-domain simulation studies and laboratory tests. A discussion of the results obtained from laboratory testing may be found in the chapter that follows.

Chapter 4

Statistical Switching Transient Measurements of a Solar Energy Inverter Source

In this chapter, results of laboratory experiments are presented with reference to specific test configurations. Data are presented in such a way as to inform the detailed simulation models of Chapters 5 and 6, and simple simulation results accompany measurements where appropriate. To aid in the development of the software models, experimental waveforms are compared with standardised test waveshapes in order to identify the most appropriate transient source representations for future study.

4.1 Background

Connection of embedded generation rated below 16A per phase into the public electricity supply is admissible subject to the given installation satisfying the connection requirements in BS EN 50438 [6]. An important requirement of this document is that a generator must disconnect from the grid in response to voltage and/or frequency excursions, as summarised in Table 4.1. These requirements are equivalent to those laid out in Energy Networks Association (ENA) Engineering Recommendation G83-1 [5].

Disconnection must be achieved by means of a two-pole electromechanical relay, such that the device is fully isolated from the grid in the event of a fault on the supply side of the consumer bus. Following restoration of the supply voltage and frequency to within the allowable ranges defined in Table 4.1, a grid monitoring system shall wait a pre-set time before re-closing the relay poles. This delay may vary from 20s for a low-inertia

Table 4.1: Disconnection Requirements of BS EN 50438 [6] and ER G83-1 [5]

Protection Setting	Max. Clearance Time (s)	Max. Trip Setting
Overvoltage (stage 1)	1.5	264V (+15%)
Undervoltage (stage 1)	1.5	207V (-10%)
Overfrequency	0.5	50.5Hz (+1%)
Underfrequency	0.5	47Hz (-6%)
Loss of Mains	0.5	-

device such as a grid inverter, to 3 minutes or more for a small induction generator, but factory settings of like devices are typically uniform and remain unchanged once installed.

Low voltage feeders with high penetration of embedded generation below 16A/phase shall, therefore, be subject to multiple simultaneous or near-simultaneous switching events in response to individual voltage or frequency excursions, with potential for associated electromagnetic switching transients and transformer inrush. The purpose of the laboratory experiments presented here is to understand and quantify the transient characteristics of individual embedded generators over the disconnect/reconnect cycle. The results shall help inform subsequent transient simulations with increased numbers of devices, such that the cumulative effects of clustered generation may be predicted.

4.2 Laboratory Test Configurations

This section summarises variations in the detailed equipment specification discussed in section 3.5, for the purpose of acquiring a range of data sets. For clarity, alterations to the standard configuration are illustrated with the use of one-line diagrams. In all cases, the solar array is connected to the inverter and available for generation.

4.2.1 Transients on Generator Reconnection

The generator was connected to the LV supply by $16m$ of $2.5mm^2$ twin and earth cable, with a switch and MCB for protection and isolation, as shown in Figure 4.1. Initial disconnection of the generator is achieved by a loss-of-mains (LoM) trip, initiated by manual opening of the circuit breaker. Supply to the generator terminals is then restored, and the transient logger armed to await reclosing of the disconnector.

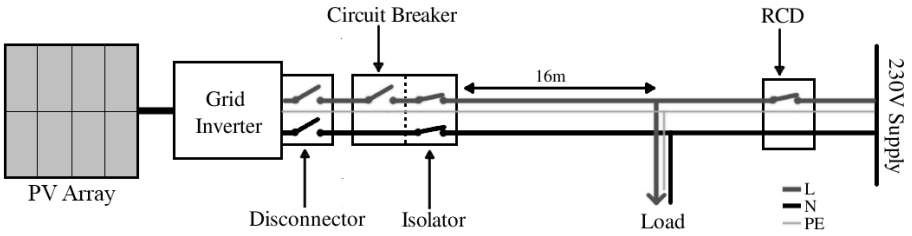

Figure 4.1: Test Configuration A: Transient Capture on Generator Reconnect

4.2.2 Effect of Supply Impedance on Voltage Peak

The fault impedance of the mains feed in the laboratory is approximately 0.012Ω at 50Hz. This is relatively low in comparison with typical fault impedance on a radial LV feeder. Table 4.2 gives a selection of indicative calculated fault impedances for different LV transformer ratings and increasing circuit length. Measured transient voltage amplitudes were found to be very small (less than 5V), and a method for the increase and variation of series supply impedance was, therefore, necessary in order to generate representative voltage transients at the generator terminals.

Table 4.2: Calculated Short-Circuit Impedance at Radial Locations on a Hypothetical LV Feeder [146] (fault level at 11kV terminals: 250MVA)

LV TF Rating	Transformer LV Terminals	+ 100m $185mm^2$ Alu (3ϕ Trunk)	+ 50m $120mm^2$ Alu (3ϕ Trunk)	+ 25m $25mm^2$ Cu (1ϕ Service)	+ 5m $2.5mm^2$ Cu (1ϕ)
500kVA	0.021Ω	0.032Ω	0.040Ω	0.058Ω	0.105Ω
100kVA	0.100Ω	0.115Ω	0.121Ω	0.144Ω	0.209Ω

The impedance compensation shown in Figure 4.2 is achieved by means of a coil of twin and earth cable, connected in one of three configurations to give additional series impedance as summarised in Table 4.3. In this manner, the effects of elevated supply impedance on transient characteristics may be determined. Results of the compensator frequency dependency tests are given in Appendix B.

Table 4.3: Series Impedance Compensation (values at 50Hz)

Configuration	Live Only	LN - Parallel	LNE - Parallel
Impedance (Ω)	0.679	0.504	0.310

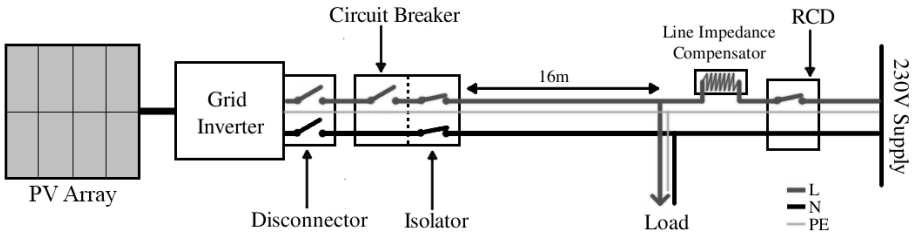

Figure 4.2: Test Configuration B: Determining Impact of Supply Impedance

4.2.3 Transients on Generator Disconnection

The capture of transients associated with the disconnection of the generator under export conditions requires that the mains supply to the terminals remain live during the entire switching cycle. A protection mechanism other than the LoM trip must, therefore, be triggered, by either voltage or frequency deviation beyond the limits defined in [5]. A variable transformer was employed to shift the feeder voltage beyond the threshold levels dictated in Table 4.1, as illustrated in Figure 4.3.

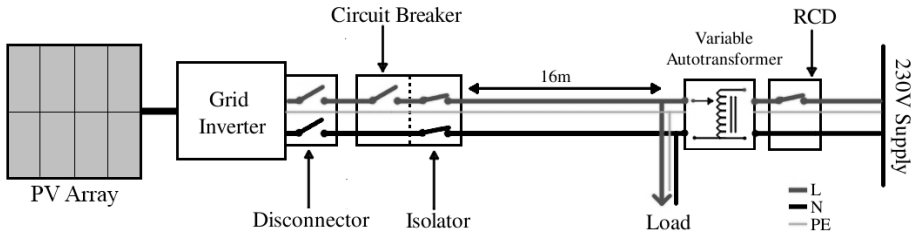

Figure 4.3: Test Configuration C: Transient Capture on Generator Disconnect

Extensive testing using configuration C produced no significant results relating to the disconnection of the generator. This is attributable to the fact that the solar inverter feeds a predominantly resistive supply circuit, and operates close to unity power factor. Current interruption therefore occurs near zero on the voltage sinusoid, and transient recovery voltages are accordingly negligible. As a result, the sections that follow are focused on re-closing operation of the inverter relay disconnect.

4.3 Experimental Results

The following section presents results of transient measurements made on reconnection of the grid inverter to the LV supply. Results are presented in the following subsections:

- Current Measurements

- Voltage Measurements
- Switch Timing Data
- Energy Content

4.3.1 Statistical Measures

All statistical distributions of measured data are presented with their sample mean value and standard deviation. In addition, a pair of statistical shape measures are employed to help describe these distributions [147]:

4.3.1.1 Skewness

The skewness of a probability distribution is a measure of its asymmetry about the mean. It acts as an indication that one tail of the distribution is longer than the other, with a sample bias to one side of the mean. A negative skewness indicates a distribution with a right-hand bias, while a positive skew indicates a left-hand bias, as depicted in Figure 4.4. For a sample of N values, the skewness is evaluated as follows:

$$\text{Skewness} = \frac{\frac{1}{N}\sum_{i=1}^{N}(x_i - \overline{x})^3}{\left(\frac{1}{N}\sum_{i=1}^{N}(x_i - \overline{x})^2\right)^{3/2}} \tag{4.1}$$

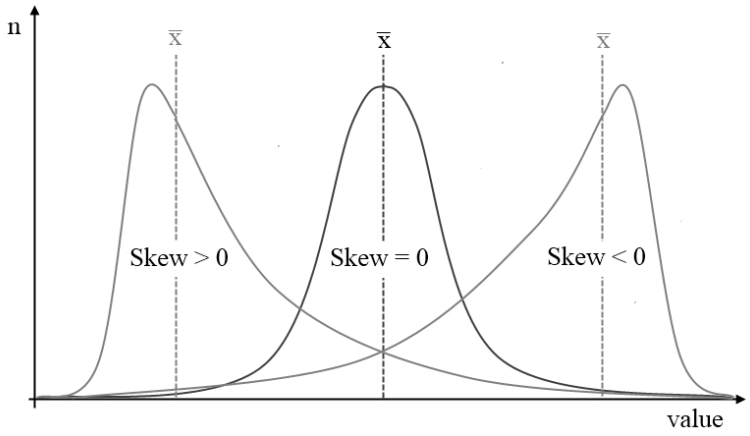

Figure 4.4: Skewness of a Distribution

4.3.1.2 Kurtosis

The kurtosis of a probability distribution is a measure of the sharpness of its peak. A negative kurtosis (platykurtosis) indicates a flattened wide peak with thin tails, while a

positive kurtosis (leptokurtosis) indicates an acute peak with heavier tails, as depicted in figure 4.5. For a sample of N values, the kurtosis is evaluated as follows:

$$\text{Kurtosis} = \frac{\frac{1}{N}\sum_{i=1}^{N}(x_i - \overline{x})^4}{\left(\frac{1}{N}\sum_{i=1}^{N}(x_i - \overline{x})^2\right)^2} - 3 \tag{4.2}$$

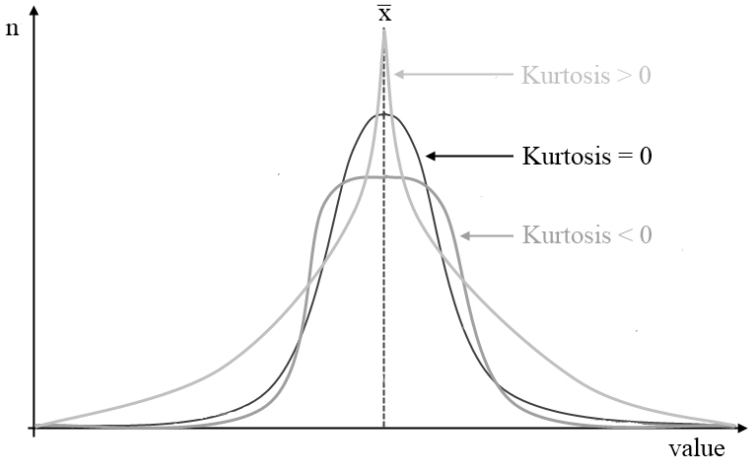

Figure 4.5: Kurtosis of a Distribution

4.3.2 Current Transients

The following current transient measurements were obtained using test configuration A (Figure 4.1), and are derived from a dataset consisting of 251 individual switching event records. Successful triggering was achieved in 89% of all tests, a figure which may be used to quantify the overall probability of a given transient current magnitude. A range of local loading scenarios were considered, but analysis reveals that the pre-existing load condition has little or no impact upon the observed current transients at the generator terminals due to the current limiting resistance in circuit on initial reconnection. Results of the different load scenarios are thus presented as a single data set in this section.

As discussed in Chapter 3, event records consist primarily of a pair of pole closures, giving rise to an initial switching transient waveform. This initial pulse may then be followed by a second transient due to capacitive inrush on the DC bus. Each set of measurements is, therefore, subdivided according to the process that generated it. The first pole closure is from here on referred to as *pole 1*, and the second as *pole 2*. A sample waveform from the data set is presented in Figure 4.6.

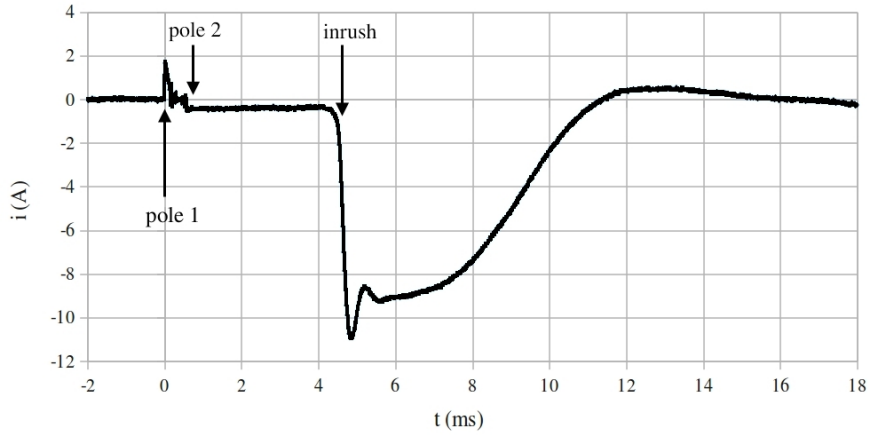

Figure 4.6: Sample Current Waveform at Generator Terminals with Test Configuration A, Illustrating Both Pole Closing Instants

4.3.2.1 Peak Measurements ($i_{max/min}$)

Figure 4.7a shows the statistical distribution of peak currents for the switching transient current waveform immediately following the closure of pole 1 of the disconnector. A near Gaussian distribution over the full data set can be observed, with a mean value of 1.35A. This low value is to be expected, as current should only flow to counteract the voltage across the contacts of pole 1 immediately prior to closure. However, high current rates of change were observed, as discussed in the next subsection.

All 251 waveforms were captured by triggering on the rising slope of the initial low-current transient. Of these, 207 (approximately 82%) captured an additional transient due to capacitive inrush. Figure 4.7b shows the distribution of peak currents for the set of 207 measurable inrush transients, with a clear cut-off around 12A due to a $33\Omega \pm 10\%$ current limiting resistance in the inverter output circuit.

As can be seen, current magnitudes due to current inrush are significantly higher than those of the initial switching transient, with a mean value of 9.12A. Significant negative skew is observed in the distribution of measured current maxima. As seen from Figure 4.6, the polarity of the second transient is reversed relative to the first (with positive current in the direction of inverter export). The second transient can, therefore, be assumed to consist primarily of the inrush current of the DC bus capacitance, a component common to all sizes of grid inverter.

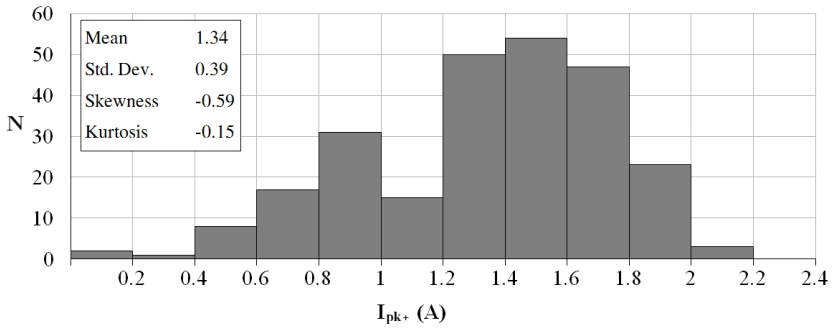

(a) Peak Current on Closing Pole 1

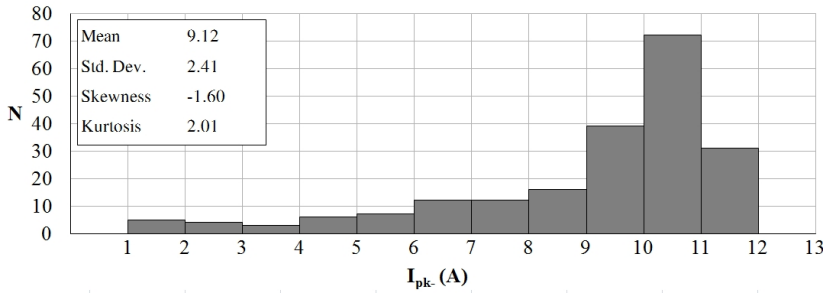

(b) Peak Inrush Current

Figure 4.7: Peak Current Distributions

4.3.2.2 Current Rate of Change $\left(\frac{di}{dt}\right)$

In addition to peak value measurement, it is important to evaluate the rate of change in the leading and trailing edges of a current waveform. Fast rising current impulses can accelerate the degradation of insulation, and may cause high voltages to develop across transformer windings and other inductive network components.

Figures 4.8a and 4.9a depict the statistical distribution of rising and falling edge rates of change for the initial current transient following pole 1 closing. Due to the low amplitude of the switching current transient, the presence of even small quantities of noise can result in errors when determining the 10% rise time. Rising edge rate of change is thus evaluated over the interval 30% to 90% of the peak value, similar to the voltage measurement techniques of IEC60 [148], giving a bimodal distribution as seen in Figure 4.8a. The measured values are split evenly between the two modes; those of mode 1 occupying the range 20-100 kA/s, with a mean value of 59.4 kA/s, and for mode 2, a range 100-200 kA/s with a mean of 144.5kA/s.

As can be seen from Figure 4.8b, there is a broadly linear relationship between the the rate of change and peak current, and the two result clusters giving rise to the

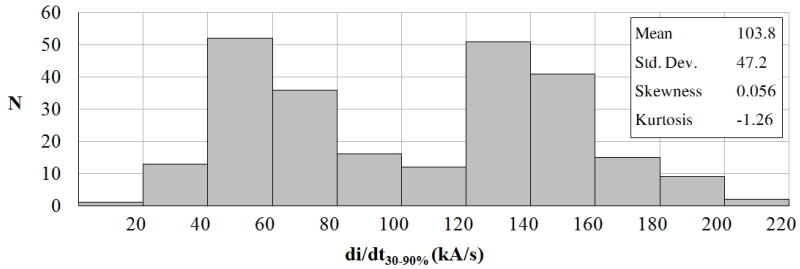

(a) Distribution of *Rising* Edge Rate of Change on Pole 1 Closure

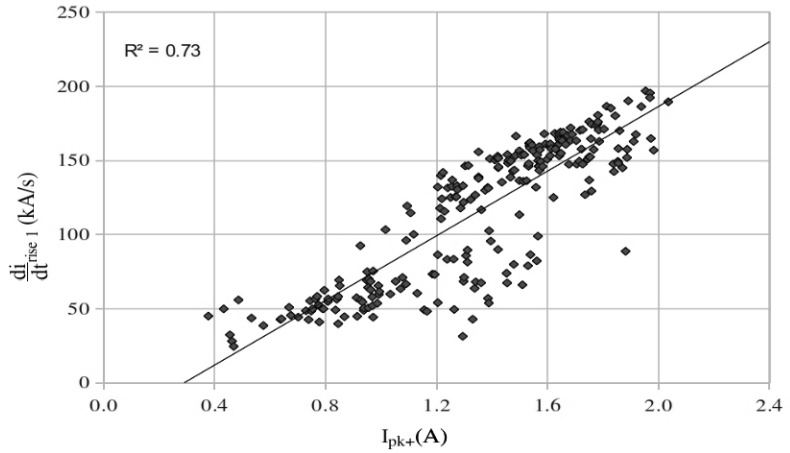

(b) *Rising* Edge Rate of Change as a Function of Peak Current (pole 1 closing)

Figure 4.8: Rate of Change of Current Transient Front following Pole 1 Closing

bimodal distribution are clearly visible. The near linear relationship means that the rise time of the leading edge should remain independent of the peak current, as analysed later in this section.

The distribution of falling edge rates of change, as depicted in Figure 4.9a, displays a positive skew with 70% of falling slopes lying in the range below 20kA/s, with an overall mean of 18.4kA/s. A significant number of events, however, can be seen to occupy the range 20-50kA/s. This weighting indicates that there is a range of waveshapes associated with the falling edge, which may be attributed to the timing of pole 2 closing. This can be confirmed from the plot ramp rate against peak current in Figure 4.9b.

Increasing the impedance of the line has the effect of reducing switching transient current magnitudes and accelerating the tail roll-off. Current transient measurements taken in the elevated impedance test configuration (B) are plotted alongside zero-impedance data in Figure 4.9b, to illustrate this effect. In both cases, there is an appreciable linear

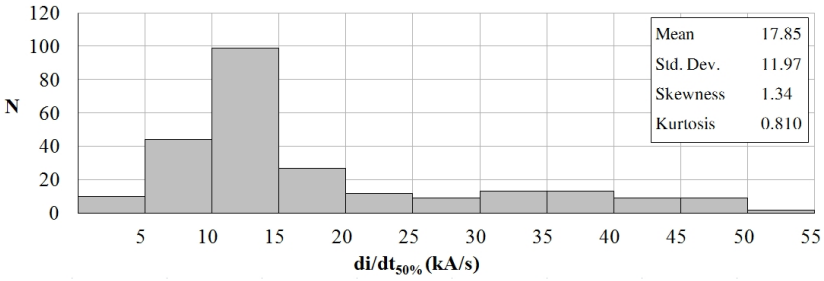

(a) Distribution of *Falling* Edge Rate of Change Following Pole 1 Closure

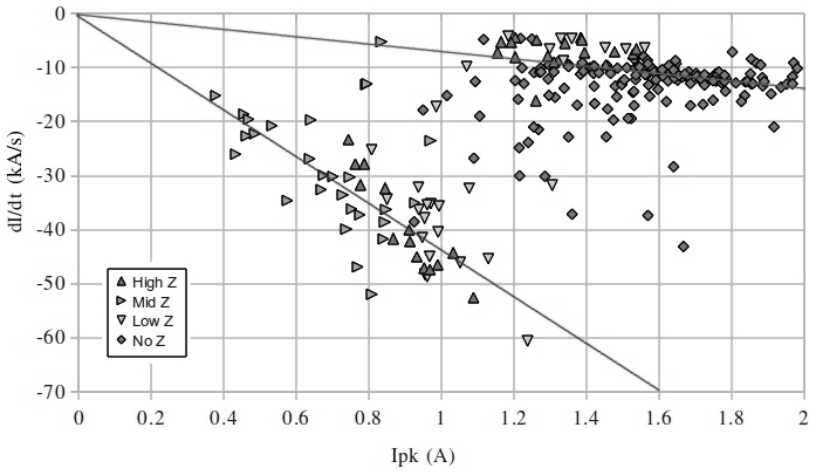

(b) *Falling* Edge Rate of Change as a Function of Peak Current (pole 1 closing)

Figure 4.9: Rate of Change of Current Transient Tail following Pole 1 Closing

relationship between the peak current and roll-off rate.

Leading edge current rates of rise for the inrush transient are summarised in the distribution of Figure 4.10a. Much like the peak current distribution, rising edge ramp rates are heavily skewed towards the upper end of the measured scale. Slope magnitudes are around 20% of those in the initial switching transient, with a mean value of -33.7kA/s, indicating a generally distinct waveshape.

Due to the current limiting resistance in the relay disconnect circuit, a linear relationship exists between the peak current and rising edge slope as can be seen in Figure 4.10b. Negative values indicate the reversal of polarity relative to that of the initial switching transient. One can, therefore, expect a near constant rise time, independent of the magnitude of the current impulse.

Experimental results of tail roll-off rate measurement are less well defined. As can

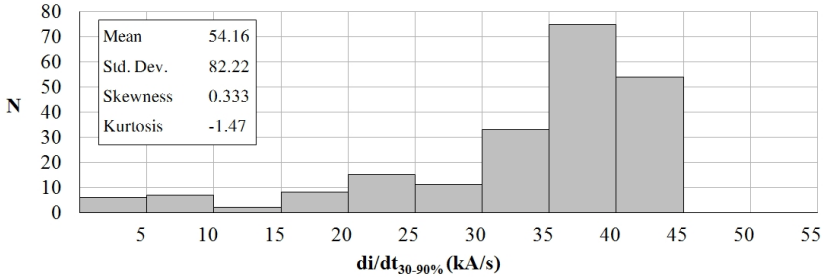

(a) Distribution of Inrush Transient *Rising* Edge Rate of Change

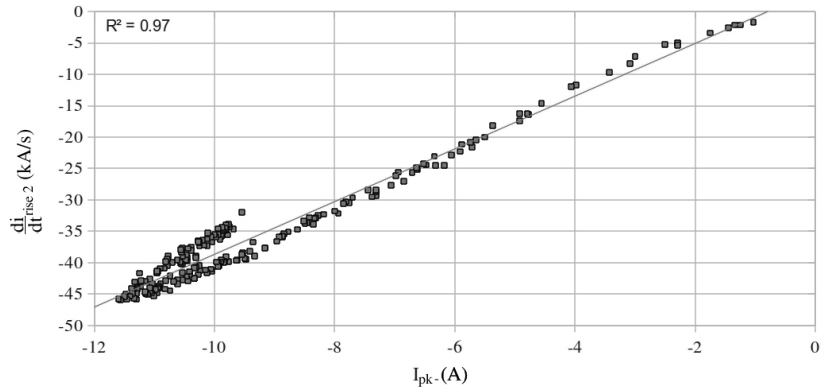

(b) Rising Edge Rate of Change as a Function of Peak Current

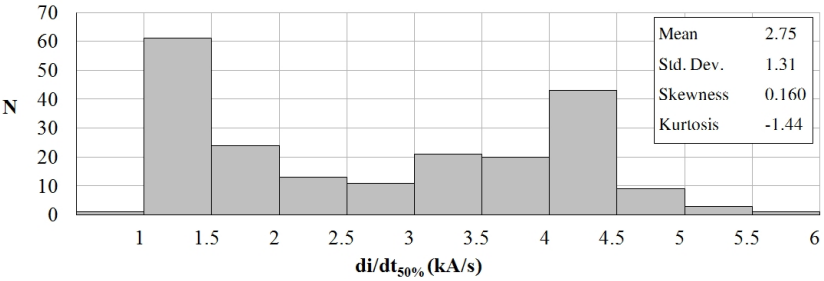

(c) Distribution of Inrush Transient *Falling* Edge Rate of Change

Figure 4.10: Inrush Current Transient: Rising and Falling Edges

be seen from Figure 4.10c, there is a rough bimodal distribution of falling edge $\frac{di}{dt}$ from peak to half magnitude. This may be partly explained from observation as follows:

1. Inrush initiated during the first quarter cycle of the supply voltage sinusoid results in a transient in which high current is sustained for the remainder of the half cycle by the still rising voltage.

2. Pole closure during the second quarter cycle results in a faster rolloff as the voltage is itself falling away and is unable to sustain the high current.

This effect can be observed in the waveform overlay of Figure 4.11. Case 1 has the effect of elongating the tail, thus reducing the effective rate of rolloff, while case 2 will

result in a far steeper slope, hence the bimodal distribution of Figure 4.10c. The exact instant of inrush inception is dependant on the prior state of charge of the DC bus capacitor.

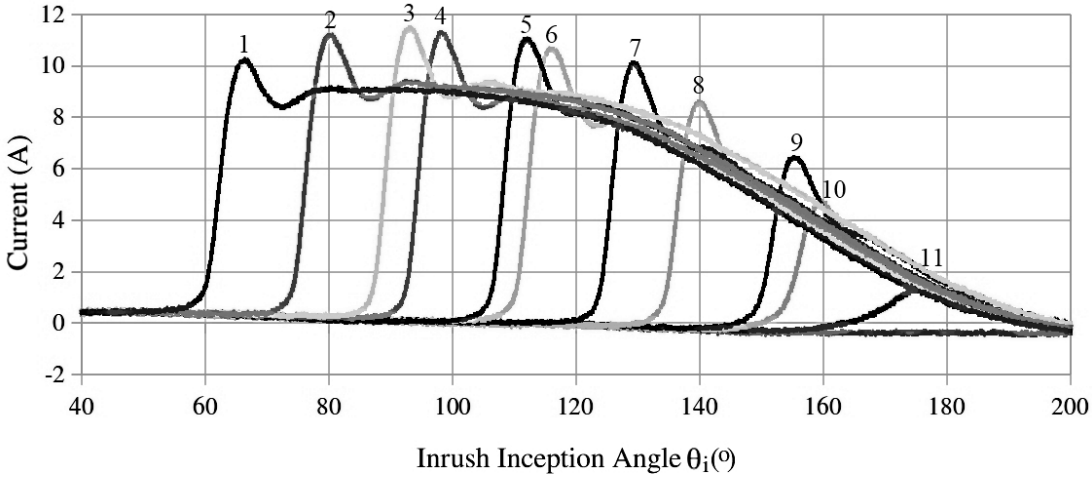

Figure 4.11: Overlay of Inrush Transient Current Waveforms Illustrating Tail Elongation Due to Switching Angle θ_i

4.3.2.3 Timing Dependence $(i(\theta))$

As alluded to in the previous subsection, the instantaneous LV supply voltage that coincides with a particular switching operation will greatly influence the characteristics of the resulting transient. It is, therefore, important to analyse the timing of switching operations with respect to the supply voltage sinusoid, and how this relative timing affects the measured current.

The presentation standard employed here considers a switching angle θ in the range -180° to 180°, with its origin centred at the positive-going zero crossing of the voltage sinusoid measured Live to Neutral. Thus, a negative value of θ indicates a switching instant during the half cycle prior to the zero crossing, while a positive θ would indicate switching in the half cycle following the positive zero crossing.

Poles 1 and 2 were found to close within a narrow range of θ, as seen from the plot of peak current against switching angle in Figure 4.12a. Closure of pole 1, therefore, always leads voltage zero by between 10 and 18 degrees and, over this range, the peak current is linearly dependent on the switching angle.

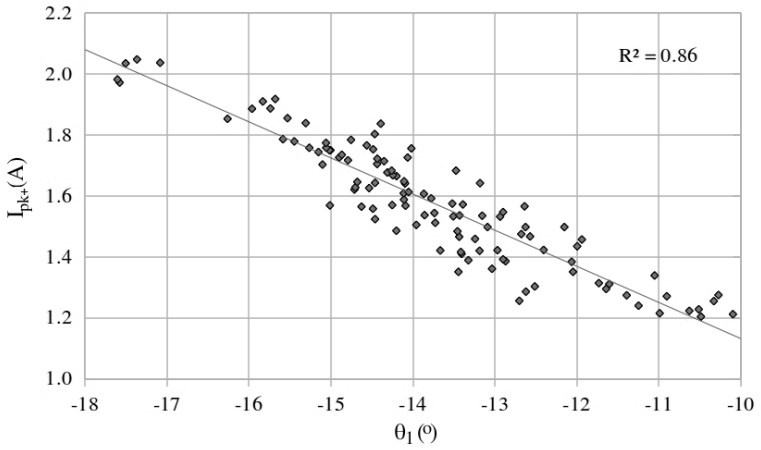

(a) Variation of Initial Transient Peak Current with Switch 1 Closing Angle (θ_{sw1})

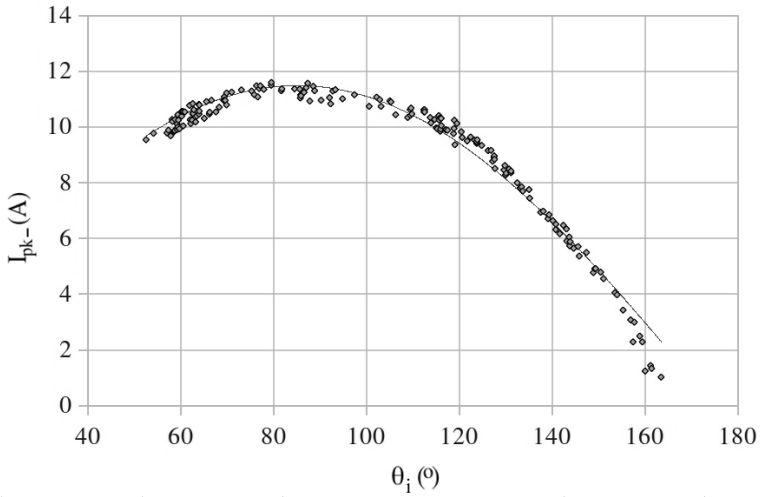

(b) Variation of Inrush Transient Peak Current with Inception Angle (θ_i)

Figure 4.12: Angular Dependence of Current Maxima

By contrast, the inrush inception angle occupies a far broader range, extending from a lag of approximately 50 degrees after voltage zero to the end of the same half cycle. In practice, switching angles beyond 160° resulted in current magnitudes indistinguishable from steady state values. Practical measurements of θ were, therefore, constrained to the range 50° to 160°. As can be seen from Figure 4.12b, over this range, the peak current is sinusoidally dependent on the switching angle, with maximum current magnitudes coincident with voltage maxima.

4.3.2.4 Waveshape Analysis

In this section, current transient waveforms are analysed in order that they may be reproduced in simulations by use of a representative test waveshape. Front and tail

times are compared with the ranges defined in Insulation Coordination Standards [120, 138, 142] for the purpose of classification.

Figure 4.14a shows the distribution of measured rise times for all captured switching current transients. The total rise time T_1 is linearly extrapolated from $T_{30-90\%}$ by multiplying by the factor 1.67 as defined in [148] for voltage measurements. The mean rise time of Figure 4.14a is approximately 15.4μs.

The tail times T_2 of the initial switching current transient are depicted in Figure 4.14b, as measured from the extrapolated switching instant to the 50% roll-off point as shown in figure 4.13. The mean tail time was found to be 80.9μs, meaning that the average switching current transient falls within the definition of a fast-front according to BS EN 60071-1 [138].

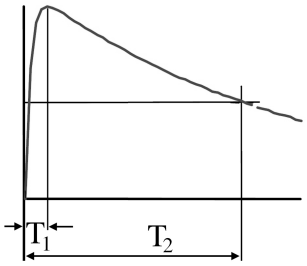

Figure 4.13: Evaluation of T1 and T2 as per [138]

An equivalent analysis has been performed for the inrush transient, with rise time distributions plotted in Figure 4.14c, and tail distributions in Figure 4.14d. Average and extreme values of the waveshape components are summarised in Table 4.4, and are used in the specification of a representative double exponential pulse for later simulations as per [120].

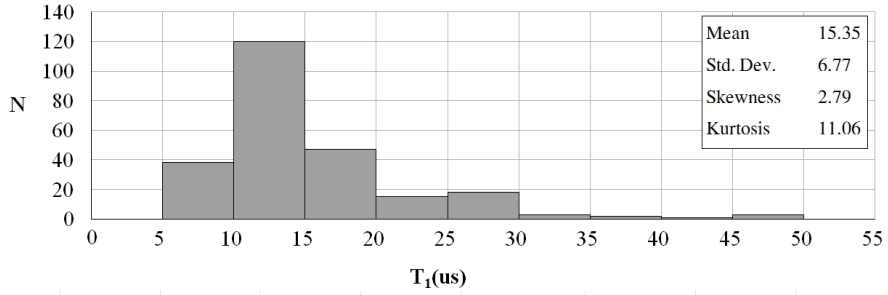

(a) Pole 1 Switching Transient Front Rise Time (T_1)

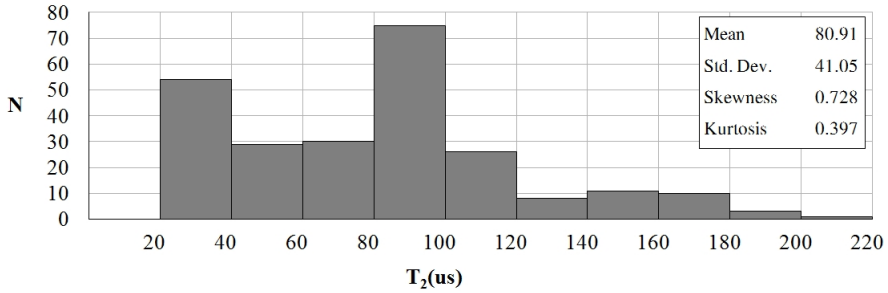

(b) Pole 1 Switching Transient Tail Times (T_2)

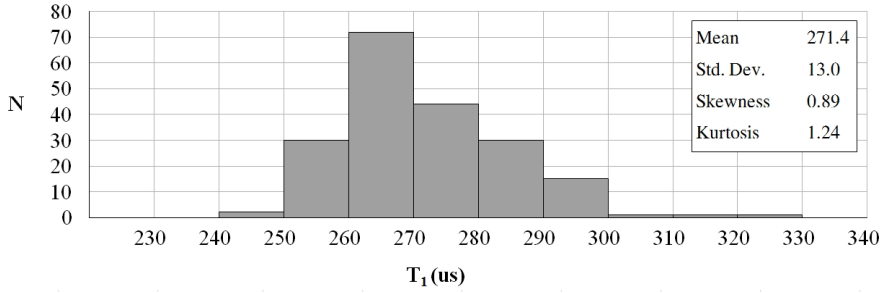

(c) Inrush Current Transient Rise Time (T_1)

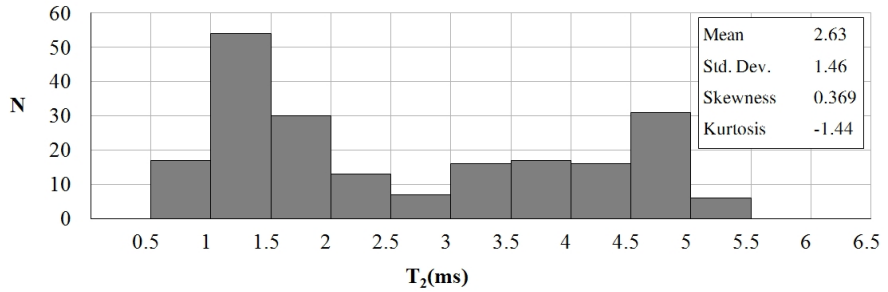

(d) Inrush Current Transient Tail Time (T_2)

Figure 4.14: Current Transient Waveshape Components

Table 4.4: Summary of Transient Current Waveshape Components

Switching Transient	I_{pk1} (A)	T_1 (μs)	T_2 (μs)
Mean Value	1.34	15.5	80.9
Minimum	0.38	8.5	22.9
Maximum	2.05	41.5	224.5
Inrush Transient	I_{pk2} (A)	T_1 (μs)	T_2 (μs)
Mean Value	9.12	270.8	2,630
Minimum	0.46	243	785
Maximum	11.6	705	5,366

4.3.3 Voltage Transients

Voltage transient measurements were obtained from a set of 120 event records using laboratory test configuration B (see Figure 4.2). The transients were isolated for analysis by subtraction of the mains voltage sinusoid, leaving a waveform consisting solely of voltage impulses and supply harmonics. This method introduces the potential for error in time-zeroing the sinusoid, and a voltage offset may occur. Absolute magnitudes may, therefore, deviate by up to 5V either side of the true value.

4.3.3.1 Peak Measurements ($v_{max},\ v_{min}$)

Peak voltages obtained without the series line impedance compensation ($Z_{min} = 0.12\Omega$) were generally too small to distinguish from background noise and supply harmonics (see Figure 4.2). The results presented here are those obtained with an elevated series impedance. From the data obtained, it is observed that an increase in series impedance beyond 0.4Ω at 50Hz has little determinable effect on voltage distortion, and Figure 4.15a illustrates the combined distribution of positive voltage peaks for low- mid- and high-impedance cases. It is possible that a larger data set would begin to illustrate some trend, but it would be inconclusive to infer such a relationship from this small data set.

Figure 4.15a gives a mean pole 1 switching transient voltage magnitude of 47.5V, at a standard deviation of 12.9V. Figure 4.15b indicates a broadly linear relationship between switching voltage and current transient magnitudes for the elevated line impedance scenario. Error bars of $\pm$5V are included.

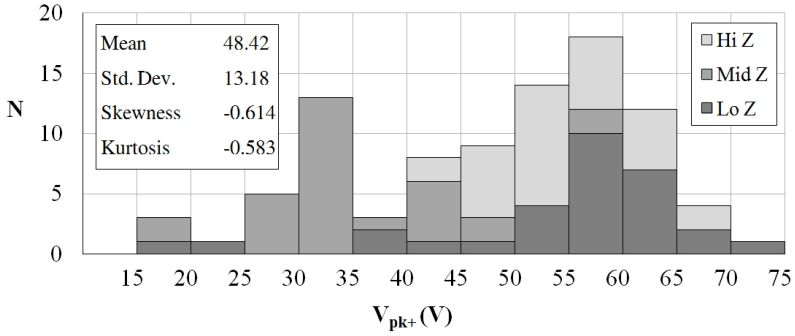

(a) Pole 1 Switching Transient Voltage Distribution with Z Compensator

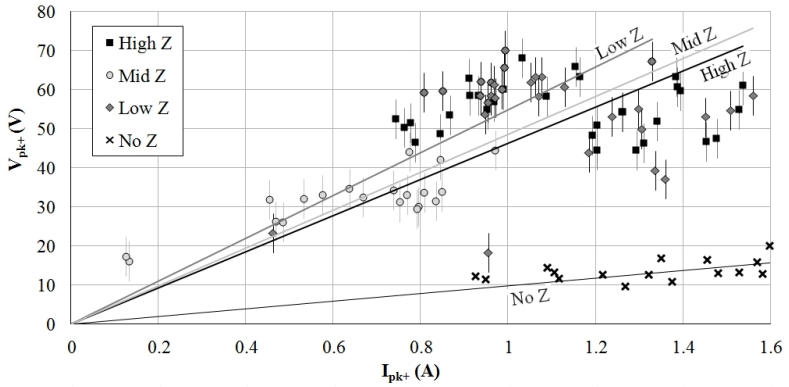

(b) Peak Voltage as a Function of Peak Current (Switching, Pole 1)

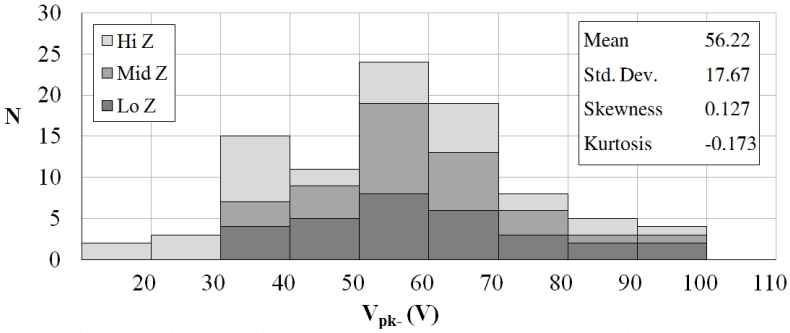

(c) Inrush Transient Voltage Distribution

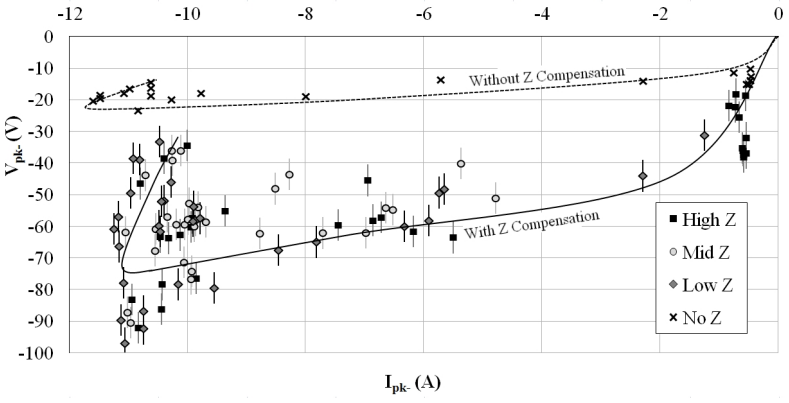

(d) Peak Voltage as a Function of Peak Inrush Current

Figure 4.15: Transient Peak Voltages on Switching and Inrush

Of the 91 switching waveforms captured under the increased line impedance scenario, 82 (90%) recorded a second additional transient due to current inrush. Inrush transient magnitudes were similarly unaltered by change in supply impedance, and are presented cumulatively in Figure 4.15c. Mean voltage magnitude is 55.7V, with a standard deviation of 17.6V.

A relationship between inrush peak voltages and currents is somewhat more pronounced than with the switching transients, as can be seen from Figure 4.15d (negative values indicating a reversal of polarity with respect to switching transient measurements). Due to a distinct weighting of results towards the upper end of the current scale, it is difficult to derive a singular relationship over the full current range. There is, however, a visible divergence of peak voltage with increasing current suggesting a two-slope or polynomial relationship.

As discussed in section 4.3.2, the rising edge rate of change of the inrush current transient varies linearly with current magnitude. For a low voltage feeder with series resistance R and reactance X, the voltage drop should be a function of both the current and its derivative, with the effect of $\frac{di}{dt}$ dominating for very steep rising edges. This explains the nonlinear slope of Figure 4.15d.

4.3.3.2 Voltage Rate of Change $\left(\frac{dv}{dt}\right)$

As with the current transients of section 4.3.2, voltage waveforms were analysed to determine rising and falling edge rates of change. General observation indicates that leading and trailing edges are nearly symmetrical, as distinct from the fast rise and relatively slow tail of the current waveforms. Voltage rates of change are, therefore, evaluated over the intervals 30%-90% and 90%-30% of peak for the front and tail respectively.

Figures 4.16a and 4.16b show the distributions of rising and falling edge voltage ramp rates respectively. Similarly, Figures 4.16c and 4.16d are the distributions of inrush rising and falling edge ramp rates. A statistical analysis of these datasets is summarised in Table 4.5.

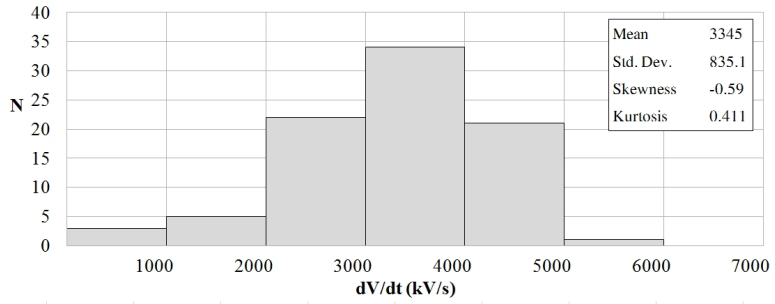

(a) Pole 1 Switching Transient Transient *Rising* Edge $\frac{dv+}{dt}$

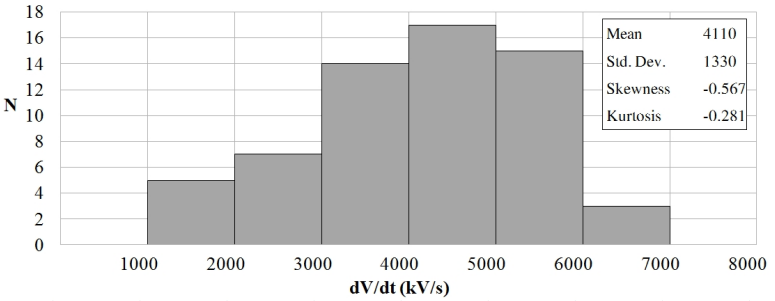

(b) Pole 1 Switching Transient *Falling* Edge $\frac{dv-}{dt}$

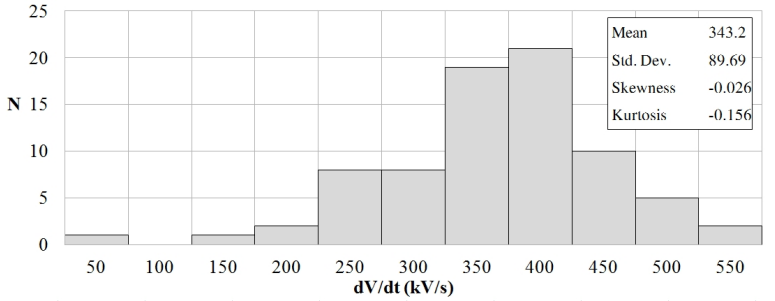

(c) Inrush Transient *Rising* Edge $\frac{dv+}{dt}$

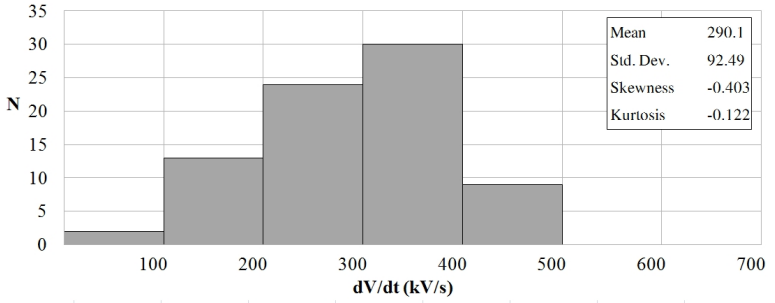

(d) Inrush Transient *Falling* Edge $\frac{dv-}{dt}$

Figure 4.16: Voltage Transient Rate of Change Statistics

Table 4.5: Statistical Variation of Measured Voltage Rates of Change

Quantity	Switching ↑	Switching ↓	Inrush ↑	Inrush ↓
$\bar{v}$	3170 kV/s	-2754 kV/s	-343 kV/s	283 kV/s
σ	1254 kV/s	2037 kV/s	90 kV/s	101 kV/s

4.3.3.3 Waveshape Analysis

Given the similarity of rising and falling edge rates of change for both switching and inrush voltage transients, a typical waveform may be expected to display a good degree of symmetry about its peak. Thus, little similarity exists between the measured waveforms and either of the standard insulation coordination test waveshapes as presented in Chapter 3. Arbitrarily treating the measured waveforms as fast-front impulses as in [138], the front and tail times (T_1, T_2) have been calculated as per Figure 4.13 and are summarised in Figures 4.17a to 4.17d.

Switching transient front times form a neat Gaussian distribution about a mean value of 15.8μs as shown in Figure 4.17a, while the tail times of Figure 4.17b, as measured from the virtual zero of the rising edge to the 50% decay point, are considerably more dispersed. A significant weighting of results in the region 10 to 30 μs keeps the mean value low at 32.3μs, but the numerous outlying results between 30 and 85μs should not be ignored.

Front and Tail times for the inrush voltage transient form a somewhat neater pair of distributions, as can be seen from Figures 4.17c and 4.17d. Mean values of 191.5 and 299.3 μs were recorded for T_1 and T_2 respectively. Statistical analyses are summarised in Table 4.6.

Table 4.6: Statistical Variation of Measured Voltage Front and Tail Times

Quantity	Switching Transient	Inrush Transient
$\overline{T_1}$	15.8 μs	191.5 μs
σ	9.8 μs	132.6 μs
$\overline{T_2}$	32.3 μs	299.3 μs
σ	26.6 μs	160.1 μs

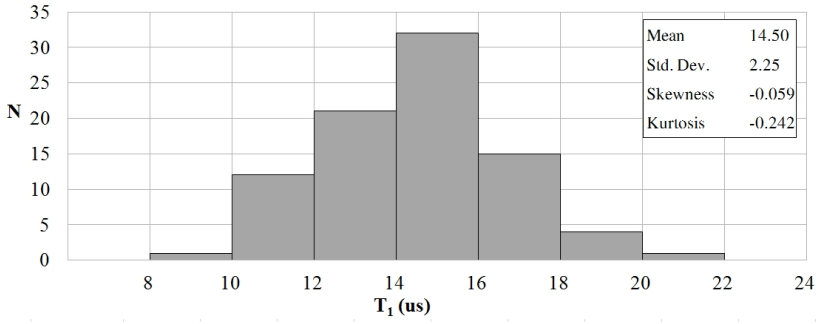

(a) Distribution of *Switching* Transient Front Times (T_1)

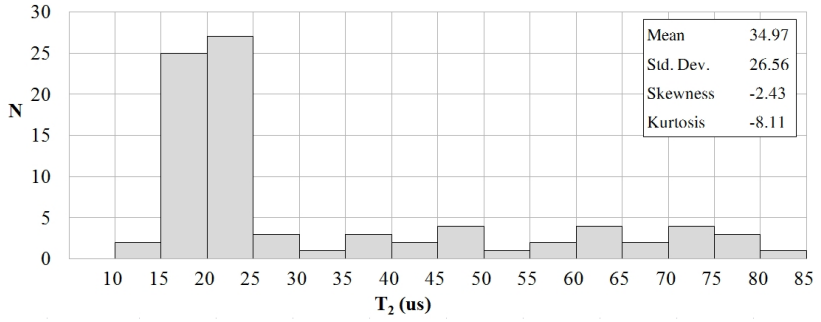

(b) Distribution of *Switching* Transient Tail Times (T_2)

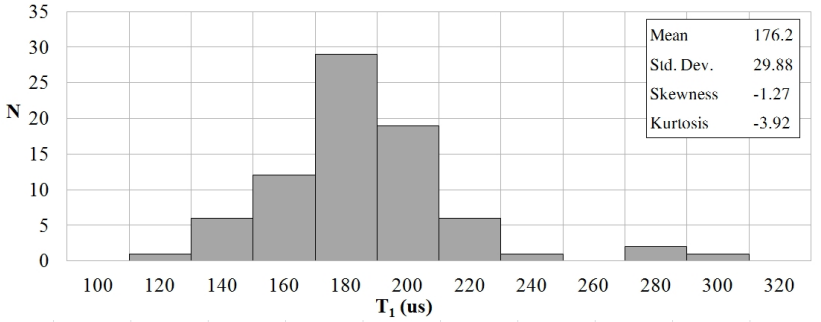

(c) Distribution of *Inrush* Transient Front Times (T_1)

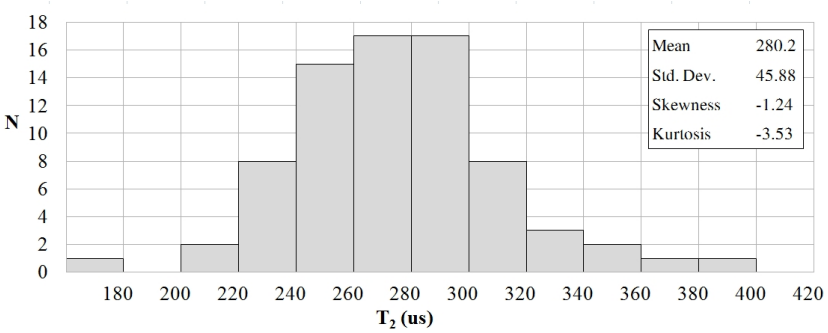

(d) Distribution of *Inrush* Transient Tail Times (T_2)

Figure 4.17: Voltage Transient Waveshape Components

4.3.4 Switch Timing

One of the most important factors to consider in the development of the simulation models is the timing of transient fronts relative to the supply voltage sinusoid, and thus the delay between the closing instants of poles 1 and 2 and instant of inrush inception. Statistical switching analyses using EMTP-ATP require that the distribution in time of pole closure times be known, while a master-slave switch implementation requires an evaluation of the pole delay statistics.

For the purpose of the following analyses, the full set of 251 current transient waveforms from section 4.3.2 have been used as they have more clearly defined switching times than the equivalent set of voltage transients. Pole closing angles are determined by identifying absolute switching times from a current waveform, then indexing the associated voltage sinusoid.

4.3.4.1 Pole Angle (θ_{sw})

Figure 4.18a gives the distribution of pole 1 closing angles. As noted earlier in this chapter, the first pole closure leads the positive-going voltage zero and is confined to a relatively narrow range of values between 6 and 20°. The distribution itself is clearly Gaussian, with a mean value of 13.8°, making the statistical switch the ideal choice for simulation of the leading pole closure.

4.3.4.2 Switch / Inrush Delay ($\tau_{sw},\ \tau_i$)

Figure 4.18b depicts the distribution of switching delays between poles 1 and 2 of the generator disconnect. The delay between closure of the first disconnector pole and the subsequent current inrush is shown in Figure 4.18c. While the switching delay τ_{sw} occupies a broadly Gaussian distribution, that of the inrush delay τ_i is comparatively flat (negative kurtosis). In the absence of additional statistical data, a continuous uniform distribution of τ_i over the range 3.5 to 10 ms has been chosen for the purpose of implementing statistical switches (see Chapter 6).

4.3.5 Transient Energy

The final quantity of interest is a measure of the energy content of the transient. This gives an indication of the duty requirements of equipment in the vicinity of the switch,

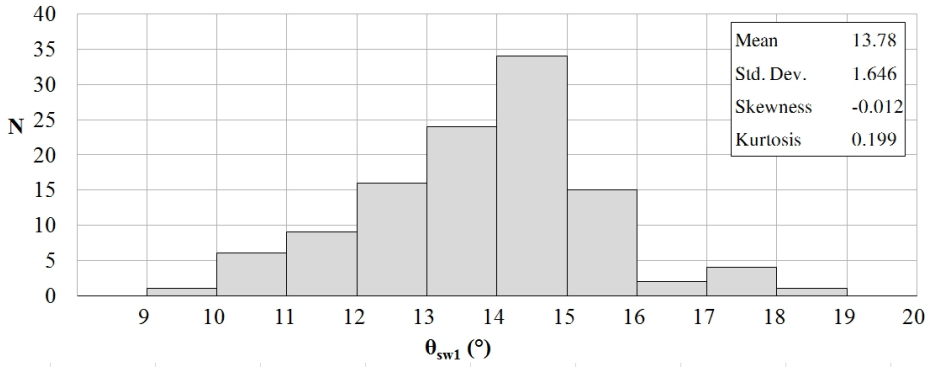

(a) Distribution of Pole 1 Switching Angles Leading Voltage Zero

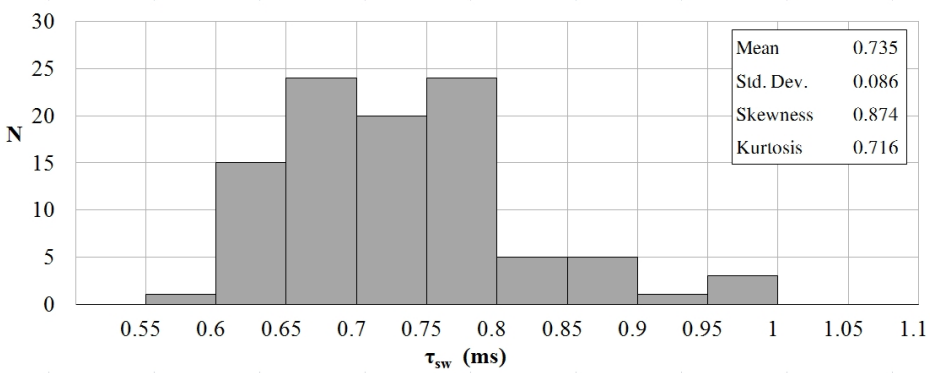

(b) Distribution of Switching Delay τ_{sw}

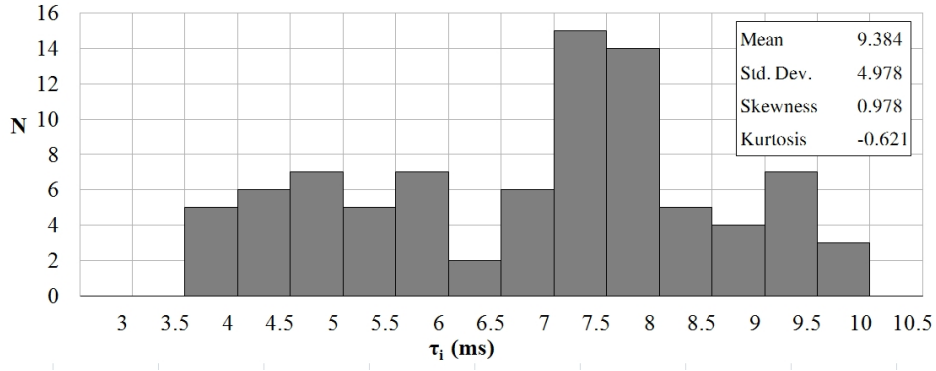

(c) Distribution of Inrush Inception Delay τ_i

Figure 4.18: Switching Angles and Delay Times

but also completes a set of measurable quantities from which equivalent EMC test waveforms may be calculated.

4.3.5.1 Current Transient Energy Measure (S_i)

Current transient energy measures are computed from the set of waveforms used in section 4.3.2, for both switching and inrush transients where applicable. The energy measure S_i was evaluated by trapezoidal integration using (4.3).

$$S_i = \int_{t=0}^{T} i^2(t)dt \tag{4.3}$$

The resulting values are plotted in Figures 4.19a and 4.19b as functions of the switching angle θ. Over the narrow range occupied by θ_1, the energy measure is roughly linearly dependent on the switching angle, much like the peak current and ramp rate. Inrush inception by contrast may occur at almost any instant in half cycle following the positive-going zero crossing of the voltage sinusoid.

As discussed in section 4.3.2, the tail time of a given inrush current transient is heavily dependent on the inrush inception angle, with high sustained currents occurring in the range $\theta_i < 90°$. The energy measure is proportional to the integral of a sinusoid between θ_i and 180°. The overlay in Figure 4.19b is a plot of this integral, with an additional scaling factor of 0.44.

4.3.5.2 Voltage Transient Energy Measure (S_v)

Measurements of the voltage transient energy measure S_v were similarly performed on the result set of section 4.3.3. As discussed earlier, amplitude measurements on this data set are subject to a potential systematic offset error due to subtraction of the voltage sinusoid during the preprocessing stage. This error is unavoidably amplified in the calculation of S_v due to the squaring of measured values. Taking as before the conservative offset error in voltage measurements as $\pm$ 5V, then for a mean switching transient voltage peak of 47.5V, the error margin in S_v becomes $\pm$22%. This is reduced to $\pm$18% for the inrush transient due to the increased mean voltage peak of 55.7V.

Figures 4.20a and 4.20b illustrate the relationship between S_v and θ for the switching and inrush transients respectively. Much like the current energy measure, S_{v1} for the

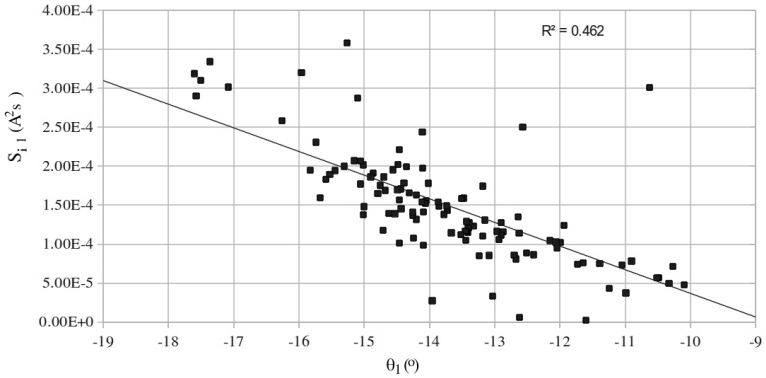

(a) Pole 1 Switching Transient S_i as Function of θ_1

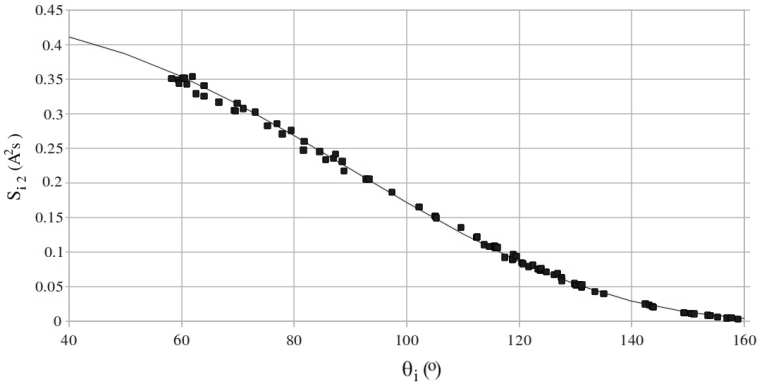

(b) Inrush Transient S_i as Function of θ_i

Figure 4.19: Current Transient Energy Measures as Functions of θ

switching transient is broadly linearly dependent on the pole angle θ_1, over the measured range.

S_{v2} by contrast is roughly proportional to $sin^2(\theta_2)$, as can be seen from the curve overlay in Figure 4.20b, with peak energy measure of approximately $1.5V^2s$ occurring at $\theta_2 \approx 90°$.

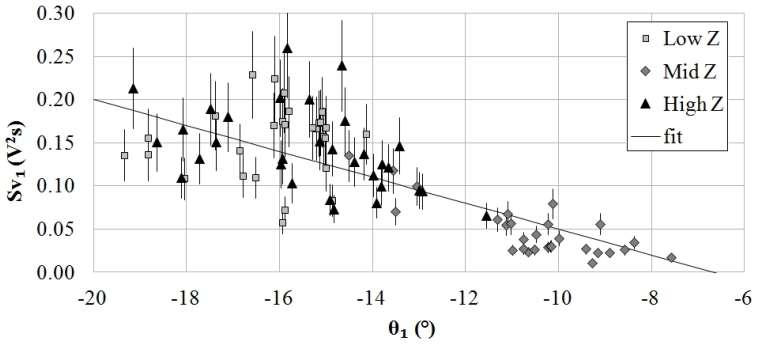

(a) Pole 1 Switching Transient S_v as Function of θ_1

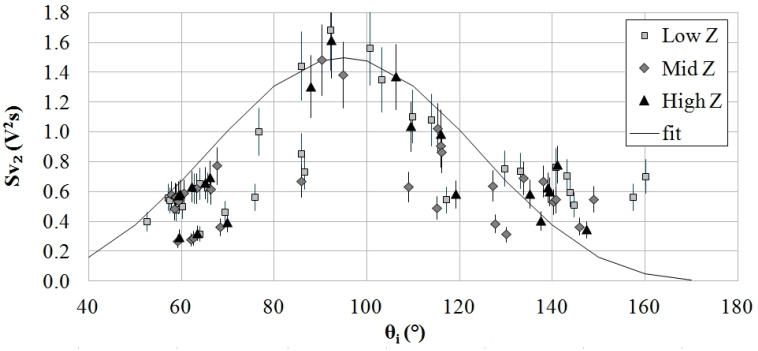

(b) Inrush Transient S_v as Function of θ_i

Figure 4.20: Voltage Transient Energy Measures as Functions of θ

4.3.5.3 Waveform Energy Content (W)

In addition to the voltage and current waveforms pairs output by the transient logger, a third waveform was constructed by multiplication of the instantaneous values of both measured quantities. The energy content of the transients can, therefore, be estimated by integration of the waveform product $v(t) \cdot i(t)$ over the pulse duration. The data set of section 4.3.2 was once again used for the calculation of energy content.

W_1, the energy content of the switching transients, is presented as a distribution in Figure 4.21a. As expected from the short duration and low magnitude of the switching

current transient, and its proximity to the voltage zero crossing, the energy content is very low, with a mean value of $8.2mJ$. The plot of Figure 4.21b illustrates the linear dependence of W_1 on the pole angle θ_1.

Of greater interest is the energy content of the inrush transient W_2. As can be seen from Figure 4.21c, typical values of W_2 are around three orders of magnitude larger than those of the switching transient, with a mean value of $5.2J$. This is due to the increased current magnitudes and slower front and tail times of the inrush transient. As with the current energy measure S_{i2}, the energy content W_2 is proportional to the integral of $\sin\theta_2$, as shown by the overlay in Figure 4.21d. The theoretical maximum value of the curve fitting is 15.5J, but in practice no switching angles smaller than 50° were observed during testing regime, effectively limiting W_2 for this particular device to approximately $13.6J$.

4.4 Standardised Test Waveform Components

This section summarises the computation of a selection of standard test waveform components from experimental quantities, as introduced in Chapter 3. This will assist in the modelling of observed phenomena as presented in Chapters 5 and 6. The section is split according to the type of standard employed, and a discussion of calculation methods included in each subsection.

4.4.1 Insulation Coordination

The standard test waveshapes of BS EN 60071-1 [138] for systems rated above 100V are summarised in Figure 4.22. Insulation Coordination standards for systems rated below 1000V (BS EN 60664 [137]) make reference to standard impulse test waveforms, but provide little assistance with regard to waveshape specifications.

4.4.1.1 Slow-Front Transient

Of the data sets analysed in this chapter, only the current inrush transient falls within the definition of a slow-front waveshape. Table 4.7 summarises the typical and worst-case shape factors for the purpose of repeat simulations.

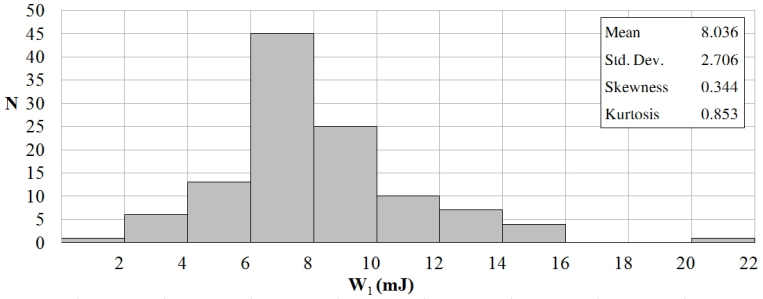

(a) Distribution of Switching Transient Energy Content (W_1)

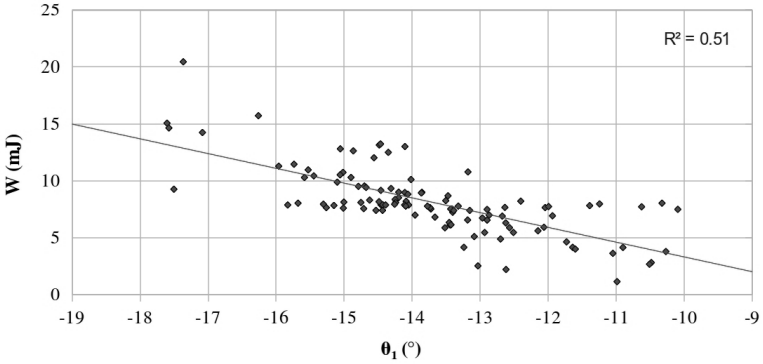

(b) Switching Transient Energy Content as Function of θ_1

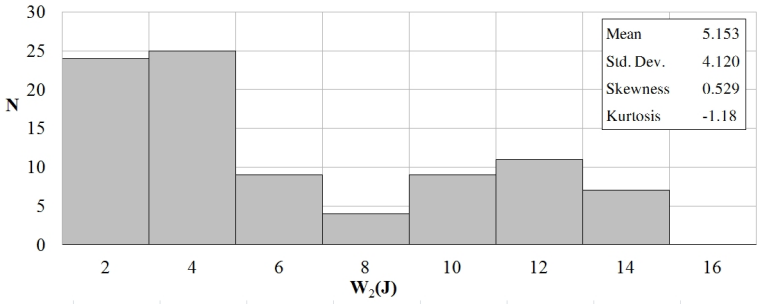

(c) Distribution of Inrush Transient Energy Content (W_2)

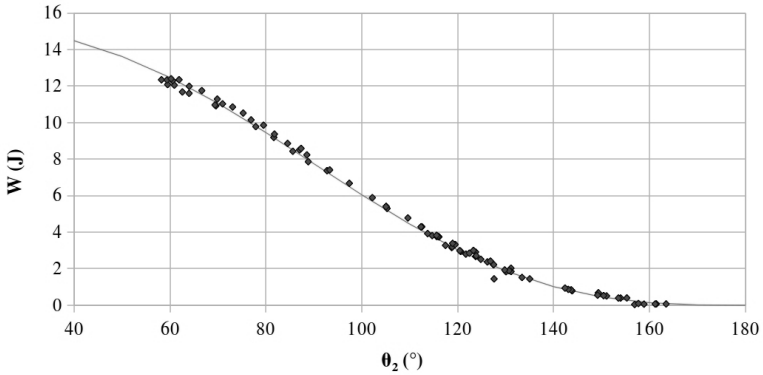

(d) Inrush Transient Energy Content as Function of θ_i

Figure 4.21: Waveform Energy Content (W)

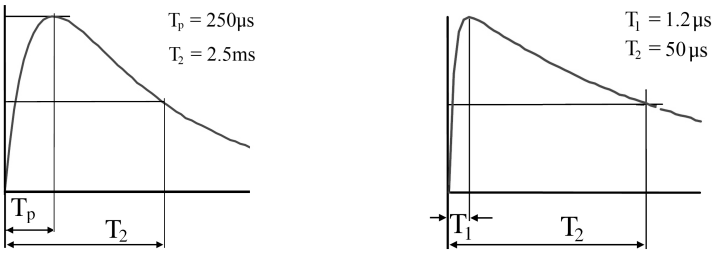

(a) Slow-Front (b) Fast-Front

Figure 4.22: Standard Waveshapes of BS EN 60071

Table 4.7: Slow-Front Waveform Components of Inrush Current Transient

		$I_{2\ pk}$ (A)	T_p (μs)	T_2 (ms)
ΔI_2	Typical	9	300	2.5
	Worst Case	12	250	5.5

4.4.1.2 Fast-Front Transient

The remaining data sets fall between the definitions of slow- and fast-front transients, and only the switching current impulse displays a classically large ratio of front and tail times. Voltage transients (switching and inrush) were found to exhibit a high degree of symmetry about the peak, lending themselves more readily to representation as symmetrical trapezoidal pulses. Table 4.8 summarises the typical and worst-case values of the fast-front waveshape components for the remaining measured data sets.

Table 4.8: Fast-Front Waveform Components of Measured Transients

		Peak Value	T_1 (μs)	T_2 (μs)
ΔI_1	Typical	1.5 A	15	80
	Worst Case	2 A	8	225
ΔV_1	Typical	50 V	16	32
	Worst Case	70 V	8	80
ΔV_2	Typical	60 V	200	300
	Worst Case	100 V	100	450

4.4.2 Electromagnetic Compatibility

A selection of typical Electromagnetic Compatibility test waveshapes, as used for the classification of low-voltage transients in [81] are presented in Figure 4.23. These waveshapes offer an alternative method for the application of experimental data to simulation, as have been chosen as their components can be easily evaluated from

known measured quantities; namely transient peak values, ramp rates, rise/fall times and energy measures.

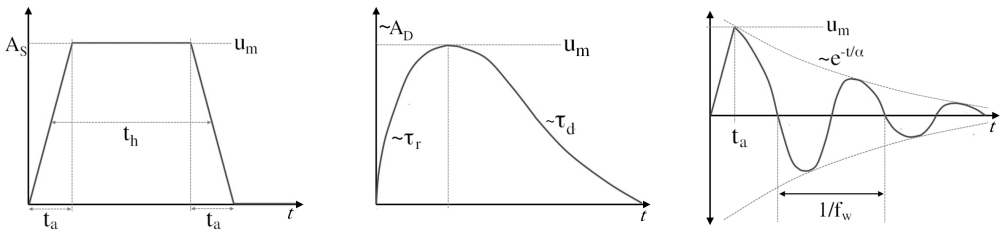

(a) STP (b) DEP (c) DOW

Figure 4.23: Standard EMC Test Waveforms [81]

4.4.2.1 Symmetrical Trapezoidal Pulse (STP)

Representation using a symmetrical trapezoidal pulse is the simplest of the three, and is well suited to waveforms with similar front and tail ramp rates. This makes it ideal for representing the measured voltage waveforms, but it is less suited to reproduction of the asymmetric current pulses. The magnitude A_S, rise/fall time t_a and half-peak pulse width t_h are calculated from known quantities by Equations (4.4) to (4.6).

$$A_S = \hat{v} \ , \ \hat{i} \tag{4.4}$$

$$t_a = \frac{A_S}{(\frac{dv}{dt})} \ , \ \frac{As}{(\frac{di}{dt})} \tag{4.5}$$

$$t_h = \frac{S}{A_S^2} + \frac{t_a}{3} \tag{4.6}$$

Typical STP equivalent waveforms have been derived for each class of measured transients, the components of which are summarised in Table 4.9. The derived waveforms are plotted on a normalised magnitude scale in Figure 4.24. Each trapezoid has a maximum value, rising edge ramp rate and energy measure equal to the equivalent measured mean values.

Table 4.9: Equivalent Waveshape Parameters for STP Representation

	A_S (A or V)	t_a (μs)	t_h (μs)
Switching Current(i_1)	1.573	13.04	60.48
Inrush Current (i_2)	9.074	289.71	1657.98
Switching Voltage (v_1)	48.42	15.09	48.38
Inrush Voltage (v_2)	59.20	179.28	265.89

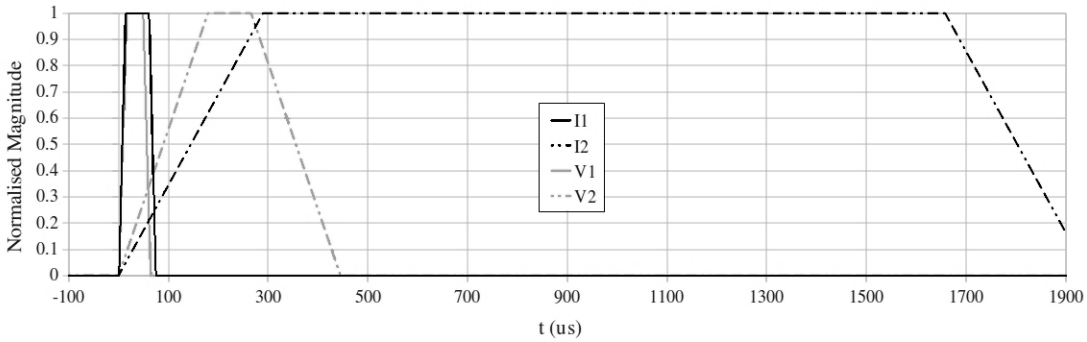

Figure 4.24: Symmetrical Trapezoidal Pulses as per Table 4.9

4.4.2.2 Double Exponential Pulse (DEP)

Components of the DEP representation were extracted from measurement by direct interrogation of the waveform rise/fall times, rather than using the approximation method of [81]. Rise and decay time constants were calculated from Equations (4.7) and (4.8).

Finally, Equation (4.9) is used to calculate the double-exponential magnitude coefficient A_D. The calculated components of the class-typical waveforms are summarised in Table 4.10, and the waveforms can be seen in Figure 4.25. The DEP is clearly far better suited to the representation of asymmetric current and voltage pulses, but becomes unstable when a high degree of symmetry is required. This is due to the DEP representation being a scaled difference of two exponentials; as the waveform front-tail symmetry increases, the difference of the exponentials diminishes and the scaling factor accordingly becomes very large $\left(\frac{r}{r-1} \to \infty\right)$.

$$\tau_R \approx \frac{T_{30-90\%}}{\ln(7)} \tag{4.7}$$

$$\tau_D \approx \frac{T_{90-30\%}}{\ln(7)} \quad or \quad \frac{T_{90-50\%}}{\ln(5)} \tag{4.8}$$

$$A_D = (\hat{v}\ ,\ \hat{i}) \cdot \frac{r}{r-1} e^{\frac{\ln(r)}{(r-1)}} \qquad \left[r = \frac{\tau_D}{\tau_R}\right] \tag{4.9}$$

As a rule of thumb, the scale factor A_D should be of the same order of magnitude as the peak of the measured waveform. As can be seen from Table 4.10, this is true for both current transients, but not voltages. Care should be taken to precisely specify the rise and decay constants τ_R and τ_D to minimise error in the pulse magnitude.

Table 4.10: Equivalent Waveshape Parameters for DEP Representation

	Peak (A or V)	A_D (A or V)	τ_R (μs)	τ_D (μs)
Switching Current(i_1)	1.57	2.67	4.20	34.21
Inrush Current (i_2)	9.07	14.14	88.79	1126.30
Switching Voltage (v_1)	48.42	172.58	5.84	12.77
Inrush Voltage (v_2)	59.20	1384.24	59.69	67.05

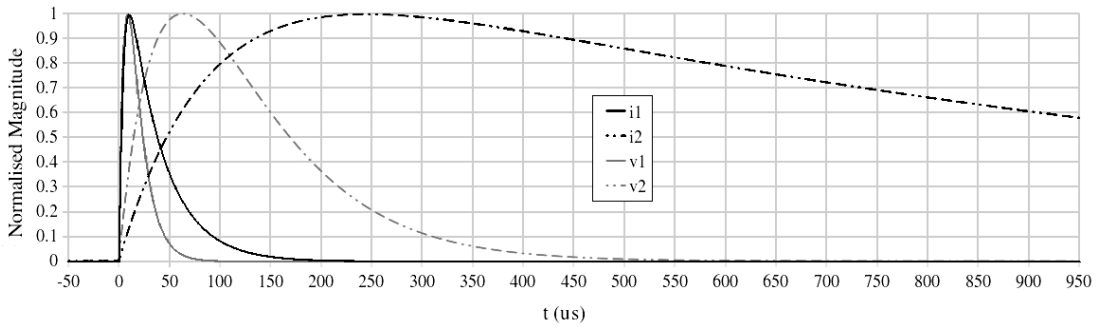

Figure 4.25: Double Exponential Pulse Representations of Table 4.10

4.4.2.3 Damped Oscillatory Waveform (DOW)

Another representation of interest is the Damped Oscillatory Waveform, in the particular case of the inrush current transient. This is because the current, rather than decaying to zero, reduces to the normal operating 50Hz sinusoid. In the case of the the other three transient classes, oscillation of voltage and current was found to be minimal, but an overdamped DOW may still be used to represent these waveshapes.

The standard DOW is determined by four quantities: a peak value A_O, rise time t_a, decay constant α and oscillatory frequency ω. A_O is numerically equal to the the magnitude of the STP (A_S) and t_a is the same as the trapezoid ramp time. The frequency ω is determined from visible oscillatory behaviour in the measured waveforms. Where none exists, a default value of 50Hz was assumed. Finally, the damping coefficient for each voltage and current waveform is constrained to a narrow range, defined from known quantities by Equation (4.10) [81]

$$\frac{3}{8} \cdot \frac{[\hat{v}, \hat{i}]^2}{3S_{v,i} - t_a[\hat{v}, \hat{i}]^2} \;\leq\; \alpha_{v,i} \;\leq\; \frac{3}{4} \cdot \frac{[\hat{v}, \hat{i}]^2}{3S_{v,i} - t_a[\hat{v}, \hat{i}]^2} \tag{4.10}$$

The median value of this range was chosen each time for the purpose of consistency. The potential error introduced in doing so is small, however, as α may only vary by a

factor of 2 over its full range. Table 4.11 summarises the calculated shape factors for the four measured transient classes.

Table 4.11: Equivalent Waveshape Parameters for DOW Representation

	A_O (A or V)	t_a (μs)	$\bar{\alpha}$ (kHz)	ω (Hz)
Switching Current(i_1)	1.57	13.04	6.914	∼1000
Inrush Current (i_2)	9.07	289.71	0.47	∼70
Switching Voltage (v_1)	48.42	15.09	18.88	∼2000
Inrush Voltage (v_2)	59.20	179.30	3.94	∼1200

Representative damped oscillatory waveforms are depicted in Figure 4.26 for both switching and inrush current and voltage transients. Typical waveforms captured with the transient logger are overlaid for reference. As can be seen from these plots, the DOW is particularly suited to the representation of slow-front inrush current transients, where sinusoidal behaviour follows the tail roll-off. For fast-front transients, however, the coefficient α is large enough to result in critical damping. In this case, the frequency ω simply becomes a shape factor that can be used to fit the exponential curve to the tail. In this mode of operation, there is little to distinguish the DOW from the double-exponential, except that the rising edge is here assumed to be linear over the rise time t_a.

4.4.3 Suitability of Waveshapes

From the analysis of measured waveshape components T_1 and T_2, it is noted that established insulation coordination test waveforms for slow- and fast-front transients do not necessarily give the best reproduction of measured phenomena. With the exception of the inrush current transient (ΔI_2), all measured characteristics fall somewhere between the standard definitions of slow-front and fast-front transients, and in the case of voltage transients (ΔV) there is a greater degree of symmetry between the front and tail than is allowed by the standard 1.2/50μs lightning impulse. Measured switching voltage transients (ΔV_1) might be better represented using the standard 8/20μs surge waveshape of BS EN 61000 [149], more commonly used for current injection tests.

The use of more arbitrarily defined EMC waveshapes (STP,DEP and DOW) gives more flexibility to reproduce specific transient characteristics, as each of these shapes

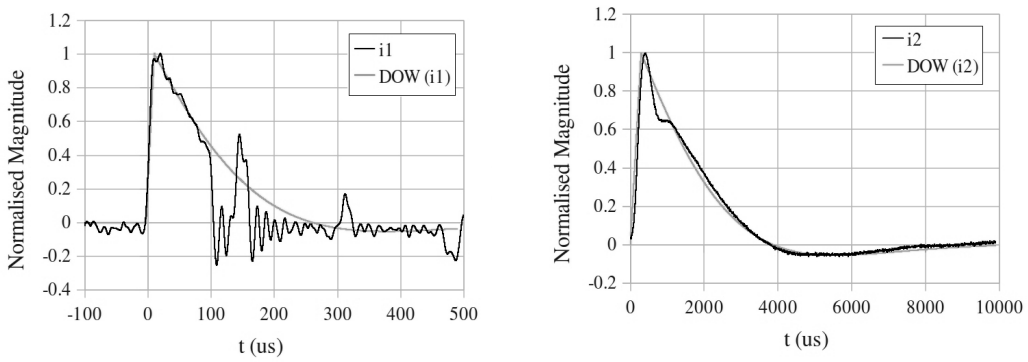

(a) Switching Transient Current

(b) Inrush Transient Current

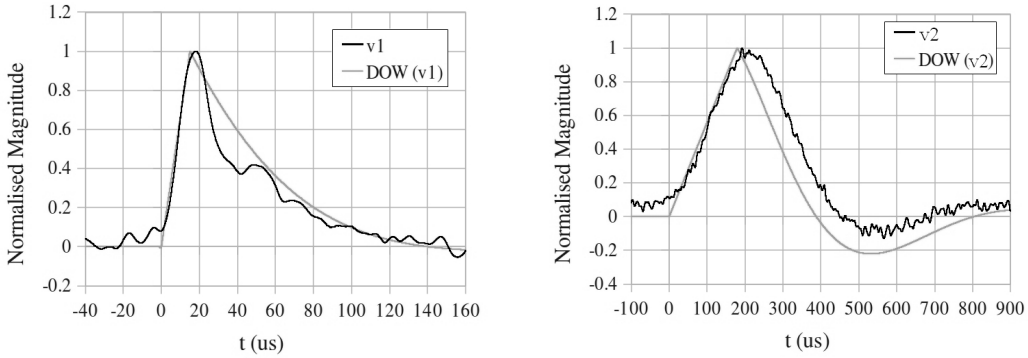

(c) Switching Transient Voltage

(d) Inrush Transient Voltage

Figure 4.26: DOW Representations of Key Transient Classes (Normalised)

can be synthesised in a straightforward manner. A symmetrical trapezoidal pulse allows linear rising edge characteristics and energy content to be modelled very well, but tail shapes are nothing like the original measured waveforms. Damped oscillatory waveforms by contrast allow the tail to be very precisely reproduced, but as the rising edge is exponentially decaying to an asymptotic value, the measured linearly rising fronts are not so well represented. The DEP is also incapable of modelling symmetrical pulses as the scaling factor A_D tends toward infinity.

The best reproduction of laboratory results is achieved by means of a damped oscillatory waveform. In this case, both linear rising edge and exponential decay are reproduced very precisely for each class of waveform as shown in Figure 4.26.

4.5 Chapter Conclusions

The main results of 18-months of laboratory testing with the Cardiff University Solar Energy Laboratory have been presented. Statistical switching transient waveshape

datasets for voltage and current magnitudes, ramp rates and energy measures have been acquired for 251 unique event records. Analysis of switching angles has been used to determine the relative timing of pole closing and inverter capacitive inrush inception, for the purpose of translation to statistically determined switching models in EMTP. The main conclusions are as follows:

- Generator *disconnection* under export conditions produces no measurable transient voltages due to current interruption occurring at $V \approx 0V$ in a predominantly resistive circuit.

- *Reconnection* operations involve the closing of a pair of relay poles at the zero-crossing of the supply voltage sinusoid, with a mean pole separation of 0.7ms.

- Relay pole closing gives rise to an initial fast front, low magnitude current transient (typical: 1.5A, 15/80μs)

- In approximately 80% of cases, switching is followed by a slow-front, higher magnitude inrush current transient (9A, 300/2500μs) associated with charging of the inverter DC bus capacitance. Mean inrush delay time was found to be approximately 9.4ms.

- A transient voltage perturbation is associated with each current transient, its magnitude dependent on the current amplitude and impedance of the incoming mains supply (switching: 16/32μs, inrush: 200/300μs)

- Measured transient characteristics may be reproduced using a variety of synthesisable test waveshapes common to insulation coordination and EMC standards. It was found that a damped oscillatory waveform representation gives the best overall reproduction of front and tail characteristics, and has the flexibility to handle each class of measured voltage and current waveshape.

Chapter 5

Simulation of Individual SSEG Installations

This chapter details the formulation of models in EMTP-ATP for the purpose of simulating individual generator switching scenarios. The models developed are at first used for the verification of laboratory data presented in Chapter 4, and permutations evaluated in terms of their accuracy and solution efficiency.

A suite of simple systematic analyses of individual generator reconnection events are undertaken, and the propagation of resulting fast-transient voltage and current waves in both urban and rural LV distribution circuits determined. The source models presented are then adapted for use in cumulative impact studies involving multiple generators supplying a single LV feeder. The results of these extensive statistical studies are then treated in depth in Chapter 6.

Throughout this chapter, important model components are illustrated or tabulated where clarity necessitates. An exhaustive breakdown of simulation model component values and set-up parameters may be found in Appendix D.

5.1 Laboratory Test Setup Modelling

The following section describes the formulation of EMTP-ATP simulation models for predicting the electrical fast-transient behaviour of small-scale embedded generators. Three distinct generator model topologies were developed for the purposes of source representation. These representations are compared and evaluated against the statistical

data generated from the laboratory tests of Chapter 4. The applicability of the developed topologies to up-scaling for large multi-source simulations is discussed with reference to solution efficiency and software capability.

5.1.1 Full Inverter Model

The most elaborate of the three topologies explicitly represents all electrical components of inverter and primary source, as illustrated in Figure 5.1. In this instance, a 640W rated photovoltaic array was chosen in line with the laboratory specification. An interchangeable lower capacity source was also specified according to the measured VI characteristic of the array.

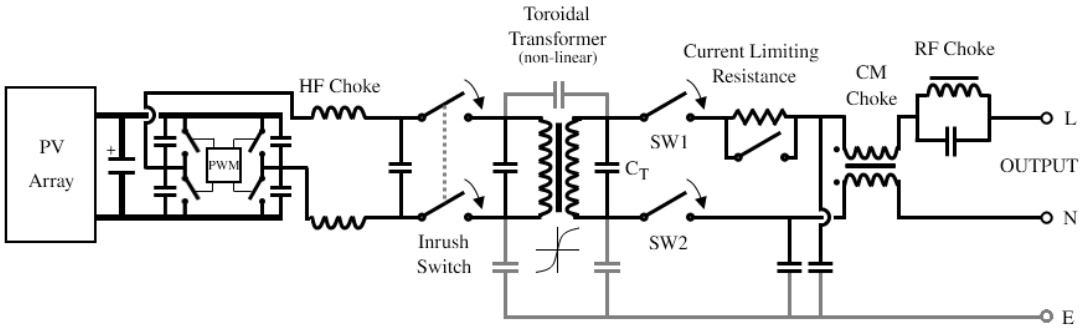

Figure 5.1: Full Inverter Model Schematic

A nonlinear current source was employed for representation of the PV array, similar to that proposed in [150]. The nonlinear source is implemented as a current generator in parallel with a diode defined by a 20-point piecewise linear approximation of the Shockley equation. The current source is fixed at the nominal short-circuit current of the array, and the diode V-I curve defined such that the full source current is circulated when V_D equals the open circuit voltage of the array. The diode characteristic knee-point is defined according to the nominal maximum power point (MPP). These quantities are summarised in Table 5.1 for both the full rating of the array and its measured performance.

Table 5.1: Nominal Design Values for PV Array Current-Source Model [145]

Quant.	Nominal	Measured	Equivalent Cct Representation (figure 5.2)
I_{sc}	4.8A	4.64A	Current Source Value (I_{DC})
V_{oc}	164V	151.1V	Diode Voltage (V_D) when $I_D = I_{sc}$
I_{mpp}	4.55A	2.83A	Difference Current $I_{sc} - I_D$ when $V_D = V_{mpp}$
V_{mpp}	138.4V	123.3V	Diode Voltage V_D when $I_D = I_{sc} - I_{mpp}$

A series resistance R_s representing the combined on-state resistance of the cell string and DC cabling is included, while the off-state leakage represented by shunt component R_p may generally be omitted. The circuit representation of the array is depicted in Figure 5.2. Simulated and measured VI curves for both standard test and laboratory conditions are plotted alongside for comparison.

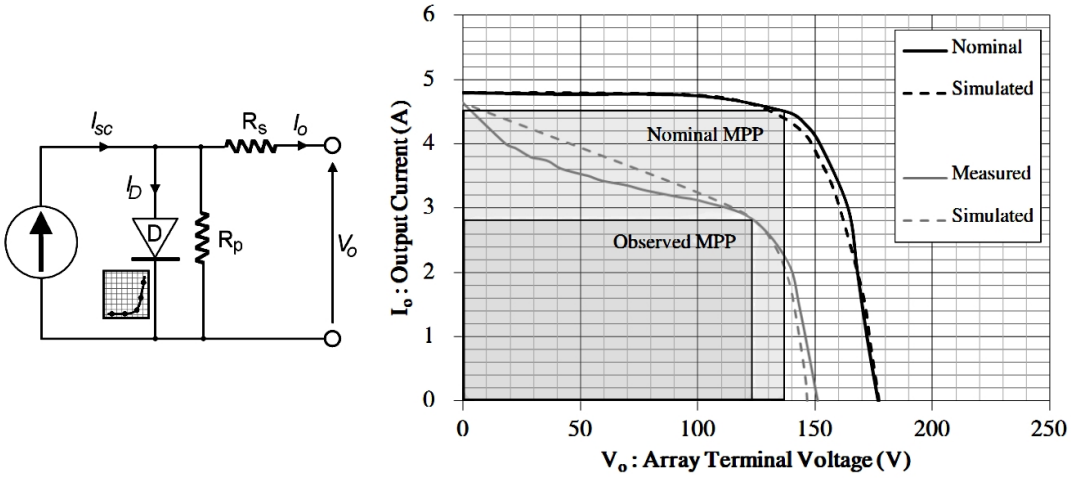

Figure 5.2: EMTP Photovoltaic Array Model

The firing of controlled switches in the inverter bridge is governed by a 16kHz PWM source constructed from TACS components, while the step-up toroidal transformer is implemented as a single-phase saturable model. The saturation characteristic of the transformer was obtained by open-circuit test and the SATURA routine invoked to convert the obtained V-I characteristic to a flux-current curve [97]. Open and short circuit test data for the transformer can be found with the exhaustive component lists in Appendix D.

Component values for the output filter, chokes and inrush current limiter are obtained directly by inspection of the inverter main board. Stray capacitances and losses in the transformer and chokes are not shown here for clarity, but each of these values was estimated, either from data sheets or by small-signal frequency scan of the individual components, and was modelled explicitly. A distinct benefit of such a representation is that each of its components may be estimated by close inspection of the device under test, and thus it may be employed as a precursor to extensive laboratory or field tests.

One of the main drawbacks with this circuit representation is its low solution efficiency. As discussed in Chapter 2, whenever the time domain solution involves the

opening or closing of a switch, partial re-triangularisation of the circuit admittance matrix must be performed before the solver can proceed. Simulation of a 16kHz PWM bridge such as that depicted in Figure 5.1 requires a minimum of 640 such operations per power frequency cycle (assuming that all four poles switch on the same time step), constituting a significant portion of the overall solution time. Every effort must, therefore, be made to minimise the extent of the solution time window.

A constraint was placed on the time taken for the circuit to settle into its steady state, prior to executing the switching operation of interest. Using such a brute-force approach, the settling time demanded by full emulation of the inverter control logic was found to be prohibitively long. Modelling of the controller has accordingly been omitted from this model, but as a consequence the initial state of the inverter (principally, the DC bus voltage and array output current) must be manually specified. While this is minor concern for simulations involving individual cases, translation of such a model for the purpose of statistical study, or for cumulative impact assessments of generator sets across multiple phases, quickly becomes cumbersome. For very large simulations, there is the added problem of potential branch and node limit violation. This aspect is covered in more detail in section 5.1.7.

5.1.2 Idealised AC Source Model

A generator disconnect operation may be represented somewhat more simply by replacing the inverter bridge and its associated firing circuit with an equivalent AC source and impedance, as depicted in Figure 5.3. This topology eliminates the most computationally inefficient component of its predecessor, namely the high-frequency switching in the bridge circuit, while preserving the type-98 piecewise pseudo-nonlinear inductance for transformer saturation.

Of the three source variants presented, it is the simplified AC model that bears greatest resemblance to that employed during the early stages of research [151, 152]. Numerous refinements have since been made in the light of laboratory tests to improve the flexibility of the model. These relate principally to the inclusion of inverter inrush currents such that the AC source model may also be used to model generator reconnection.

Transformer inrush is handled by means of a single-phase nonlinear transformer

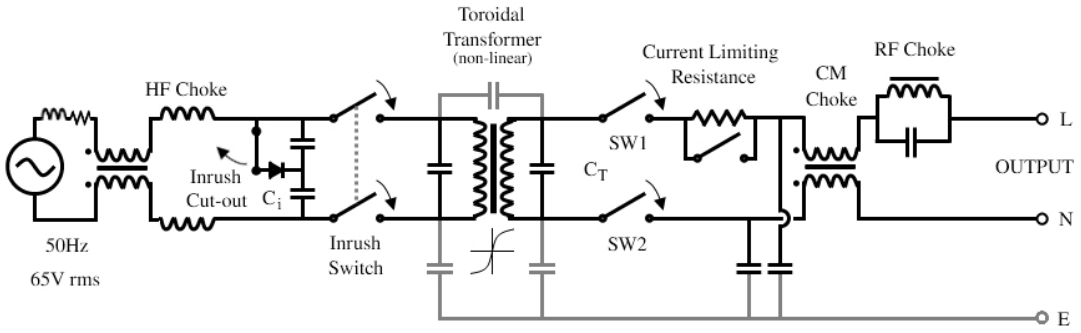

Figure 5.3: Reduced AC Source Model Schematic

model, taken directly from the PWM inverter circuit of 5.1.1. In the absence of the inverter bridge, the capacitive component of the inrush current is initially absent.

On closing the generator output breakers, the inverter DC bus capacitor is charged from the grid [153], the bypass diodes of the off-state power-electronic switches acting as a bridge rectifier as depicted in Figure 5.4a. As was noted in Chapter 4, the inrush duration is generally very short, and the instantaneous current magnitude drops to less than 1A within 10ms of inception. This behaviour may be simply represented by means of a pair of series connected capacitors as shown in Figure 5.4b, with an inrush capacitance C_i many times larger than the initially bypassed steady-state capacitor C_s. With the aid of measured current waveforms for calibration purposes, the capacitive inrush is artificially restored by adding this branch on the source side of the transformer as depicted in Figure 5.3.

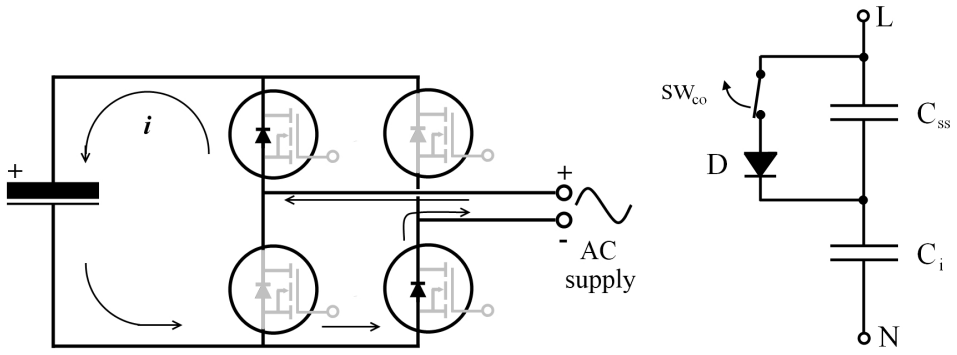

(a) DC capacitor charging in off-state (b) Artificial Inrush Circuit

Figure 5.4: Capacitive Inrush Mechanism and Modelling

For the remainder of the positive half cycle following closure of the inrush switch

sw_i, C_s is bypassed by the diode allowing a large charging current to flow. After the first negative-going voltage zero, the diode becomes reverse biased and the current reduced accordingly. For simulation cases spanning multiple 50Hz cycles, repeated fictitious capacitive inrush is prevented by opening the cut-out switch sw_{co} prior to the next positive-going voltage zero. A delay of 10ms between closing sw_i and opening sw_{co} is sufficient for this purpose. A typical switch timing arrangement is illustrated in Figure 5.5 with reference to the terminal voltage sinusoid.

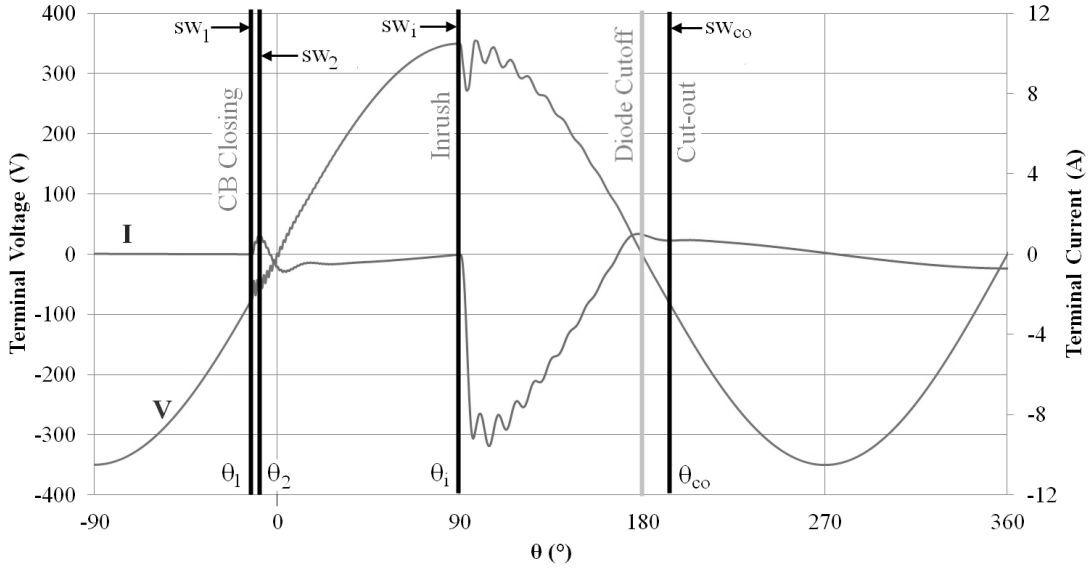

Figure 5.5: Switch Timing for Capacitive Inrush Circuit

5.1.3 Capacitive Inrush Model

Further reduction in source model complexity may be achieved if one is interested solely in transient phenomena related to generator-grid reconnection. Analysis of laboratory data has shown that it is the reconnection process that gives rise to the most pronounced voltage and current perturbations. By contrast, the initial disconnection of a generator in response to voltage or frequency deviations was found to be comparatively uneventful.

In such a scenario, the generator can be modelled most satisfactorily by reduction to a network of purely passive components. Explicit modelling of the distributed energy source itself, by means of either a PWM bridge or an equivalent AC circuit, is not necessary in this case. A further increase in computational efficiency may be achieved by substituting the type-98 pseudo-nonlinear transformer model for an ideal equivalent.

In the absence of the core saturation characteristic, transformer inrush and capacitive inrush may be efficiently combined into a single lumped equivalent capacitance. The final simplified circuit is shown in Figure 5.6.

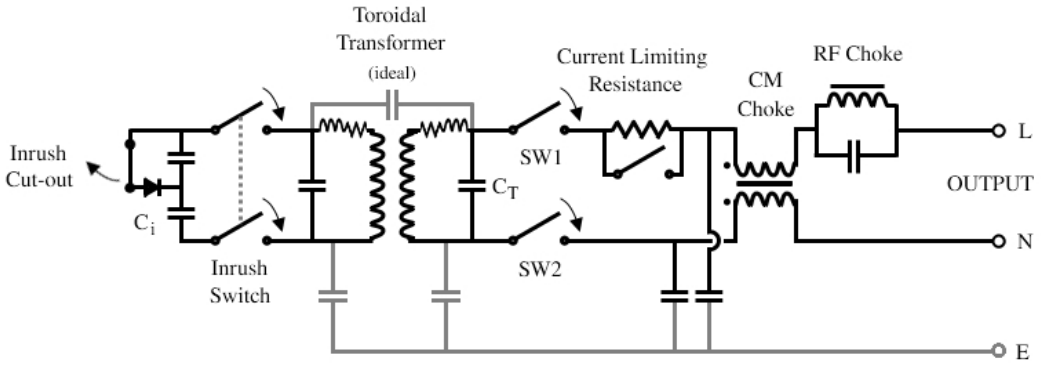

Figure 5.6: Capacitive Inrush Model Schematic

The generation of meaningful simulation results from the use of this greatly simplified model requires prior knowledge of the switching characteristics of a given device. The equivalent inrush and steady-state capacitances are precisely specified by inspection of the measured transient waveforms. Specification of the model in this way was found to give extremely good results. In the absence of such data, an approximation of device performance may be made if component values of the output filter and current limiting resistance are known.

The primary benefit of the capacitive inrush model is a greatly increased solution efficiency, due in part to the total absence of pseudo-nonlinear components. Switching operation counts are reduced to four per generator per simulation case, in comparison to the many thousands required of the PWM model. Sparing use of components also allows for minimisation of overall branch and node counts. While this economy may be trivial in the case of individual switching studies, it is critical to the formulation of large and complex models for the purpose of cumulative impact study. Such studies may involve hundreds of independently switched generators across multiple phases, and due care must be taken in order to remain within the predefined limits of the software. This aspect is discussed in more detail in Chapter 6.

5.1.4 Cable Models

A library of LCC models was created in EMTP for the representation of cable elements. A variety of standardised geometries of domestic mains cables in both flex and flat configurations [154–156], underground LV trunk and service cables [157] and overhead Aerial Bundled Conductors (ABC) [139, 158] were modelled using the modal domain frequency-dependent line representation (JMartí). Discrete section lengths were chosen such that, for a wavefront travelling with a phase velocity determined by the dielectric properties of the cable insulation, the total travel time τ becomes an integer multiple of the solution time step Δt as per (5.1), thereby minimising the potential error introduced through linear interpolation. Insulator materials were assumed to be homogeneous, and the frequency dispersion of the cables was ignored as a first approximation.

$$\tau = \frac{l\sqrt{\varepsilon_r}}{c} = n\Delta t \;\; (n = 1, 2, 3...) \tag{5.1}$$

Domestic cable models were verified in the laboratory by small-signal open and short circuit square pulse tests using the circuit of figure 5.7 (more details may be found in Appendix). Figures 5.8 and 5.9 show the results of such tests on a 12-metre length of PVC insulated mains flex ($2.5mm^2$ Live/Neutral,$1.5mm^2$ Protective Earth). The test set-up was reconstructed in EMTP using an empirical voltage source for representation of the pulse generator, using data from a scope-captured waveform. The time step of the simulation was set equal to the acquisition step size of the oscilloscope. Simulated results are plotted alongside the measured data for comparison.

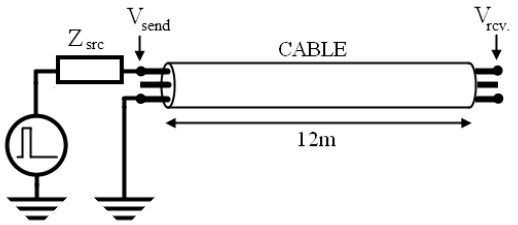

Figure 5.7: Laboratory Cable Test Circuit

From the open circuit tests of Figure 5.8, it is clear that the travel time and attenuation observed in the laboratory results agree well with those generated using the modal domain frequency-dependent cable model. The ability of the simulation model to accurately mimic the dispersive effect on high frequency components is less favourable, as the frequency dependence of the dielectric and hence that of the phase

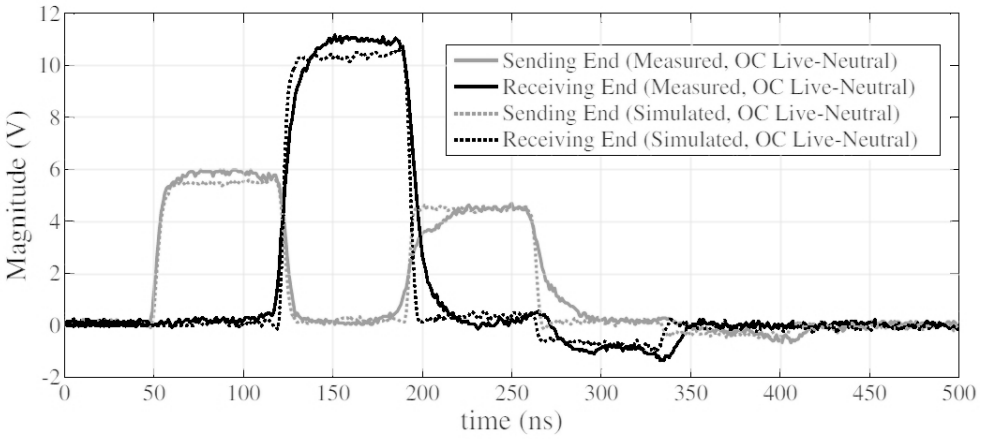

Figure 5.8: Open Circuit Pulse Test - $2.5mm^2$ Mains Flex

velocity are ignored. The effects of dispersion manifest themselves in a time-spreading of the measured reflected pulse on its return to the source, reducing the initially sharp definition of its rising edge. The simulated pulse by contrast remains well-defined following its transit. Though clearly a problem for studies in the MHz domain, for the purpose of switching transients in the frequency range 10-500kHz, this discrepancy was deemed acceptable.

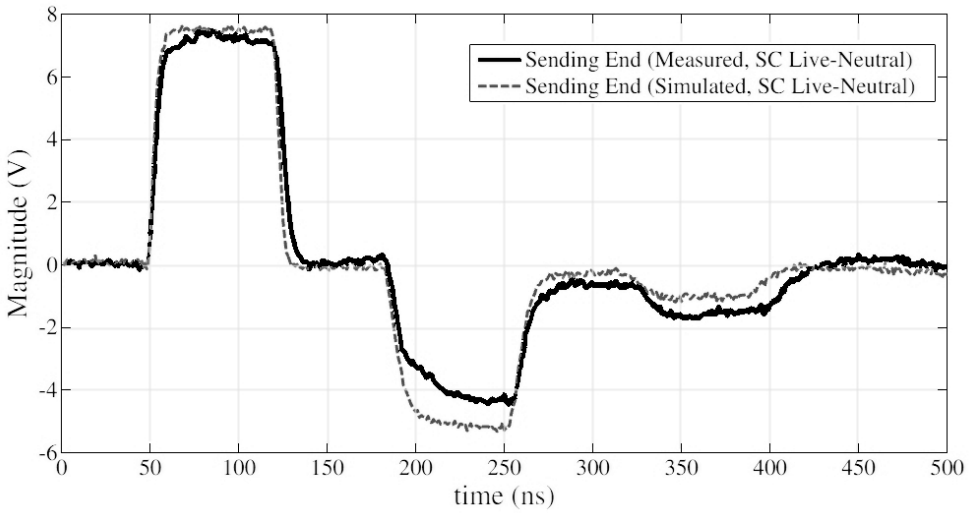

Figure 5.9: Short Circuit Pulse Test - $2.5mm^2$ Mains Flex

The short circuit test of Figure 5.9 again gives a good reproduction of the time delay for the propagation of a $75ns$ square pulse. The only major discrepancy is that due to the necessary omission of proximity effects in the calculation of the series resistance, the attenuation of the LCC model is less pronounced than that observed for the real cable. This effect is compensated at the frequency of interest by the addition of a small

series resistance in the final simulation models.

5.1.5 Load Modelling

The local load for the laboratory rig simulations was modelled as a resistance, with a small parallel stray capacitance determined from a frequency scan of the test load bank.

5.1.6 Final Rig Model

The completed single-phase rig model is shown in Figure 5.10a. The interchangeable source models are each depicted in increasing complexity by Figures 5.10b, 5.11a and 5.11b. For the purpose of the following comparative studies, a $50ms$ solution window was specified to allow for a one-cycle settling time, and a solution time step of $20ns$ chosen in line with the time-resolution of laboratory data.

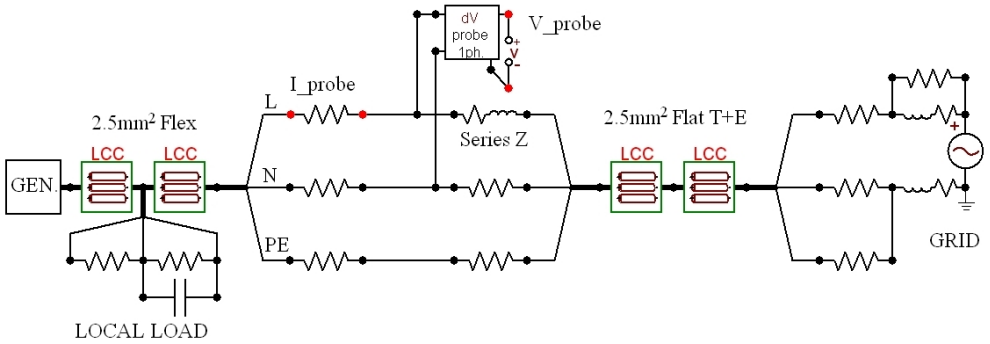

(a) EMTP Simulated Laboratory Rig Model

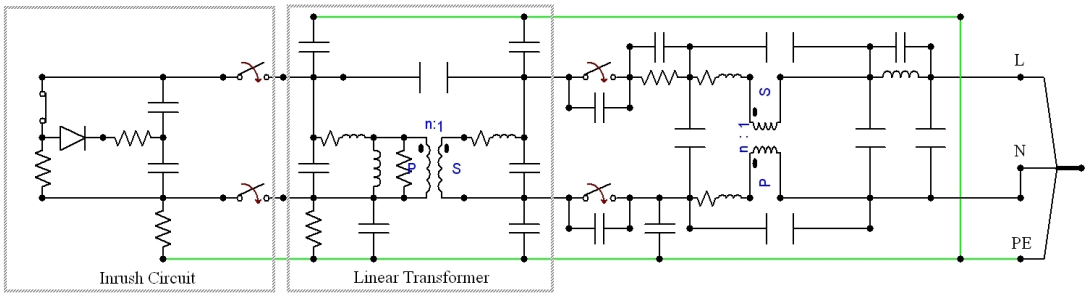

(b) Capacitive Inrush Model

Figure 5.10: Laboratory Rig Model in ATPDraw and Capacitive Inrush Source

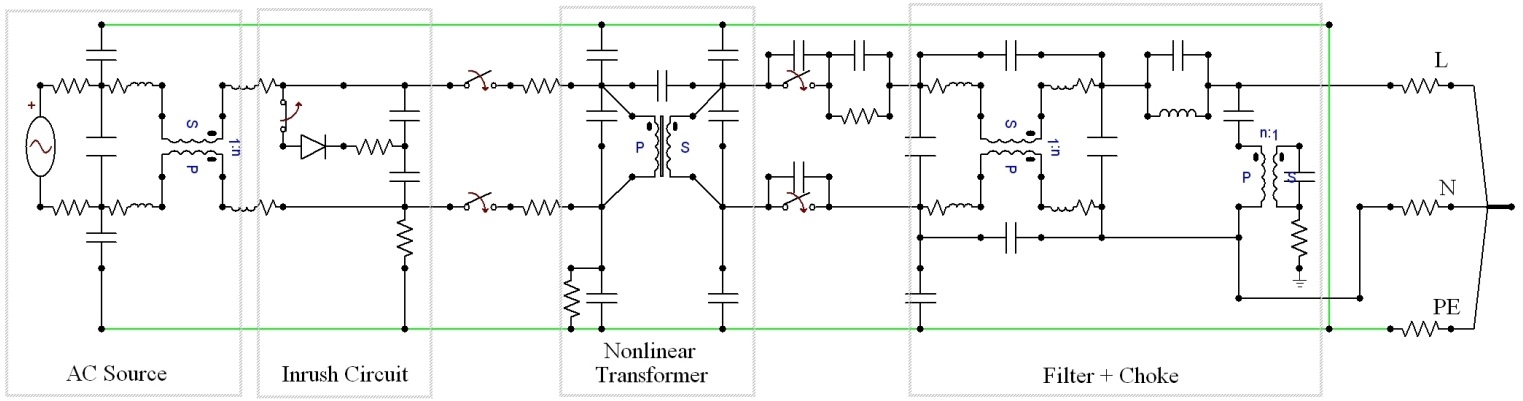

(a) Equivalent AC Model

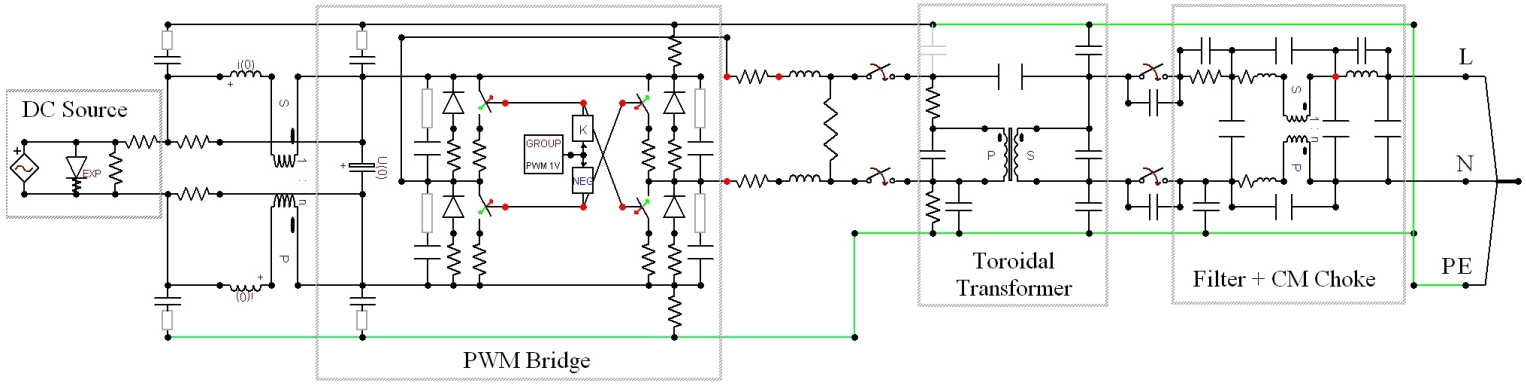

(b) PWM Model

Figure 5.11: Reduced AC and Full PWM Source Representations (ATPDraw)

5.1.7 Comparison of Generated Waveforms

Figures 5.12, 5.13 and 5.14 compare equivalent waveforms generated using the three source variants with a sample capture taken from the laboratory data. The former is a plot of current in the live terminal conductor (measured in the direction of positive export), with the rising edge of the measured inrush lagging the positive-going voltage zero by a quarter cycle ($\theta_i = 90^o$).

The capacitive model was found to give the best reproduction of the measured inrush waveform, followed closely by the AC equivalent model. In both cases the magnitude and slope of the current surge closely match the data, though the AC model is slightly conservative in its estimate of peak current, falling short relative to capacitive inrush model by approximately 1.5A. The introduction of the equivalent inrush capacitance in both models allows for fine control of the angle of inrush θ_i, and as such the timing of the rising edge can be tuned to match the data very closely.

The same cannot be said of the full PWM model, however, which despite giving a reasonable reproduction of the overall wave-shape offers little in the way of controllability, as evidenced by the inherent delay visible in the waveform of Figure 5.12. Such behaviour is due primarily to a portion of the inrush current being determined by the transformer saturation characteristic, which does not in itself account for the effects of remnant flux in the core. Correct representation of such effects would likely provide better control of the current front timing, but in order to do so, initial conditions would need to be individually specified on a case by case basis. This requirement would render the formulation of statistical studies, involving tens or hundreds of cases, entirely impractical.

Measurable perturbations in the terminal voltage occur initially on closing the electromechanical relays in the inverter disconnector. A second voltage peak may also be observed in conjunction with the aforementioned current inrush. Figure 5.13 compares the simulated terminal voltage perturbation on CB closing with that obtained by measurement. In this case, the perturbation is dominated by an oscillation between the transformer output capacitor and line reactance. Since in each of the three source models the components on the grid-side of the toroidal transformer are identical, there

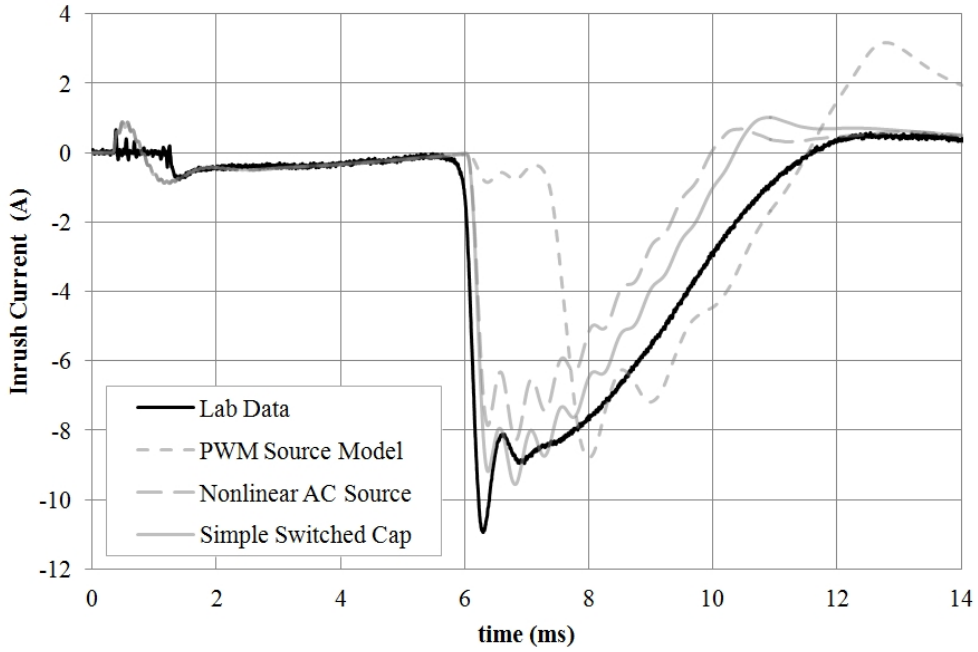

Figure 5.12: Inrush Current Wavevorms for $\theta_i = 90^o$

is little to distinguish between their behaviours. V_{max} and $\frac{dV}{dt}_{max}$ in each case were found to lie within 5% of the measured value, though some higher frequency components in the measured results are absent from the simulations, most likely due to simplifying assumptions in modelling of the filter circuit. The second pole closing operation is also visible in the measured waveform, while coincident switching has been assumed in the simulation models.

Reproduction of the secondary voltage perturbation was found to be somewhat less straightforward. As can be seen from Figure 5.14, the measured dV consists of a single voltage dip, with a magnitude around twice that of Figure 5.13, while the rate of rise is reduced roughly fivefold. This behaviour is partially reproduced by the Capacitive Inrush and AC models, but both also give rise to a lightly damped oscillation following the initial peak, persisting for 1-2ms at a frequency of roughly 2kHz. This discrepancy may be due either to an under-estimation of inherent damping in the supply cables, or more likely the use of ideal components in the simulated notch filter network. Additional refinement of the source models in the light of these differences shall be a focus of future work. The PWM model significantly underestimates the peak voltage by around 40%, and suffers also from the delay caused by a poorly initialised transformer inrush characteristic.

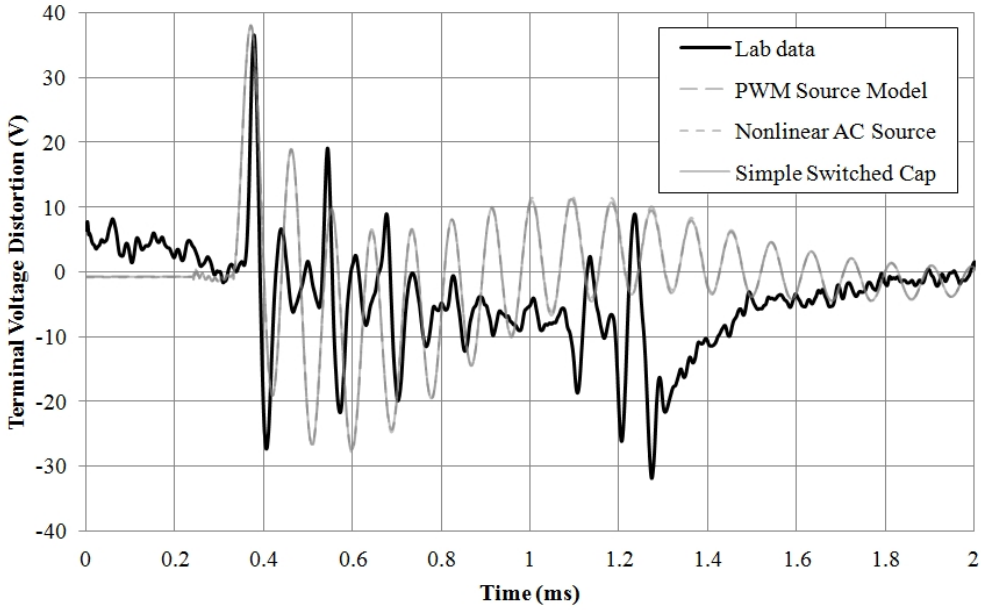

Figure 5.13: Terminal Voltage Perturbation on Switch Closing

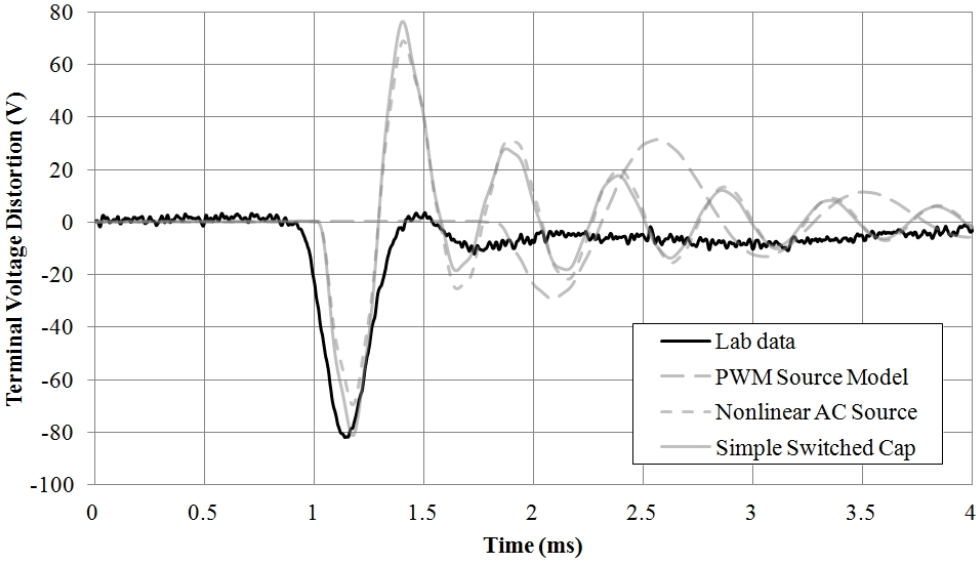

Figure 5.14: Terminal Voltage Perturbation on Inrush

5.1.8 Solution Efficiency

Table 5.2 summarises the scaling of overall solution time by source count and topology. Solution times in *CPU-seconds* were logged for cases executed sequentially on a single machine. Twenty executions were performed for each case and averaged solution times

normalised to that of the shortest case (5.2).

$$T_{norm.} = \frac{T_{soln.}}{T_{min}} \tag{5.2}$$

Table 5.2: Normalised Solution Time

Case	Capacitive Inrush Model	AC Equivalent	Full PWM
1 Generator	1.0	1.83	2.07
2 Generators	1.53	2.07	2.32
4 Generators	2.13	2.72	3.76

For cases involving individual generators, significant CPU time savings can be made by utilising a simple capacitive inrush source representation in place of the AC or PWM equivalents. As the number of generators involved increases the relative economy diminishes, though an absolute reduction in solution time is still clearly visible from Figure 5.15.

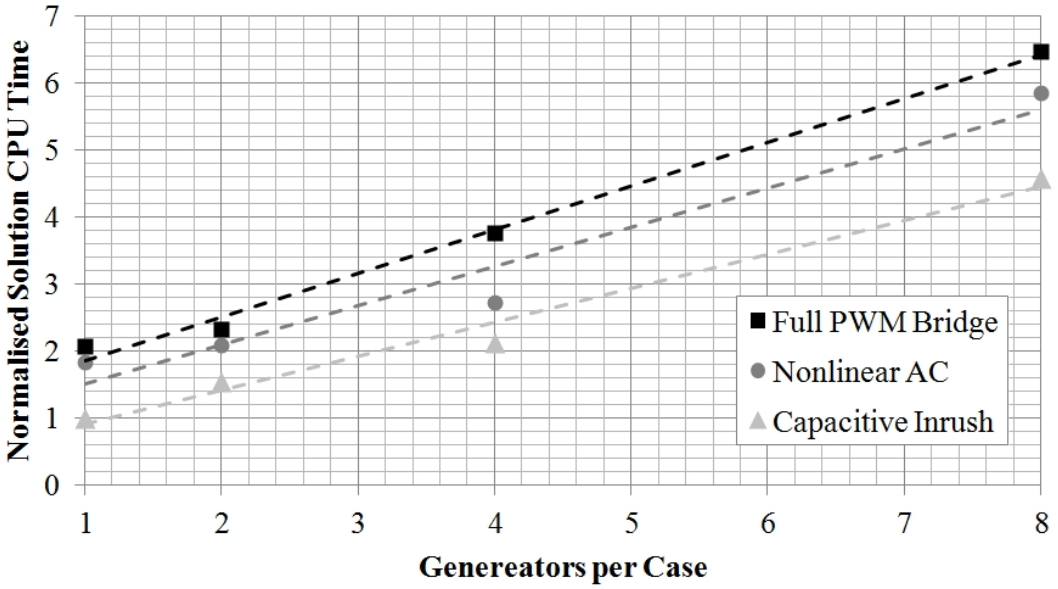

Figure 5.15: Normalised Solution Time with Successive Doubling of Generator Count

5.1.9 Statistical Switch Definition

The laboratory rig model variants were adapted for use in system studies by replacing the single-shot timed switches sw_1, sw_2, sw_t and sw_c with statistical equivalents. Closing times for both poles of the disconnector were defined by a Gaussian distribution, as corroborated by laboratory measurement. Closing times for the fictitious inrush

switch sw_i were modelled as a linear distribution over the measured range, in the absence of more clearly defined behaviour.

In order to minimise the independent switch count in a given simulation, absolute switch time distributions were converted to the following set of delay distributions:

1. Absolute closing time of first breaker pole: $t_{sw\ 1}$
2. Breaker pole delay: $\Delta t_{sw\ 1-2} = t_{sw\ 2} - t_{sw\ 1}$
3. Inrush delay: $\Delta t_{sw\ 1-i} = t_{sw\ i} - t_{sw\ 1}$
4. Arbitrary cut-off delay: $\Delta t_{sw\ i-c} = t_{sw\ c} - t_{sw\ i}$

The newly defined delay quantities are depicted in Figure 5.16 with reference to a typical output current waveform. Using this representation, the sequence of switching operations within the generator model can be replicated by a cascaded master slave representation as depicted in Figure 5.17.

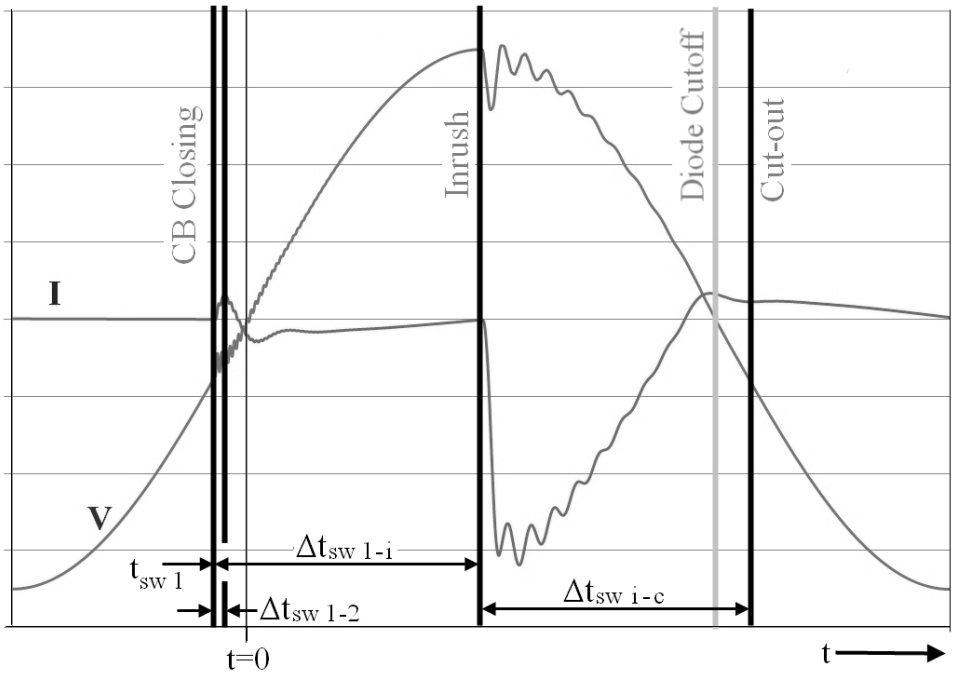

Figure 5.16: Switch operating times as delay terms

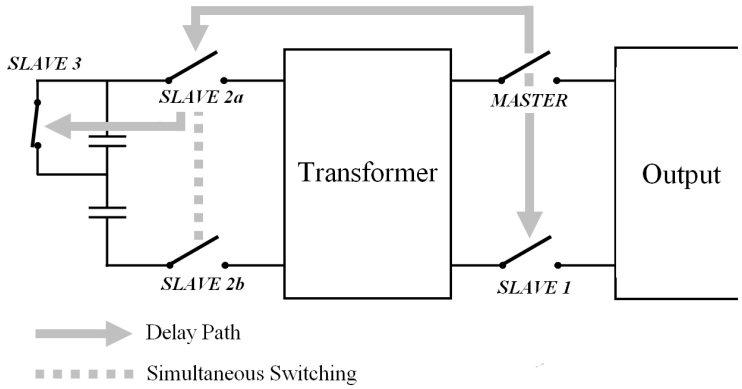

Figure 5.17: Master-Slave cascaded switch representation in EMTP

5.1.10 Statistical Evaluation

Switch time distributions for a 250 case statistical study are plotted in Figure 5.18, the absolute time substituted by an electrical angle relative to the terminal voltage zero crossing. Also shown are the measured distributions determined from laboratory tests in Chapter 4.

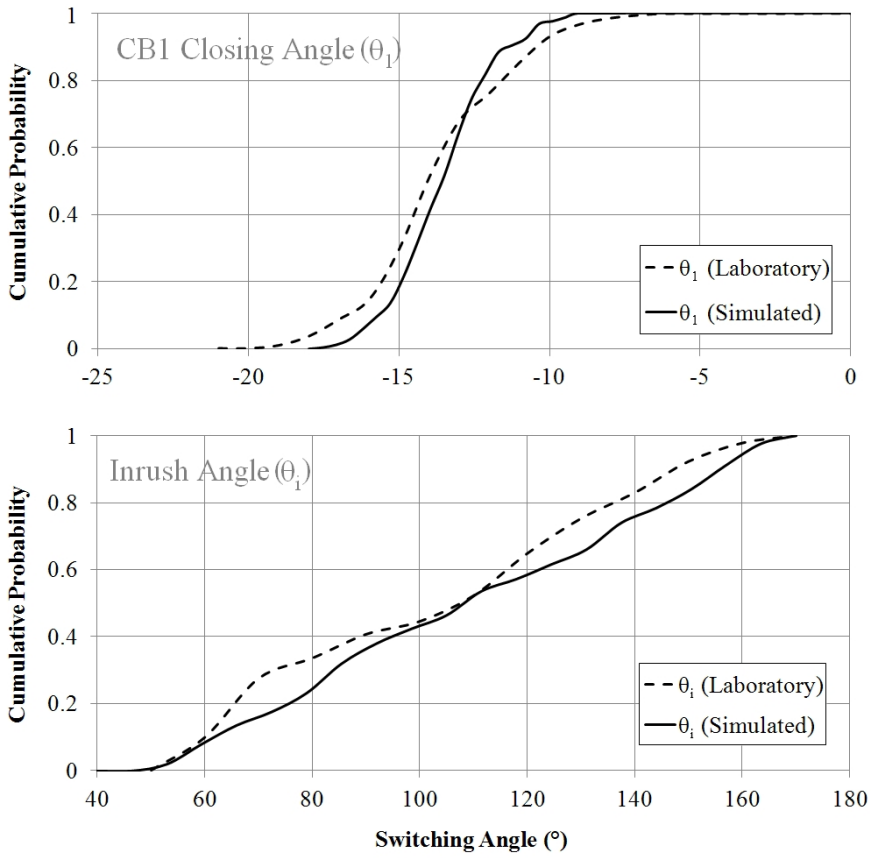

Figure 5.18: Closing angle distributions for cascaded Statistical Switch

Having converted the time domain source model to a statistically determined one, the single shot case of section 5.1.7 can be extended to many cases in order to verify the dependence of peak currents and voltages on switching angle. Figure 5.19 compares such a dependence of the measured inrush current peak on the angle θ_i, together with that generated using statistically switched capacitive inrush model.

Of the three cases, the capacitive inrush model was found to give the best reproduction of the $\theta_i - I_{max}$ relationship. The AC and PWM models each introduce a systematic error associated with the fixed initial conditions governing residual transformer core flux. A similar behaviour is noted regarding maximum voltage deviation. The dependence of voltage transient magnitude on θ_i for the statistical capacitive inrush model is compared with laboratory measurement in Figure 5.20. Two local loading scenarios are presented, and good agreement of measurement and simulation observed in each. Beyond $\theta_i \approx 140^o$, ΔV_2 reduces to a small value and the simulation results accordingly become less well defined as the solver output summary is unable to distinguish between the two peaks ΔV_1 and ΔV_2.

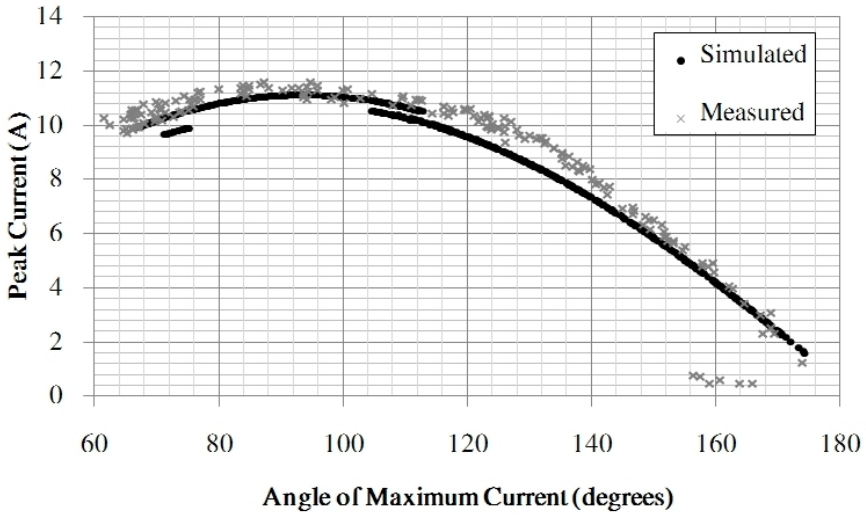

Figure 5.19: Dependence of peak current on inrush angle θ_i

The relationship between peak voltage and current by contrast is well represented in the simulation case (Figure 5.21). Identical behaviour to that of the CI model was observed with both EAC and PWM models, as the V-I characteristics are governed those components common to each model. It can be safely assumed that the output filter network and upstream cabling models are an adequate representation of their hardware equivalents.

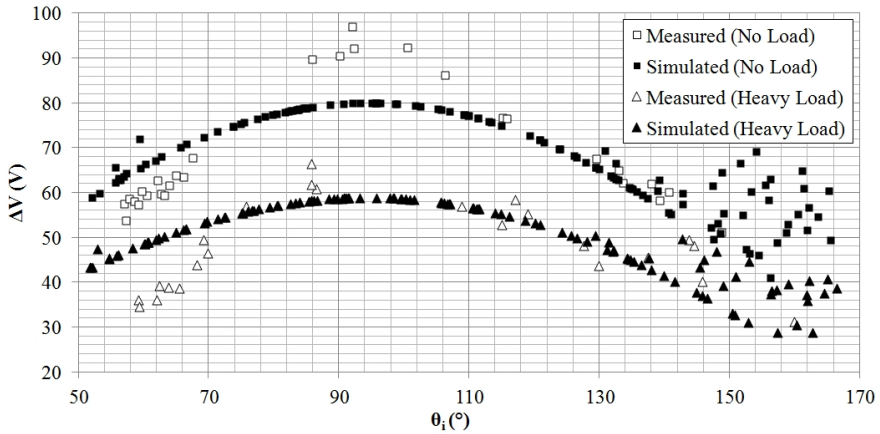

Figure 5.20: Dependence of peak voltage on switching angle θ

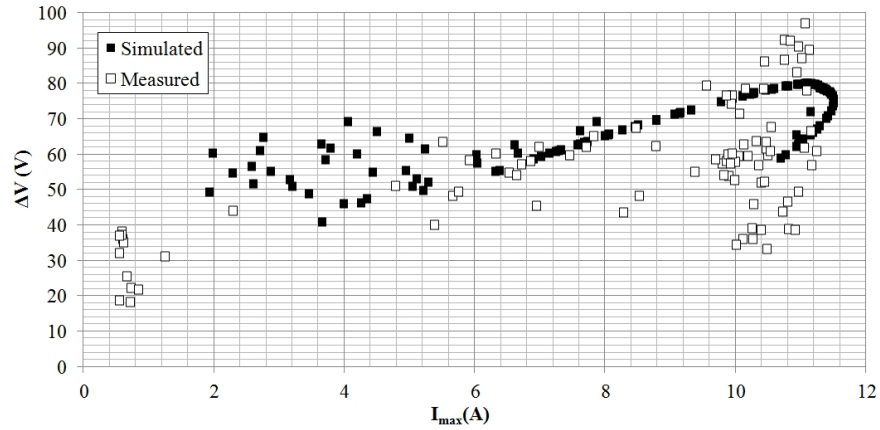

Figure 5.21: Peak Voltage vs Peak Current over 250 simulated switching events

5.1.11 Discussion of Test Set-up Model and Results

The merits and drawbacks of three alternative source representations have been discussed. It has been shown that those SSEG switching operations of greatest interest may be represented by means of the simplest simulation model - namely the equivalent capacitive inrush model. This is an important finding as it is desirable to minimise the computational burden posed by simulating large numbers of embedded generators, where software limitations begin to impose practical constraints on the model's extent.

For the purposes of small network studies and short simulation regimes, a model explicitly representing the source (either as a PWM bridge or equivalent AC source) may be employed. Though this additional complexity is unnecessary for the representation of generator reconnection and inrush, it does afford a degree of flexibility in allowing a single model topology to represent all permutations of switching operations. Subject

to the precise specification of initial conditions, these models are able to give excellent results, but their increased complexity and associated solution inefficiency precludes their applicability to extensive study.

5.2 Generic Domestic Model

5.2.1 Overview

Given the near infinite variety of domestic wiring and load configurations, the specification of a *typical* domestic model is at best an exercise in the arbitrary. However, a number of circuit features and wiring topologies common to domestic installations may be identified (with reference to [156]), and some general assumptions may be made regarding household load scenarios from the available aggregated demand figures [159]. This section is concerned with formulation of a domestic cabling and load model in EMTP for the purpose of SSEG switching studies.

5.2.2 Cable Models

A library of frequency-dependent cable sections was generated using the modal domain travelling wave representation of Marti [160]. PVC insulated and shrouded cables in both flat and round flex configurations were modelled with power conductor geometries in the range of $1.5 - 6mm^2$.

One difficulty faced in modelling domestic wiring by this method is in specifying the resistivity ρ of the ground medium. Given the variety of possible surface and ballast materials (brick, concrete, wood, plasterboard, pvc conduit ...), and taking into account the effects of moisture content and ambient temperature, values of ρ may vary from 100 to tens of thousands of Ωm, and as such it is impossible to typify the electrical properties of all surrounding media.

However, given the proximity of the protective earth to both power conductors, it was assumed that the electrical characteristics of a cable should remain largely independent of the properties of the ground medium. This is particularly true in the case of building materials with a high volume resistivity, an assertion confirmed by parametric study (see Appendix D). For the purpose of this study, a fairly large ground resistivity value ($500\Omega m$) was chosen, resulting in numerically stable models in

the majority of cases. An adjustment of $\pm 5\Omega m$ was necessary in certain instances in which stability was found to be marginal.

5.2.3 Loads

A set of domestic load configurations was specified, as summarised in Table 5.3. First, a *Base* load representing common background demand (refrigerator compressors, emergency lighting, standby equipment etc.) was defined in line with the minimum average load scenarios presented in [25]. Secondly, a *Normal* occupancy scenario supplements the base case with a combination of linear and nonlinear loads to represent lighting, small consumer appliances, computers and other low power equipment [92], based on typical household demand [159].

Table 5.3: Domestic Load Scenarios

Load Configuration	**Magnitude**	**Power Factor**	**Stray Cap.**
Base Load	160W	0.95	500pF
Normal Load (Linear)	+200W	0.95	500pF
Normal Load (Nonlin.)	+140W	0.5	470nF
Heavy Load	+800W	1.0	500pF

Finally, a *Heavy* load scenario is specified with reference to the generic UK LV network model [22–25] by splitting the 11/0.4kV transformer capacity evenly among all 384 supplied customers (approximately 1.3 kW). The difference between *Normal* and *Heavy* load scenarios was assumed to be taken up by water/space heating and cooking and, as such, is modelled purely as a resistance.

A small stray capacitance of the order of a few hundred pF was added in each case, with the exception of the nonlinear load which incorporates an input capacitance typical of a small power electronic interface (CFL, SMPS ...).

5.2.4 Source Model

Since generator reconnection is of most interest from an electromagnetic transient standpoint, the capacitive inrush model (section 5.1.3) was chosen for all studies involving the generic domestic circuit.

5.2.5 Model Set-up

The layout of the finalised generic domestic model incorporating each of the discussed components is shown in Figure 5.22. Appearing as a common sub-network of each of the scenarios presented in section 5.3, the generic domestic model may be used to investigate the role of local load variation and geographic location in determining the transient behaviour of an SSEG.

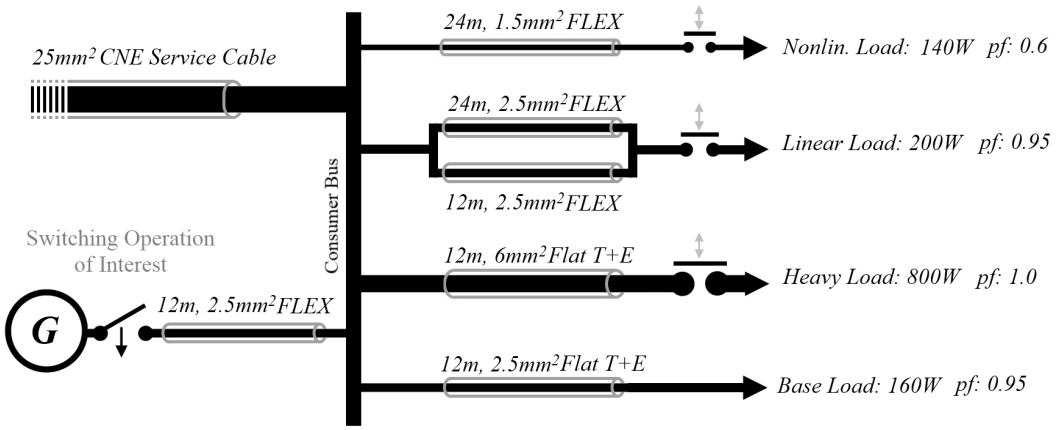

Figure 5.22: Generic household supply and load model (with SSEG)

5.3 Single Generator Network Scenarios

The propagation an attenuation of individual SSEG-induced switching transients within the connected LV network was evaluated using two simplified circuit topologies:

1. An urban undergrounded trunk cable model, and;
2. A rural aerial bundled conductor (ABC) model

This section is concerned with a discussion of each topology.

5.3.1 Urban LV Infeed Configuration

An single-trunk urban feeder model was adapted for eletromagnetic transient simulation from the generic UK LV network model detailed in [23, 24]. In this simplified form, a 450 metre, 3-phase trunk cable is modelled in six sections of equal length, with graded phase CSA from $185mm^2$ down to $95mm^2$, as shown in Figure 5.23.

Cable branches fed from the main trunk nodes have been ignored as a first approximation in order to simplify the analysis of the circuit. A comprehensive travelling wave

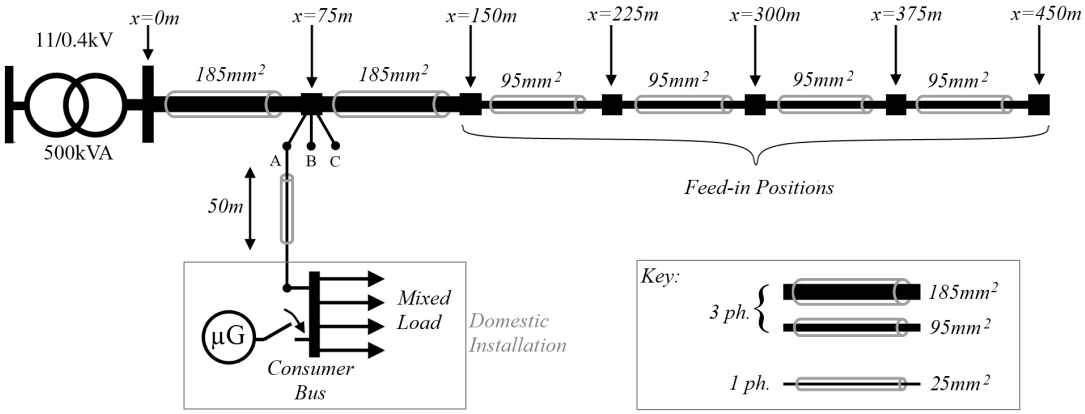

Figure 5.23: SSEG feeding an urban underground LV circuit

analogue of the UK generic LV network is presented in Chapter 6. The sectored geometry of the trunk cable [111, 157] is approximated by an equivalent circular cable pipe model as discussed in Chapter 2.

A 50-metre length of single-phase $25mm^2$ service cable links the consumer bus of the generic domestic model to phase A of any of the six trunk nodes ($x = 75m \rightarrow 450m$). In this way, the combined effect of a generator's local load and its position relative to the LV terminals of the 11/0.4kV transformer may be investigated.

Each of the aforementioned trunk nodes, together with the transformer terminal ($x = 0m$) and consumer bus, is fitted with a TACS filtered voltage probe. This allows straightforward identification of high frequency voltage transient peaks in which the magnitude lies below the steady-state amplitude of the grid supply voltage ($< 325V$).

The 11kV grid supply and circuit (not shown) are represented as an ideal voltage source behind a parallel source/surge impedance network [120], and a 1500-metre length of 11kV cable, modelled in the same fashion as the LV trunk cables.

5.3.2 Rural LV Infeed Configuration

A similar topology was specified for investigating an SSEG connecting into a rural overhead LV circuit. In the absence of an established generic LV model for the simulation of rural networks, a library of wood-pole mounted Aerial Bundled Conductors (ABC) as standardised in [139] was created in line with typical DNO guidelines for new and replacement lines [158]. A trunk circuit of length 1400m was constructed using line

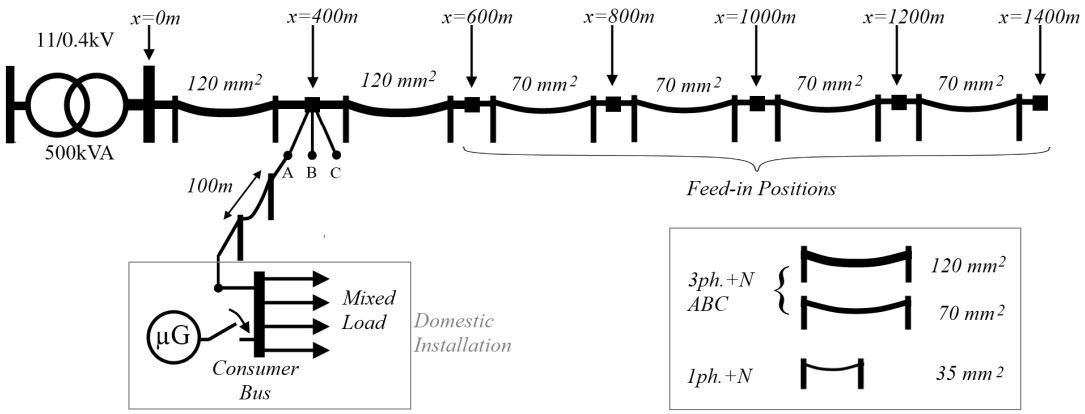

Figure 5.24: SSEG feeding a rural overhead LV circuit

spans of 50m, with graded CSA from $120mm^2$ down to $70mm^2$ as shown in Figure 5.24.

The consumer is fed from one of the trunk nodes by 100m of single phase $35mm^2$ service line, for a total effective circuit length of 500-1500m. A 3.6km section of the 11kV bare conductor OHL circuit upstream of the transformer (not shown) is modelled according to [161].

5.3.3 Ground Resistivity

In both the urban and rural models, ground resistivity for the LV distribution circuit was assumed to be $100\Omega m$ as per the guidelines of [120]. This is in contrast to the higher resistivity ground ($500\Omega m$) chosen for the domestic cable models. The effects of adjacent conductive media (pipelines, telegraph cables etc.) have been ignored for the generalised case.

5.4 Switching Transient Simulation Results

There follows a summary of simulation results for scenarios with a single generator feeding each of the simplified LV circuits. Unless otherwise specified, statistical data is based on a regime of 100 test cases in each scenario, with generator switch distributions according to section 5.1.9.

5.4.1 Urban LV Feeder Simulation Results

Transient voltage magnitudes were recorded at each node ($x = 0,\ 75, ...\ 450m$) for each of the generator feed-in locations x_g. Figure 5.25 shows the mean voltage magnitude

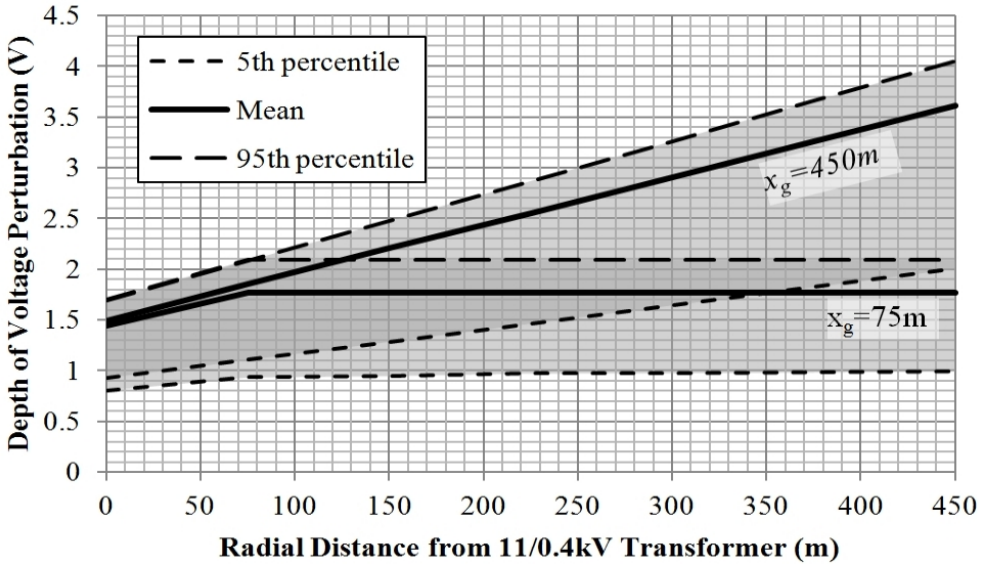

Figure 5.25: Range of urban feeder voltage magnitude profiles for $x_g = 75m$ and $x_g = 450m$ (minimum load)

profiles under minimum load conditions, for generators connected adjacent to the 11/0.4kV transformer ($x_g = 75m$) and at the remote end of the feeder ($x_g = 450m$). The range of values obtained in both cases is illustrated by means of the 5^{th} and 95^{th} percentile values, also plotted in Figure 5.25.

It is clear that the voltage magnitudes encountered with a single generator feeding an urban cable network are near immeasurable (0.01 pu in the worst case). However, it is of interest to note the effect of position on the voltage profile. The results indicate a linearly attenuated transient voltage magnitude in the region $x = 0 \rightarrow x_g$, and a subsequent plateauing effect along the circuit downstream of x_g. This is more clearly illustrated by Figure 5.26a. Here, the mean spike magnitude profile is plotted explicitly for each of the six in-feed positions.

The same plot is reproduced in Figure 5.26b, with a larger voltage scale to include the range of simulated voltages at the consumer bus ($\bar{v}_{con}$) for each value of x_g. It is clear that the magnitude of the voltage transient is greatly curtailed by the short length of service cable linking the consumer bus and the LV trunk node. In this instance, the results is a mean attenuation of 5.5V from an initial magnitude in the range 7.0-9.5V. Despite this observation, the magnitudes encountered remain of no concern from the standpoint of either insulation coordination or electromagnetic compatibility.

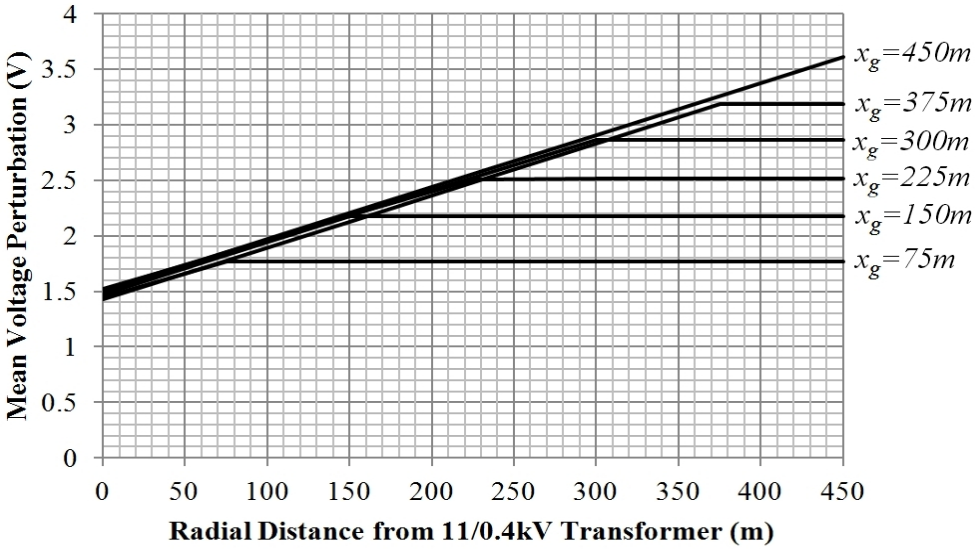

(a) Mean urban voltage magnitude profiles by in-feed location (min. load)

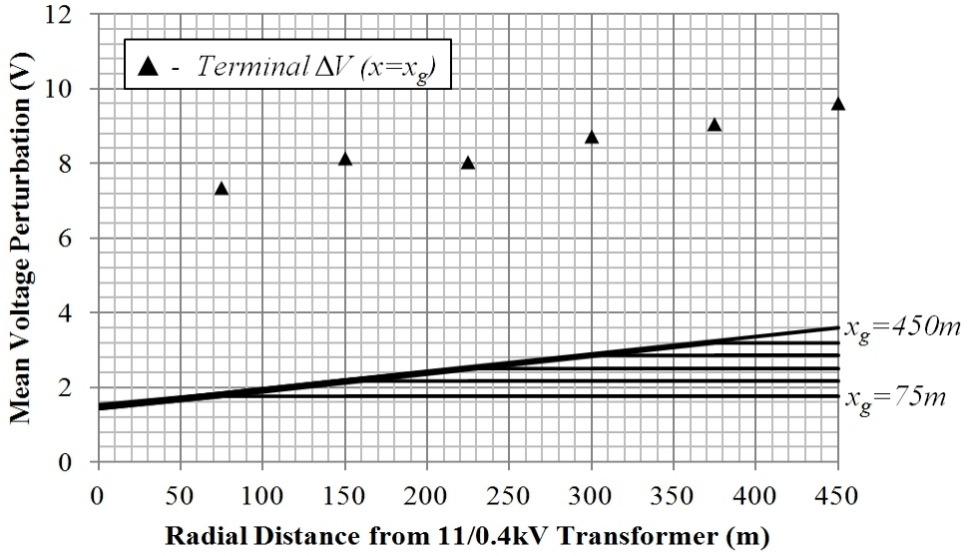

(b) Mean urban magnitude profiles including consumer bus (min. load)

Figure 5.26: Voltage Magnitude Profiles on a One-Line Urban Feeder

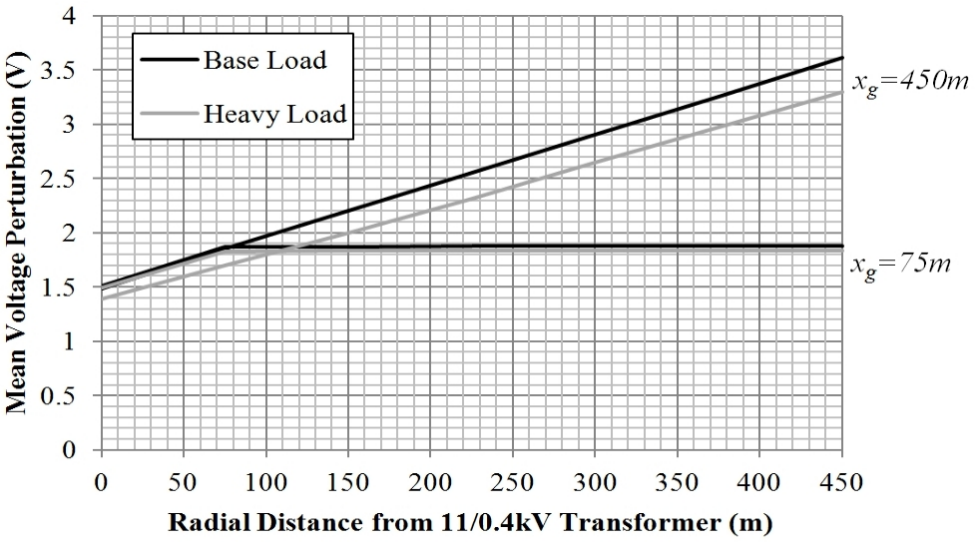

Figure 5.27: Magnitude profiles for $x_g = 75m$ and $450m$ under minimum and heavy load conditions (urban)

The final plot of figure 5.27 illustrates the effect of consumer bus loading on transient peak voltage. Mean magnitude profiles are illustrated for generators at $x_g = 75m,\ 225m$ and $450m$ for the minimum load scenario. This is overlaid with the same set of profiles generated under the heavy load scenario.

It is clear that some curtailment of the transient voltage is attributable to the local load condition, the extent of this effect being dependant on the customer's position relative to the transformer LV bus. Switching under heavy load conditions for example will typically reduce peak voltages by around 10% for a remotely connected customer, compared to the minimum load case. For an equivalent customer connected close to the transformer, the effect is negligible.

5.4.2 Rural LV Feeder Simulation Results

The analyses of the previous section were repeated for the rural feeder model, this time with customers connected in 200m intervals up to 1400m from the transformer. Figure 5.28 illustrates the effect of feed-in position on the expected transient voltage magnitude.

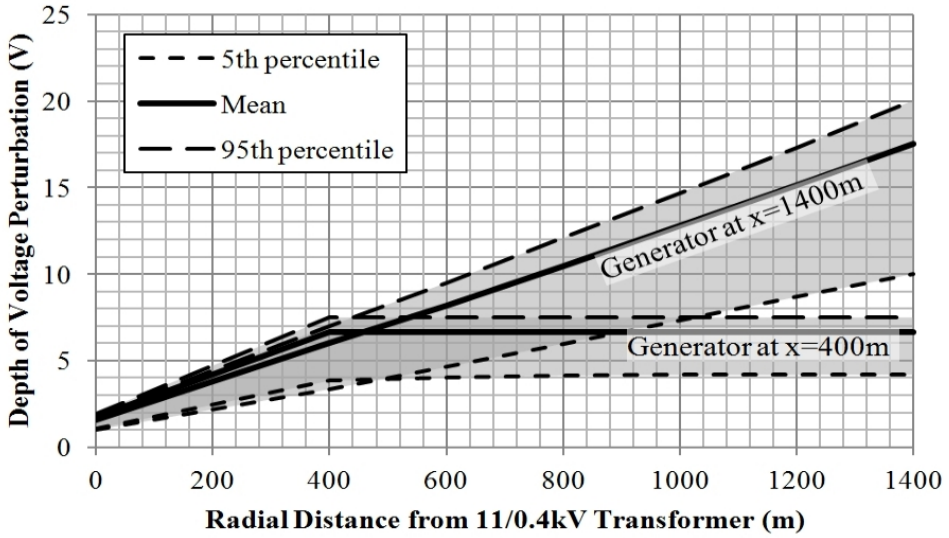

Figure 5.28: Range of rural feeder voltage magnitude profiles for $x_g = 400m$ and $x_g = 1400m$ (minimum load)

The behaviour of the rural circuit is very similar to the urban case in this regard, though some elevation in voltage is to be observed in the rural circuit. The gradient of the transient magnitude profile is approximately doubled over an equivalent length of overhead circuit, with mean voltages rising to around 17V for a generator located 1500m from the LV terminals of the pole transformer.

The dependence of dV on x_g is once again a linear one as can be seen from Figure 5.29, but unlike the underground circuit of the urban case, the attenuation attributable to the single phase overhead service line is comparatively minimal, despite its increased length. A reduction in magnitude of only 1-2V can be expected to occur in propagation from the customer bus to its adjacent trunk node.

Finally, the attenuation of a typical transient due to local load conditions is somewhat less pronounced in the rural case. An equivalent reduction of 10% in the transient

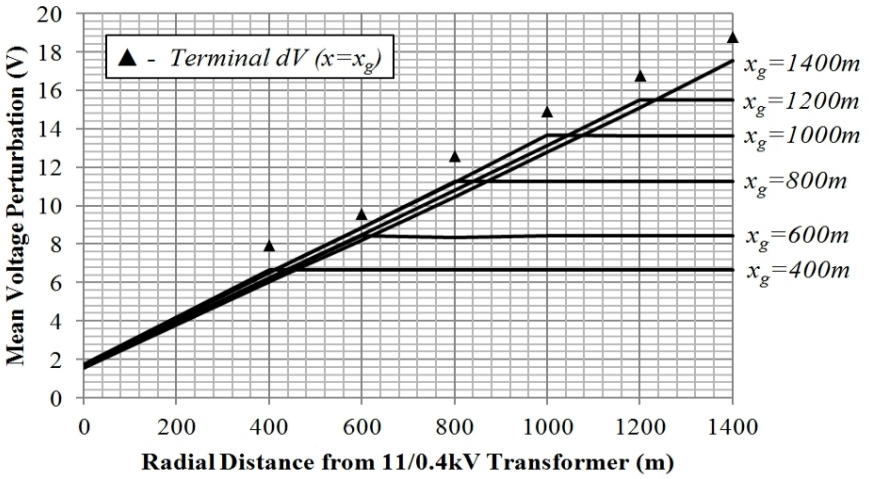

Figure 5.29: Mean rural voltage magnitude profiles by in-feed location (min. load)

voltage magnitude under heavy load for example requires approximately 800m of ABC between the consumer and the LV transformer (in contrast to 450m of underground cable in the urban case). This is illustrated in Figure 5.30.

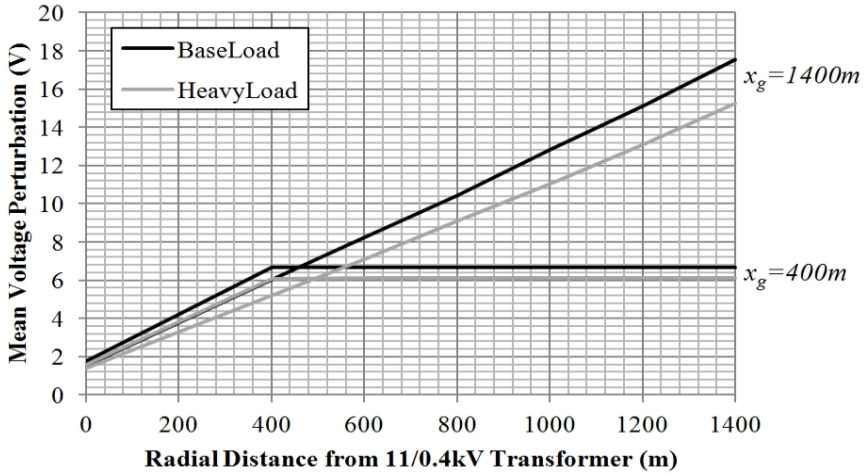

Figure 5.30: Magnitude profiles for $x_g = 400m$ and $1400m$ under minimum and heavy load conditions (rural)

5.5 Chapter Conclusions

In this chapter, simulation models for the representation of embedded generators rated below 16A/phase have been developed and compared according to their flexibility and solution efficiency. A generic model for the representation of domestic power circuitry has been proposed and, in conjunction with simplified single trunk models of urban and rural LV utility circuits, used to estimate transient voltage magnitudes due to generators switching at different radial feeder positions. Principal conclusions are as follows:

- The most severe generator switching transients (those associated with grid-reconnection) may be modelled using a simplified capacitive inrush circuit representation, ignoring all components behind the inverter DC bus.
- Relay pole closing and inrush inception may be accurately reproduced by means of a cascaded master-slave switch representation, useful for statistical/systematic study in EMTP.
- Typical simulated transient voltage magnitudes are extremely low for simulations involving single generators, with worst cases of 1.03 and 1.06 p.u. for simplified urban and rural network topologies respectively.
- Simulated voltages were found to be largely independent of localised loading conditions.

Chapter 6 builds on this work, using the developed source models to investigate the cumulative effect of multiple generators switching in response to common network conditions.

Chapter 6

Cumulative Electromagnetic Transient Impact of SSEG

BUILDING on the laboratory and simulation results of Chapters 4 5, a suite of cumulative impact studies was drawn up to assess the combined impact of multiple generators switching in response to common stimuli. In order that these simulation studies could be performed, it was necessary to develop a best optimised EMTP-ATP LV network model, as distinct from the simple one-line source evaluation model presented in Chapter 5. This work has resulted in the development of a complete travelling-wave equivalent of a 400/230V circuit, as broadly defined in the generic UK LV distribution network.

The explicit representation of such extensive networks and large numbers of generators presents its own challenges in terms of complexity and computational efficiency, and there is a need to be mindful of the practical operating limits of the software. Clearly, the network topology itself shall have some effect on the results of a given simulation, but given the variety of LV network configurations that might be encountered, consideration of all possible scenarios would be extremely time-consuming. An approach based on DNO-approved generic models has therefore been adopted as a first approximation, allowing these results to tie in with other studies based on generic networks [22–25]. Future work may then begin to consider the nuances of various network configurations.

In this chapter, an analysis of the various design choices and constraints and the resulting hierarchical network models is undertaken. A set of simulation scenarios is proposed based on generator penetration, using the capacitive source representation

developed in Chapter 5 (Figure 5.10b), and a variety of network loading profiles. The results of extensive statistical simulations are presented and discussed in the sections that follow.

6.1 Generic Low-Voltage Network Models

6.1.1 The Generic UK LV Network

The DNO-approved generic UK LV network as presented in [25] is depicted in figure 6.1. The model consists of a parallel pair of 33/11kV transformers supplying six identical 11kV feeders. Each 11kV feeder supplies eight 400V buses through 500kVA 11/0.4kV transformers, and each bus in turn supplies four feeders supplying 384 evenly distributed customers. The total circuit length from 11kV bus to most remote customer node is 1.5km. Table 6.1 gives a breakdown of the total number of downstream consumer nodes at each level of the model.

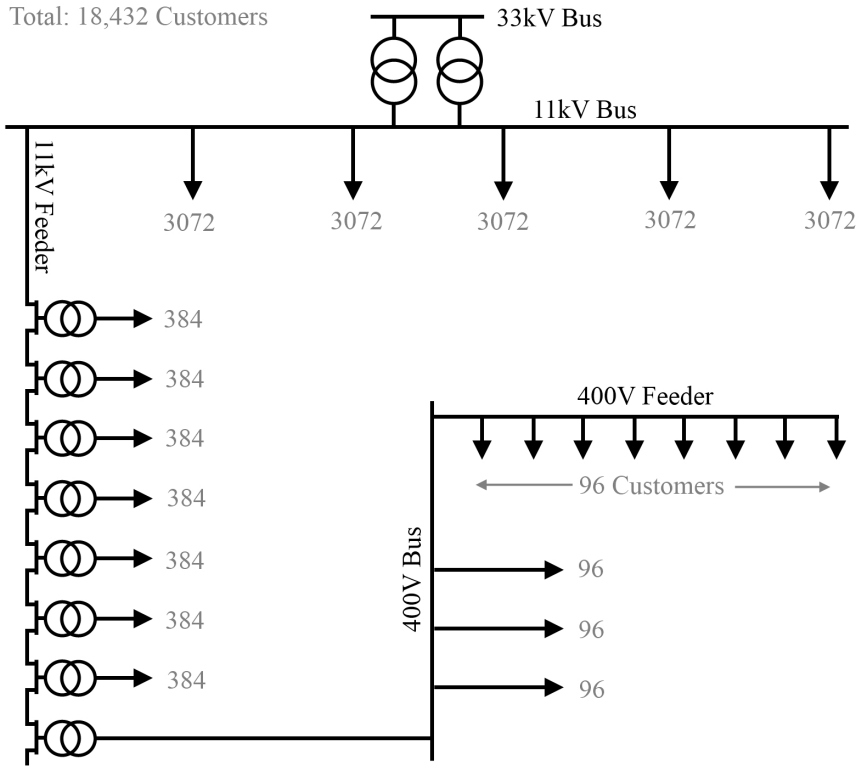

Figure 6.1: Generic UK LV Network Model

Table 6.1: Total Downstream Customer Nodes by Location

Position	Customers	Minimum Load (kVA)	Maximum Load (kVA)
11kV Bus	18432	3000	24000
11kV Feeder	3072	500	4000
400V Bus	384	61.4	500
400V Feeder	96	15.4	125

Load is assumed uniformly distributed across the network, ranging from a minimum of approximately 160VA per customer up to a maximum defined by the rating of the 500kVA transformers (approximately 1300VA per customer).

For the purpose of electromagnetic transient simulation, modelling of the complete 11kV and 400V radial network with its 18,432 individual consumer nodes was deemed impracticable within the constraints imposed by even the most liberally specified EMTP *listsize* variables. It was noted, however, that for transient overvoltages generated on the 400/230V side of the transformer, the effect of coupling to the 11kV circuit should be negligible. Indeed, an overvoltage of almost 30 p.u. would be needed to register any significant disturbance which, though theoretically plausible in the case of lightning induced overvoltages from strikes to nearby structures, is at least an order of magnitude higher than that expected to occur due to switching.

The interaction between neighbouring 400V buses was, therefore, ignored for the purposes of this study, and only one 400/230V circuit modelled explicitly. The 11kV circuit upstream of the 500kVA transformer is represented simply by means of a 1.5km length of 3-phase underground cable, as in the simplified models of Chapter 5. A one-line diagram of the LV bus/feeder sections to be modelled is shown in Figure 6.2.

6.1.2 Modelling Constraints

The permissible extent of a simulation model in EMTP-ATP is constrained by a set of variable dimensioning limits defined in the *listsize* file of the EMTP installation. Those limiting values of particular interest are summarised in Table 6.2. Default values for the standard *atpmingw* software build packaged with the ATP easy installer [162] are listed. Equivalent limiting values are also given for an alternative software build (*gigmingw*) available from [163] which, though potentially less stable than the standard release, is capable of handling simulation models with far greater volumes of network

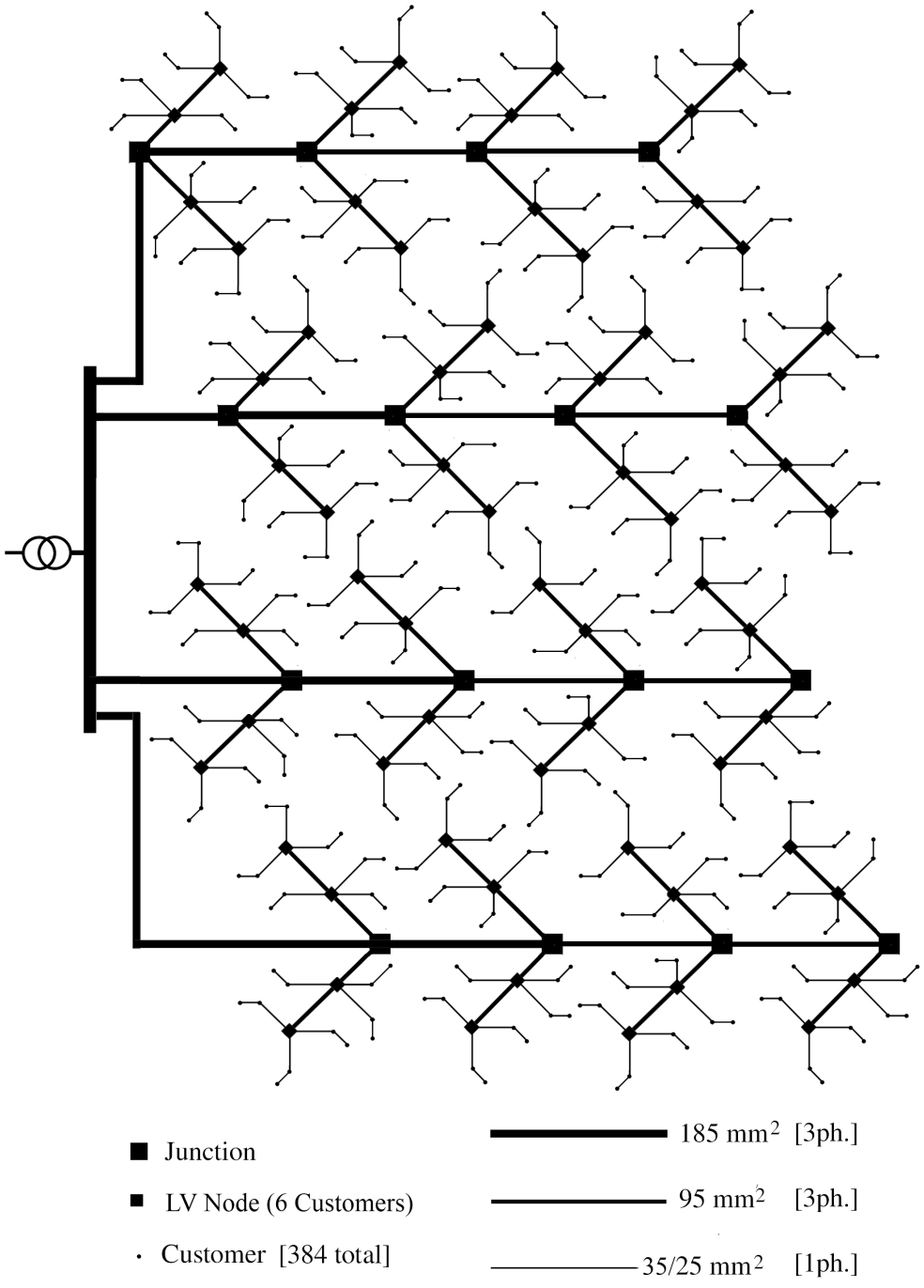

Figure 6.2: 400/230V LV Network Layout

elements [164].

Table 6.2: Limiting *Listsize* Variables for Large Network Models [95]

Variable	Description	*atpmingw*	*gigmingw*
LBUS	Maximum number of network nodes	6,000	100,000
LBRNCH	Maximum number of network branches	10,000	200,000
LSWTCH	Maximum number of switches, diodes and thyristors	1,200	6,000
LFSEM	Storage space for frequency-dependent lines/cables $\approx$ 7×Number of poles required to represent branch Z_0 and A_1	100,000	400,000
LFD	Storage space for frequency-dependent line/cable transformation matrices $\approx 2N^2$ for each unique N-phase line	3,000	12,000
LHIST	Additional frequency-dependant storage $\approx$ 15×Number of coupled phases	15,000	60,000

In predicting potential limit violations in either ATP distribution, the following quantities are defined with reference to the generic LV model, as illustrated in more detail in Figure 6.3.

- n_L: Number of customer load buses per feeder = 96
- n_g: Number of generator buses per feeder $\leq$ 96
- $n_{c3\phi}$: Number of 3-phase cable segments per feeder = 20
- $n_{c1\phi}$: Number of 1-phase cable segments per feeder = 96
- n_f: Total Number of 400/230V feeders
- n_m: Total Number of measurement positions

6.1.2.1 Node Limits

The number of nodes required to represent a given network scenario may be estimated by Equation (6.1), where N_L is the number of nodes required to represent an aggregated customer load (*3*), N_g the node count of the chosen generator model (*25* $\rightarrow$ *43*) , N_m the

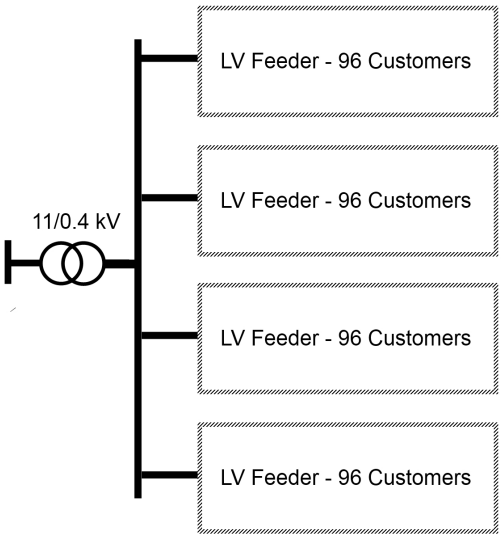

(a) 400/230V Bus

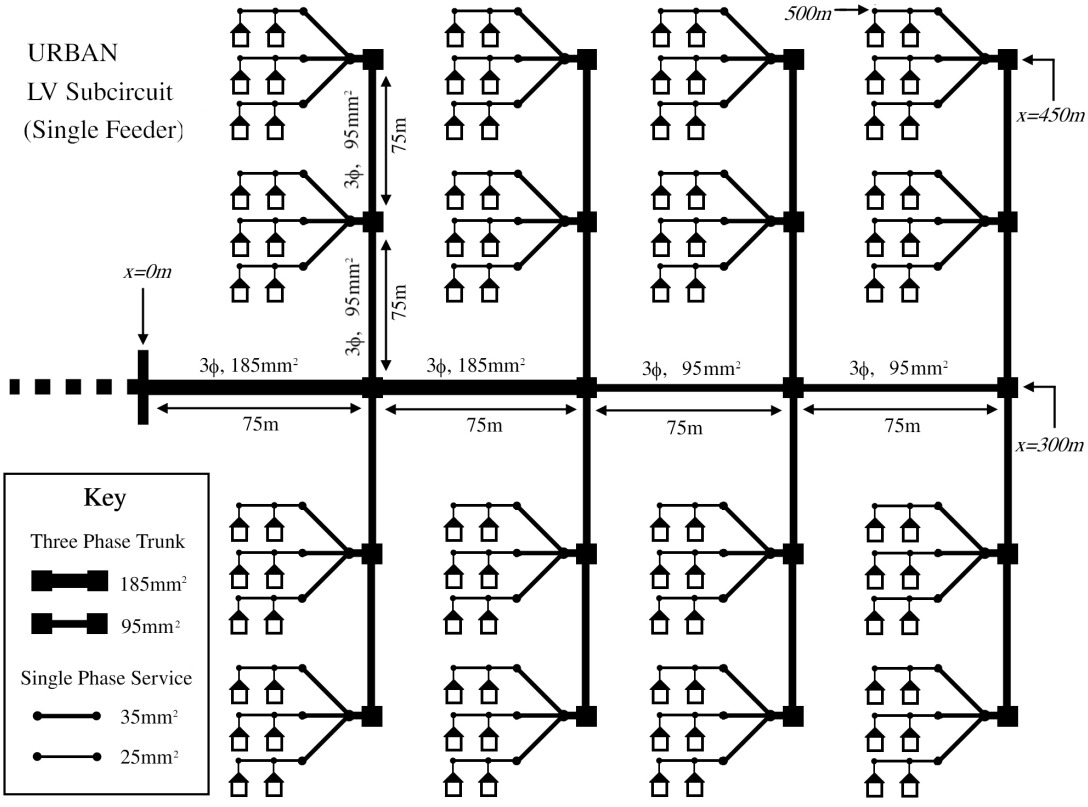

(b) Individual Feeder Detail

Figure 6.3: Generic LV Network Modelled in EMTP

node count per phase for each voltage measurement group (≈ 15) and k_N is a constant accounting for network nodes necessary for representing the network upstream from, and including, the LV transformer (≈30).

$$n_{node} \approx n_f \times (n_L N_L + n_g N_g + 4n_{c3\phi} + 2n_{c1\phi}) + 3n_m N_m + k_N \tag{6.1}$$

Table 6.3 summarises the predicted node counts by generator model and SSEG % penetration (ρ_g) on a four-feeder generic LV network. It is clear that based on node/bus counts alone, only low penetration scenarios can be fully represented using the standard *atpmingw* distribution. For a ρ_g scenarios in excess of 25%, the additional capacity afforded by the *gigmingw* distribution becomes necessary, even when using the minimal-node capacitive inrush generator model.

Table 6.3: Approximate Node Count for Increasing SSEG Penetration Scenarios

Generator Model	ρ_g		
	25%	50%	100%
Capacitive Inrush	4,900	7,300	12,100
AC Equivalent	6,500	10,600	18,600
Full Inverter	6,600	10,800	19,000

6.1.2.2 Branch Limits

Branch counts for the same circuit may be estimated by Equation (6.2) where B_L is the branch count of an aggregate customer load (4), B_g the branch count for the chosen generator model (44 → 128) and B_m is the number of branches in a single phase measurement block (15). The constant k_B is used to factor in those network branches upstream of the 400V bus (≈50). Predicted branch counts are summarised in Table 6.4.

$$n_{branch} \approx n_f \times (n_L B_L + n_g B_g + 4n_{c\ 3\phi} + 2n_{c\ 1\phi}) + 3n_m B_m + k_B \tag{6.2}$$

Table 6.4: Approximate Branch Count for Increasing SSEG Penetration Scenarios

Generator Model	ρ_g		
	25%	50%	100%
Capacitive Inrush	7,300	11,700	20,600
AC Equivalent	10,000	17,100	31,300
Full Inverter	15,400	27,800	52,800

Once again, predicted component counts greatly exceed the limits imposed by the standard installation in all but the lowest penetration scenarios. The large branch counts required for high ρ_g scenarios can, therefore, only be expected to compile with the *gigmingw* distribution.

6.1.2.3 Switch Limits

Possibly the most restrictive of the listsize variables, *LSWTCH* limits the total number of individual switches (timed, statistic and systematic), diodes, thyristors and valves for an individual simulation case. Since the switch count is dependent on the choice of generator model as well as the total number of embedded generators, an estimate of the switch count can be obtained from Equation (6.3), where S_g is the switch count for the chosen generator model (6 for the capacitive inrush and AC equivalents, 15 for the PWM bridge). Table 6.5 gives the expected switch count for each of the penetration scenarios already discussed.

$$n_{switch} = n_f n_g S_g \tag{6.3}$$

Table 6.5: Approximate Switch Count for Increasing SSEG Penetration Scenarios

Generator Model	ρ_g		
	25%	50%	100%
Capacitive Inrush	576	1,152	2,304
AC Equivalent	576	1,152	2,304
Full Inverter	1,440	2,880	5,760

Not only is the switch limit (*1200*) exceeded for ρ_g in excess of 50%, the switch count for maximum SSEG penetration using the full inverter model is very close to the limit for the *giga* version (*6000*). It is advised where possible to use either the Capacitive Inrush or Equivalent AC models so as to avoid unwanted errors should LSWTCH be

exceeded, and to minimise the total number of partial Y-matrix re-traingularisation operations associated with the opening and closing of switches.

6.1.2.4 Frequency-Dependent Line Limits

The remaining three *listsize* variables governing use of frequency-dependent transmission lines are independent of ρ_g, as the topology of the cable network does not change between simulations. The required values for LFSEM, LFD and LHIST can be estimated by the equations in Table 6.6.

Table 6.6: Approximate Listsize Values for Frequency Dependent Line Modelling

Variable	Approximation	Single Feeder	4 Feeders
LFSEM	$14n_f P_{Z0}\left(4n_{c3\phi} + 2n_{c1\phi}\right)$	76,000	305,000
LFD	$2\left(4u_{c3\phi} + 2u_{c1\phi}\right)^2$	800	800
LHIST	$15n_f\left(7n_{c3\phi} + 2n_{c1\phi}\right)$	5,200	21,000

P_{Z0} and P_{A1} are the number of poles required to fit Z_0 and A_1 respectively for each branch. A curve fitting of 20 points per decade from $1mHz$ up to $10MHz$ was found to give good results for all cable geometries, from $25mm^2$ single phase service lines up to the $185mm^2$ three-phase trunk cable, with the number of poles rarely exceeding $P_{Z0} = P_{A1} \approx 20$. The quantities $u_{c1\phi}$ and $u_{c3\phi}$ are the number of uniquely defined single and three-phase cables respectively. Since it is desirable to minimise these quantities as far as possible, only a limited range of conductor grades have been included in the finalised generic LV model, consistent with the specification of the generic UK LV model.

6.1.2.5 ATPDraw Display Limits

In order that the finalised generic model be portable for further application, the display limitations of typical graphical preprocessors should also be adhered to. *ATPDraw*, the most commonly used preprocessor to EMTP-ATP imposes its own constraints on the number of objects in a single circuit. In addition, since the finished model shall include hundreds of generators, loads and cables, it is desirable to make maximal use of the circuit compression function in order to avoid a sprawling and convoluted network

topology. The number of hierarchical compressed groups that may exist in a single model is also constrained. Limiting values are summarised in Table 6.7.

Table 6.7: ATPDraw Display Limits

Constraint	Value
Object Limit	10,000
Group Limit (pre version 5.6)	255
Group Limit (version 5.6 onwards)	2047

Estimates of the object and group counts may be obtained from Equations (6.4) and (6.5). The number of circuit objects is approximately equal to the number of circuit branches plus the number of compressed groups. The compressed group count, in turn, assumes a hierarchical structure in which each aggregated customer load and each generator is assigned its own group. Customers are then compressed into groups of six to be fed from each of sixteen LV trunk nodes, all of which are further compressed into a single LV feeder group. This hierarchical structure is depicted in Figure 6.4.

$$n_{objects} \approx n_{branch} + n_{groups} \tag{6.4}$$

$$n_{groups} \approx n_f \cdot \left(\frac{7}{6} n_L + n_g + 1\right) + n_m \tag{6.5}$$

The ATPDraw object and group counts are summarised in Table 6.8 for different penetration scenarios on a four-feeder network. Use of the capacitive inrush generator model is assumed.

Table 6.8: Approximate Object/Group Counts for Different SSEG Penetrations

Count	ρ_g		
	25%	50%	100%
Objects	7,800	12,400	20,500
Groups	560	650	850

It is clear from a comparison of Tables 6.7 and 6.8 that in order for the generic LV model to be useful, there is necessarily a major constraint on extent and complexity imposed by the display limits of the GUI. Maximal use of the *gigamingw* distribution's expanded capabilities is, therefore, unachievable on practical grounds. It can be seen that for even low penetration scenarios, the anticipated object count is close to the

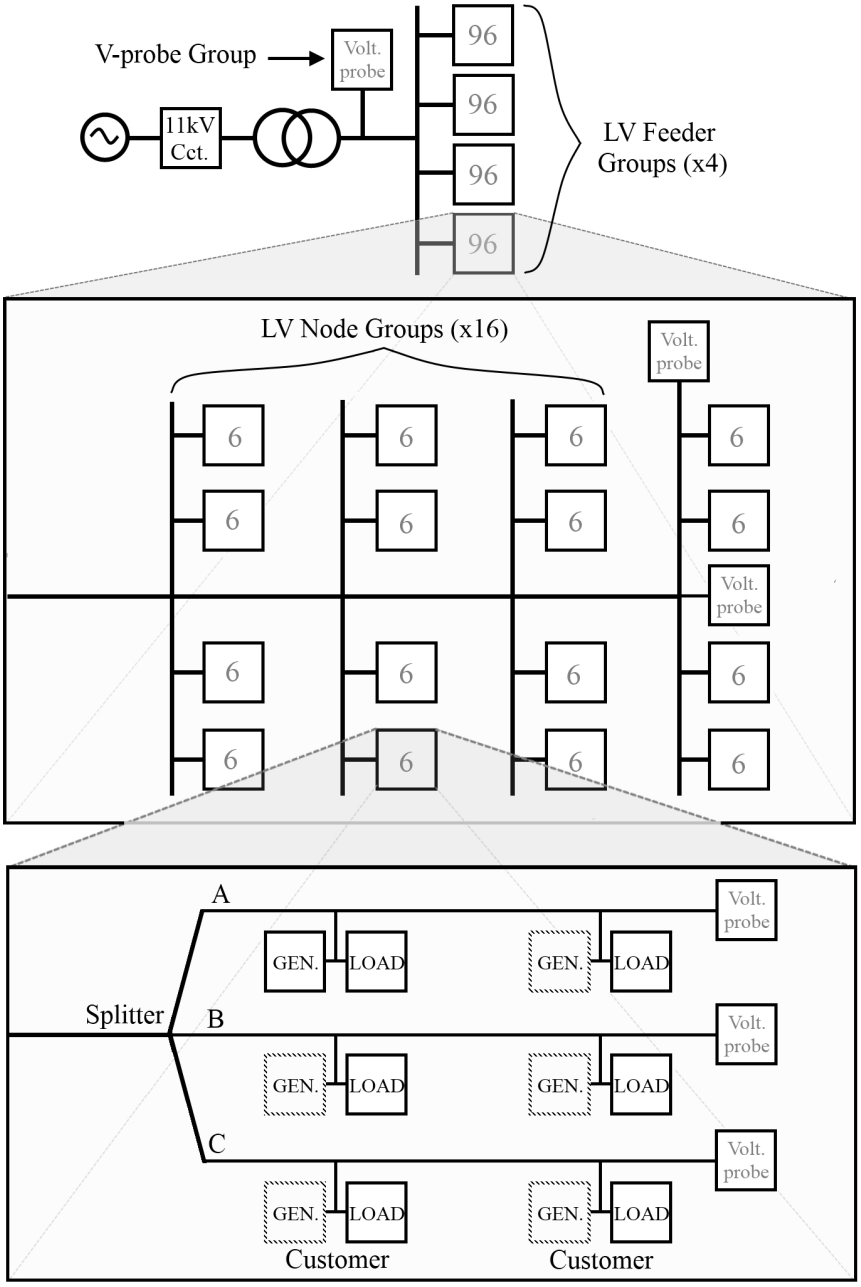

Figure 6.4: ATPDraw Hierarchical Group Structure

allowable limit of 10,000, and indeed some further aggregation of consumer loads has been necessary in order to obtain a functional 50% ρ_g model.

6.1.3 Consideration of Solution Efficiency

The inherent complexity of models for the purpose of cumulative generator impact studies means that significant computational power is required in order to generate a statistically significant number of results. It is desirable, therefore, that the time step be as large as possible without compromising the solution accuracy, and also that the extent of the solution time window be minimised.

Node and branch economy is achieved by modelling the consumer as a single lumped equivalent RL load connected directly to the single-phase service line of the LV network. The short 12m lengths of cable that appear in the generic domestic model of Chapter 5 are omitted here, being replaced by small equivalent series resistances. The shortest travel time of the model becomes that of the 25m service line, and the maximum permissible time-step is doubled accordingly.

This economy is partially negated by the need to accommodate switching operations on all three phases. As such, the solution time window has to be extended relative to the single phase case by $\frac{2}{3}$ of a cycle in order to guarantee that transient waveforms in phases B and C are correctly recorded. The resulting solver setup requires a time step Δt of 40ns for simulation over a window T_{max}=60ms for a total of 1.5 million data points per voltage or current probe.

6.1.4 Switch Control

While the specification of master-slave switching arrangements is straightforward for single generator studies, switch control becomes considerably more complex in scenarios involving multiple sources. Ideally, each generator in the system would have its own independent master-slave arrangement, but the number of independent switches allowed in any one study is limited by statistical practicality to five [165]. Since as many as 192 generators split across three phases are to be simulated at the same time, an elaborate arrangement of slave switch control paths must be employed.

Selecting one generator in phase A of the first feeder as a master, each other generator becomes a slave unit with a delay term determined by the phase arrangement of that generator (A=0ms, B=6.667ms, C=13.333ms). In this way, the switch time distribution of the first closing pole of each disconnector is maintained, but a small offset is introduced in each case, dependent on the actual closing time of the master switch. Since the standard deviation of this offset is very small, being equal to the standard deviation of the master switch pole, this arrangement may be deemed an acceptable approximation to coincident independent switching behaviour. The arrangement of switch delay paths is depicted in Figure 6.5

6.1.5 Simulated Urban Single Feeder

The completed single LV feeder model is depicted in Figures 6.6 and 6.7. By limiting the model extent to only one feeder, 96 customers may be represented explicitly, each with its own incoming service cable.

6.1.6 Urban LV Network - *Four* Feeders

As discussed, the object limits of ATPDraw become prohibitive for very large models and as a result a complete 4-feeder model cannot simply be generated using carbon copies of Figure 6.6. The LV node groups in this case are simplified by lumping each customer phase-pair into a single equivalent load at the terminal of a 50m service cable as depicted in Figure 6.8. In this way, all four feeders may be represented as shown in Figure 6.9.

6.1.7 Generic Rural Network

In order to assess the cumulative impact of generators in rural networks, it was necessary to also develop a representative rural LV circuit. In the absence of an established reference network model, a topology based on that of the generic UK LV network was adopted, but with a geographic load density around one tenth that of the urban network, as in [92]. The network itself is a single feeder arrangement constructed using aerial bundled conductor (ABC) cable models in 35, 70 and 120mm^2 CSA, suspended in 50m spans from 9m tall wood poles as recommended by DNO planning guidelines [158].

The rural LV feeder structure is depicted in Figure 6.10, while Figure 6.11 is the

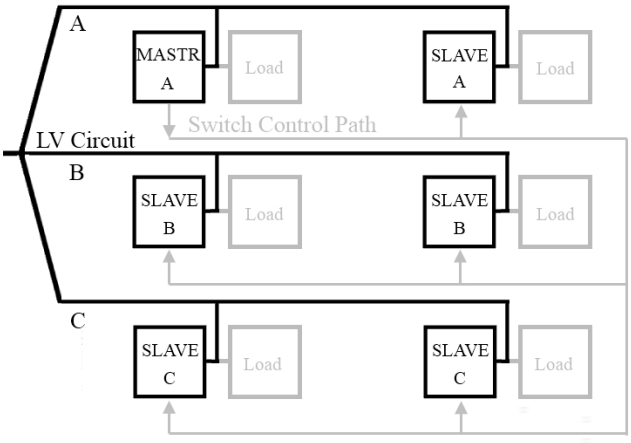

(a) Single LV Node (6 Customers)

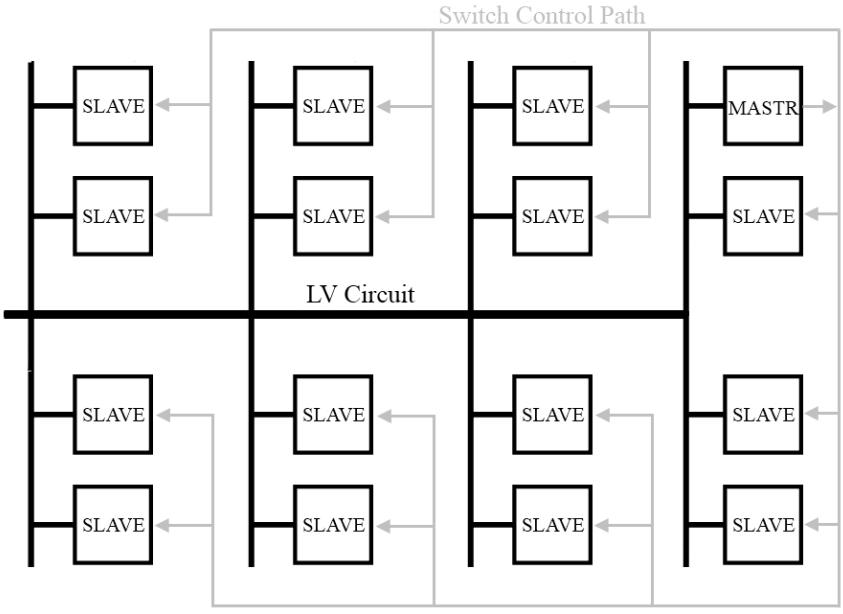

(b) Whole Feeder (16 LV Nodes)

Figure 6.5: Master-Slave Generator Switching Arrangement and Delay Paths

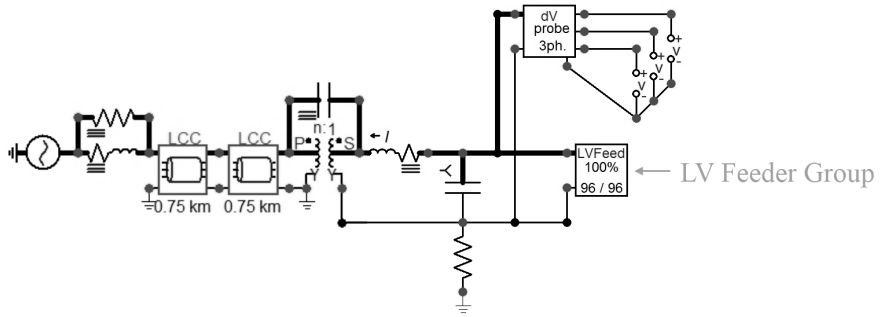

(a) Tier 1 - Network Source and 11/0.4kV Transformer)

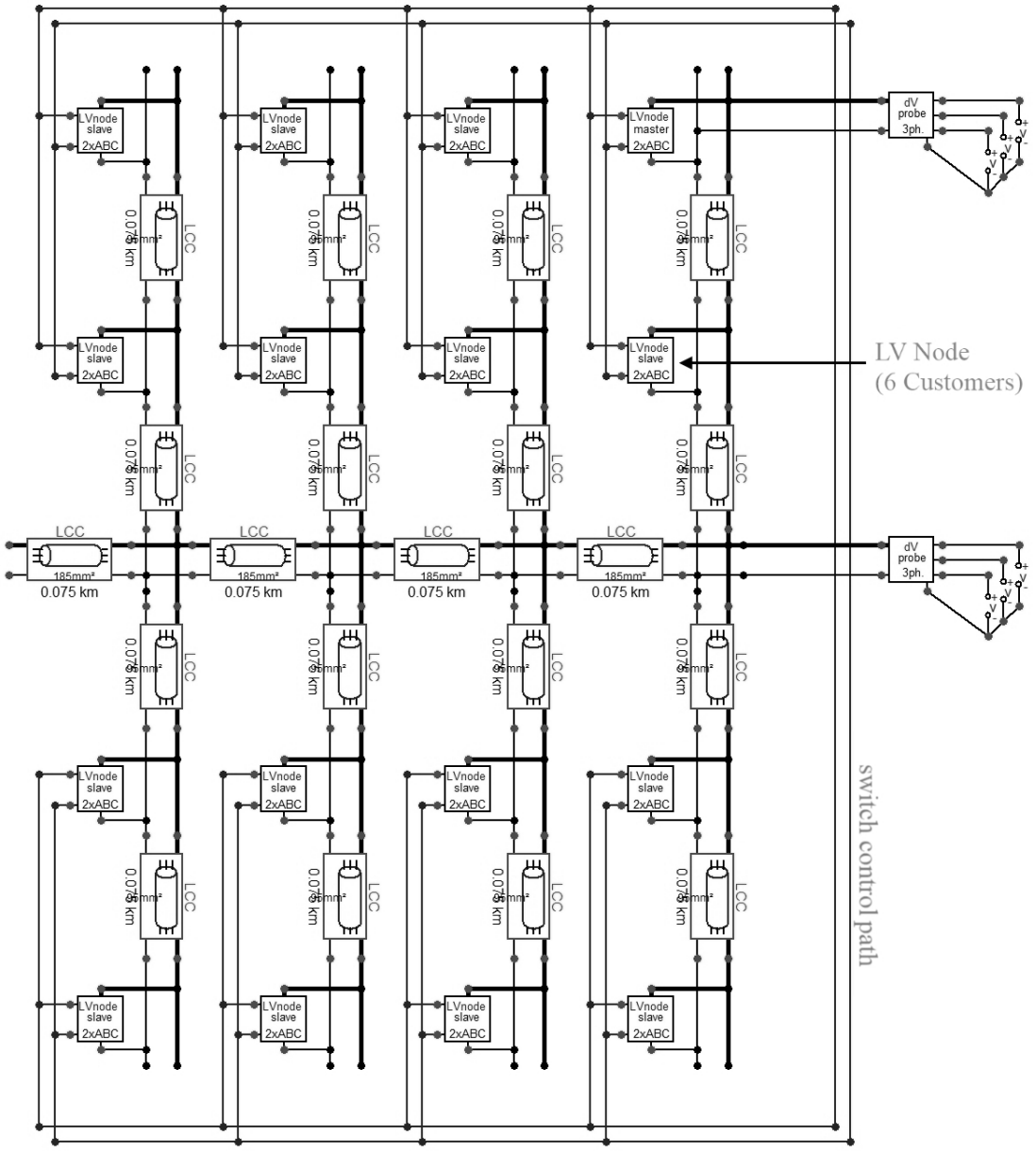

(b) Tier 2 - LV Feeder with 16 Nodes

Figure 6.6: EMTP Single Feeder Model - Tiers 1 and 2

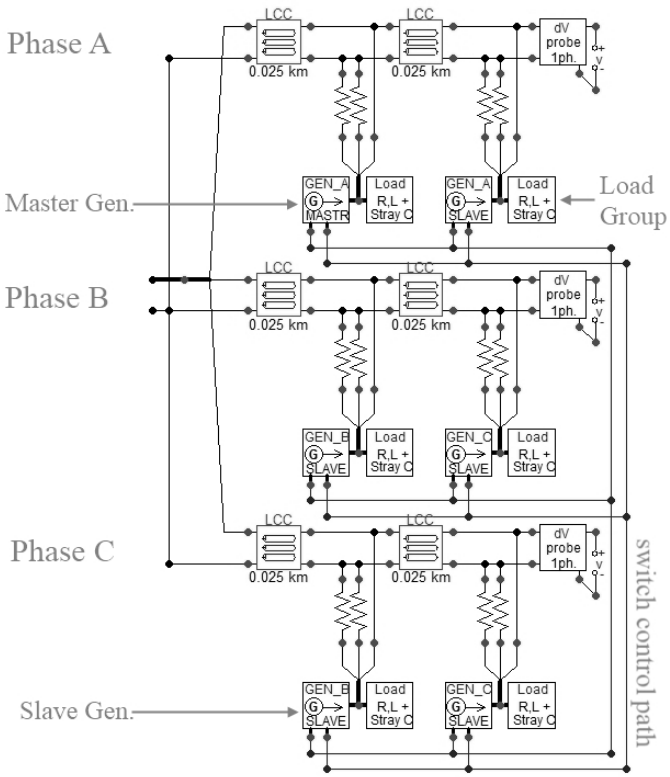

Figure 6.7: EMTP Single Feeder Model - Tier 3 - 6 Customer Nodes

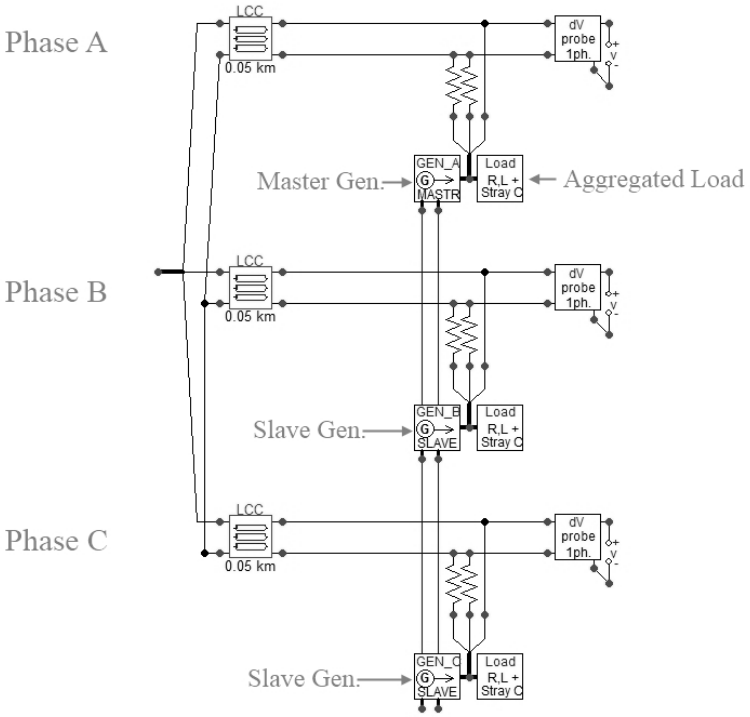

Figure 6.8: EMTP *Four* Feeder Model - Reduced Tier 3 Group

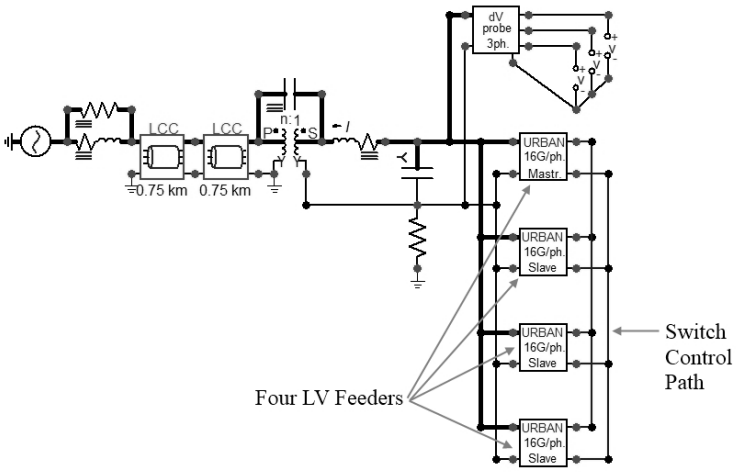

Figure 6.9: Generic LV Distribution Model in EMTP

same network topology as it appears in ATPDraw. Higher resolution EMTP feeder model images for both the urban and rural circuits are reproduced in Appendix D for clarity.

6.2 Simulation Scenarios

Using the generic LV (Urban) and rural network models developed in section 6.1, it is possible to estimate the magnitude and attenuation of switching transients occurring in a typical LV network due to increasing penetrations of small-scale embedded generation. The following section outlines the considered scenarios.

6.2.1 SSEG Penetration

Considering a single feeder supplying 96 evenly distributed customers, six penetration scenarios have been considered, assuming a balance of customer installations among LV bus phases A,B and C. The author recognises that, given the consumer-driven nature of new microgeneration projects, uniform distribution of sources is unlikely to occur, at least for initially low ρ_g. Moving to higher SSEG adoption, the constraints imposed by voltage unbalance associated with phase-bias [22] will likely force DNOs to favour new connection applications where some degree of balance restoration will result. As an example an LV feeder with multiple generators on phase A alone shall have very little capacity for new connections on said phase until ρ_g in phases B and C has been increased.

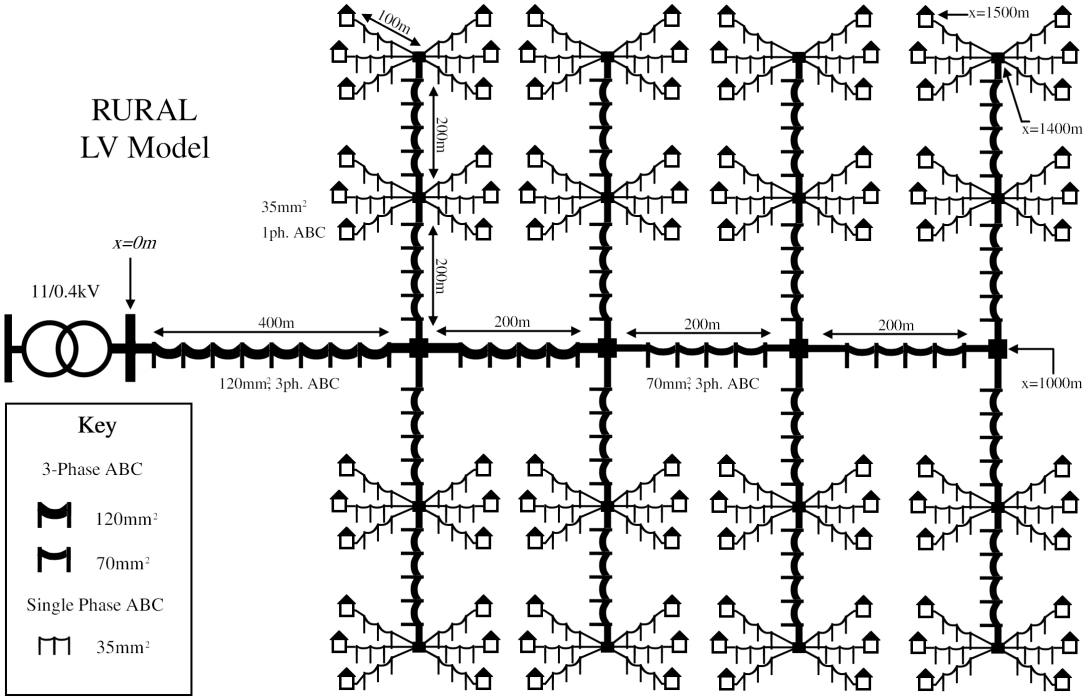

Figure 6.10: Rural Network Topology

As a result, the distribution of SSEGs among the phases of a typical LV feeder should become increasingly balanced as the overall ρ_g increases. A uniform distribution of generators thus becomes a more reliable estimate of SSEG adoption patterns for high penetration cases. Table 6.9 summarises the six uniform generation scenarios considered here.

Table 6.9: SSEG Adoption Scenarios for EMTP Simulations

SSEG Adoption	Generators per Feeder Phase	Total
Very Low	1	12
Low	2	24
Moderate	4	48
High	8	96
Very High	16	192
100%	32	384

Splitting a generic LV network feeder into sixteen zones, the six penetration scenarios may be summarised pictorially using the simplified topography of Figure 6.12. Each block represents a single LV node, feeding 6 customers, as modelled in Figure 6.6. The number within a individual block then simply represents the per-phase penetration

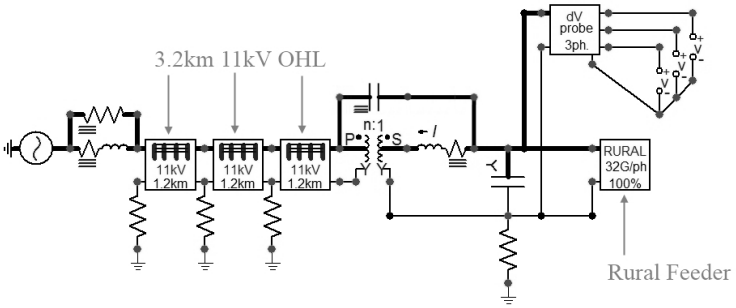

(a) Tier 1 - Network Source and 11/0.4kV Transformer)

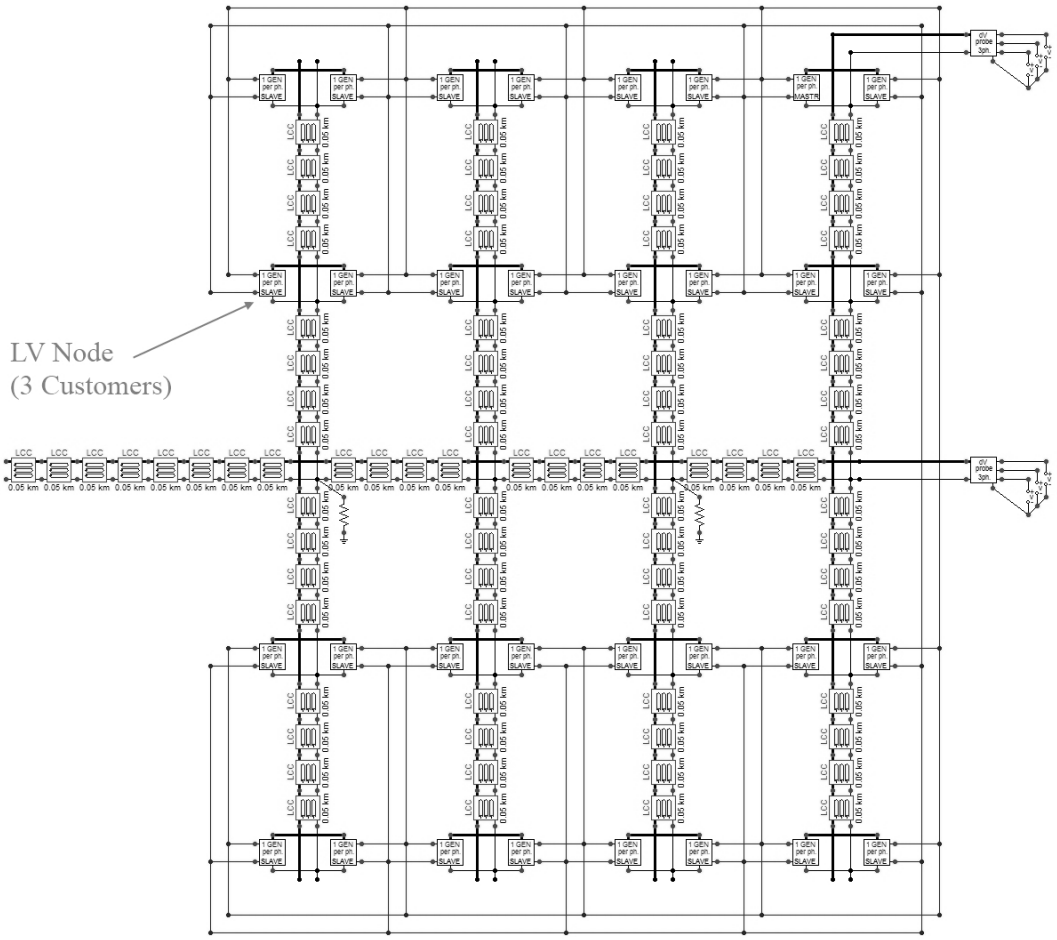

(b) Tier 2 - LV Feeder with 32 Nodes (Three Customers per Node)

Figure 6.11: EMTP *Rural* Feeder Model

for for that LV node (max. 2 generators/phase for a total of 6). A similar pictorial representation may be seen in Figure 6.13 for the thirty-two customer groups of the rural equivalent network (Figure 6.11). A different notation is used here as only one customer is supplied per single-phase service line in the rural case, halving the size of a customer grouping to 3. An empty block in both cases indicates that no SSEG feeds that LV node (load only).

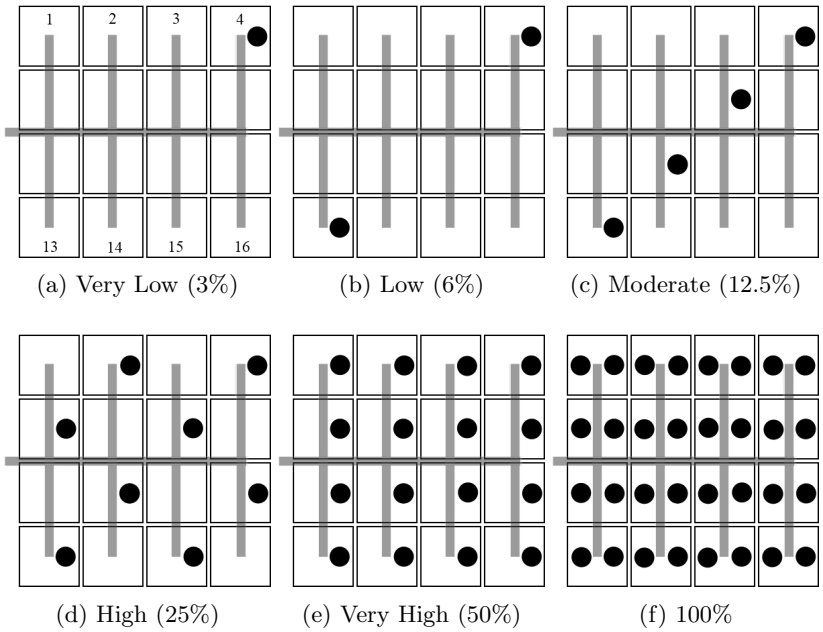

(a) Very Low (3%) (b) Low (6%) (c) Moderate (12.5%)

(d) High (25%) (e) Very High (50%) (f) 100%

Figure 6.12: Urban Feeder Penetration - 16 LV Blocks of 6 Customers Each (2 Customers per Phase, dot indicates presence of 1 SSEG per phase at a node)

6.2.2 Customer Load

Customer load is assumed to be uniformly distributed throughout the network, with each customer modelled as a series linear RL branch based on average domestic load power factor, with shunt stray capacitance of a few tens of picofarads. No diversity in the load is taken into account here. Maximum and minimum load conditions are defined as in Chapter 5 to be 160VA and 1300VA respectively, and a third *typical* load of 500VA is arbitrarily defined. A no-load condition is also considered in order to define the lower limits of statistical current distributions for each ρ_g case. Load configurations are summarised in Table 6.10.

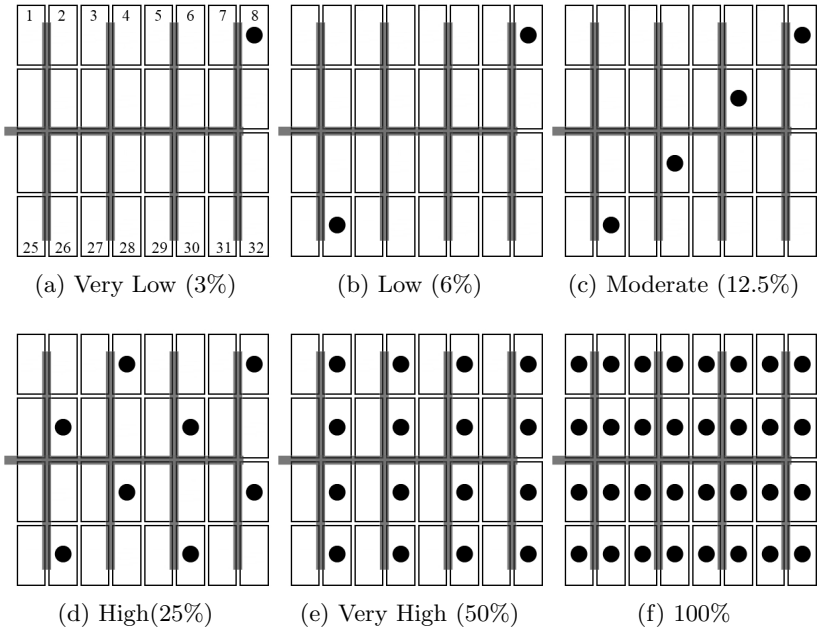

(a) Very Low (3%) (b) Low (6%) (c) Moderate (12.5%)

(d) High(25%) (e) Very High (50%) (f) 100%

Figure 6.13: Rural Feeder Penetration - 32 LV Blocks of 3 Custmers Each (1 Customer per Phase, dot indicates presence of 1 SSEG per phase at a node)

Table 6.10: Consumer RL Load Configurations for Network Models

Condition	Load VA	$Cos(\theta)$	Feeder kVA
Minimum	160	0.95	15
Typical	500	0.95	48
Maximum	1300	0.95	125
No Load	1	1	0.1

6.2.3 Voltage and Current Probes

Four sets of voltage probes are connected at various points throughout the LV network models in order to detect the magnitude of voltage perturbations due to generator switching events. Each voltage probe is connected into the circuit via a notch filter based on that used in [80], to remove any fundamental power frequency component from the results. The positions of the measurement blocks relative to the 500kVA transformer LV bus ($x = 0$) are summarised in Table 6.11. In both cases, *Block 1* is located at the transformer LV terminals, while *Block 4* is a set of single phase probes connected to the most remote consumer bus in each phase (see Figures 6.6, 6.7 and 6.11)

Table 6.11: Voltage Measurement Block Positions

Model	Volt Probe Position			
	Block 1	Block 2	Block 3	Block 4
Urban	$x = 0m$	$x = 300m$	$x = 450m$	$x = 500m$
Rural	$x = 0m$	$x = 1,000m$	$x = 1,400m$	$x = 1,500m$

Current probes are located on the LV winding of the 11/0.4kV transformer to measure the peak cumulative inrush current drawn from the grid due to coincident switching operations.

6.2.4 Solution Time

For any statistical simulation study, the processing requirements are heavily dependent on the number of non-concurrent switching operations, and as a consequence the total solution time shall depend on the penetration scenario being considered. Using a time step of 40ns over a window of 60ms, solution times of 250-case statistical studies were found to increase with ρ_g from 10 to 72 hours on a typical laboratory workstation (2.8GHz dual core, 3GB RAM).

6.3 Simulation Results

The following section summarises the results obtained from simulations of each of the outlined generator/load scenarios. Statistical data is generated from data sets, each consisting of 250 repeat cases with switch closing and delay times statistically distributed in the same manner as in Chapter 5. Results are presented by network topology, starting with the urban single feeder model and progressing to the generic four-feeder and rural models.

6.3.1 Urban Single-Feeder Model

6.3.1.1 Current Transients (Urban Feeder)

The plot in Figure 6.14a shows the statistical distribution of peak currents measured at the LV terminal of the 500kVA transformer. A normalised combined data set of all three phases (750 results per curve) is plotted. Only the no load and maximum load conditions are shown here to avoid overlapping ranges, and the lowest ρ_g scenarios are omitted for clarity. The dashed vertical line at approximately 245A marks the phase

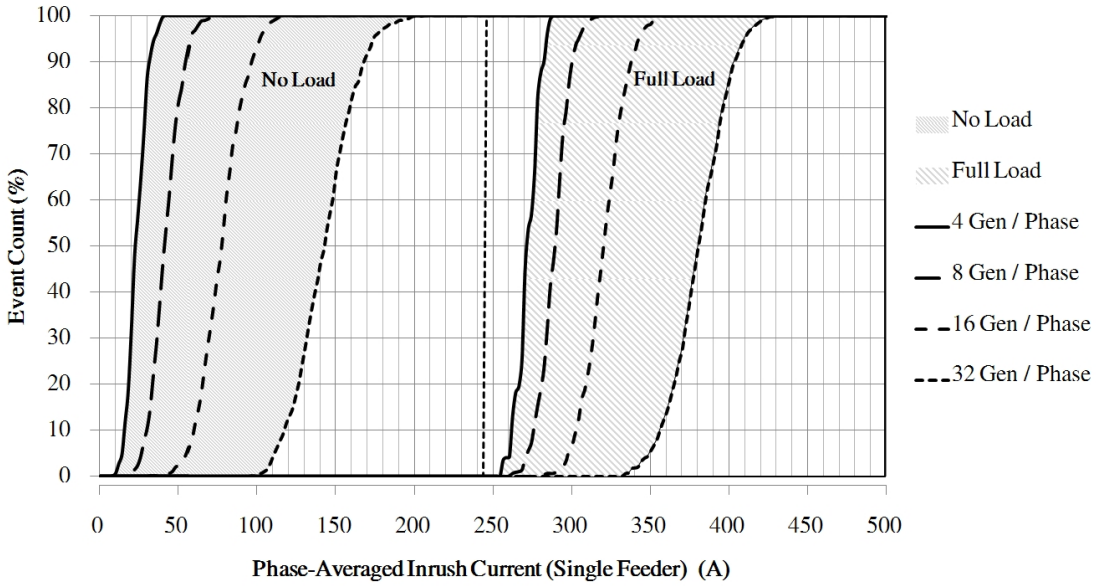

(a) Statistical Distributions of LV Bus Peak Current by SSEG Penetration (All Phases)

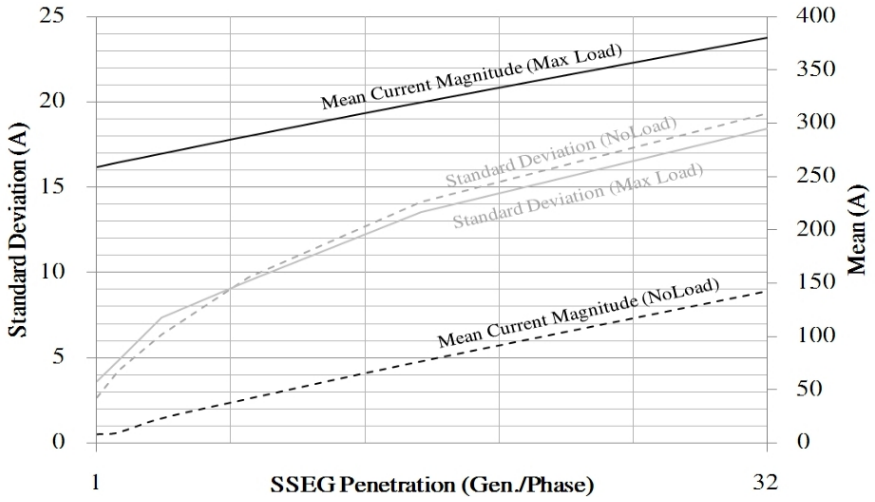

(b) Dependence of Inrush Current Statistics on Generator Count.

Figure 6.14: Cumulative Network Inrush Currents - *Urban* Feeder

current amplitude under maximum load condition with no SSEG (assuming the supply voltage to be approximately $240V_{rms}$), and forms the a base line for that condition, much as $I = 0A$ forms the base line for the no load case.

It can be seen that for a given load scenario, an increase in the number of concurrent SSEG switching operations leads to an increase in the mean current magnitude above the base line. This is a linear relationship as can be seen from Figure 6.14b. By contrast, the dispersion of peak current distribution displays a square-root proportionality with ρ_g.

$$\overline{I_{pk}} \propto \rho_g \qquad \sigma_{I_{pk}} \propto \sqrt{\rho_g}$$

It is also noted that the deviation, skew and kurtosis of current distributions are all independent of the pre-existing load condition. Thus current distributions in the full load case are the same as at no load, but offset by a value equal to the phase load current amplitude (245A in this case). Given that the magnitude of the inrush for each generator is governed by a current limiting resistance, such behaviour is to be expected if one assumes an invariant bus voltage.

6.3.1.2 Voltage Transients (Urban Feeder

Figure 6.15 shows how the transient voltage magnitudes at the extreme ends of the LV feeder are related to ρ_g on said feeder under a no-load condition. The lower of the two solid black lines depicts the mean voltage transient magnitude (ΔV) at the transformer 400V bus. The same measure is also plotted for a remote customer bus ($x = 500m$) with an installed SSEG unit.

Simulated data ranges are indicated for both by means of greyed area plots bounded above and below by 5^{th} and 95^{th} percentiles. For ρ_g in excess of 4 units per phase (12.5%), some crossover of these ranges occurs. The grey dotted line is the envelope of maximum ΔV from all 250 repeat cases at at any feeder location.

A linear relationship exists between $\overline{\Delta V}$ and the number of concurrently switched generators (n_g) in a given phase, though voltage magnitudes themselves remain very low even in the worst case. For the highly improbable scenario in which all generators on an LV feeder with $\rho_g = 100\%$ happen to switch on the same cycle, the magnitude of the voltage perturbation is unlikely to exceed ±40V (0.125 pu) at any point on the feeder. The distribution of peak voltage along the line for two penetration scenarios is plotted in Figure 6.16.

In contrast to the linearly decreasing profiles of the single-phase cases of Chapter 5, voltage profiles obtained from cumulative impact study suggest a far flatter response, particularly in the highest penetration scenarios. The combined effect of concurrently switched but spatially dispersed generators serves to boost transient voltage magnitudes

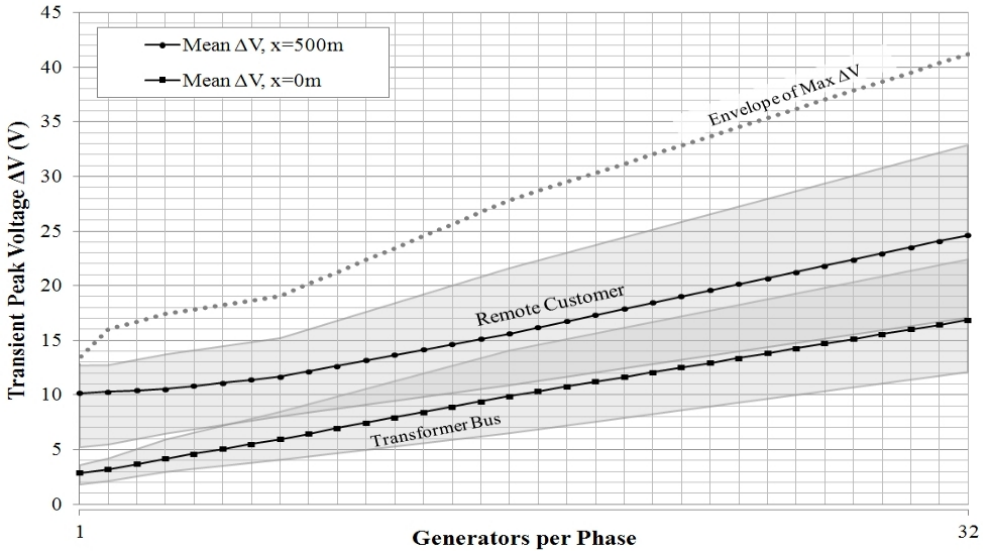

Figure 6.15: Transient Voltage Magnitude at Transformer and Customer Buses as a Function of SSEG Penetration, Single Urban Feeder, No Load (All Phases)

near to the LV transformer to a greater degree than those a the customer supply point. This is primarily due to the successive reduction of inrush current in each cable stage as circuits tee off the main trunk. A broad spread of results is still observed, however, in the region bounded by the 5^{th} and 95^{th} percentiles, with this range widening with distance from the transformer terminals. This is in agreement with the results of Chapter 5 (Section 5.4.1).

A theoretical maximum ΔV can be said to occur when inrush inception for all generators on a given feeder occurs simultaneously. A timed switch equivalent urban feeder model has been constructed to demonstrate this case. Current inrush inception is taken to occur at $\theta_i = 90^{\circ}$ (voltage maximum). The simulated theoretical maximum voltage profile is plotted alongside the statistical data of Figure 6.16.

It is clear that time-dispersion of switch pole closing and inrush inception greatly limits the maximum transient voltage magnitude that can be expected to occur on each disconnect/reconnect cycle. Voltage maxima with statistically determined inrush inception are consistently reduced to 35-40% of their theoretical maxima along the full length of the feeder.

Theoretical maximum ΔV profiles are plotted in Figure 6.17 for the four penetration scenarios (12.5 - 100%), indicating a linear dependence of theoretical ΔV_{max} on ρ_g. It

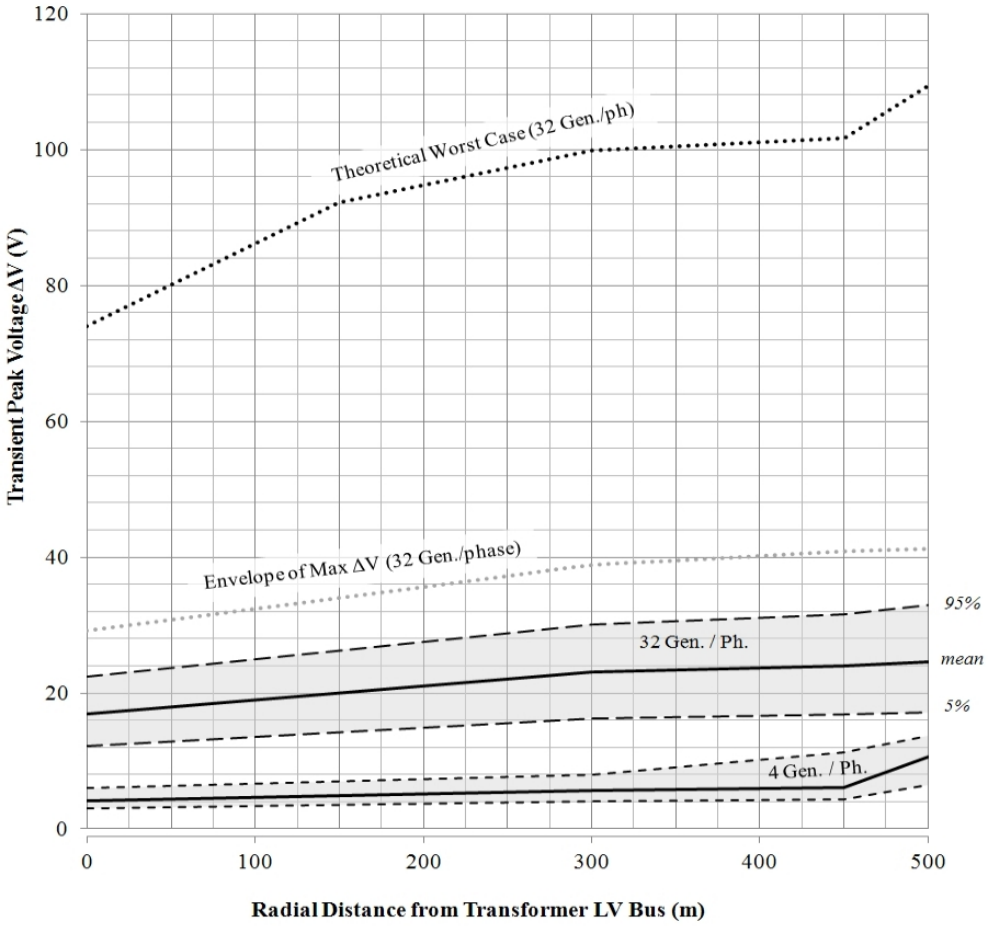

Figure 6.16: ΔV Profile for Different Penetration Scenarios, Single Urban Feeder (All Phases)

is interesting to note that the angle of generator inrush inception is itself dependent on the state of charge on the DC bus capacitor prior to switching. Since all generators on a feeder are assumed to have initially disconnected in response to a common stimulus, be it overvoltage, frequency deviation or temporary loss of mains, the expected variation in charge states of the DC bus capacitor for equally rated devices will not be great.

It is hypothesised that the statistical distribution of θ_i for a group of generators will in reality occupy a narrower range than that assumed in this study, and that truly representative voltage maxima shall lie in the region bounded by the dotted lines of Figure 6.16. Confirmation of this hypothesis will require exhaustive field testing on an LV feeder with high SSEG penetration, and is proposed for future work.

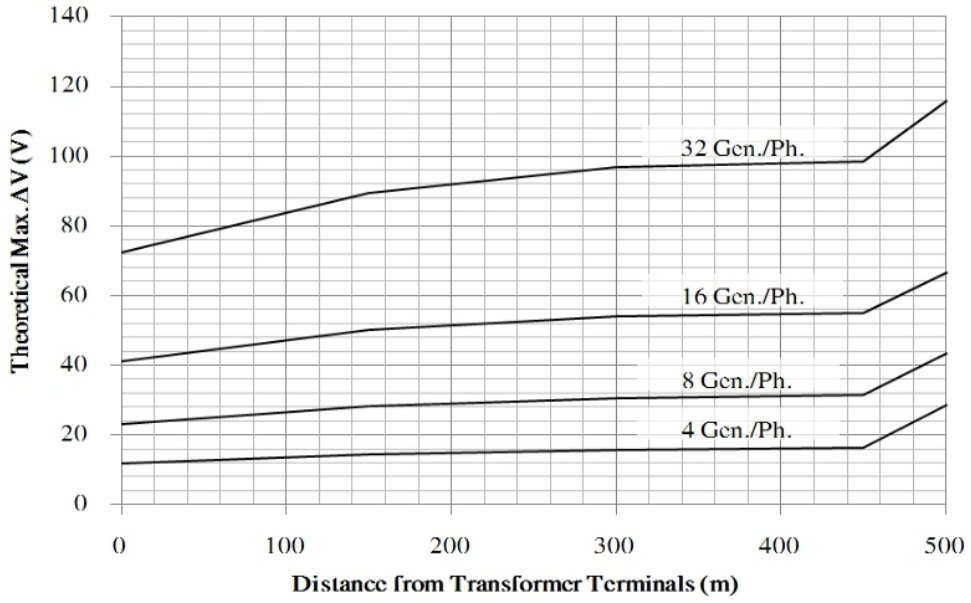

Figure 6.17: Theoretical Maximum ΔV Under No-Load Conditions

6.3.2 Generic UK LV Model

The analyses of section 6.3.1 have been repeated for the four feeder case. As explained earlier in this chapter, the highest SSEG penetration scenario investigable using the 3-phase statistical switching model is 50%, due to the limitation on object counts imposed by *ATPDraw*.

6.3.2.1 Current Transients (Generic UK LV)

The statistical distributions of phase peak inrush current, as measured at the LV terminals of the 500kVA transformer, are plotted in Figure 6.18 for three distinct load scenarios. As with the single feeder model the effect of the existing load condition on a particular current distribution is to shif it to the right by an amount equivalent to the steady-state current amplitude.

In this case, however, some compression of the current range is observed for the maximum load case as the customer bus voltage is pulled down. The effect of a lower generator terminal voltage v_g is to reduce the magnitude of the inrush current for a given current-limiting resistance R_{LIM}. Under low-load conditions, v_g may conversely be expected to rise above the nominal, thus increasing the expected inrush magnitude.

$$|i_{inr.}| \approx \frac{v_g(\theta_i)}{R_{LIM}} \tag{6.6}$$

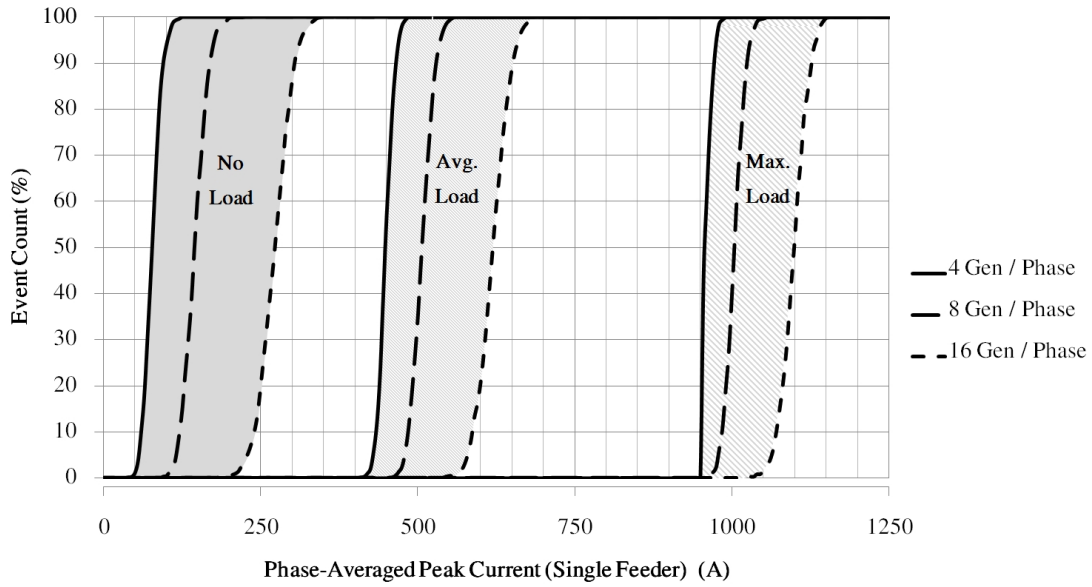

Figure 6.18: Statistical Distributions of LV Bus Peak Inrush Current by SSEG Penetration, Full Generic LV Network (All Phases)

For an allowable customer voltage regulation of 230V -6%/+10%, a theoretical maximum cumulative phase inrush current magnitude for a four-feeder network under minimum load is 1.316kA (assuming $R_{LIM} = 33\Omega$ for each source). Inrush current is reduced to 1.186kA under heavy load, though this is in addition to a peak load current background of 1.02kA.

6.3.2.2 Voltage Transients (Generic UK LV)

Figure 6.19b illustrates the effect of SSEG penetration level on expected transient voltage magnitudes in an urban LV network. As in the single feeder case, there is a broadly linear relationship between ρ_g and $\overline{\Delta V}$ at the transformer bus. An elevation of mean voltage is observed with increasing radial distance from the transformer terminals, but average values remain below 40V for ρ_g=50%.

The effect of time dispersion in switch and inrush inception is visible from the maximum voltage envelope, with the worst case from a statistical study of 250 cases being around 55V.

Since a 100% penetration model is unavailable, an indicative phase-biased generation model with SSEG concentrated on phase A only ($\rho_{g\ A}$=100%, $\rho_{g\ B}$=$\rho_{g\ B}$=0) was constructed for the purpose of identifying the worst case ΔV attributable to each

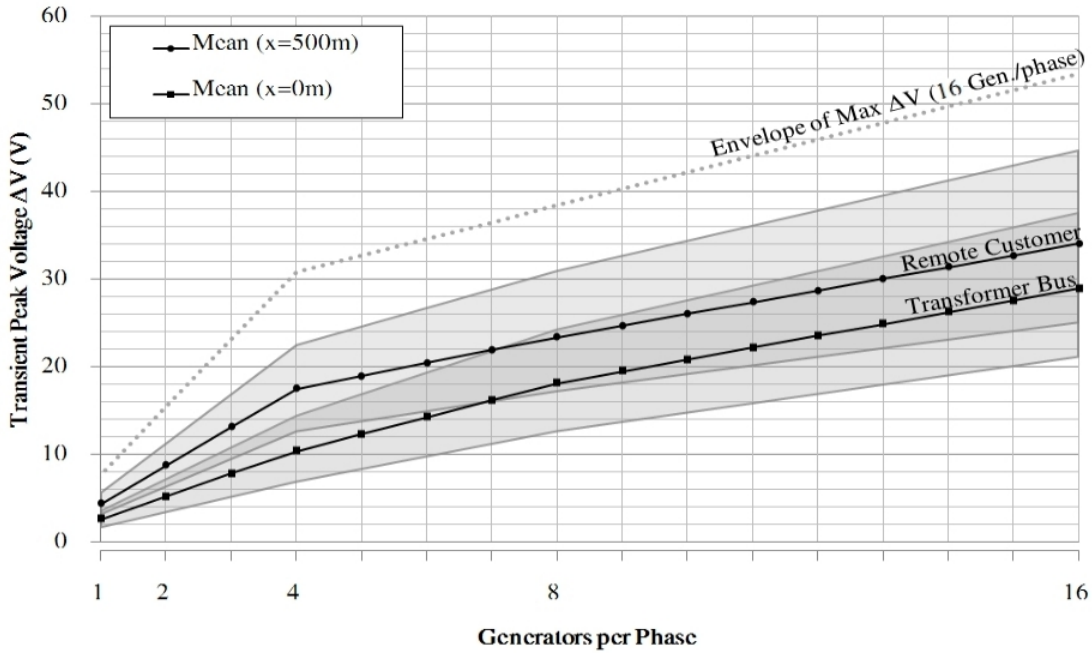

(a) Transient Voltage Magnitude at Transformer and Customer Buses by SSEG Penetration(All Phases)

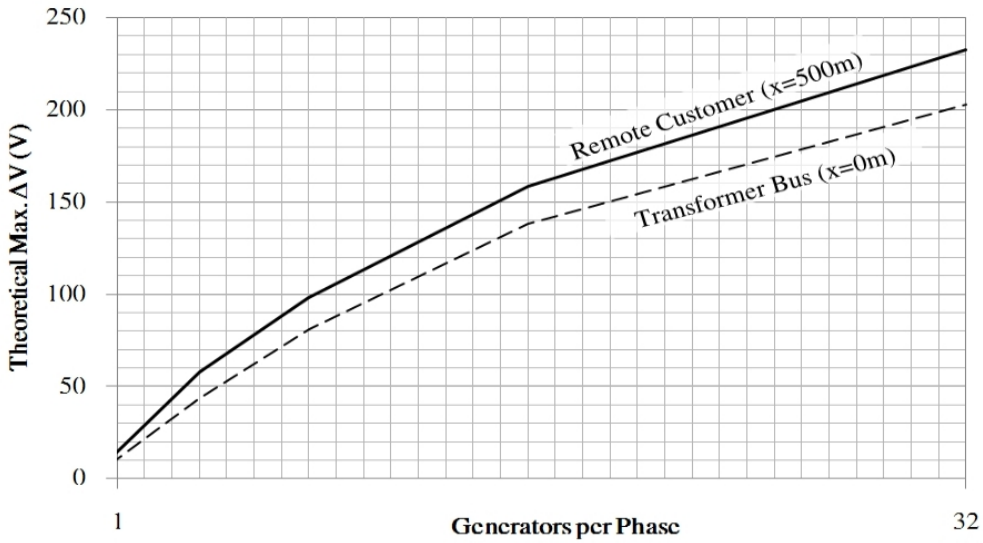

(b) Theoretical Maximum ΔV by SSEG Penetration

Figure 6.19: Effect of SSEG Penetration on Transient Voltage - *Generic LV* Model

penetration scenario. The results of this model are depicted in Figure 6.19b, indicating a theoretical maximum consumer bus ΔV of 230V under a 100% ρ_g scenario. This is reduced to approximately 160V for ρ_g=50%, a roughly three-fold increase relative to the upper ΔV envelope of Figure 6.19a. Dispersion of θ_i can, therefore, be said to have a greater limiting effect on transient voltage magnitude as the extent of the simulation network increases.

Feeder voltage magnitude profiles for the generic LV network are shown in Figure 6.20a for two ρ_g scenarios (12.5 and 50%). Continuing the trend of the single feeder model, the peak voltages observed along the main LV trunk are nearly constant as the cable impedance is inversely related to its current handling capacity. This may be contrasted with the linearly position-dependent voltage profile associated with an individual generator - see Chapter 5 (Section 5.4.1). Some attenuation is observed, however, across the single phase service cable between consumer and adjacent LV node (last 50m).

Figure 6.20b in turn depicts the theoretical maximum voltage profiles generated from a coincident timed switch model ($\theta_i = 90^\circ$). As with the single phase feeder model, it is anticipated that field testing on a real network will generate ΔV profiles lying between the values of Figures 6.20a and 6.20b.

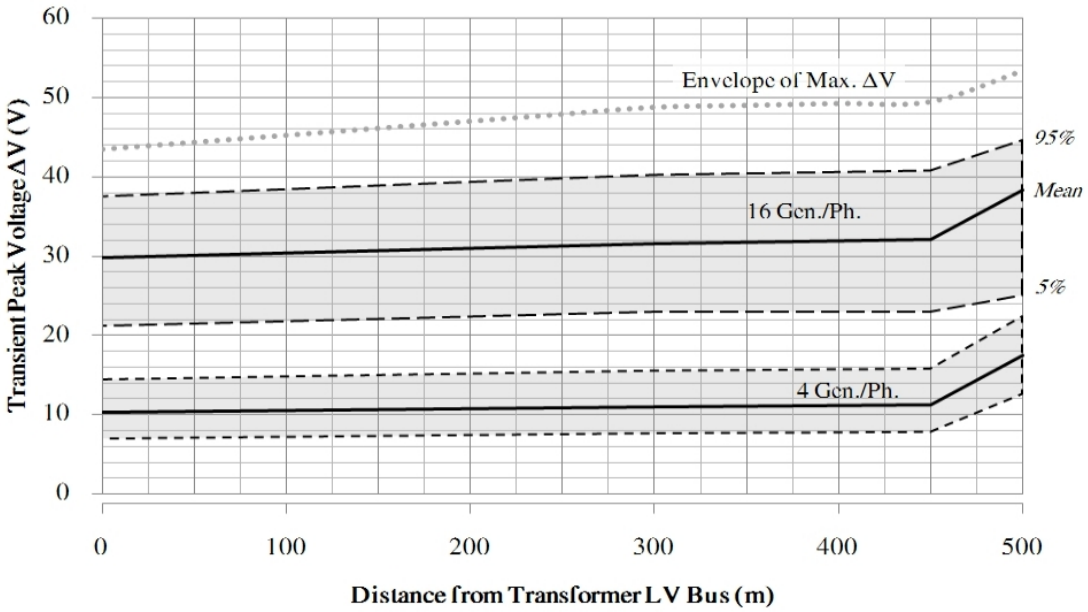

(a) Transient Voltage Magnitude Profiles (All Phases)

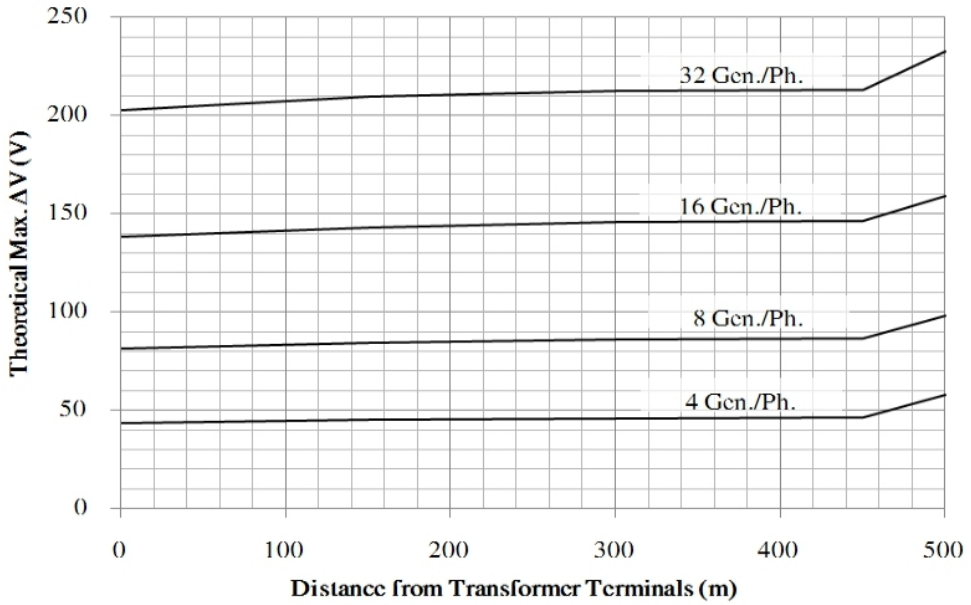

(b) Theoretical Maximum ΔV Profile Under No-Load Conditions

Figure 6.20: Voltage Transient Magnitude Profiles - *Generic LV* Model

6.3.3 Rural LV Feeder

A number of distinctions have been observed between transient propagation characteristics in the urban and rural networks. A discussion of results obtained with the single *generic* rural feeder model follows.

6.3.3.1 Current Transients (Rural)

Cumulative phase current distributions as measured at the LV transformer terminals are consistent with those of the single urban feeder model. A minor reduction in peak current and narrowing of the current range at full load are both attributable to the increased series impedance of the network relative to the urban case. Normal load current amplitude for the full load case is indicated by the vertical dashed line of Figure 6.21.

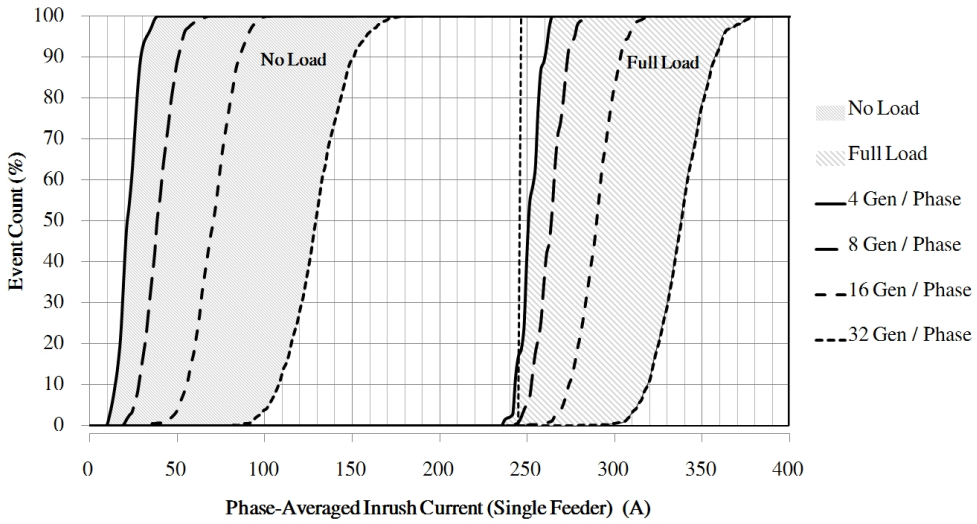

Figure 6.21: Statistical Distributions of LV Bus Peak Inrush Current by SSEG Penetration, Rural Feeder (Per-Phase)

6.3.3.2 Voltage Transients (Rural)

Figure 6.22 shows how the concentration of embedded generation within a rural network impacts upon expected voltage transient magnitudes at different feeder locations.

The first distinction between the rural and urban results is in the measurement location giving rise to the worst case ΔV. In an urban network, the most severe transient voltage magnitudes are observed at the remote customer bus. The rural network by contrast gives rise to a maximum ΔV at the adjacent LV node (x=1400m),

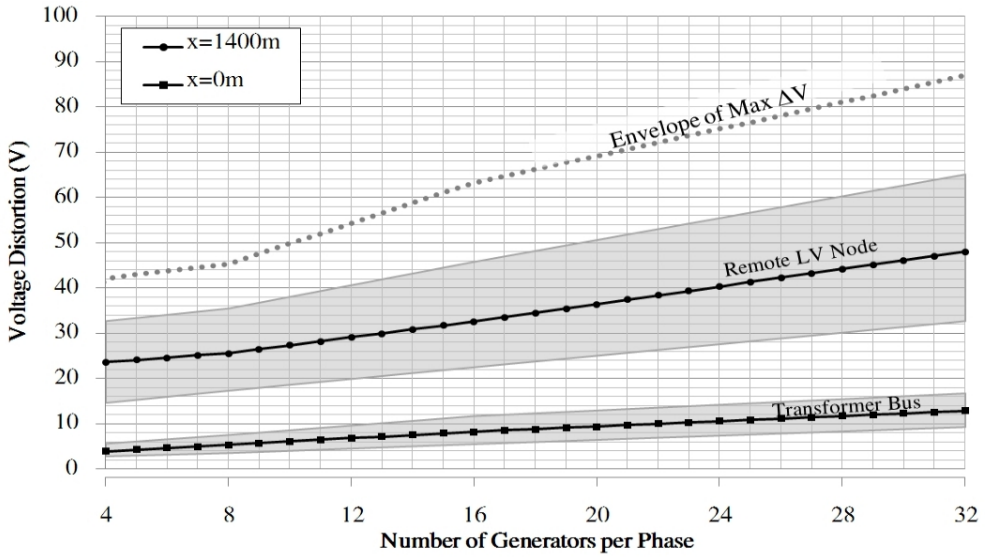

Figure 6.22: Transient Voltage Magnitude at Transformer and Customer Buses as a Function of SSEG Penetration, Rural Network (All Phases)

as is visible from Figures 6.23a and 6.23b.

Mean voltage transient magnitudes at the LV node are approximately 50V for 100% ρ_g, approximately twice their equivalent values from the urban case. ΔV at the same location for ρ_g=50% (16 generators/phase) is equivalent to that of the generic LV model under the same penetration scenario.

Of note is the greatly reduced transient magnitude at the transformer terminals. It is clear that attenuation of SSEG-induced switching transients is greater in the overhead rural circuit than in the underground urban network, due to the combined increase in length and series impedance of the 230V circuit. The highest ΔV values are, therefore, confined to the more remote rural nodes. This behaviour may also be partly attributed to the elevated capacitance of underground circuits, though this effect is only marginal as insulated aerial bundled conductors themselves are highly capacitance compared with separated conductors.

The statistical and theoretical maximum ΔV profiles, of Figures 6.23a and 6.23b respectively, indicate that a worst case transient magnitude of 240V occurs at a remote LV node under a 100% SSEG penetration. This is to be contrasted with a 120V maximum observed in the urban feeder model, suggesting that generators switching under ER G83-1 [5] have a greater electromagnetic transient impact on rural feeders

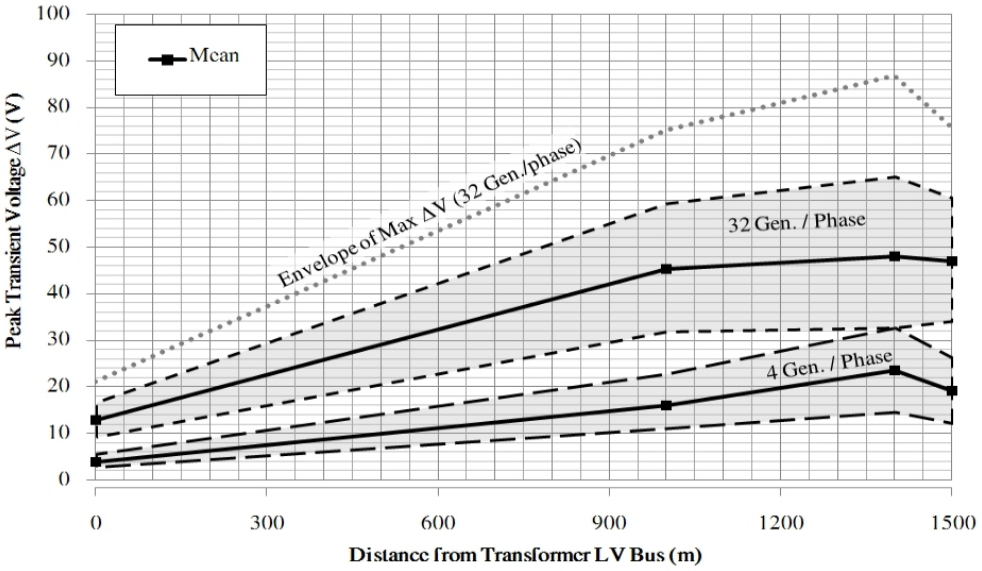

(a) Transient Voltage Magnitude Profiles (All Phases)

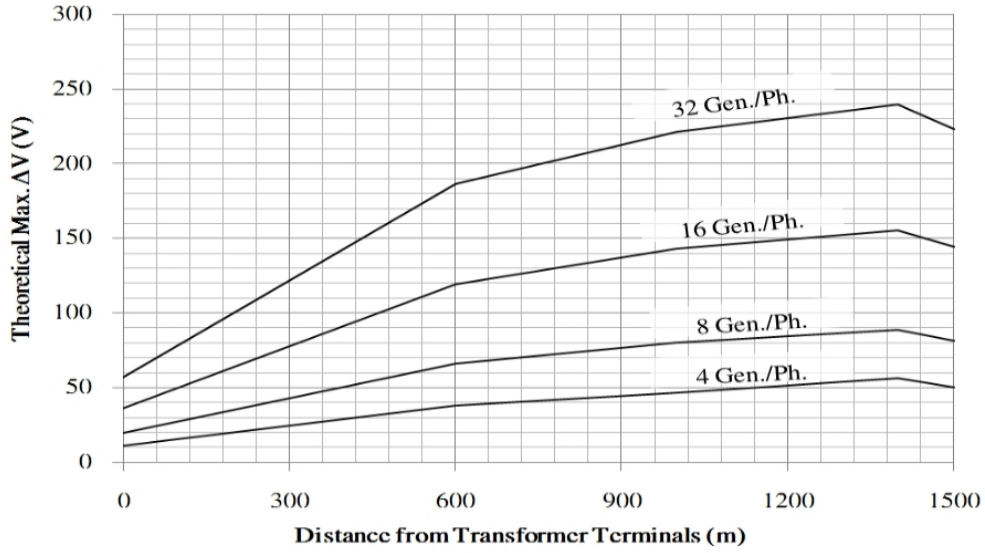

(b) Theoretical Maximum ΔV Profile Under No-Load Conditions

Figure 6.23: Voltage Transient Magnitude Profiles - *Rural* Model

than on an urban network.

6.3.4 Results Overview

Key results of the three simulation studies are collected in Tables 6.12 and 6.13. Mean and 95^{th} percentile values for ΔV from statistical study, and theoretical ΔV_{max} from timed switching, are collectively summarised for a range of ρ_g scenarios.

Table 6.12: Summary of Results - Urban Network Models

		Transformer Terminals			Remote Worst Case		
	ρ_g (%)	$\overline{\Delta V}$	ΔV_{95}	ΔV_{MAX}	$\overline{\Delta V}$	ΔV_{95}	ΔV_{MAX}
Single Feeder	12.5	4.17	5.94	11.83	10.54	13.72	28.64
	25	5.97	8.49	23.19	11.67	15.22	43.52
	50	9.90	14.10	41.11	15.63	21.62	66.55
	100	16.88	22.44	**72.25**	24.63	32.90	**115.68**
Generic LV	12.5	10.35	14.45	43.20	17.48	22.46	58.05
	25	18.12	24.29	81.22	23.36	30.94	98.32
	50	28.93	37.58	138.33	34.05	44.71	158.81
	100	-	-	**202.85**	-	-	**232.80**

Table 6.13: Summary of Results - Rural Network Model

		Transformer Terminals			Remote Worst Case		
	ρ_g (%)	$\overline{\Delta V}$	ΔV_{95}	ΔV_{MAX}	$\overline{\Delta V}$	ΔV_{95}	ΔV_{MAX}
Single Feeder	12.5	3.90	5.63	11.28	23.59	32.71	50.25
	25	5.36	7.52	19.95	25.56	35.50	81.50
	50	8.22	11.67	36.09	32.56	45.82	144.31
	100	12.85	16.68	**56.79**	48.02	65.15	**223.23**

An increase in expected transient voltage magnitude with SSEG penetration has been observed, as predicted in Chapter 5, but the majority of cases have been found to pose little concern from the perspective of overvoltage protection. Theoretical maximum voltage perturbations have been derived for both urban and rural network models, with 100% penetration scenarios yielding worst case values of 232.8V (1.72pu) and 223.23V (1.69pu) respectively. Time-dispersion of switching operations, however, reduces mean transient magnitudes to approximately 25% of the theoretical worst case, such that typical switching transients for even very high penetrations of generators should not exceed some 65V.

At this voltage level, transients due to generator switching would be indistinguishable from the regularly occurring low-magnitude background perturbations recorded by Bull [80] and Goedbloed [81] (see Figure 1.15 on p33). If, as predicted, the frequency of disconnection events was to rise along with SSEG penetration, there would likely be some cause for concern regarding power quality and insulation degradation due to frequently occurring low-magnitude, fast-front switching transients. This aspect shall require further study in order to make any definite conclusions.

6.4 Scenario Probability

The probability that any of the simulated scenarios shall be encountered in practice is of course dependent on the speed with which each generator responds to detection of an abnormal system condition. Engineering recommendation G83-1 [5] requires that generators disconnect within 1 second of over/under-voltage detection (0.5 seconds in the case of over/under-frequency and/or loss of mains). It is anticipated that all generators shall disconnect in a time well within these limits, and a Gaussian distribution of disconnection times is assumed.

If all generators subsequently undergo a homogeneously specified grid monitoring procedure, reconnection times shall occupy a similar distribution, though discretised into 20ms segments by successive positive zero-crossings of the terminal voltage. The number of concurrent switching events on each cycle shall then be proportional to the normalised area under the continuous probability curve for the duration of that cycle. An example is depicted in Figure 6.24 for a group of generators disconencting with a mean time of 250ms, and a standard deviation of pole opening instants of 50ms.

Reconnection occurs after a grid-monitoring time τ_G (assuming that by this time normal voltage/frequency conditions have been resumed), giving rise to the discretised switch distribution on the right hand side. In this case, the maximum proportion of generators switching on the same cycle (effective penetration, ρ_{eff}) should be reduced to approximately 16% of the total penetration.

Taking as an example the 100% penetration scenario in the Generic LV Model, the effective penetration due to such switching characteristics would be reduced from

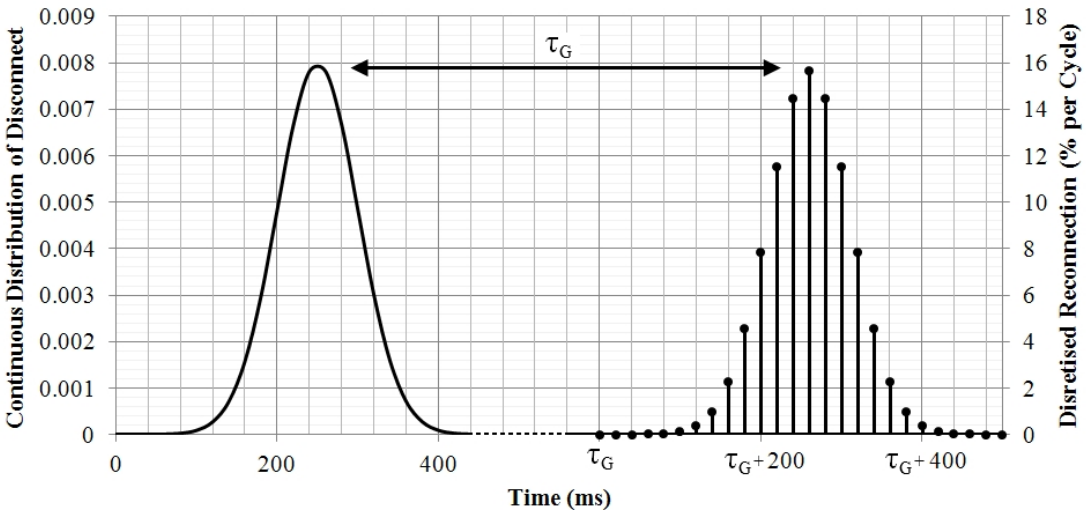

Figure 6.24: Probability of Coincident Switching for a Group of Generators

32 generators per feeder phase to only 5, and in such case the appropriate simulation results for a lower ρ_g shall apply. Though this does not rule out coincident switching of *all* generators, the probability of such an event is significantly reduced, depending on the switching characteristics of each generator.

Table 6.14 summarises the effective penetration ρ_{eff} reconnecting on a single cycle for a group of generators, based on the standard deviation of pole opening times.

Table 6.14: Proportion of Generator Group Switching on One Cycle

σ_{sw} (ms)	20	50	100
Effective Penetration on Median Cycle(%)	35	16	8

6.5 Options for Mitigation

Where switching transients are deemed to problems on LV networks from the perspective of either insulation coordination or power quality. the most obvious course of action is to prevent a high-coincidence scenario by manipulation of the grid monitoring delay τ_G.

Factory specification of grid inverters shall normally fix τ_G to 180 seconds as per general recommendations in the connection standards [5, 6], which is unlikely to be changed after installation in a customer's premises. However the minimum allowable τ_G for inverter based systems is 20s, and the author proposes that new installations take advantage of this additional range so as to effect a dispersion of switching delays.

Adjustment to τ_G might either be made manually at the point of commissioning, or automatically by means of a pseudo-random delay term generated on device firmware installation.

6.6 Chapter Conclusions

Results of cumulative impact studies involving multiple spatially dispersed embedded generators on an LV network have been presented. Key to the acquisition of these results has been the development in EMTP-ATP of an extensive travelling wave equivalent of the Generic LV Network model, as approved by UK DNOs. Smaller generic single-feeder models have also been developed for high penetration studies relating to urban and rural installations. It has been found that:

- LV networks incorporating up to 192 individually specified and spatially dispersed embedded generators (50% of total households) may be modelled in detail in EMTP for the purpose of systematic and statistical analyses while remaining within the operational limits of the software;
- By treating embedded generation within a network on a per-phase basis, penetration scenarios may be increased to 100% for the purpose of timed-switching (worst-case) analyses;
- For the highest SSEG penetration scenarios, the theoretical maximum transient voltage at the most remote point of the network due to mass reconnection of generators is approximately 233V for the generic UK urban LV model (223V for a rural feeder)
- Typical transient magnitudes at these locations are reduced to approximately 25% of their theoretical maxima due to temporal dispersion of switch closing times and inrush inception angles.
- Transient voltage peak values are attenuated to a greater degree in rural overhead circuits than in urban underground cables, with simulated maximum amplitudes at the LV transformer terminals dropping to 203V (urban) and 57V (rural).
- For lower penetrations of SSEG, there is little to distinguish the characteristics of a typical cumulative transient event from the switching of a large load, thus

demanding little concern from the perspective of insulation coordination or EMC.

Statistical studies have revealed that time-dispersion between switch closing and inrush inception instants of each generator significantly limits the magnitude of generated transients, with mean voltage magnitudes at the customer bus and transformer terminals reducing to 1.13 and 1.12 pu respectively for the generic UK LV network model. It is hypothesised that these results may be conservative, due to overly randomised inrush inception timing, and that true behaviour shall lie closer to the theoretical maxima. It has been noted that diversity in the response times of grid disconnects serves to reduce the effective penetration of coincidently switched generators.

As a general observation, Dommel's EMTP method (using trapezoidal integration) was found give a good balance between performance and solution speed for the large-scale studies presented here. No significant problems were reported on the grounds of solution stability or numerical oscillation. Some economy of model components might be achieved in future, allowing for more extensive networks with higher SSEG penetrations to be analysed using the same freely available software tools. At the present time, there would appear to be no technical benefit in switching to alternative (Euler, Gear 2^{nd} Order, Runge-Kutta ...) or novel solution methods, though these options may be exploited in future for verification purposes.

Conclusions

THE primary focus of this thesis has been the development of models for the computation of electromagnetic fast-transient propagation within LV networks, and the application of said models in the context of an ever increasing penetration of small embedded generators with ratings below 16 Amps per phase. This chapter charts the most significant project findings and deliverables, and a number of ideas are presented for further refinements and ongoing work.

As the gap between supply of and demand for electrical energy narrows, and concern over climate change and primary fuel availability rises, there is an increasing need to move towards a more distributed power generation model in order to accommodate the necessary levels of renewable generation to meet long-term renewables and emissions targets. With ever growing numbers of small generators feeding into public supply networks, the consumer is set to play an increasingly active role in the energy market. From the perspective of a network operator, however, there is little to distinguish between a small generator rated at or below 16A per phase on the one hand and a similarly rated load on the other. Indeed, the only distinction is in the direction of real power flow and, for this reason, there is a tendency to regard such generators as negative loads.

This designation at present precludes the use of such small scale embedded generation for ancillary service provision, with a requirement instead that generators should disconnect in response to excessive grid voltage or frequency deviation. It is hypothesised that as the penetration of embedded generators on a given LV bus increases, these disconnection requirements shall give rise to an increased incidence and severity of localised switching transients on the 400/230V circuit above that already encountered. This thesis has

sought to predict the magnitudes of switching transients for a range of network topologies and increasing SSEG penetration scenarios, and to propose options for mitigation in cases where excessive voltages or currents are predicted.

Practical considerations pertinent to time-domain simulation of low-voltage networks were first addressed including solution time-step limits imposed by short travelling wave line segments and circuit time constants, and the need for an appropriate numerical representation of compact non-circular conductor geometries. An evaluation of modal- and phase-domain frequency dependent line models was undertaken, and found to yield improved results over the simplified Π-equivalent employed in earlier work.

Generator switching patterns and associated transient characteristics were evaluated from extensive testing of a photovoltaic inverter rig within the Cardiff University Solar Energy Laboratory. Statistical analyses of amplitudes, front/tail times, ramp rates and energy measures were used to formulate a suite of easily synthesised representative test waveforms suitable for application to future laboratory and field tests. It was found that capacitive inrush gave rise to the worst case transient current magnitudes, and that the depth of voltage perturbations is heavily dependent on the impedance of the LV circuit. Timing data of relay pole closing instants and inrush inception with respect to the supply voltage sinusoid was used to specify statistical rules for the control of switches in complex simulation models.

A trio of alternative source representations of varying complexity was developed in EMTP-ATP for modelling transient behaviour associated with a range of switching operations. The most versatile of these models incorporates an explicit representation of the inverter DC bus and power electronic circuitry, and allows both disconnect and reconnect operations to be investigated using a single model. The provision of such flexibility, however, comes at the expense of solution accuracy, and a sensitivity to initial conditions makes complex source representation undesirable for large studies.

Having determined experimentally that it is the generator reconnection process that gives rise to the most significant transient voltages and currents, it was possible to adopt a far simpler and more efficient reconnection-only model for the most computationally demanding cumulative impact studies. This was a major benefit as the very largest

system studies undertaken required such extensive models that exhaustion of simulation component limits was a frequent occurrence.

Indicative LV network feeder models were developed for fast transient analysis from existing dynamic system studies and DNO planning guidelines. Indeed, the primary novelty of this work has been the formulation of a detailed travelling wave equivalent of the generic UK LV Network model, as recognised by the UK Distribution Network Operators. It is intended that the developed model should remain useful for studies beyond the scope of this document. The display limitations of the ATPDraw preprocessor have been adhered to in order to maximise ease of use, and solution times of 250-case statistical studies vary by complexity between 10 and 72 hours for a typical modern workstation (2.8GHz dual core, 3GB RAM).

For the purpose of the cumulative studies, both generator penetration and aggregated background load were assumed to have an even phase distribution and geographical dispersion, with a discrete set of fixed scenarios proposed. Such an assumption was deemed appropriate to the needs of this work, in order that the initial number of variables be manageable. It is anticipated that more realistic diversity and imbalance scenarios shall be incorporated into future studies.

Extensive simulations involving the generic UK LV network equivalent and rural feeder models indicate absolute worst case maximum transient voltage magnitudes at any location in the region of 233V and 223V respectively, for a 100% penetration scenario in which each and every customer has some form of converter-interfaced generating equipment, be it a PV system, micro CHP unit or small wind turbine. A broadly linear relationship is found to exist between SSEG penetration and typical transient voltage magnitudes, but some plateauing of maximum theoretical values is observed due to partial voltage collapse on current inrush.

Time dispersion of switch pole closing and inrush inception, according to the statistical behaviour determined from laboratory tests, was found to limit the severity of transients, and envelopes of maximum voltage spike amplitudes were found to drop to around 35-40% of their theoretical maxima. It has been postulated that these results are somewhat conservative, as in practice the diversity of inrush inception across a population

of generators should be constrained according to the charge states of each inverter's DC bus capacitance. Though highly variable from one switching event to the next, variation between sources for the same event is likely to be minimal.

Regardless of such conservative statistical results, worst-case voltages and currents are found to be more than manageable from the general perspective of insulation coordination. There remains, however, the secondary consideration of electromagnetic compatibility and received power quality, which must be addressed on a case by case basis. A method for the artificial dispersion of switch timing by implementation of a pseudorandom grid-monitoring delay has been proposed.

Suggestions for Future Work

Generic LV Model: Further Development

As discussed in Chapter 6, some difficulty was encountered in statistical representation of very high SSEG penetration scenarios using the generic UK LV model, due to an exhaustion of allowable network object counts. Efforts are ongoing to identify economies that will in future work allow all possible penetration scenarios to be considered.

The limitation of the LCC routine with regard to handling of sectored conductors is identified as a possible source of error in simulations of LV networks. It is proposed that a finite-element frequency scan preprocessing stage be integrated into the cable geometry specification for future studies, in place of the existing method in which equivalent circular conductors are assumed and satisfaction of the assumptions of Carson's equations and correction factors cannot be guaranteed.

Consideration of Load/Generator Diversity

It is proposed that ongoing simulation studies using these updated models should also account for diversity of instantaneous power demand by incorporating a variety of customer load profiles, and giving consideration to the effect of load/generation phase imbalance. Both of these aspects may be investigated with minimal adjustment to the existing models.

Disconnection Frequency Sensitivity Analysis

It is proposed that a study be undertaken to quantify the expected frequency of disconnection events for a typical grouping of generators on an LV feeder, and how the size of a given generator group can be expected to impact this frequency. The cascading effect of undervoltage protection relays under heavy load conditions is of particular interest, as this is the most likely cause of simultaneous switching.

Field Study on a Real LV Feeder

Field measurements are proposed in order to confirm a number of this work's assertions - principally that inrush diversity across a generator group shall in practice be lower than that assumed here, resulting in an increase of typical transient current and voltage magnitudes. Since such a study would necessitate consideration of high SSEG feeder penetrations, appropriate test networks would likely be limited to suburban housing developments in which embedded generation has been installed at the time of construction. Failing this, a representative laboratory based feeder model employing multiple inverters could be constructed for the purpose of verifying statistically determined switching behaviour.

Such a field study would also allow the simulation models presented in this thesis to be developed from generic network approximations to true system representations in which a real circuit topology is explicitly represented. Such an approach would permit investigation of the effects of network topology on the frequency and severity of the generated transients.

References

[1] "The growth potential for microgeneration in England, Wales and Scotland - report by Element Energy Ltd to BERR," Department for Business Enterprise and Regulatory Reform, Tech. Rep., 2008.

[2] M. Landy, "Analysis of renewables growth to 2020 - report to DECC," AEA Technology, Tech. Rep., 2010.

[3] "Investigation into the Scope for the Transport Sector to Switch to Electric Vehicles and Plugin Hybrid Vehicles - Report by ARUP to BERR," Department for Busiess Enterprise and Regulatory Reform: Department of Transport, Tech. Rep., 2008.

[4] M. F. McGranaghan, R. M. Zavadil, G. Hensley, T. Singh, and M. Samotyj, "Impact of utility switched capacitors on customer systems: Magnification at low voltage capacitors," in *Proceedings of the IEEE Power Engineering Society Transmission and Distribution Conference - Dallas, TX*, 1991, pp. 908–914.

[5] *Engineering Recommendation G83/1 - Recommendations for the Connection of Small-Scale Embedded Generators (Up to 16A Per Phase) in Parallel with Public Low-Voltage Distribution Networks*, Energy Networks Association Std., 2003.

[6] *BS EN 50438:2007 - Requirements for the Connection of Micro-generators in Parallel with the Public Low-voltage Distribution Network*, British Standards Institution Std., 2007.

[7] *Vision and Strategy for Europe's Electricity Grids of the Future - European SmartGrids Technology Platform.* Office for Official Publications of the European Communities, 2006.

[8] *Strategic Research Agenda for Europe's Electricity Networks of the Future - European SmartGrids Technology Platform.* Office for Official Publications of the European Communities, 2007.

[9] J. Watson, A. S. Bahaj, and P. A. James, "Unlocking the power house - innovation brief," Sussex Energy Group, SPRU, University of Sussex; Sustainable Energy Research Group, School of Civil Engineering and the Environment, University of Southampton, Tech. Rep., 2006.

[10] *Renewable Energy Route Map for Wales.* Welsh Government, 2008.

[11] *Microgeneration Action Plan for Wales.* Welsh Government, 2007.

[12] "Potential for microgeneration - study and analysis (final report)," Energy Saving Trust, Econnect and Element Energy, Tech. Rep., 2005.

[13] *Microgeneration Strategy.* Department for Energy and Climate Change (DECC), 2011.

[14] *Microgeneration Government-Industry Group Action Plan.* Energy Efficiency Partnership for Homes, 2011.

[15] J. Watson, R. Sauter, P. A. James, L. Myers, T. Venables, and R. Wing, "The regulatory impacts of domestic-scale microgeneration - response to Ofgem consultation," Sussex Energy Group, SPRU, University of Sussex; Dept. of Civil and Environmental Engineering, University of Southampton; Tanaka Business School, Dept. of Civil Engineering, Imperial College London, Tech. Rep., 2005.

[16] M. C. Claudy, C. Michelsen, and A. O'Driscoll, "The diffusion of microgeneration technologies - assessing the influence of perceived product characteristics on home owners' willingness to pay," *Energy Policy*, vol. 39, no. 3, pp. 1459 – 1469, 2011.

[17] S. Ropenus, H. K. Jacobsen, and S. T. Schröder, "Network regulation and support schemes - how policy interactions affect the integration of distributed generation," *Renewable Energy*, vol. 36, no. 7, pp. 1949 – 1956, 2011.

[18] *Energy Act 2004, Part 2; Sustainability and Renewable Energy Sources, Chapter 1: Sustainable Energy, Section 82: "Microgeneration".* UK Government.

[19] *Connecting a Microgeneration System to a Domestic or Similar Electrical Installation (In parallel with mains supply).* Electrical Safety Council, 2007.

[20] *The Electricity Safety, Quality and Continuity Regulations 2002.* UK Government - Crown Copyright, 2002.

[21] *Engineering Recommendation G59/1 - Recommendations for the Connection of Embedded Generation Plant to the Public Electricity Suppliers' Distribution Systems*, Energy Networks Association Std., 1991.

[22] P. Trichakis, P. C. Taylor, L. M. Cipcigan, P. F. Lyons, R. A. Hair, and T. Ma, "An investigation of voltage unbalance in low voltage distribution networks with high levels of SSEG," in *UPEC '06: Proceedings of the 41st International Universities Power Engineering Conference - Newcastle upon Tyne, UK*, P. C. Taylor, Ed., vol. 1, 2006, pp. 182–186.

[23] L. M. Cipcigan and P. C. Taylor, "Investigation of the reverse power flow requirements of high penetrations of small-scale embedded generation," *Renewable Power Generation, IET*, vol. 1, no. 3, pp. 160–166, 2007.

[24] L. M. Cipcigan, P. C. Taylor, and P. Trichakis, "The impact of small scale wind generators on LV distribution system voltage," in *International Conference on Clean Electrical Power (ICCEP) - Capri, Italy*, 2007, pp. 9–13.

[25] P. Trichakis, P. C. Taylor, P. F. Lyons, and R. Hair, "Predicting the technical impacts of high levels of small-scale embedded generators on low voltage networks," *IET Renewable Power Generation*, vol. 2, no. 4, pp. 249–262, 2008.

[26] Mott-Macdonald, "System integration of additional microgeneration (SIAM)," Department of Trade and Industry and Ofgem, Tech. Rep., June 2004.

[27] H. Perhad and B. Madden, "Numbers of microgeneration units installed in England, Wales, Scotland, and Northern Ireland - Final report for BERR," Department for Busiess Enterprise and Regulatory Reform, Tech. Rep., 2008.

[28] C. McNaught and H. Haydock, "The AEA Microgeneration Index Quarterly Summary Report 1 (October)," AEA, Tech. Rep., 2010.

[29] C. McNaught and H. Haydock, "The AEA Microgeneration Index Quarterly Summary Report 2 (December)," AEA, Tech. Rep., 2010.

[30] R. Harper, "UK trends in microgeneration adoption," RWE nPower, Tech. Rep., 2008.

[31] D. Infield and F. Li, "Integrating micro-generation and distribution systes - a review of recent research," *IEEE Power and Energy Society General Meeting: Conversion and Delivery of Electrical Energy in the 21st Century - Pittsburgh, PA*, 2008.

[32] J. Harrison, "Micro combined heat and power," EA Technology, Tech. Rep., 2003.

[33] P. F. Lyons, P. C. Taylor, L. M. Cipcigan, P. Trichakis, and A. Wilson, "Small scale energy zones and the impacts of high concentrations of small scale embedded generators," in *UPEC '06. Proceedings of the 41st International Universities Power Engineering Conference - Newcastle upon Tyne, UK*, vol. 1, 2006, pp. 128–132.

[34] C. McNaught and H. Haydock, "The AEA Microgeneration Index Quarterly Summary Report 3 (March)," AEA, Tech. Rep., 2011.

[35] *Photovoltaics in Buildings: Guide to installation of PV Systems (2nd Edition)*. Depatment of Trade and Industry, 2006.

[36] *Photovoltaic Module Datasheets for Systems up to 600V*, SHARP, last access date: July 2011. [Online]. Available: http://www.sharpusa.com/SolarElectricity/SolarProducts/LiteratureDownloads.aspx

[37] *Photovoltaic Module Datasheets for Systems up to 600V*, BPSolar, last access date: August 2011. [Online]. Available: http://www.bp.com/sectiongenericarticle.do?categoryId=9019590&contentId=7036980

[38] RenSMART. (2011) PV comparison table. Last access date: July 2011. [Online]. Available: http://www.rensmart.com/Products/SolarPV

[39] R. Ramakumar and J. E. Bigger, "Photovoltaic systems," *Proceedings of the IEEE*, vol. 81, no. 3, pp. 365–377, 1993.

[40] K. Akhmad, F. Belley, A. Kitamura, F. Yamamoto, S. Akita, H. Takakura, H. Okamoto, and Y. Hamakawa, "Effect of installation conditions on the output characteristics of photovoltaic modules," in *First IEEE World Conference on Photovoltaic Energy Conversion; Twenty Fourth IEEE Photovoltaic Specialists Conference - Waikoloa, Hawaii*, vol. 1, 1994, pp. 730–733.

[41] G. Sinden, "Wind power and the UK wind resource," Environmental Change Institute, University of Oxford, Tech. Rep., 2005.

[42] *Installing small wind-powered electricity generating systems.* Energy Saving Trust - Energy Efficiency Best Practice in Housing, 2004.

[43] A. Mirecki, X. Roboam, and F. Richardeau, "Architecture complexity and energy efficiency of small wind turbines," *Industrial Electronics, IEEE Transactions on*, vol. 54, no. 1, pp. 660–670, 2007.

[44] "Domestic roof-mounted wind turbines - the current state of the art," Mid Wales Energy Agency, Tech. Rep., 2005.

[45] S. J. Watson. (2007) Predicting the yield of micro-wind turbines in the roof-top urban environment. Centre for Renewable Energy Systems Technology (CREST), Loughborough University. Last access date: July 2011. [Online]. Available: http://www.warwickwindtrials.org.uk/resources/Microwind.pdf

[46] G. Y. Pam and E. J. Bala, "Potential output power from the 20 kW jacobs wind turbine generator across 19 sites in northern Nigeria," in *Proceeding of the 5th European-African Conference on Wind Engineering (EACWE) - Florence, Italy*, 2009.

[47] *Proven WT2500 2.5kW Wind Turbine Datasheet*, Proven Engineering Products Ltd, Wardhead Park, Stewarton, Ayrshire, KA3 5LH.

[48] A. Glass and G. Levermore, "Micro wind turbine performance under real weather conditions in urban environment," *Building Services Engineering Research and Technology*, vol. 32, no. 3, pp. 245–262, August 2011.

[49] S. Turan, A. Peacock, and M. Newborough, "Micro and small wind turbine applications in the built environment," *INESCO Science and Technology Vision*, vol. 3, no. 3, pp. 106–110, 2007.

[50] R. Gross, G. Jenkins, O. Paish, B. W. Leyland, N. Eyre, J. Harrison, C. Mahkamov, K. andHurley, J. L. Slowe, B. WIlliams, R. Hacker, R. Heap, L. Magistry, and I. Burdon, *Micro Energy Systems: Review of Technology, Issues of Scale and Integration*, M. Knowles, I. Burdon, and R. Beith, Eds. Professional Engineering Publishing, 2004.

[51] R. Lasseter, A. Akhil, C. Marnay, J. Stevens, J. Dagle, R. Guttromson, A. S. Meliopoulos, R. Yinger, and J. Eto, "The CERTS Microgrid Concept - White paper on Integration of Distributed Energy Sources," 2002.

[52] N. Hatziargyriou, H. Asano, R. Iravani, and C. Marnay, "Microgrids," *Power and Energy Magazine, IEEE*, vol. 5, no. 4, pp. 78–94, 2007.

[53] C. Marnay and G. Venkataramanan, "Microgrids in the evolving electricity generation and delivery infrastructure," in *IEEE Power Engineering Society General Meeting*, 2006.

[54] (2012) Profile: Baxi ecogen micro-chp unit. The Combined Heat and Power Association. Last access date: February 2012. [Online]. Available: http://www.chpa.co.uk/micro-chp_190.html

[55] J. Harrison. (2012) Stirling engines. Last access date: July 2012. [Online]. Available: http://www.microchap.info/stirling_engine.htm

[56] M. Pielke and M. Kurraat, "Integration of combined heat and power micro units into the low voltage network by using a grid-oriented operation mode," in *CIRED Seminar 2008: SmartGrids for Distribution*, Frankfurt, Germany, 2008.

[57] R. Jablko, C. Saniter, R. Hanitsch, and S. Holler, "Technical and economical comparison of micro CHP systems," in *International Conference on Future Power Systems - Amsterdam, Netherlands*, 2005, p. 6 pp.

[58] G. Meeks, D. Sowden, and C. Yates. (2012) Press release - industry welcomes forthcoming rise in feed-in tariff for microCHP. Combined Heat and Pwoer Association (CHPA). Last access date: February 2012. [Online]. Available: http://www.chpa.co.uk/industry-welcomes-forthcoming-rise-in-feed-in-tariff-for-microchp-_659.html

[59] R. Mallwitz and B. Engel, "Solar power inverters," in *6th International Conference on Integrated Power Electronics Systems (CIPS)*, 2010, pp. 1 –7.

[60] J. A. Baroudi, V. Dinavahi, and A. M. Knight, "A review of power converter topologies for wind generators," *Renewable Energy*, vol. 32, no. 14, pp. 2369–2385, 2007.

[61] A. S. Emhemed, R. M. Tumilty, G. M. Burt, and J. R. McDonald, "Transient performance analysis of single-phase induction generators for microgeneration applications," in *4th IET Conference on Power Electronics, Machines and Drives (PEMD) - York, UK*, 2008, pp. 345–349.

[62] P. Chiradeja and R. Ramakumar, "Voltage profile improvement with distributed wind turbine generation: A case study," in *IEEE Power Engineering Society General Meeting - Totonto, Canada*, vol. 4, 2003, p. 2336.

[63] P. Chiradeja and R. Ramakumar, "An approach to quantify the technical benefits of distributed generation," *IEEE Transaction on Energy Conversion,*, vol. 19, no. 4, pp. 764–773, 2004.

[64] T. Tran-Quoc, C. Andrieu, and N. Hadjsaid, "Technical impacts of small distributed generation units on LV networks," in *IEEE Power Engineering Society General Meeting - Toronto, Canada*, C. Andrieu, Ed., vol. 4, 2003, p. 2464.

[65] R. O'Gorman and M. A. Redfern, "The difficulties of connecting renewable generation into utility networks," in *IEEE Power Engineering Society General Meeting - Toronto, Canada*, vol. 3, 2003, p. 1471.

[66] N. Silva and G. Strbac, "Optimal design policy and strategic investment in distribution networks with distributed generation," in *CIRED Seminar: Smart Grids for Distribution - Frankfurt, Germany*, 2008.

[67] M. Thomson and D. Infield, "Network power-flow analysis for a high penetration of distributed generation," *IEEE Transactions on Power Systems*, vol. 22, no. 3, pp. 1157 –1162, 2007.

[68] *BS EN 50160:2007 - Voltage characteristics of electricity supplied by public distribution networks*, British Standards Institute Std., 2007.

[69] S. Conti, S. Raiti, G. Tina, and U. Vagliasindi, "Distributed generation in LV distribution networks: voltage and thermal constraints," in *Proceedings of the IEEE Power Tech Conference - Bologna, Italy*, vol. 2, june 2003.

[70] G. Bärwaldt and M. Kurrat, "Application of energy storage systems minimizing effects of fluctuating feed-in of photovoltaic systems," in *CIRED Seminar: Smart Grids for Distribution - Frankfurt, Germany*, 2008.

[71] S. Conti, S. Raiti, and G. Tina, "Small-scale embedded generation effect on voltage profile: an analytical method," *IEE Proceedings on Generation, Transmission and Distribution*, vol. 150, no. 1, pp. 78 – 86, jan. 2003.

[72] S. Fletcher, K. Meah, and S. Ula, "Simulation and analysis of a solar photovoltaic generation system for voltage support in a distributed generation scheme," in *Proceedings of the IEEE Region 5 Technical Conference - Fayetteville, AR.* Institute of Electrical and Electronic Engineers, 2007.

[73] B. Renders, W. R. Ryckaert, K. De Gussemé, K. Stockman, and L. Vandevelde, "Improving the voltage dip immunity of converter-connected distributed generation units," *Renewable Energy*, vol. 33, pp. 1011–1–18, 2008.

[74] R. Ramakumar and P. Chiradeja, "Distributed generation and renewable energy systems," in *IECEC '02 - The 37th Intersociety Energy Conversion Engineering Conference - Washington, DC*, 2002, pp. 716–724.

[75] P. Chiradeja, "Benefit of distributed generation: A line loss reduction analysis," in *IEEE/PES Transmission and Distribution Conference and Exhibition: Asia and Pacific - Dalian, China*, 2005, pp. 1–5.

[76] L. Tao, C. Schwaegerl, and N. Hermann, "Impact of microgrids concept on low voltage network reliability," in *CIRED Seminar: Smart Grids for Distribution - Frankfurt, Germany*, 2008.

[77] A. Bhowmik, A. Maitra, S. M. Halpin, and J. E. Schatz, "Determination of allowable penetration levels of distributed generation resources based on harmonic limit consideration," *IEEE Power Engineering Review*, vol. 22, no. 4, pp. 79–79, 2002.

[78] L. Gertmar, P. Karlsson, and O. Samuelsson, "On DC injection to AC grids from distributed generation," in *European Conference on Power Electronics and Applications - Dresden, Germany*, 2005.

[79] *Sunny Boy 700 - Technical Description. Solar Inverter for Photovoltaic Plants*, 1st ed., SMA Reglesysteme GmbH.

[80] J. Bull and W. Nethercot, "The frequency of occurrence and the magnitude of short duration transients in low-voltage supply mains," *Radio and Electronic Engineer*, vol. 28, no. 3, pp. 185 –190, 1964.

[81] J. Goedbloed, "Transients in low-voltage supply networks," *IEEE Transactions on Electromagnetic Compatibility*, vol. 29, no. 2, pp. 104 –115, May 1987.

[82] W. Rhoades, "Congruence of low voltage power main transient designs," in *IEEE National Symposium on Electromagnetic Compatibility - Denver, CO*, may. 1989, pp. 285 –293.

[83] A. Tjäder and J. Daalder, "Transients due to load energizing in low voltage systems," in *Proceedings of the 18th International Conference on Electricity Distribution (CIRED) - Turin, Italy*, 2005.

[84] D. Mansson, T. Nilsson, R. Thottappillil, and M. Backstrom, "Propagation of UWB transients in low-voltage installation power cables," *IEEE Transactions on Electromagnetic Compatibility*, vol. 49, no. 3, pp. 585 –592, 2007.

[85] D. Mansson, R. Thottappillil, and M. Backstrom, "Propagation ability of UWB transients through junctions of low-voltage power installation cable," in *Asia-Pacific Symposium on Electromagnetic Compatibility and 19th International Zurich Symposium on Electromagnetic Compatibility - Singapore*, May 2008, pp. 279 –282.

[86] A. Ametani, K. Hashimoto, and N. Nagaoka, "Modeling of incoming lightning surges into a house in a low-voltage distribution system," *EMTP Journal*, vol. 11, 2006.

[87] F. J. Pazos, J. Amantegui, F. Ferrandis, and A. Barona, "Overvoltages in low voltage systems due to normal medium voltage switching," May 21-24 2007.

[88] I. Metwally and F. Heidler, "Influence of line routing and terminations on transient overvoltages in lv power installations," in *18th International Zurich Symposium on Electromagnetic Compatibility*, sep. 2007, pp. 313 –316.

[89] P. Osmokrovic, B. Loncar, and S. Stankovic, "The new method of determining characteristics of elements for overvoltage protection of low-voltage system," *IEEE Transactions on Instrumentation and Measurement*, vol. 55, no. 1, pp. 257–265, 2006.

[90] D. Paul, "Low voltage power system surge overvoltage protection," in *IEEE Industrial and Commercial Power Systems Technical Conference - Clearwater Beach, FL*, 2000, pp. 21–29.

[91] F. Fiamingo, M. Marzinotto, C. Mazzetti, Z. Flisowski, G. B. Lo Piparo, and G. L. Amicucci, "Evaluation of SPD protection distance in low-voltage systems," *Journal of Electrostatics*, vol. 65, no. 5-6, pp. 363–370, 2007.

[92] F. Silva, S. Pinto, and J. Silva, "Impact of microgeneration on the quality of power: Effect on the voltage waveform," in *35th Annual Conference of Industrial Electronics (IECON) - Porto, Portugal*, nov. 2009, pp. 3672 –3678.

[93] N. Tse and L. Zhou, "Detection of voltage variations due to distributed energy resources," in *IEEE Power Energy Society General Meeting*, 2009, pp. 1 –5.

[94] F. Pazos and E. Navarro, "Field experience of power frequency overvoltages in wide-scale photovoltaic systems," in *CIGRE/IEEE PES Joint Symposium: Integration of Wide-Scale Renewable Resources Into the Power Delivery System - Calgary, Canada*, 2009, p. 1.

[95] A. Ametani, M. Kizilcay, M. P. Pereira, B. J. Elliott, W. S. Meyer, J. Choo, C. Huang, and W. Levy, *Rule Book - Alternative Transients Program - Part I*, 1987.

[96] H. W. Dommel, "Digital computer solution of electromagnetic transients in single-and multiphase networks," *IEEE Transactions on Power Apparatus and Systems*, vol. PAS-88, no. 4, pp. 388–399, 1969.

[97] A. Ametani, M. Kizilcay, M. P. Pereira, B. J. Elliott, W. S. Meyer, J. Choo, C. Huang, and W. Levy, *Rule Book - Alternative Transients Program - Part IV*, 1987.

[98] T. Noda and A. Ametani, *User Instructions of Noda Setup in ATP*, 1997.

[99] A. Ametani, M. Kizilcay, M. P. Pereira, B. J. Elliott, W. S. Meyer, J. Choo, C. Huang, and W. Levy, *Rule Book - Alternative Transients Program - Part V*, 1987.

[100] A. Ametani, M. Kizilcay, M. P. Pereira, B. J. Elliott, W. S. Meyer, J. Choo, C. Huang, and W. Levy, *Rule Book - Alternative Transients Program - Part III*, 1987.

[101] J. Martinez, J. Mahseredjian, and R. Walling, "Parameter determination: procedures for modeling system transients," *IEEE Power and Energy Magazine*, vol. 3, no. 5, pp. 16 – 28, 2005.

[102] J. Martinez, B. Gustavsen, and D. Durbak, "Parameter determination for modeling system transients - part I: overhead lines," *IEEE Transactions on Power Delivery*, vol. 20, no. 3, pp. 2038 – 2044, 2005.

[103] B. Gustavsen, J. Martinez, and D. Durbak, "Parameter determination for modeling system transients-part II: Insulated cables," *IEEE Transactions on Power Delivery*, vol. 20, no. 3, pp. 2045 – 2050, 2005.

[104] J. Martinez, R. Walling, B. Mork, J. Martin-Arnedo, and D. Durbak, "Parameter determination for modeling system transients-part III: Transformers," *IEEE Transactions on Power Delivery*, vol. 20, no. 3, pp. 2051 – 2062, july 2005.

[105] J. Martinez and D. Durbak, "Parameter determination for modeling systems transients-part V: Surge arresters," *IEEE Transactions on Power Delivery*, vol. 20, no. 3, pp. 2073 – 2078, july 2005.

[106] J. Martinez, J. Mahseredjian, and B. Khodabakhchian, "Parameter determination for modeling system transients-part VI: Circuit breakers," *IEEE Transactions on Power Delivery*, vol. 20, no. 3, pp. 2079 – 2085, july 2005.

[107] B. Johnson, H. Hess, and J. Martinez, "Parameter determination for modeling system transients-part VII: Semiconductors," *IEEE Transactions on Power Delivery*, vol. 20, no. 3, pp. 2086 – 2094, july 2005.

[108] O. Hevia, "Alternative transients program - comparison of transmission line models."

[109] T. Tran-Anh and P. Auriol, "Distribution network modelling for power line communication applications," in *International Symposium on Power Line Communications and Its Applications*, 2005.

[110] W. Scott-Meyer, T. Liu, and H. W. Dommel, *The Electromagnetic Transients Program (EMTP) Theory Book.* Bonneville Power Administration, Portland, Oregon, 1995.

[111] G. F. Moore, Ed., *BICC Cables: Electric Cables Handbook.* Blackwell Science, 1997.

[112] D. da Silva, G. Fernandez, and R. Rivas, "Calculation of frequency-dependent parameters of pipe-type cables: Comparison of methods," in *TDC '06. IEEE/PES Transmission Distribution Conference and Exposition: Latin America - Caracas, Venezuela*, 2006, pp. 1 –6.

[113] G. T. Andreou, D. P. Labridis, and G. K. Papagiannis, "Modelling low voltage distribution cables for powerline communications," in *Proceedings of the IEEE Power Tech Conference - Bologna, Italy*, 2003.

[114] G. T. Andreou and D. P. Labridis, "Electrical parameters of low-voltage power distribution cables used for power-line communications," *IEEE Transactions on Power Delivery*, vol. 22, no. 2, pp. 879 –886, april 2007.

[115] S. Matsuura, T. Noda, A. Asakawa, and S. Yokoyama, "EMTP modelling of a distribution line for lightning overvoltage studies," in *IPST07 - Proceedings of the International Conference on Power Systems Transients - Lyon, France*, 2007.

[116] R. Keyhani and D. Birtwhistle, "Modelling high frequency signal propagation over low voltage overhead distribution networks using EMTP," in *IEEE International Symposium on Power Line Communications and its Applications - Orlando, FL*, 2006, pp. 80 –85.

[117] P. N. Mikropoulos, T. E. Tsovilis, Z. Politis, and A. G. Kagiannas, "Evaluation of fast-front overvoltages arising at a 20/0.4 kV distribution transformer," in *7th Mediterranean Conference and Exhibition on Power Generation, Transmission, Distribution and Energy Conversion (MedPower 2010) - Agia Napa, Cyprus*, nov. 2010, pp. 1 –6.

[118] A. Morched, J. Marti, and J. Ottevangers, "A high frequncy transformer model for the EMTP," *IEEE Transactions on Power Delivery*, vol. 8, no. 3, pp. 1615–1626, 1993.

[119] C. Brozio and H. Vermeulen, "Wideband equivalent circuit modelling and parameter estimation methodology for two-winding transformers," *IEE Proceedings on Generation, Transmission and Distribution*, vol. 150, no. 4, pp. 487 – 492, july 2003.

[120] *PD IEC TR 60071-4:2004 - Insulation co-ordination, Part 4: Computational guide to insulation co-ordination and modelling of electrical networks*, British Standards Institution Std., 2004.

[121] A. Ametani, M. Kizilcay, M. P. Pereira, B. J. Elliott, W. S. Meyer, J. Choo, C. Huang, and W. Levy, *Rule Book - Alternative Transients Program - Part IX*, 1987.

[122] C. Ramírez and P. A. Calva, "Simultaion of electric power circuit breakers in the emtp incorporating electric arc models: Alpplication to reactor bank switching and short line fault," in *Annual Report Conference on Electrical Insulation and Dielectric Phenomena*, 2001.

[123] N. Watson and J. Arillaga, *Power Systems Electromagnetic Transients Simulation*, 1st ed., ser. IET Power and Energy Series 39. The Institution of Engineeering and Technology, London, UK, 2003.

[124] L. Cipcigan, P. C. Taylor, T. Funabashi, and P. F. Lyons, "Active voltage control in small-scale energy zones," *Transactions of the Japanese Institute of Electrical Engineer (IEEJ)*, vol. 124, pp. 1–10, 2004.

[125] J. J. Grainger and W. Stevenson, *Power Systems Analysis*, A. B. Akay and E. Castellano, Eds. London, UK: McGraw-Hill Inc, 1994.

[126] E. Peskin, *Transient and Steady-State Analysis of Electrical Networks.* D. Van Nostrand Company (Canada) Ltd, 1961.

[127] L. Freris and D. Infield, *Renewable Energy in Power Systems.* John Wiley and Sons, Ltd, 2008.

[128] L. Cipcigan, "Numerical oscillations in electromagnetic transients programs," in *11th International Symposium on System Theory, Automation, Robotics, Computers, Informatics, Electronics and Instrumentation (SINTES) - Craiova, Romania*, 2003.

[129] N. Chiesa and H. K. Høidalen, "On the calculation of fluxl inkage/current-characteristics for delta-coupled transformer windings." EEUG - European EMTP User Group, 2005.

[130] T. Noda, N. Nagaoka, and A. Ametani, "Phase domain modeling of frequency-dependent transmission lines by means of an ARMA model," *IEEE Transactions on Power Delivery*, vol. 11, no. 1, pp. 401 –411, jan 1996.

[131] *BS IEC 60287-1-1:2006 - Electric cables. Calculation of the current rating. Current rating equations (100% load factor) and calculation of losses. General*, British Standards Institution Std., 31 January 2007 2006.

[132] W. Mingli and F. Yu, "Numerical calculations of internal impedance of solid and tubular cylindrical conductors under large parameters," *IEE Proceedings on Generation, Transmission and Distribution*, vol. 151, no. 1, pp. 67 – 72, January 2004.

[133] *BS 7870-3.40:2001 LV and MV polymeric insulated cables for use by distribution and generation utilities. Specification for distribution cables of rated voltage 0.6/1 kV. XLPE insulated, copper wire waveform concentric cables with solid aluminium conductors*, British Standards Institution Std., 2001.

[134] *BS 6004:2000 - Electric cables: PVC insulated, non-armoured cables for voltages up to and including 450/750V, for electric power, lighting and internal wiring*, British Standards Institution Std., 2000.

[135] *BS 7870-3.10:2001, LV and MV polymeric insulated cables for use by distribution and generation utilities. Specification for distribution cables of rated voltage 0.6/1 kV. PVC insulated combined neutral and earth copper wire concentric cables with copper or aluminium conductors*, British Standards Institution Std., 2001.

[136] *BS 7870-3.20:2001 - LV and MV Polymeric Insulated Cables for use by Distribution and Generation Facilities - Part 3: Specification for Distribution Cables of Rated Voltage 0.6/1 kV - Section 3.20: PVC Insulated Split Concentric Cables with Copper or Aluminium Conductors (Implementation of HD 603)*, British Standards Institution Std., 2001.

[137] *BS EN 60664-1:2007 - Insulation coordination for equipment within low-voltage systems, Part 1: Principles, requirements and tests*, British Standards Institution Std., 2007.

[138] *BS EN 60071-1:2006 - Insulation co-ordination, Part 1: Definitions, principles and rules*, British Standards Institution Std., 2006.

[139] *BS 7870-5:2011 - LV and MV polymeric insulated cables for use by distribution and generation utilities Part 5: Polymeric insulated aerial bundled conductors (ABC) of rated voltage 0.6/1 kV for overhead distribution (Implementation of HD 626)*, British Standards Institution Std., 2011.

[140] N. R. Watson, A. M. Cola, G. D. Irwin, and O. Nayak, "Z-domain frequency-dependent network equivalent for electromagnetic transient studies," in *Proceedings of the International Conference on Power Systems Transients (IPST) - Budapest, Hungary*, 1999.

[141] Y. Wang and N. Watson, "Z-domain frequency-dependent AC-system equivalent for electromagnetic transient simulation," *IEE Proceedings - Generation, Transmission and Distribution*, vol. 150, no. 2, pp. 141–146, 2003.

[142] *BS EN 60071-2:1997, IEC 60071-2:1996 Insulation co-ordination. Application guide*, British Standards Institution Std., 1997.

[143] *BS 6662:1985, IEC 60816:1984 - Guide to methods of measurement of short duration transients on low voltage power and signal lines*, British Standards Institution Std., 1985.

[144] *BS EN 60904-3:2008 - Photovoltaic devices. Measurement principles for terrestrial photovoltaic (PV) solar devices with reference spectral irradiance data*, BSi Std., 2008.

[145] *BP 380 Datasheet - 80 Watt Photovoltaic Module: High-efficiency photovoltaic module using silicon nitride multicrystalline silicon cells*, BP Solar, 2006.

[146] S. McFayden. (2012, June) Low-voltage fault tables. Myelectrical. Last access date: August 2012. [Online]. Available: http://myelectrical.com/notes/entryid/193/low-voltage-fault-tables

[147] D. Shchiff and R. D'Agostino, *Practical Engineering Statistics*. Wiley, New York, 1996.

[148] *BS EN 60060-1: 2010 - High-voltage test techniques, Part 1: General definitions and test requirements*, British Standards Institution Std.

[149] *BS EN 61000-4-5:2006 - Electromagnetic compatibility (EMC). Testing and measurement techniques. Surge immunity test*, British Standards Institution Std., 2006.

[150] M. Azab, "Improved circuit model of a photovoltaic array," *International Journal of Electrical Power and Energy Systems Engineering*, vol. 2:3, 2009.

[151] D. Clark, A. Haddad, H. Griffiths, and N. N. Schulz, "Analysis of switching transients in domestic installations with grid-tied microgeneration," in *North American Power Symposium (NAPS) - Starkville, MS*, oct. 2009, pp. 1 –6.

[152] D. Clark, A. Haddad, and H. Griffiths, "Switching transient analysis of small distributed generators in low voltage networks," in *CIRED 2009. 20th International Conference and Exhibition on Electricity Distribution - Prague, Czech Republic*, june 2009, pp. 1 –4.

[153] A. Maknouninejad, N. Kutkut, and I. Batarseh, "Analysis and control of PV inverters operating in VAR mode at night," in *IEEE PES Innovative Smart Grid Technologies (ISGT) - Manchester, UK*, 2011.

[154] *BS EN 50525-1:2011 - Electric cables - Low voltage energy cables of rated voltages up to and including 450/750 V. Part 1: General requirements*, British Standards Institution Std.

[155] *BS EN 50525-2-11:2011 - Electric cables. Low voltage energy cables of rated voltages up to and including 450/750V. Cables for general applications. Flexible cables with thermoplastic PVC insulation*, British Standards Institution Std.

[156] *BS7671: Requirements for Electrical Installations - IEE Wiring Regulations 17th Edition*, British Standards Institution Std., 2008.

[157] *BS 7870-3.11:2001 - LV and MV polymeric insulated cables for use by distribution and generation utilities. Specification for distribution cables of rated voltage 0.6/1 kV. XLPE insulated combined neutral and earth copper wire concentric cables with copper or aluminium conductors (Implementation of HD 603)*, British Standards Institution Std., 2001.

[158] *NSP/004/041 - Specification for LV ABC Overhead Lines*, CE Electric UK Std., January 2007.

[159] K. Brennan and M. Anderson. (2010) Consultation - review of typial domestic consumption values. Office of Gas and Electricity Markets (OFGEM). [Online]. Available: http://www.ofgem.gov.uk/Markets/RetMkts/Compl/Consumption/Documents1/Review%20of%20typical%20domestic%20consumption%20values.pdf

[160] A. Ametani, M. Kizilcay, M. P. Pereira, B. J. Elliott, W. S. Meyer, J. Choo, C. Huang, and W. Levy, *Rule Book - Alternative Transients Program - Parts XVII-XVIII*, 1987.

[161] B. Wareing, *Wood Pole Overhead Lines*, A. T. Johns and D. F. Warne, Eds. IET Power and Energy Series, 2005.

[162] Japanese atp user group secure server. Last access date: December 2011. [Online]. Available: thunderbird.kuee.kyoto-u.ac.jp

[163] European emtp user group secure server. Last access date: March 2012. [Online]. Available: www.eeug.org

[164] B. Mork, R. Nelson, B. Kirkendall, and N. Stenvig, "Determination of high-frequency current distribution using emtp-based transmission line models with resulting radiated electromagnetic fields," in *Proceedings of the IEEE International Symposium on Power Line Communications and its Applications Rio de Janeiro, Brazil*, 2010.

[165] A. Ametani, M. Kizilcay, M. P. Pereira, B. J. Elliott, W. S. Meyer, J. Choo, C. Huang, and W. Levy, *Rule Book - Alternative Transients Program - Part VI*, 1987.

[166] V. Brandwajn, "Damping of numerical noise in the EMTP solution," *EMTP Newsletter*, vol. 2, pp. 10–19, 1982.

[167] F. Alvarado, "Eliminating numerical oscillations in trapezoidal integration," *EMTP Newsletter*, vol. 2, no. 3, pp. 20–32, 1982.

Appendix A

Numerical Solution of Circuits Using EMTP

A.1 The Trapezoidal Rule and Linear Circuits

For the purpose of digital simulation, continuous systems must be converted to discrete time equivalents, either as a z-domain transfer function or set of branch difference equations. This is most commonly achieved using the closed first order Newton-Cotes numerical integration method, commonly known as trapezoidal integration, and is the method employed in the EMTP-ATP simulation package. Table A.1 summarises representations of Resistive, Inductive and Capacitive components using the trapezoidal rule.

An inductive or capacitive element may be represented in the time-domain as a Norton equivalent current source I_{hist}, based on the historical state of its terminal voltages and branch current, in parallel with an equivalent resistance R_{eff}, which itself is dependant on the chosen time-step. In solution methods involving the trapezoidal approximation, the current source is determined from the historical state of the system at only the immediately preceding time step $(t - \Delta t)$. The trapezoidal integrator is thus regarded as providing a first order approximation of a given exact solution, and care must be taken to minimise numerical errors to ensure that solutions are as precise as possible. Higher order integrators can be used, such as the 2^{nd} order method proposed by Gear [123], but are not utilised in these studies.

The effective resistances R_{eff} are determined by the chosen solution time step Δt, and as such will change whenever the desired solver resolution is altered. Once all the components of a given linear network have been discretised, the conductance matrix $[G]$ can be formed and the circuit solved using the nodal equation:

$$[G]\,\mathbf{v}(t) = \mathbf{i}(t) + \mathbf{I}_{hist} \tag{A.1}$$

where $\mathbf{v}(t)$ is the vector of nodal voltages, $\mathbf{i}(t)$ is the vector of present external current sources, and $\mathbf{I}_{hist}$ the vector of current sources which represents the state of system at the previous time step.

A.1.1 Accuracy of Solution

One of the potential pitfalls of the trapezoidal rule, as a tool for the time-domain analysis of electromagnetic transients, is its inherent truncation error. This is a byproduct

Table A.1: Discrete Time RLC Equivalents using Trapezoidal Approximation

Continuous Representation	Discretised EMTP Implementation
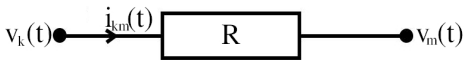	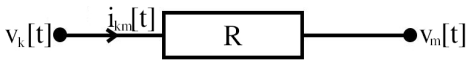
$i_{km(t)} = \frac{1}{R}\left(v_{k(t)} - v_{m(t)}\right)$	$i_{km[t]} = \frac{1}{R}\left(v_{k[t]} - v_{m[t]}\right)$
	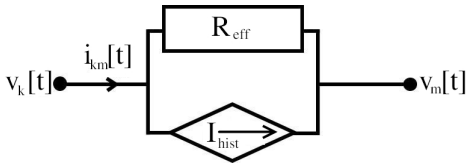
$i_{km(t)} = i_{km(t-\Delta t)} + \frac{1}{L}\int_{t-\Delta t}^{t}(v_k - v_m)dt$	$i_{km[t]} = I_{hist} + \frac{1}{R_{eff}}\left(v_{k[t]} - v_{m[t]}\right)$ $I_{hist} = i_{km[t-\Delta t]} + \frac{\Delta t}{2L}\left(v_{k[t-\Delta t]} - v_{m[t-\Delta t]}\right)$ $R_{eff} = \frac{2L}{\Delta t}$
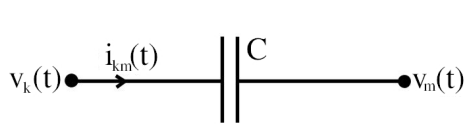	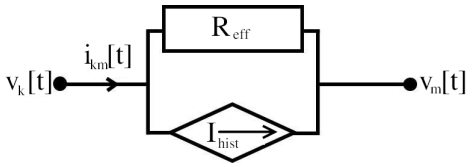
$i_{km(t)} = C\frac{d\left(v_k - v_m\right)}{dt}$	$i_{km[t]} = I_{hist} + \frac{1}{R_{eff}}\left(v_{k[t]} - v_{m[t]}\right)$ $I_{hist} = -i_{km[t-\Delta t]} - \frac{2C}{\Delta t}\left(v_{k[t-\Delta t]} - v_{m[t-\Delta t]}\right)$ $R_{eff} = \frac{\Delta t}{2C}$

of its equivalence to a first-order approximate Taylor series expansion of the exponential function. This is illustrated by analysis of the simple series RL branch of Figure A.1.

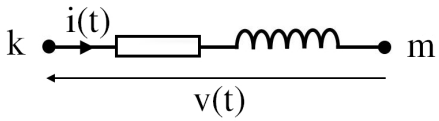

Figure A.1: Series RL Branch

Application of the trapezoidal rule in discretising this series arrangement results in the difference equation (A.2) for the present state branch current [96, 123]:

$$i[t] = \frac{\left(1 - \frac{\Delta t R}{2L}\right)}{\left(1 + \frac{\Delta t R}{2L}\right)} i[t - \Delta t] + \frac{\frac{\Delta t}{2L}}{\left(1 + \frac{\Delta t R}{2L}\right)} \left(v[t] + v[t - \Delta t]\right) \tag{A.2}$$

The exact analytical solution of the RL circuit current or central node voltage is a first order exponential decay, while the difference equation defined from the trapezoidal rule is found by observation to be a combination of first order taylor series expansions of the exact exponential:

$$e^{-x} = \frac{e^{-\frac{x}{2}}}{e^{\frac{x}{2}}} \simeq \frac{1 - \frac{x}{2} + \cdots}{1 + \frac{x}{2} + \cdots} \tag{A.3}$$

where $x = \frac{\Delta t R}{L}$. This approximation results in a truncation error which is dependent on the ratio of solution timestep and branch time constant. Δt must, therefore, be carefully chosen to account for the shortest time constants and highest frequency components in the system. It is preferable to select a value no greater than one third of the shortest time constant of the circuit [128] (τ_{min}) in order that erroneous circuit behaviour be avoided.

It is possible to minimise such errors through the use of exponential functions in the system difference equations, thereby better approximating an analytical solution. This method is known as the Root Matching (Euler) approach, in that it exactly maps the roots of the frequency domain equivalent admittance matrix from the s- to the z-domain without the truncation error described above. There exist two variants of this method discussed later in the chapter.

A.1.2 Stability

Another point of note is the requirement that the digital solution be numerically stable. As already mentioned, the truncation error due to the trapezoidal approximation is a function of the chosen simulation time step, and results in an imperfect mapping of the system transfer function from the continuous to the discrete time domain.

One important property of the trapezoidal rule, however, is that if the continuous time transfer function of the network being modelled is stable, its mapping to the z-domain will always be stable [123]. This is a property not shared, for example, by

the more efficient forward Euler method and is one of the reasons that the EMTP (employing the trapezoidal integral) is the favoured solution method in this work.

It must be emphasised, however, that the stability of a solution does not imply its exactness, nor indeed vice versa. Certain circuit configurations involving minimally damped RLC branches or short τ values are susceptible to marginal numerical stability when the trapezoidal rule is employed in its differential form. The result is typically an output that fluctuates alternately about the exact solution with each successive time-step, known as Numerical Oscillation.

A.1.3 Numerical Oscillation

The effects of numerical oscillation are illustrated in Figure A.2. Here, a step response has been computed in EMTP-ATP for a simple RL circuit, with different Δt - τ ratios. The damping factor K is the ratio of the parallel damping resistance R_p and the effective resistance of the inductive branch R_{eff}.

$$K = \frac{R_p}{R_{eff}} = \frac{R_p \Delta t}{2L} \tag{A.4}$$

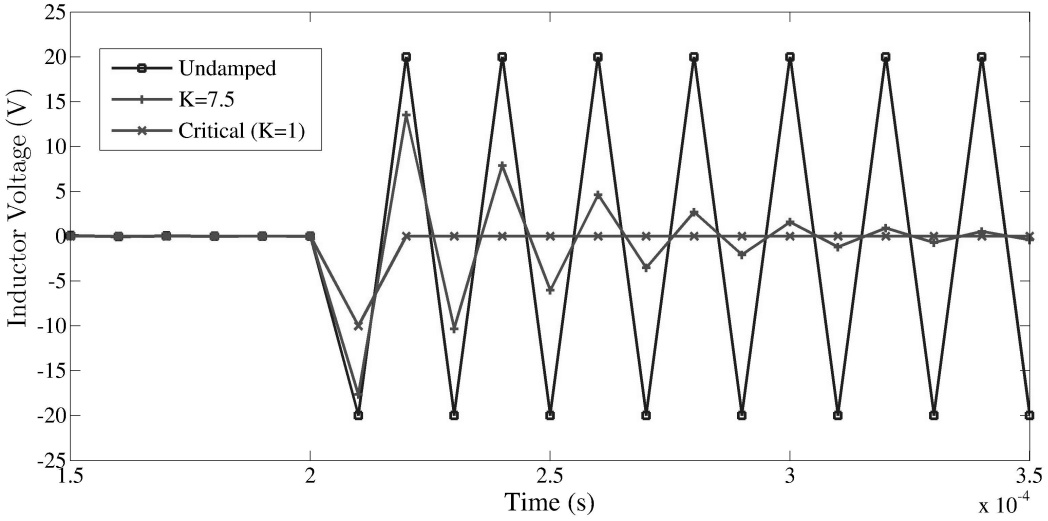

Figure A.2: Numerical Oscillation following current interruption in an RL circuit

It is clear from this example that the time-step must be well conditioned in order to reflect the characteristics of the circuit, or the circuit suitably damped to relax the resolution requirement of low values of τ. This is a potentially resource-intensive requirement in the simulation of low-voltage networks as individual component values are typically far smaller than their equivalents in high voltage systems for which the program was originally intended. This is a limiting consideration in the case of RC branches where both values are likely to be very small.

The detrimental effects of numerical oscillation can be reduced with the conservative application of damping resistance [110]. Where no existing stray or internal resistance can be quantified in the real circuit being modelled, problematic LC components may be damped by inclusion of fictitious resistances, placed either in parallel with inductances or in series with capacitances. Employment of very short solver time steps ($< 1\mu s$)

will tend to increase the incidence of numerical oscillation as the gradients of current and voltage discontinuities increases. The physical nature of Low-Voltage networks will invariably demand time steps in the low nanosecond range, and as such damping of numerical errors becomes increasingly important.

The choice of appropriate damping resistance is a compromise between maximising the rate of response, and minimising the introduction of phase errors in the solution [110], but the detrimental impact of artificial damping on the accurate representation of a problem should always be considered. Table A.2 gives a range of recommended values for damping resistances suitable for the treatment of spurious numerical oscillation in the EMTP. The values preceding the effective resistance expressions are the damping coefficients Kp (parallel) and Ks (series) which can be modified within the EMTP.

Table A.2: Resistance Values for the Damping of Numerical Oscillation

Parallel Damping of an Inductor	Series Damping of a Capacitor
$R_p = K_p \cdot \frac{2L}{\Delta t} \quad (5.4 \leq K_p \leq 9.4)$	$R_s = K_s \cdot \frac{\Delta t}{2C} \quad (0.1 \leq R_s \leq 0.2)$ [166]
$R_p = \frac{20}{3} \cdot \frac{2L}{\Delta t}$ [167]	

The inclusion of damping resistance in parallel with the an inductor modifies the form of the branch difference equation of Table A.1. For a branch current i and volt drop v:

$$v[t] = \frac{1}{\frac{\Delta t}{2L} + \frac{1}{R_p}} \cdot (i[t] - i[t - \Delta t]) - \alpha \cdot v[t - \Delta t] \tag{A.5}$$

where α is the reciprocal of the damping factor:

$$\alpha = \frac{R_p - \frac{2L}{\Delta t}}{R_p + \frac{2L}{\Delta t}} \tag{A.6}$$

Numerical oscillation in the inductor voltage will, therefore, be damped for any value of α less than 1. By setting the parallel resistance value equal to the effective resistance of the inductor R_{eff}, critical damping may be achieved, reducing the oscillation to zero in a single time step. This has the effect of removing the historic voltage term $v[t - \Delta t]$ from Equation (A.5), making the solution a function of present and past branch *currents* only. This critically damped case of the trapezoidal rule solution is known as the backward Euler method, and is discussed alongside other alternatives in the next subsections. A similar result is obtained for the critical series damping of oscillatory capacitor current.

A.1.4 Alternative Methods

The development of branch central difference equations by Dommel's method is arguably the most straightforward and flexible approach to the time-domain computation of electromagnetic transient phenomena. As discussed, however, this approach is prone to numerical oscillation when applied to simulations involving step voltages or current interruption [123]. An alternative to employing damping resistance in the EMTP is to use an exponential form of the branch difference equation. With reference to Equation (A.3), the expression derived by numerical integrator substitution for the current in a series RL branch is in fact a truncated taylor series representation of the analytically exact exponential decay.

The error associated with this truncated form of the solution manifests itself in the imprecise mapping of system poles and zeros from the continuous s to the discrete z domain - it is in fact the time-domain equivalent of the bilinear transform [123]. Errors can be minimised by selecting a suitably short time step in relation to the branch time constant, but this can give rise to excessively long simulation times when a far smaller Δt is required to satisfy the circuit characteristics than is needed to represent the highest frequency component of the transient. This requirement can be relaxed by extending the Taylor series to an infinitely large number of terms, thereby giving rise to the exponential form of the difference equation which is capable of computing exact solutions regardless of the choice of time step. A desirable consequence of switching to this method is the total elimination of spurious numerical oscillation, as it is in effect a critically damped trapezoidal rule solution.

The exponential form of the difference equation is known as the root-matching method, because it eliminates the truncation error associated with the mapping of roots from the s to z domain. Two frequently used forms of the root matching method are the Forward and Reverse Rectangular (Euler) methods, as illustrated in Figure A.3.

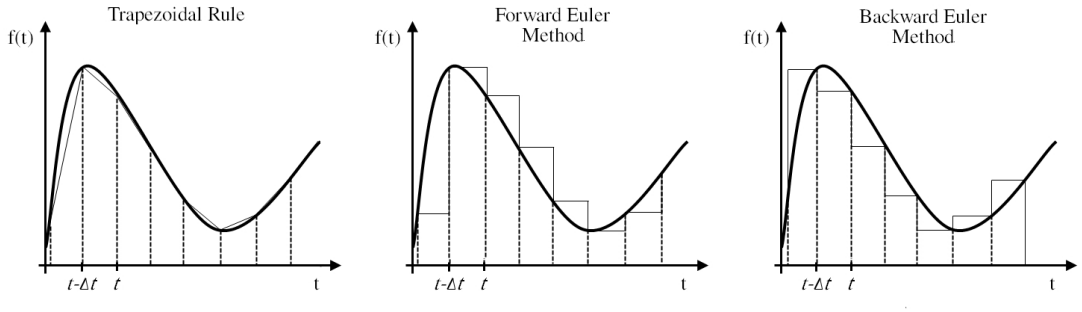

Figure A.3: Rectangular and Trapezoidal Integrators

The use of a rectangular integrator has the effect of removing one term from the difference equation. For example, the voltage across an RL branch using the Dommel method is dependent on the branch voltage and current at the previous time step, and also the current at the present time. By contrast, the forward Euler method is dependent only on the past history terms $v\,[t - \Delta t]$ and $i\,[t - \Delta t]$, while the backward Euler solution is independent of the historic voltage term $v\,[t - \Delta t]$. This has the effect of increasing the computation efficiency, but care must be taken with the forward rectangular method as the feed-forward nature of the solution makes it prone to instability.

Application of the backward Euler root matching method to an arbitrary RL branch generates a past history term I_{hist} and equivalent Norton resistance R_{equiv} much in the same way as Dommel's method, but the components of Figure A.4 are quite different.

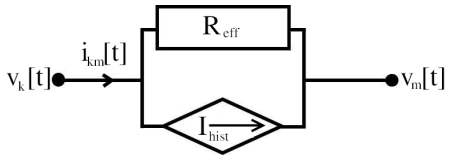

Figure A.4: RL branch representation in the EMTP

Equations (A.7) and (A.8) summarise the components of Figure A.4 for both Dommel and backward Euler solutions. Similar equivalents can be developed for RC and RLC branches.

Using Dommel's method, we have

$$I_{hist} = \frac{1 - \dfrac{\Delta t R}{2L}}{1 + \dfrac{\Delta t R}{2L}} \cdot i\left[t - \Delta t\right] + \frac{\dfrac{\Delta t}{2L}}{1 + \dfrac{\Delta t R}{2L}} \cdot v\left[t - \Delta t\right]$$

$$R_{eff} = R + \frac{2L}{\Delta t} \tag{A.7}$$

with the Backward Euler method, we get

$$I_{hist} = e^{-\frac{\Delta t R}{L}} \cdot i\left[t - \Delta t\right] \qquad R_{eff} = \frac{R}{1 - e^{-\frac{\Delta t R}{2L}}} \tag{A.8}$$

Much like numerical integrator substitution using the trapezoidal rule, difference equations developed from the backward Euler root matching method are inherently stable, provided that the network being represented is itself stable. All poles and zeros of the continuous transfer function located in the left hand side of the complex plane in the s-domain shall be mapped to a region within the unit circle in the discrete z-domain as depicted in Figure A.5 [110]. Coupled with the inherent critical damping of numerical oscillation at points of current or voltage discontinuity, it would seem that root matching methods would be preferable to Dommel's trapezoidal approximation, with its inherent truncation error and marginal stability when used as a differentiator.

This is generally not the case, however, as the equivalence of root matching to the critically damped trapezoidal solution discussed earlier can cause misrepresentation of real circuit behaviour. In achieving an exact solution, the circuit itself has been altered to some degree, and as such, an undamped trapezoidal approximation is almost always preferable to a critically damped one. Dommel's method of course allows the user to tailor the damping coefficient as required, which entails a greater degree of flexibility as a general solution method.

Though not a feature currently available in the EMTP-ATP, it is possible for a

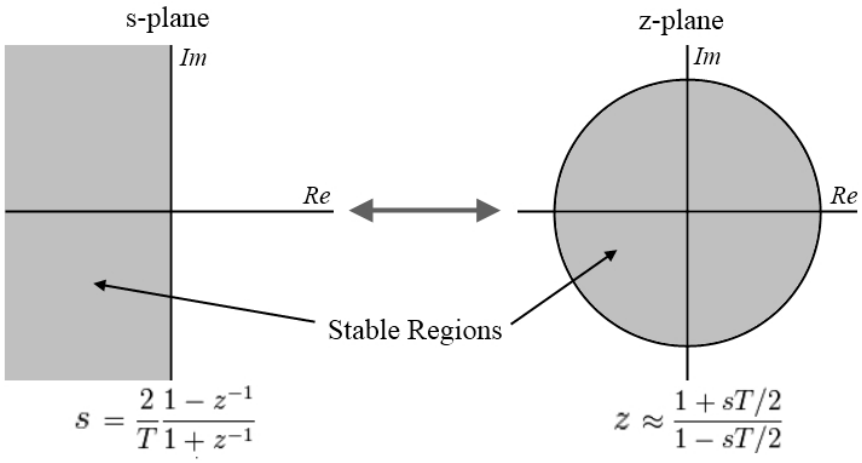

Figure A.5: Mapping of Stable Poles from s- to z-domain

time-domain simulation to switch between solution methods using more than one form of branch difference equation, provided that they are equivalent. Other software using the commercial EMTP Development Coordination Group or Electric Power Research Institute (DCG/EPRI) licensed versions, such as Manitoba HVDC Research Centre's EMTDC, offer the capability to reinitialise a simulation at the instant of current or voltage discontinuity (switching) by invoking a critical damping function [123, 128]. The circuit is solved for the first few time steps after switching using the backward Euler method, then reverts back to Dommel's algorithm and continues as before.

This technique allows the benefit of numerical oscillation damping in the Euler method to be exploited without adversely impacting the long term behaviour of the model. There is an additional computational burden with the reinitialising procedure which makes this method somewhat less efficient for solutions involving fast-switching devices such as bridge inverters (see section 2.6). It does, however, represent an alternative to damping networks in cases where numerical oscillation in results is deemed a major concern.

A.2 Frequency Dependent Transmission Lines

Since the parameters of a given transmission line may be expressed as rational functions of frequency, it is logical to treat the model in the frequency domain, converting back to time-domain representation as a final step by an appropriate process. In the frequency domain, the characteristic impedance of the line becomes:

$$Z_C(\omega) = \sqrt{\frac{Z'(\omega)}{Y'(\omega)}} = \sqrt{\frac{R_{DC}(\omega) + j\omega L'(\omega)}{G'(\omega) + j\omega C'(\omega)}} \tag{A.9}$$

And the propagation constant:

$$\gamma(\omega) = \sqrt{(R_{DC}(\omega) + j\omega L'(\omega)) \cdot (G'(\omega) + j\omega C'(\omega))} = \alpha(\omega) + j\beta(\omega) \tag{A.10}$$

where the prime notation indicates unit-length quantities [123]. The input-output matrix for a transmission line connecting nodes k and m, thus, becomes:

$$\begin{pmatrix} V_k(\omega) \\ I_{km}(\omega) \end{pmatrix} = \begin{bmatrix} a(\omega) & b(\omega) \\ c(\omega) & d(\omega) \end{bmatrix} \cdot \begin{pmatrix} V_m(\omega) \\ -I_{mk}(\omega) \end{pmatrix}$$
$$= \begin{bmatrix} cosh(\gamma(\omega)l) & Z_C(\omega) \cdot sinh(\gamma(\omega)l) \\ \dfrac{1}{Z_C(\omega)} \cdot sinh(\gamma(\omega)l) & cosh(\gamma(\omega)l) \end{bmatrix} \cdot \begin{pmatrix} V_m(\omega) \\ -I_{mk}(\omega) \end{pmatrix} \quad \text{(A.11)}$$

The parameters *a, b, c* and *d* are $n \times n$ frequency-dependent sub-matrices for an n-phase transmission line, while V_k, I_{km} and V_m, I_{mk} are the voltage and current vector pairs looking in at ends k and m respectively. The transfer matrices can be rearranged to give the sending and receiving end currents as a function of the terminal voltages - a form better suited to the EMTP G-matrix solution.

By employing forward and backward travelling wave expressions at each end of the line and introducing a propagation matrix $A(\omega)$, the Norton equivalent representation of a frequency-dependent transmission line may be derived as shown in (A.12), and is depicted in Figure A.6.

$$I_k(\omega) = Y_C(\omega) \cdot V_k(\omega) - A(\omega) \cdot [I_m(\omega) + Y_C(\omega) \cdot V_m(\omega)] \quad \text{(A.12)}$$

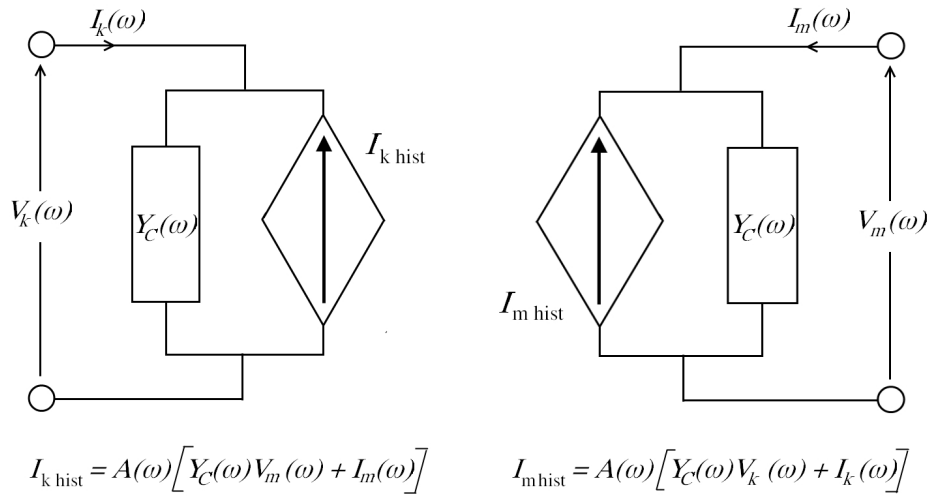

Figure A.6: Norton Equivalent of a Frequency Dependent Transmission Line

The propagation matrix consists of both attenuation and phase-shift terms of (A.13). The necessary convolution process translates the phase shift component into a time delay, and as such, a time-domain model implementation of such a transmission line must correctly implement this propagation delay.

$$A(\omega) = e^{-\Gamma l} = e^{-\gamma(\omega)l} = e^{-\alpha(\omega)l} \cdot e^{-j\beta(\omega)l} \quad \text{(A.13)}$$

The propagation delay of a transmission line means that the present voltages and currents at one end of the line are completely independent of the present states at the other. Therefore, mutual coupling in the equivalent conductance matrix of two subsystems *A* and *B* linked by a transmission line disappears, allowing the subsystems

to be represented as diagonal sub-matrices in [**G**]:

$$[\mathbf{G}] = \begin{bmatrix} [G_A] & \\ & [G_B] \end{bmatrix} \tag{A.14}$$

The increased sparsity of the conductance matrix arising from the use of transmission line sections can greatly reduce the computational burden in simulating extensive meshed networks. It is preferable to use a transmission line model in all cases, except those in which it would itself impose prohibitively short Δt requirements.

Appendix B

Laboratory Equipment and DAQ

B.1 Test and Measurement

Table B.1: Photovoltaic Test Rig Hardware

Mfr/Model	Qty	Description and Specification
BP380J	8	**BPSolar Multicrystalline SiN PV Module** Nominal Power: 80W (±5%) Nominal Voltage: 12V Voltage at P_{max}: 17.6V Current at P_{max}: 4.55A Short Circuit Current: 4.80A Open Circuit Voltage: 22.1V Max. System Voltage: 600V
SMA SB700	1	**SMA SunnyBoy 700 Solar Inverter** Inverter: Sine Wave, Current Source, 16kHz PWM Selected DC Input Range: <200V Max. DC Input Power: 670W Nominal DC Bus Voltage: 125V MPP Voltage Range: 100-160V AC Nominal Power: 600W THD: <3% Maximum Efficiency: 93.3% Certified Efficiency: 91.5%
WY NH204/63	1	**Wylex 2 Way Consumer Unit** Main DP Switch: 63A Single Pole MCB: 16A
HA Birch B9427/2	1	Dummy Load - 0.4-31A

Table B.2: Measurement and Data-Acquisition (Transient)

Qty	Model	Description	Spec.
1	-	DAQ Workstation	Intel Core 2 E8400 (3GHz) 4GB RAM, Windows XP Pro SP3
1	LeCroy Waverunner 64Xi	600MHz Oscilloscope	Bandwidth: 600MHz BW Limit: 20/200MHz Channels: 4 Interleaved Sample Rate: 10GS/s Vertical Resolution: 8 bit
2	Pintek DP25	Differential Voltage Probe	Bandwidth: 25MHz CM Voltage: 1000V AC pk Attenuation: x20, x50, x200 Input R: 4MΩ ±2% Input C: 1.2pF ±5%
2	Tektronix AM503-A	Current Probe Amplifier	Bandwidth: DC - 50MHz
2	Tektronix A6302	Current Probe	Bandwidth: DC - 50MHz Current Rating: 20A Continuous / 50A pk

Table B.3: Measurement and Data-Acquisition (Steady-State)

Qty	Model	Description	Spec.
1	NI USB 6212	Multifunction Data-Acquisition Board	Resolution: 16 bit Sample Rate: 400kS/s Analogue IN (Diff): x8 Analogue OUT: x2 Digital I/O: x32
1	NI GPIB-USB-HS	National Instruments GPIB Controller	-
2	LeCroy SI9000	Differential Voltage Probe	Bandwidth: DC-15MHz Input Z: 2MΩ Attenuation: x20, x200 CMRR (dB, 50Hz): -80 Maximum Voltage (diff): ±700V
3	LEM PR20	AC/DC Current Probe	Bandwidth: DC - 20kHz Current Range: ±30A Working Voltage: 300V rms
1	Keithley 2000	Multimeter	Bandwidth: 3Hz - 300kHz Input Z: 1MΩ ±2%, 100pF Max Voltage: 1000V pk

B.2 Line Impedance Compensator

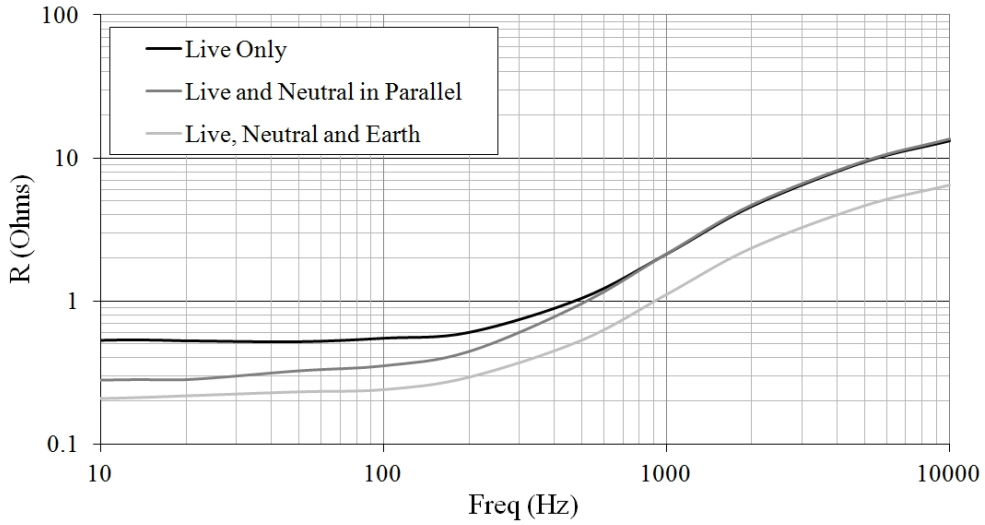

(a) Series Resistance, $R(\omega)$

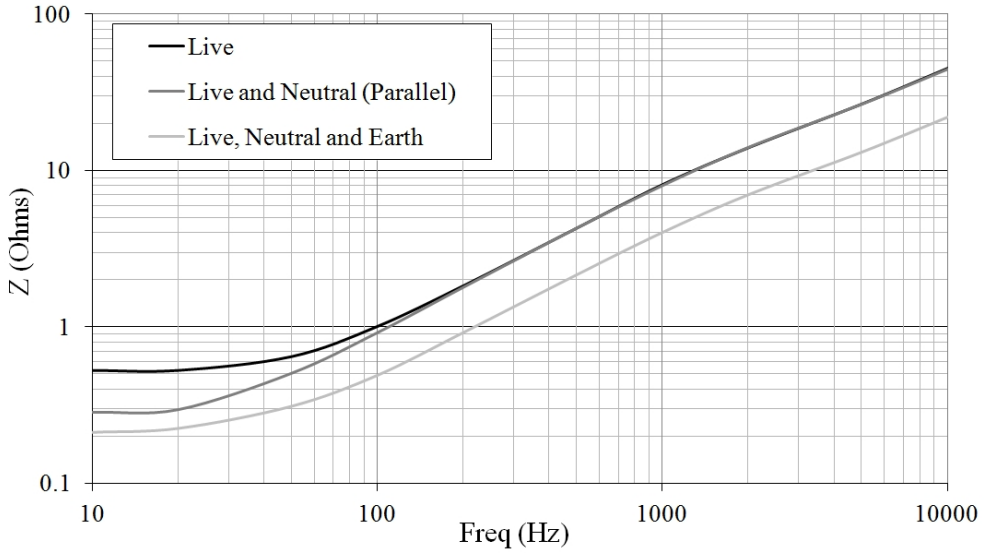

(b) Impedance Magnitude $|Z|(\omega)$

Figure B.1: Line Impedance Compensation Frequency Scans

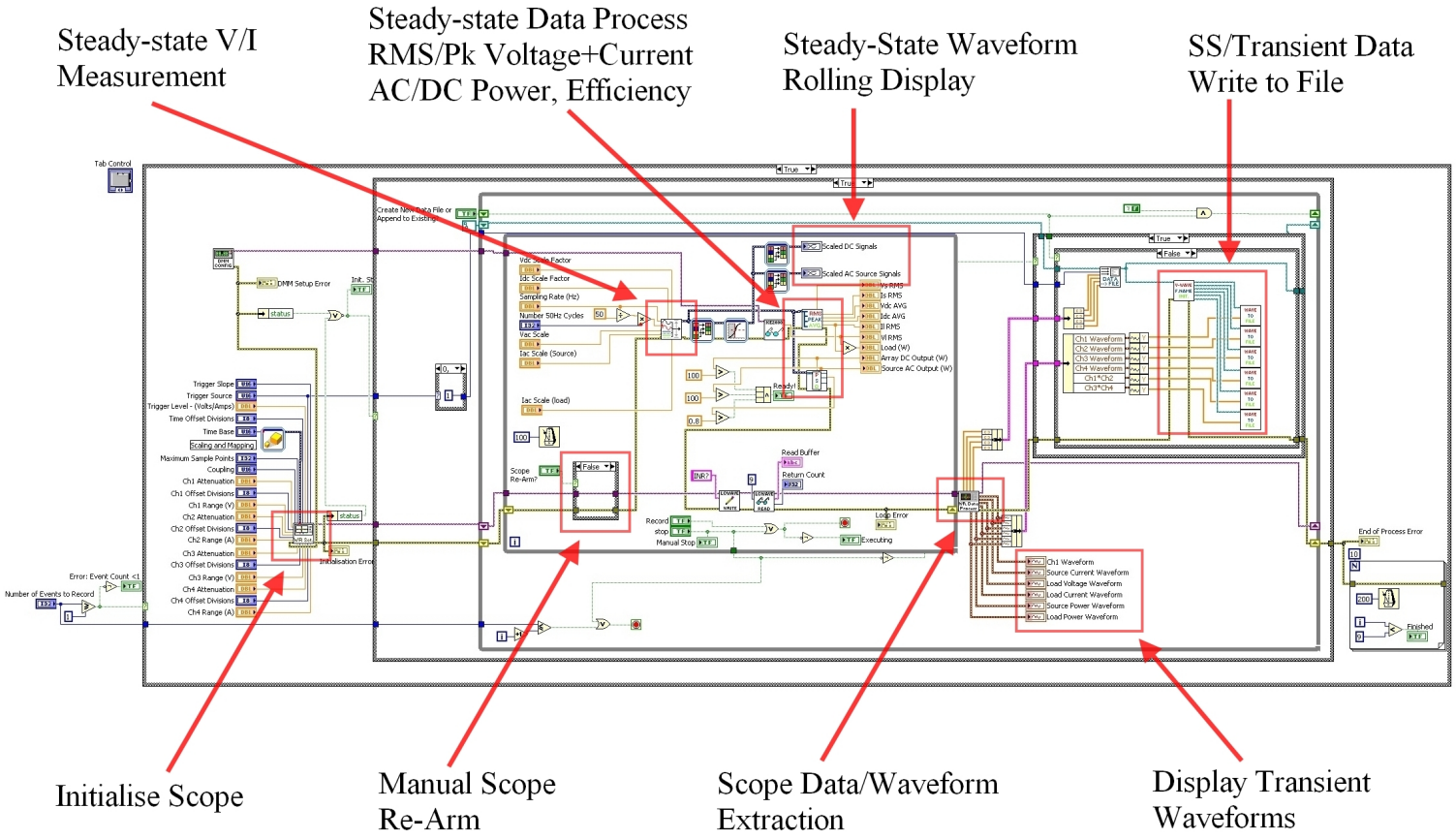

Figure B.2: LabVIEW Data Logger - Block Diagram

With reference to the LabVIEW block diagram in figure B.2, a breakdown of the individual sub-vi components and their functions follows:

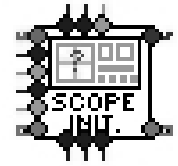

ScopeInit.vi is run as the first step of each test. It starts by fully resetting the scope to a default configuration, and then sets each measurement parameter in sequence according to the user inputs. This function is time-consuming at around 10 seconds, but is only performed once per test as it is assumed that the same setup parameters are required for each event in a particular test. The only additional scope setup requirement is the re-arming of the trigger between events which can be performed much more efficiently by a second *vi*.

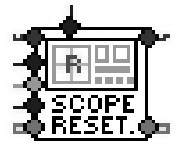

ScopeReset.vi allows the user to re-arm the trigger between events. This is achieved by adjusting the trigger from *Stop* to *Auto* and back to *Single* with a time delay suitable to allow the scope to cycle fully. Since this does not require a complete scope reset, the process is much faster than the initial setup, and the program need only pass the original trigger setup values to this *vi*.

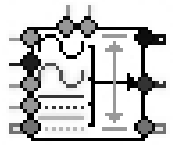

AcquireData.vi takes a snapshot of the steady-state voltages and currents in the system with a sampling rate and duration defined in the initial test setup. Quantities to monitor are extracted via predefined global channels, and scaled according to the user-input scaling factors (e.g. the attenuation of the probes used). The scaled signals are combined in a dynamic data cluster, and triggered relative to a rising edge of the AC voltage cycle to maintain a stable display.

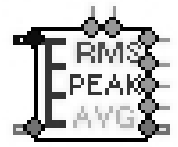

SSDataProcess.vi takes the dynamic data cluster output from the previous *vi*, and performs a set of statistical tests to extract information about the present steady-state of the system. The *vi* returns mean DC voltage and current, and both peak and rms AC voltage and current for each successive snapshot.

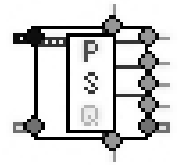

PowerAnalysis.vi takes the same data cluster, and applies a *power analyser* module to the DC and AC signals. The *vi* returns the average DC input power to the inverter over the acquired time window, together with P, Q, S and power-factor readings for the AC inverter output. The overall converter efficiency is also computed as a percentage.

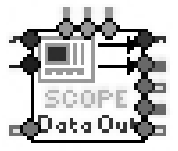

ScopeDataOut.vi extracts a set of internally defined measurements from the waveform captured by the scope. These include positive and negative peak values, and rise times for the instantaneous voltage and current traces. Instantaneous power data is also returned via the math function of the scope. This data is compiled into three arrays (V, I and P), and is output from the *vi* along with the captured waveforms themselves.

DataFileInit.vi is called if the user requests a new file in the test setup. It will create a new Excel spreadsheet file, complete with column headings ready to accept any new data.

DataToFile.vi appends an existing file with newly acquired measurement data, each successive event being saved to a new row in the file. Since data files are only accessed when new data is ready, the chances of data corruption should the program crash for any reason are minimised.

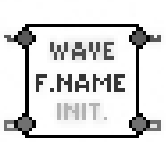

WaveFileInit.vi creates a new file path for saving the raw waveform data if *new file* is selected on the input screen. It takes the file path of the measurement file and appends the string *waveforms* to create a sister file for storing the acquired data points. For example, a measurement file with the name *abc.xls* would generate a second file *abcwaveforms.xls*.

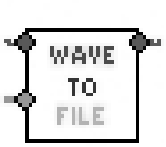

WaveToFile.vi appends waveform data to the accompanying waveform file. The *append to file* function in LabVIEW is not suitable for this task as it will only add data to a new row - the waveforms on the other hand, being large data sets, are best stored in columns. This *vi* must therefore extract the existing data from the waveform file to an array, transpose to rows, and append the new data set before transposing again back to columns and resaving to the same file.

Appendix C

Simulation Hardware/Software

Table C.1: Simulation Machine Hardware

Machine	Processor	RAM	OS
M1-M3	Intel Core 2 6420 (2.13GHz)	2GB	Windows XP Pro SP3
M4	Intel Pentium 4 3.2 GHz	2GB	Windows XP Pro SP3
M5-M11	Intel Core 2 6420 (2.13GHz)	2GB	Windows XP Pro SP3
M12	Intel Core 2 E8400 (3GHz)	4GB	Windows XP Pro SP3

Table C.2: Simulation Software Versions

Software	Description	Version	Release
ATP_MingW32	ATP-EMTP for Windows (32-bit) *Giga*-version (*gigmingw*		18-Oct-2011
ATPDraw	Graphical ATP Preprocessor	5.7p4	20-Jun-2011
PlotXWin	Plotting Application for ATP Easy-Install		24-Nov-2009
ATPLauncher	Program Launcher for ATP	1.17	31-Aug-2009
ReadLis	.lis file Reader (Dr. M. Albano)	0.10.19.05	24-Sep-2010

Appendix D

Simulation Models and Data

D.1 ATPDraw Model Topologies

Urban Single Feeder model, tier 1. 11kV circuitry and 11/0.4kV transformer.

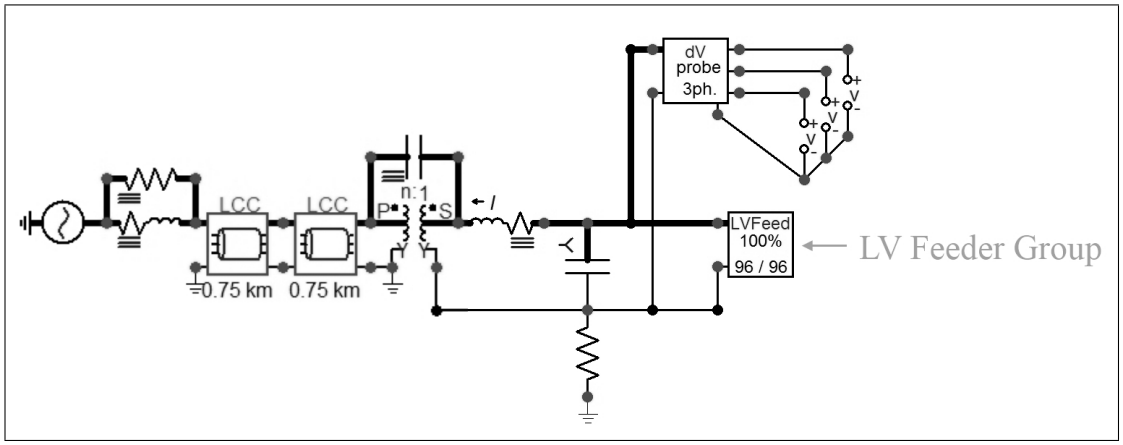

Figure D.1: Urban Single Feeder - Tier 1

Urban Single Feeder model, tier 2. 400V main trunk and 3-phase service cables feeding 16 LV node blocks (tier 3)

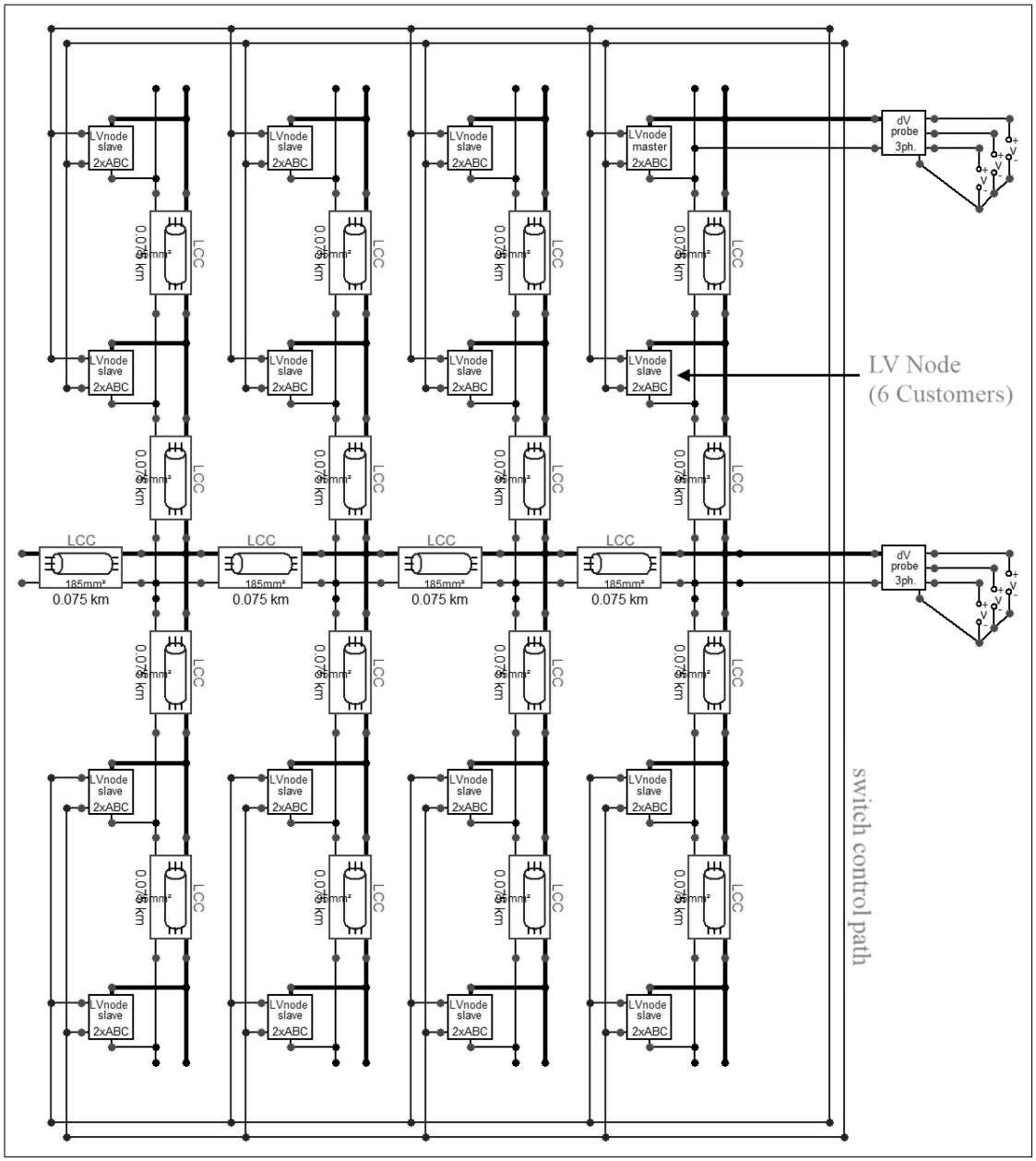

Figure D.2: Urban Single Feeder - Tier 2

Urban Single Feeder model, tier 3. LV node; 6 customers connected to main trunk by single-phase service cables.

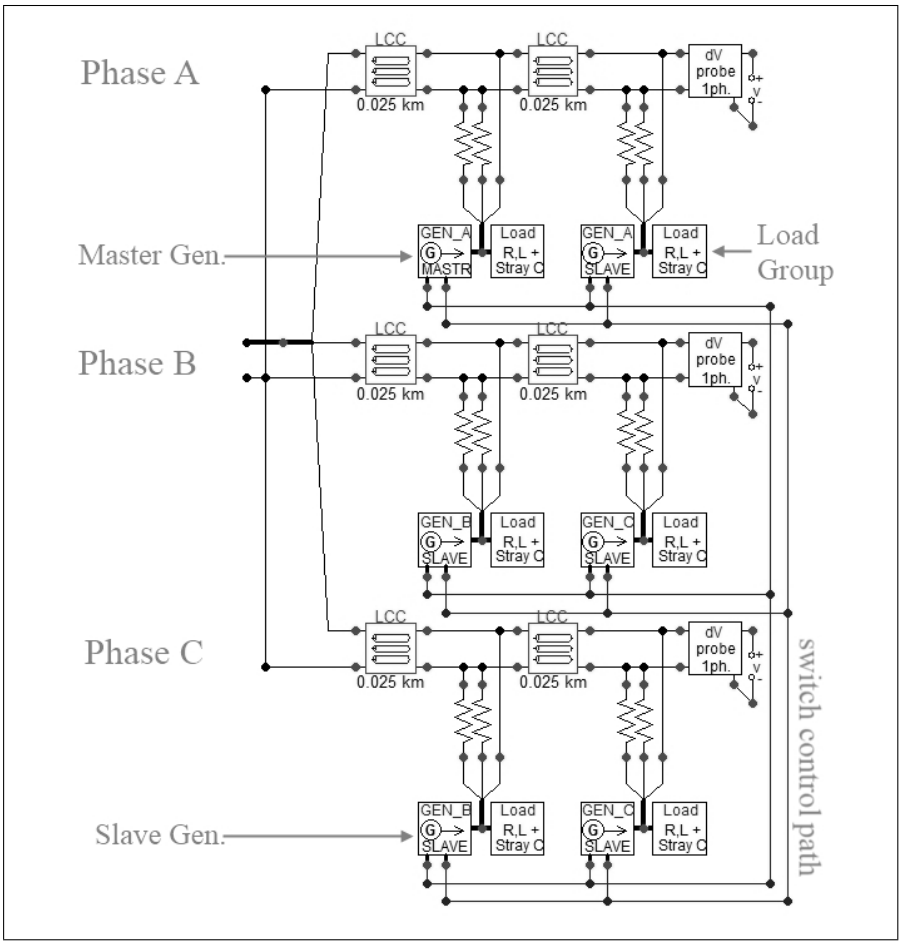

Figure D.3: Urban Single Feeder - Tier 3

Generic UK LV Network model, tier 1. 11kV circuit, transformer and four LV feeder blocks (tier 2)

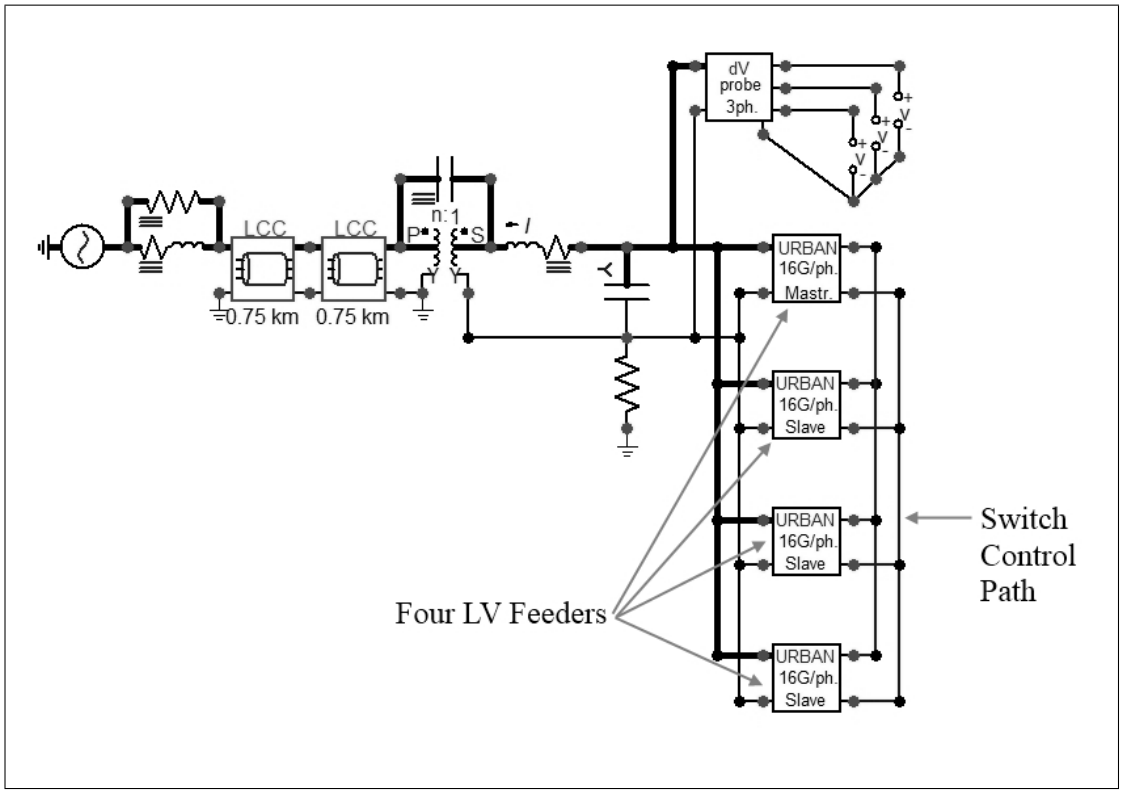

Figure D.4: Urban Generic LV - Tier 1

Generic UK LV Network model, tier 2. Identical to the single feeder case (figure D.2)

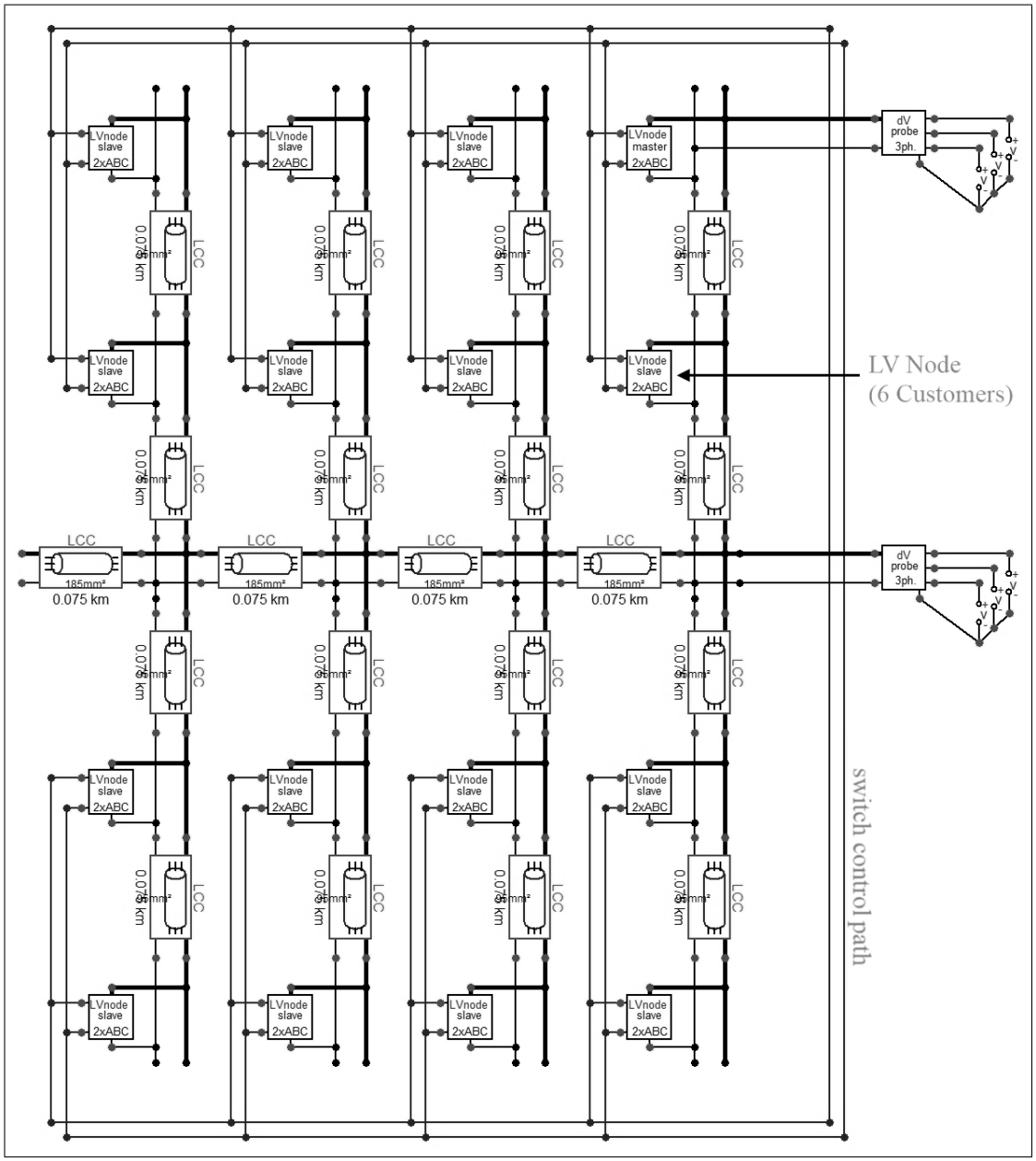

Figure D.5: Urban Generic LV - Tier 2

Generic UK LV Network model, tier 3. Phase-aggregated load, generator count limited to one per phase.

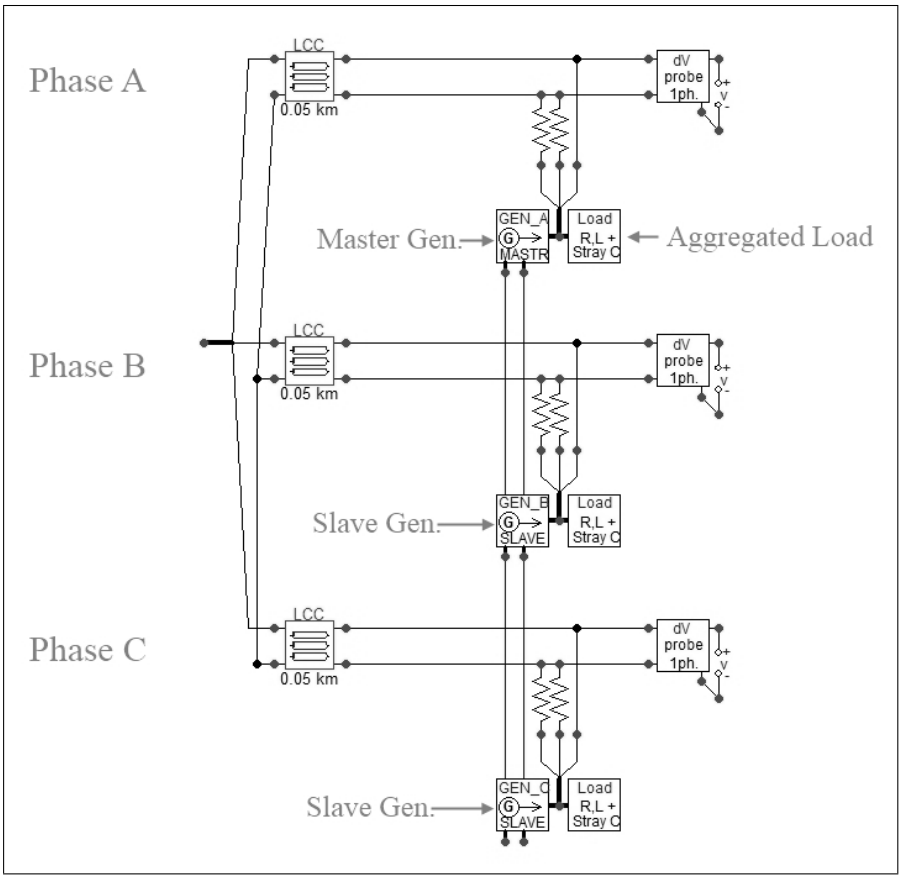

Figure D.6: Urban Generic LV - Tier 3

Rural LV Feeder model, tiers 1 and 2. 11kV circuit, transformer, main LV trunk and 3-phase service lines. 32 LV node blocks (tier3) connected.

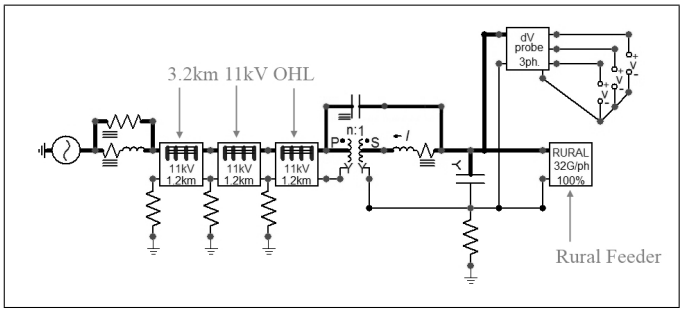

(a) Rural LV - Tier 1

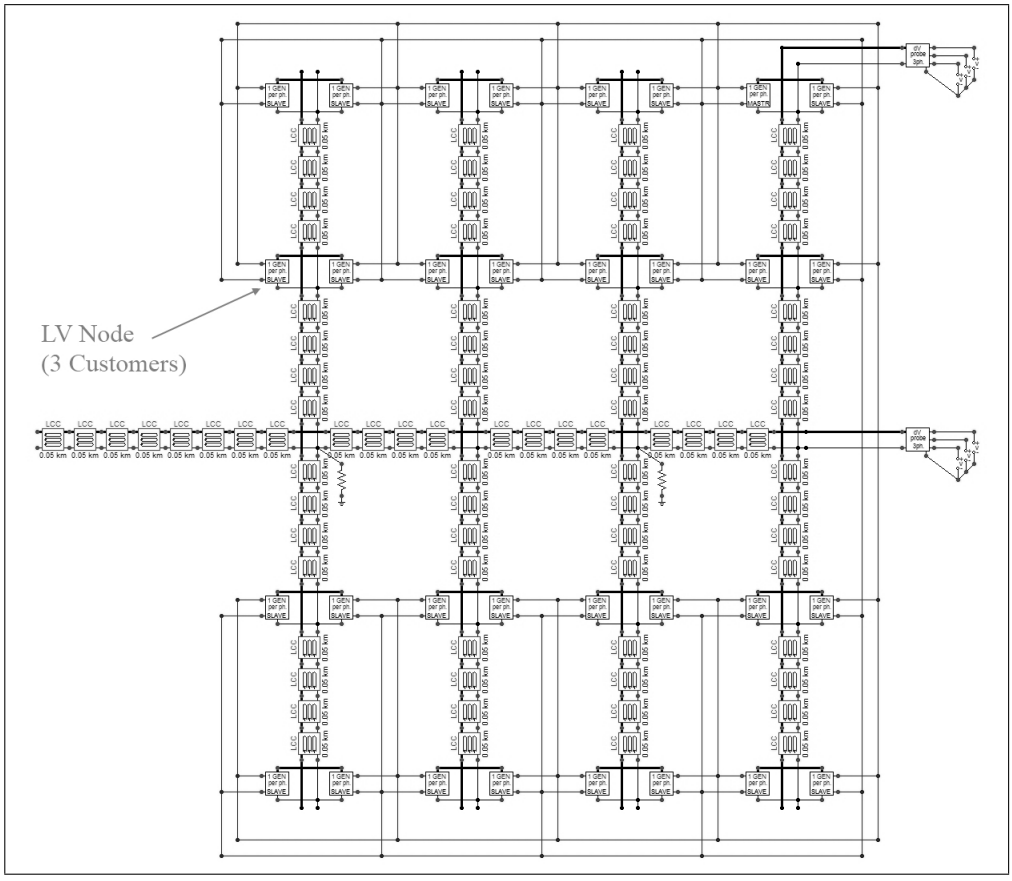

(b) Rural LV - Tier 2

Figure D.7: Rural LV Model - Tiers 1 and 2

Rural LV Feeder model, tier 3. One customer per phase, connected by single-phase overhead service lines.

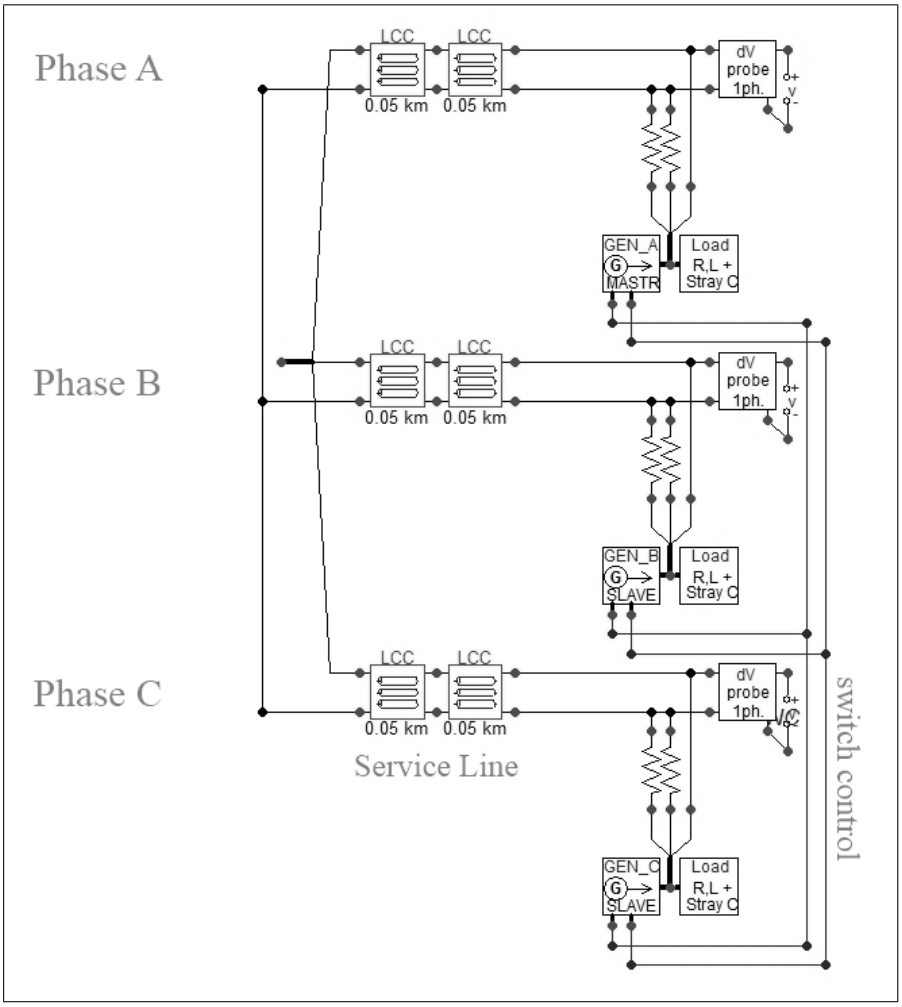

Figure D.8: Rural LV - Tier 3

ΔV Measurement Blocks with notch filter circuitry; Single and Three-phase.

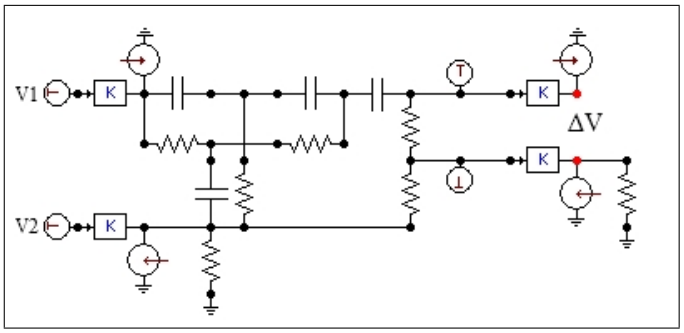

(a) Single-Phase

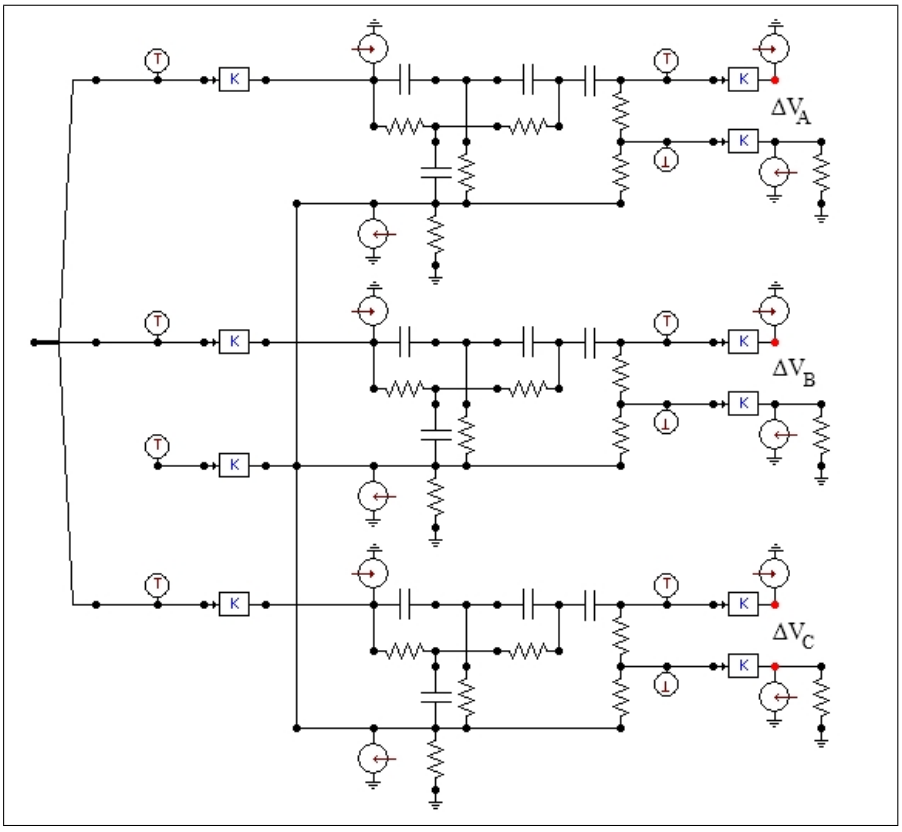

(b) Three-Phase

Figure D.9: Voltage Measurement Blocks

D.2 Statistical Switch Timing

Table D.1: Master Switch (Closing, Phase A)

	Mean Time Preceding V_A=0	Std.Dev.	Distribution
sw_1 (master)	0.76ms	92.0μs	Gaussian

Table D.2: Slave Switches (Closing, All Phases)

	Phase A		Phase B		Phase C		
	Delay	Std.Dev.	Delay	Std.Dev.	Delay	Std.Dev.	Distr.
sw_1	0ms	92.0μs	6.67ms	92.0μs	13.33ms	92.0μs	Gaussian
sw_2	98.5μs	33.1μs	6.765ms	33.1μs	13.432ms	33.1μs	Gaussian
sw_i	6.75ms	1.876ms	13.42ms	1.876ms	20.08ms	1.876ms	Uniform

Table D.3: Inrush Bypass Switch (Opening, All Phases)

	Delay Folowing sw_i	Std.Dev.	Distribution
sw_c	10.0ms	0ms	Uniform

D.3 Conductor Geometries

Table D.4: Single-Phase Service Cable Data (Underground)

CSA(mm^2)	R_{core}(mm)	$R_{ins.}$(mm)	$R_{neutr.}$(mm)	$R_{tot.}$(mm)	Depth(m)	$\rho_{core}(n\Omega\text{m})$	$\rho_{neutr}(n\Omega\text{m})$	$\varepsilon_{ins.}$	ε_{out}
25	2.821	3.721	4.571	5.971	0.5	28.2	16.8	2.1	2.1
35	3.338	4.238	5.278	6.780	0.5	28.2	16.8	2.1	2.1

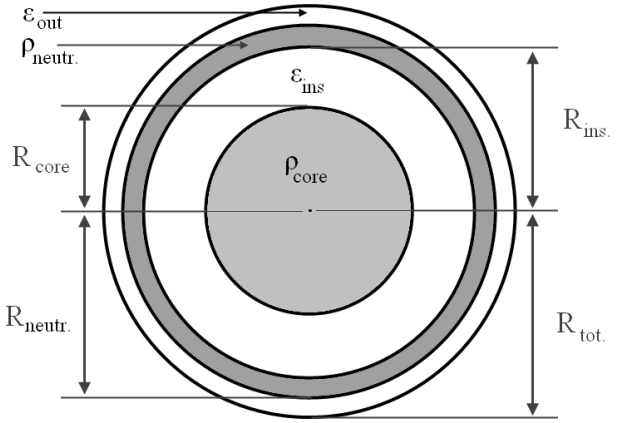

Figure D.10: Single-Phase Service Cable Geometry

Table D.5: Three-Phase Trunk Cable Data (Underground, Radii and Displacements in mm)

CSA	R_{core}	$R_{ins.}$	D	θ	R_{in}	R_{out}	$R_{tot.}$	Depth	ρ_{core}	$\rho_{neutr.}$	$\varepsilon_{r\ ins.}$	ε_{in}	ε_{out}
$95mm^2$	5.5	6.6	7.69	120°	14.57	16.16	18.26	0.5m	$28.2n\Omega$m	$16.8n\Omega$m	2.1	2.1	2.1
$185mm^2$	7.674	9.27	10.84	120°	21.8	23.5	26.0	0.5m	$28.2n\Omega$m	$16.8n\Omega$m	2.1	2.1	2.1

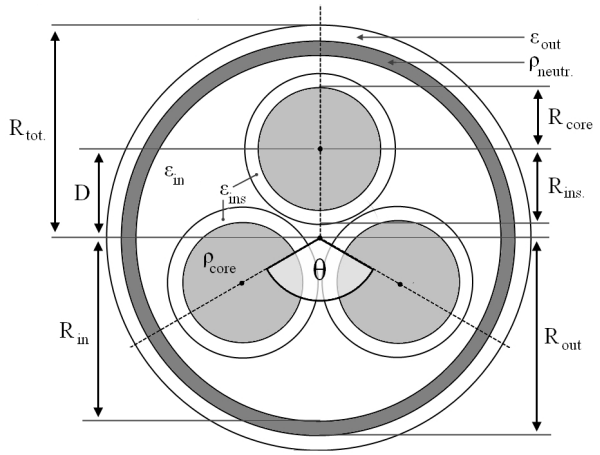

Figure D.11: Three-Phase Trunk Cable Geometry (400/230V)

Table D.6: Single-Phase Aerial Bundled Conductor (ABC) Data

CSA	R_{core}	$R_{ins.}$	ΔX	H	ρ_{core}	$\rho_{neutr.}$	$\varepsilon_{r\ ins.}$
$35mm^2$	3.34mm	4.79mm	9.6mm	10m	$28.2n\Omega$m	$28.2n\Omega$m	2.4

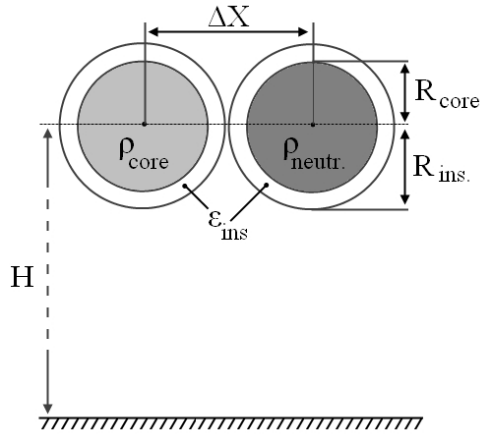

Figure D.12: Single-Phase ABC Geometry (400/230V)

Table D.7: Three-Phase Aerial Bundled Conductor (ABC) Data

CSA	R_{core}	$R_{ins.}$	ΔX	ΔY	H	ρ_{core}	$\rho_{neutr.}$	$\varepsilon_{r\ ins.}$
$70mm^2$	4.9mm	6.39mm	12.8mm	12.8mm	10m	$28.2n\Omega$m	$28.2n\Omega$m	2.4
$120mm^2$	6.5mm	8.2mm	16.4mm	16.4mm	10m	$28.2n\Omega$m	$28.2n\Omega$m	2.4

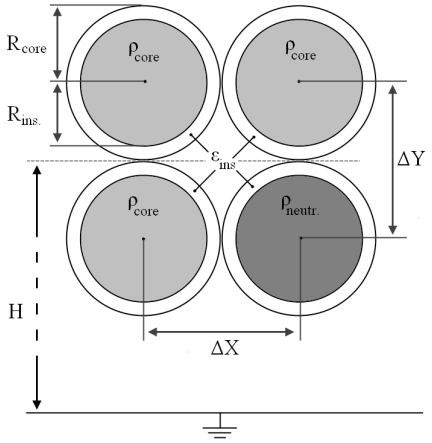

Figure D.13: Three-Phase ABC Geometry (400/230V)

Table D.8: Domestic Cable Data (Flat and Round Configurations)

Type	CSA	R_{core}	$R_{ins.1}$	R_e	$R_{ins.2}$	ΔX	ΔY	ρ	$\varepsilon_{r\ ins.}$
Flat Twin + Earth	$1.5mm^2$	0.691mm	1.391mm	0.564mm	1.264mm	-	-	$16.8n\Omega m$	3.5
	$2.5mm^2$	0.892mm	1.692mm	0.564mm	1.391mm	-	-	$16.8n\Omega m$	3.5
Flex	$1.5mm^2$	0.691mm	1.391mm	0.564mm	1.264mm	2.782mm	2.30mm	$16.8n\Omega m$	3.5
	$2.5mm^2$	0.892mm	1.692mm	0.564mm	1.391mm	3.386mm	2.60mm	$16.8n\Omega m$	3.5

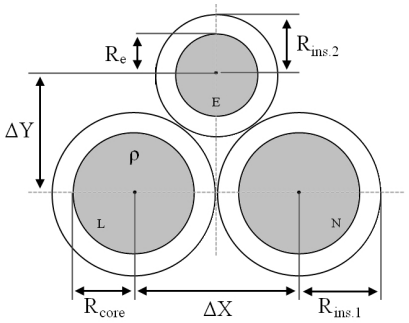

FLEX

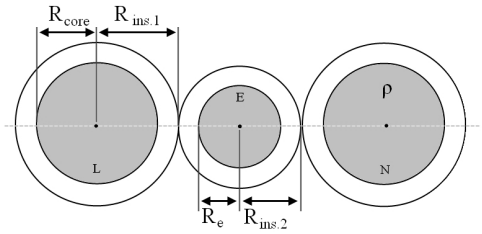

FLAT TWIN+EARTH

Figure D.14: Domestic Cable Geometries (230V)

D.4 Cable Propagation Tests (Domestic)

The following plots are the results of low voltage square pulse and step propagation testing of domestic cables, undertaken in the Cardiff School of Engineering Power Systems Laboratory. The signal source was a Thandar TG105 pulse generator and measurements were made using a LeCroy Waverunner 64Xi oscilloscope. Two cable samples were subjected to test, with the following configurations:

1. Flat Twin and Earth with solid copper conductors
2. Flex with stranded copper conductors

Each 12m cable section was double PVC insulated with a $2.5mm^2$ conductor CSA ($1.5mm^2$ Protective Earth), and held at a fixed height of approximately 1m above ground, as depicted in Figure D.15.

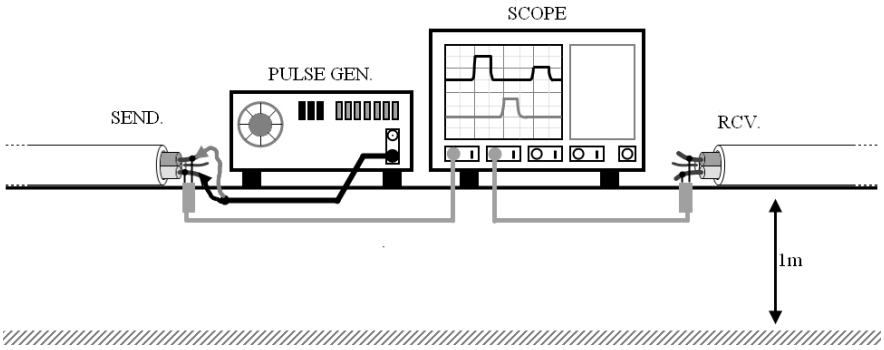

Figure D.15: Test Configuration for Cable Travel Tests

The test configuration has been reconstructed in EMTP using an empirical voltage source representation of the pulse generator. Results obtained using four variants of each cable model (*Pi, Bergeron, JMarti* and *Noda*) are plotted for comparison.

D.4.1 Open Circuit Test - Square Pulse

Flat Twin and Earth configuration, pulse applied between *Live* and *Neutral*.

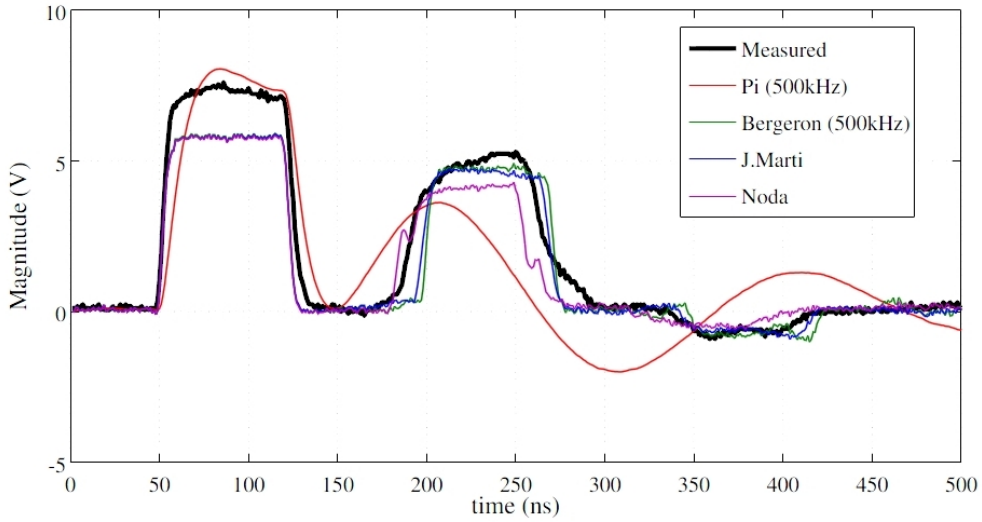

(a) Sending End

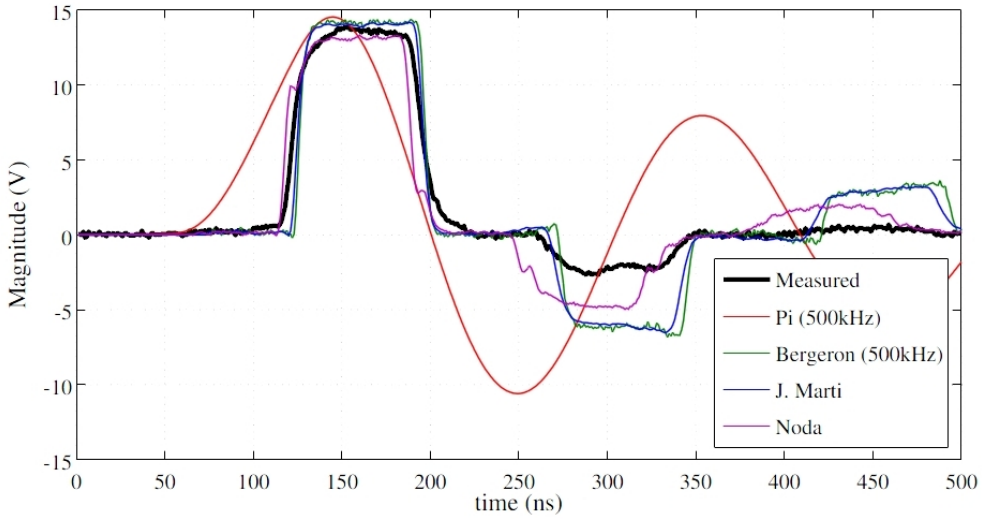

(b) Receiving End (Open)

Figure D.16: Flat Twin and Earth - Measured Live-Neutral

Flat Twin and Earth configuration, pulse applied between *Live* and *Earth*.

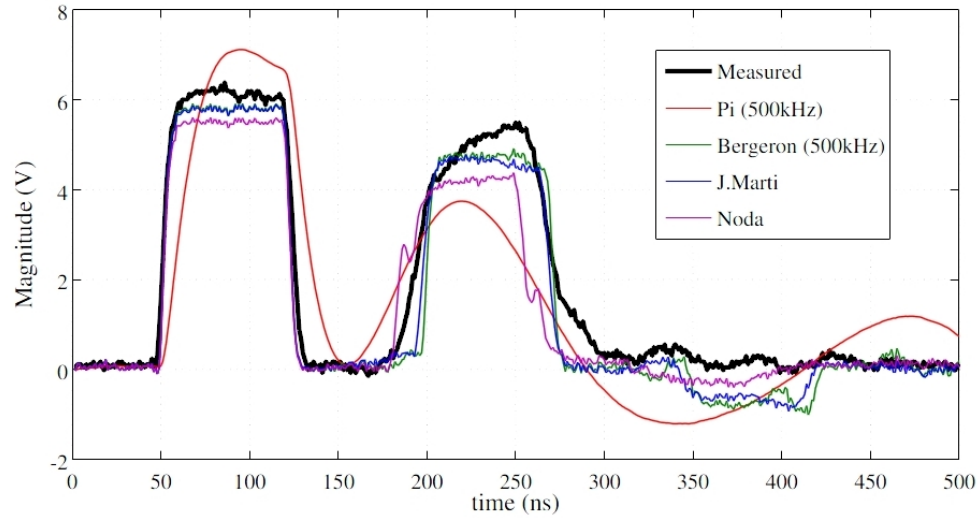

(a) Sending End

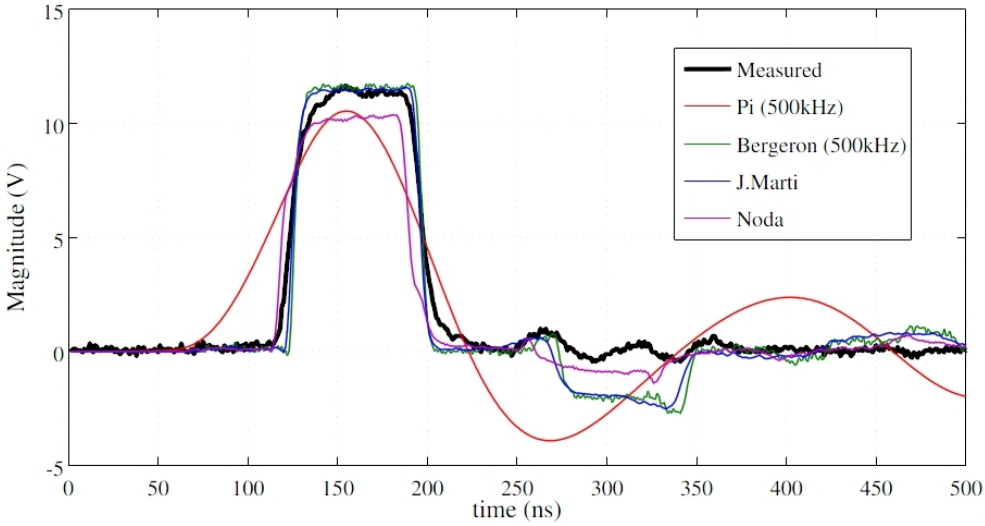

(b) Receiving End (Open)

Figure D.17: Flat Twin and Earth - Measured Live-Earth

Circular Flex configuration, pulse applied between *Live* and *Neutral*.

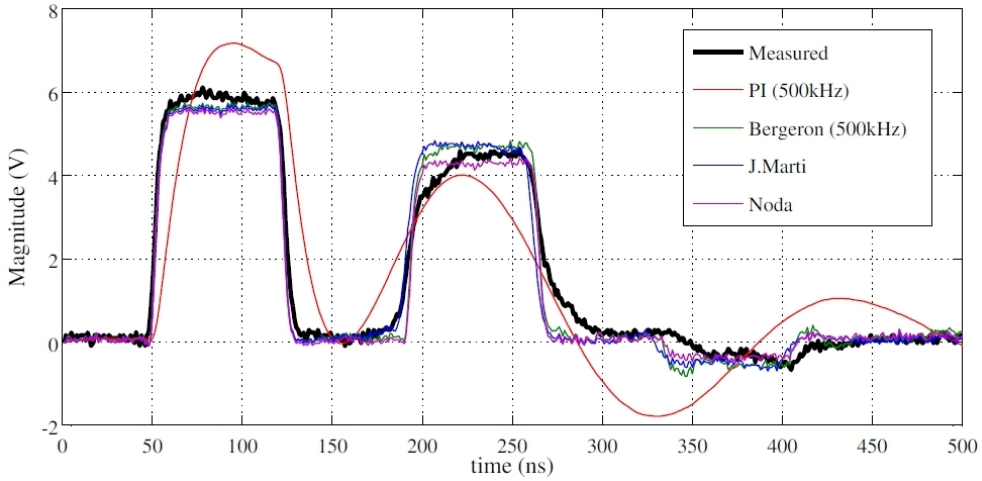

(a) Sending End

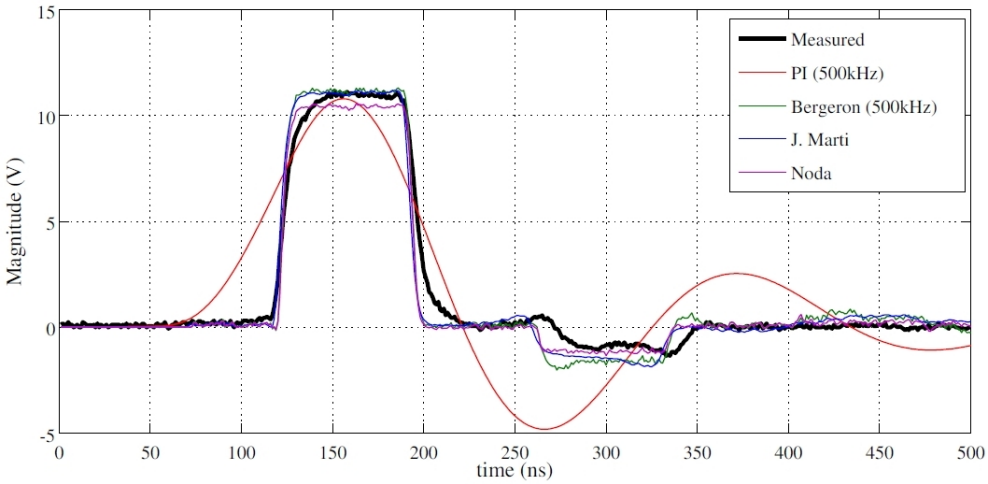

(b) Receiving End (Open)

Figure D.18: Mains Flex - Measured Live-Neutral

Circular Flex configuration, pulse applied between *Live* and *Earth*.

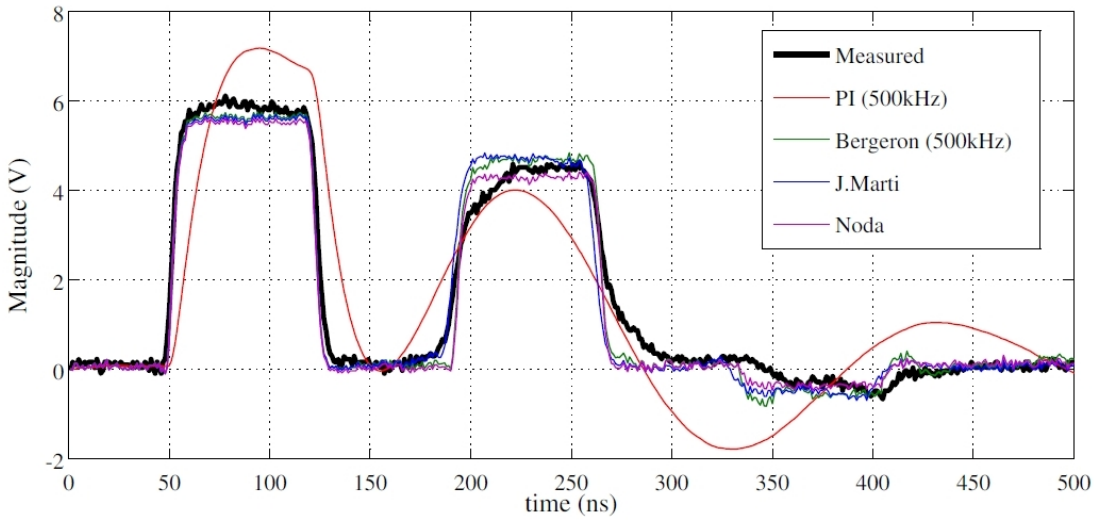

(a) Sending End

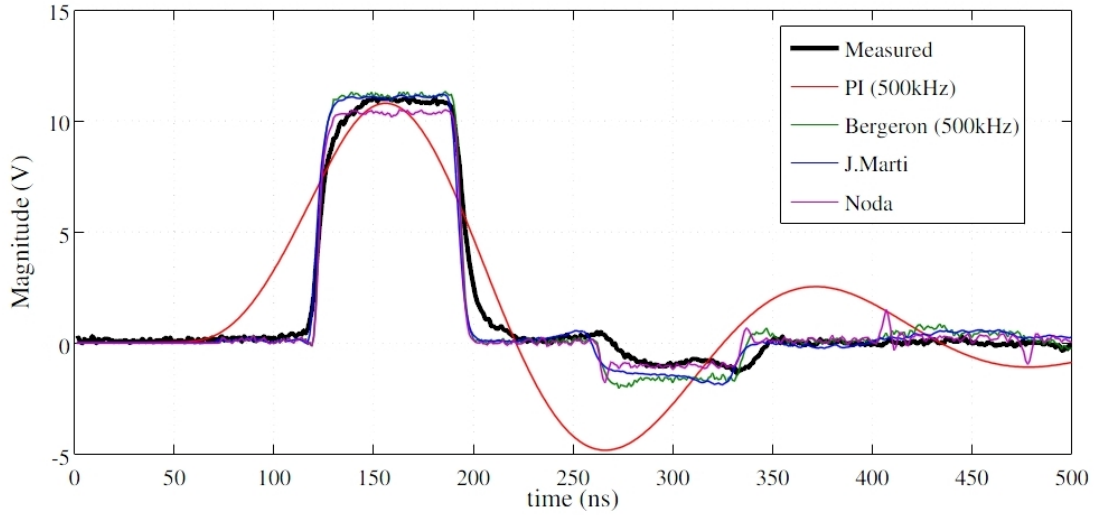

(b) Receiving End (Open)

Figure D.19: Mains Flex - Measured Live-Earth

D.4.2 Open Circuit Test - Step

Flat Twin and Earth configuration, step applied between *Live* and *Neutral*.

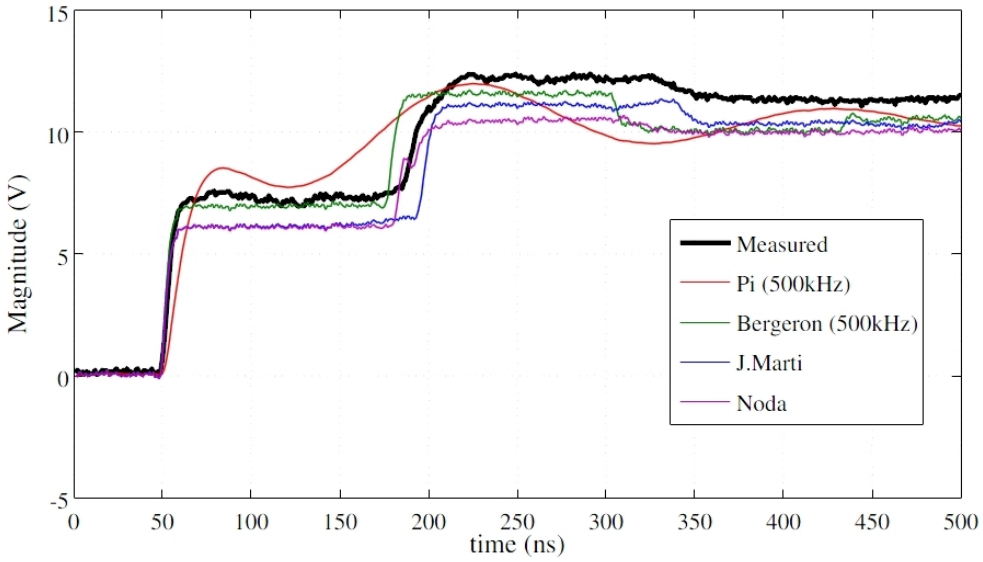

(a) Sending End

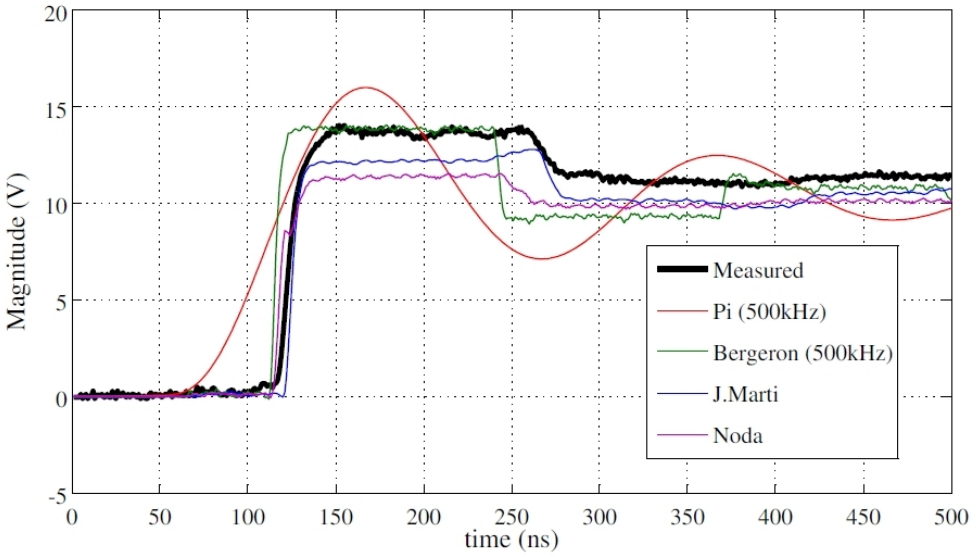

(b) Receiving End (Open)

Figure D.20: Flat Twin and Earth - Measured Live-Neutral

Flat Twin and Earth configuration, step applied between *Live* and *Earth*.

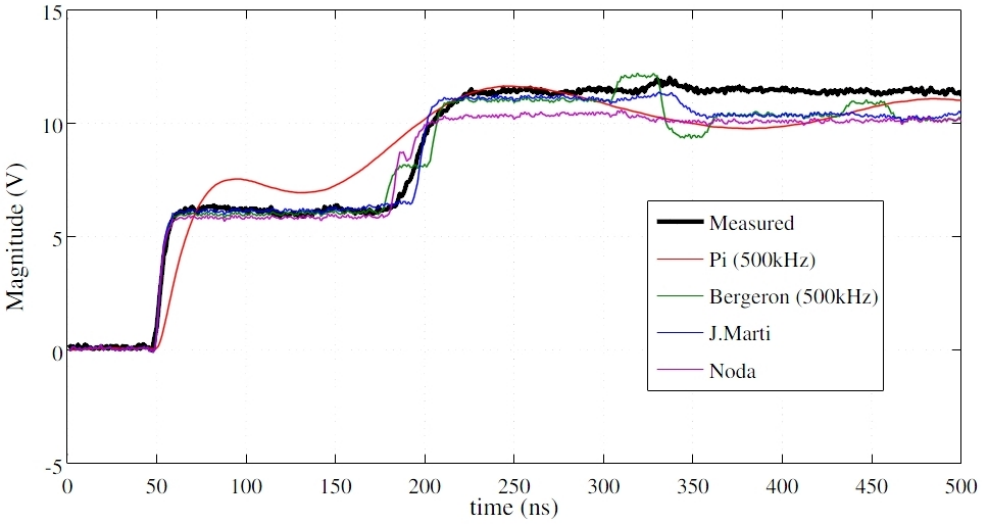

(a) Sending End

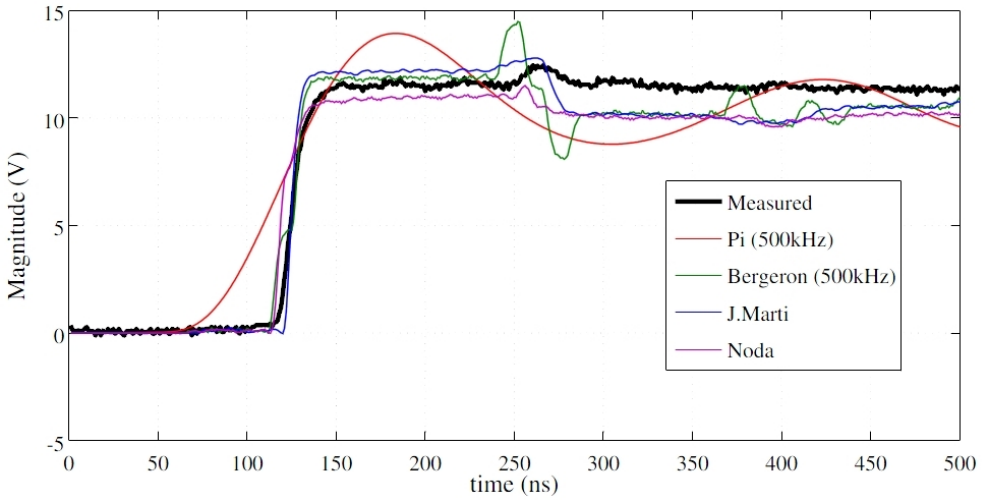

(b) Receiving End (Open)

Figure D.21: Flat Twin and Earth - Measured Live-Earth

Circular Flex configuration, step applied between *Live* and *Neutral*.

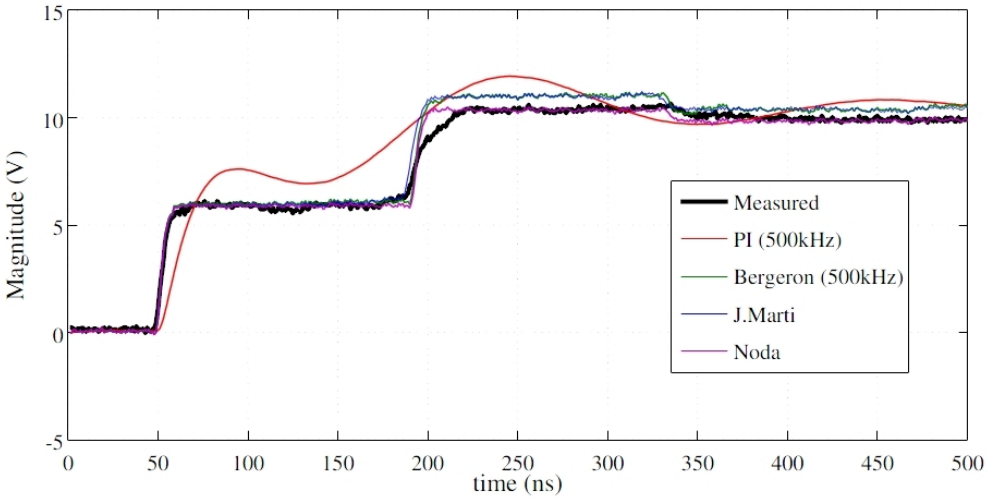

(a) Sending End

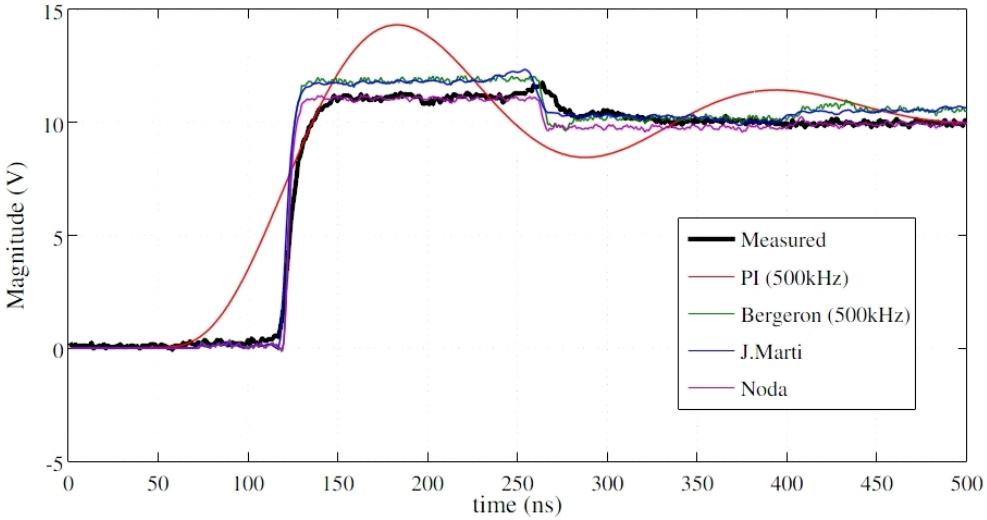

(b) Receiving End (Open)

Figure D.22: Mains Flex - Measured Live-Neutral

Circular Flex configuration, step applied between *Live* and *Earth*.

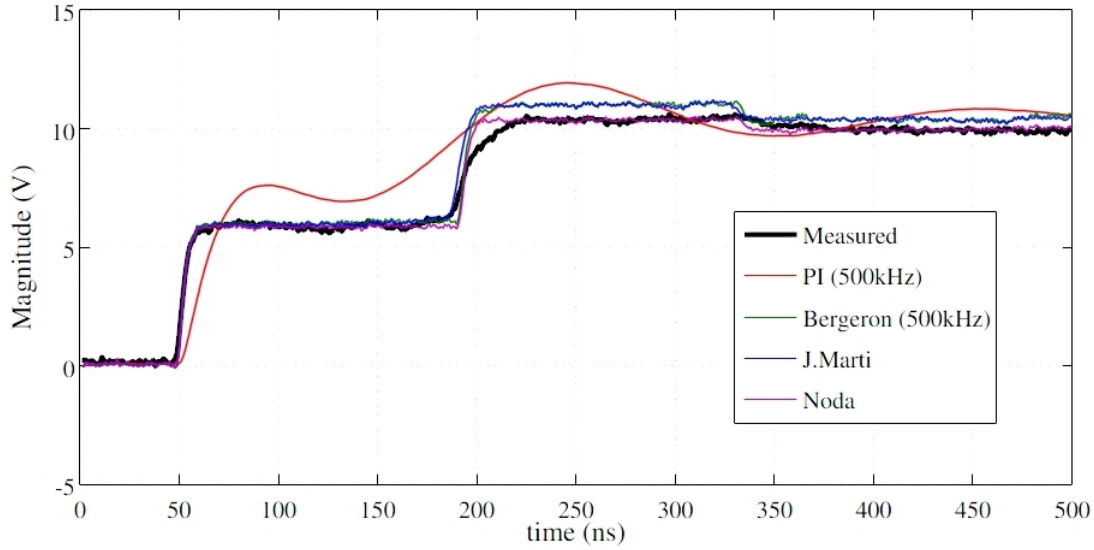

(a) Sending End

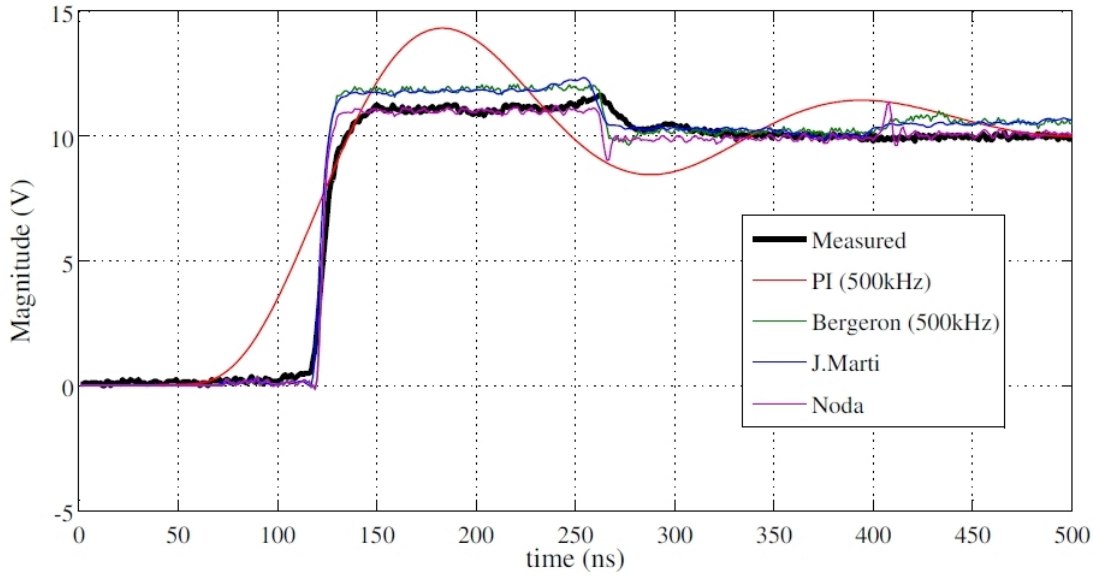

(b) Receiving End (Open)

Figure D.23: Mains Flex - Measured Live-Earth

D.4.3 Short Circuit Test - Square Pulse

Flat Twin and Earth configuration, pulse applied between *Live* and *Neutral*.

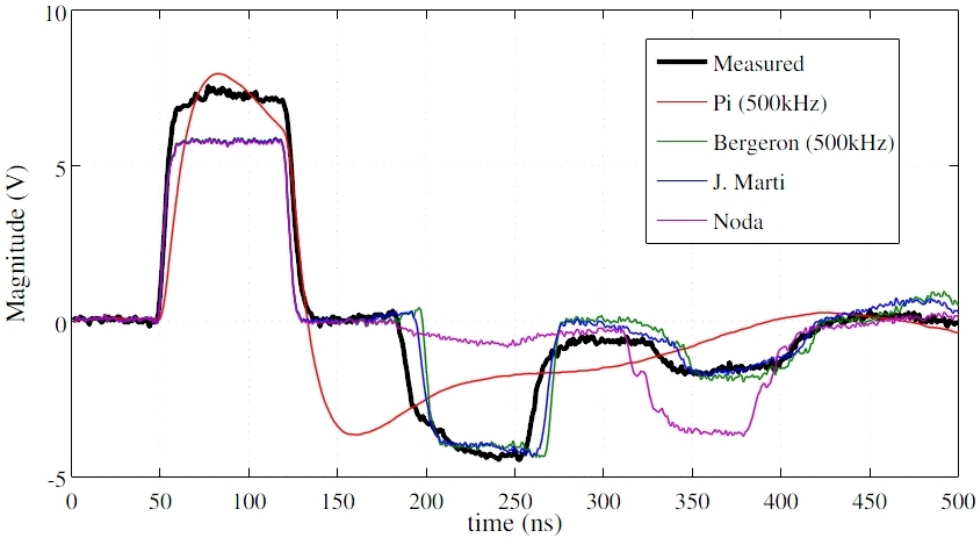

Figure D.24: Flat Twin and Earth - Pulse Applied Live-Neutral (Receiving End Short Cct)

D.5 Sensitivity Analyses

Simulations were performed to determine the sensitivity of Domestic, Urban Underground and Rural Overhead cable models to variation in soil resistivity and height/depth relative to the ground plane.

Frequency scans of the self and mutual impedance characteristics were performed by the current injection method at 1A as illustrated in Figure D.25.

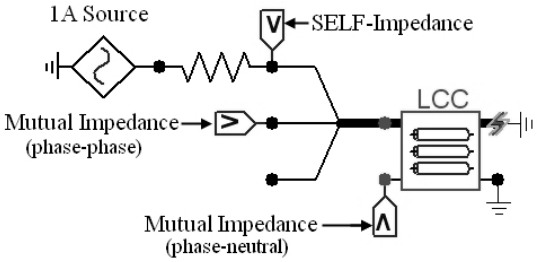

Figure D.25: Current Injection Method for Determining Cable Impedances (3ϕ)

Square pulse and step tests were performed using a TACS-controlled voltage source with a magnitude of 10V and rise time equal to one time-step Δt, behind a 50Ω source impedance (Figure D.26).

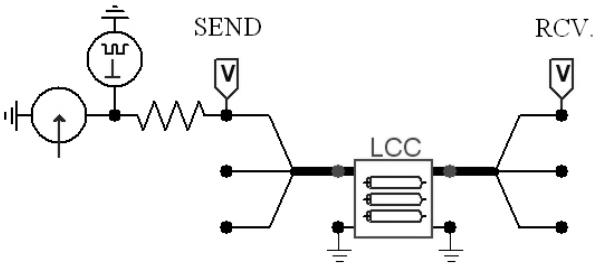

Figure D.26: Square Pulse and Step Test Simulation Circuit

Results are summarised in the following subsections.

D.5.1 Domestic Flat Twin and Earth

The following test simulations were performed on a 12 metre long section of $2.5mm^2$ Flat Twin and Earth cable as specified in section D.3.

D.5.1.1 Effects of Earth Resistivity

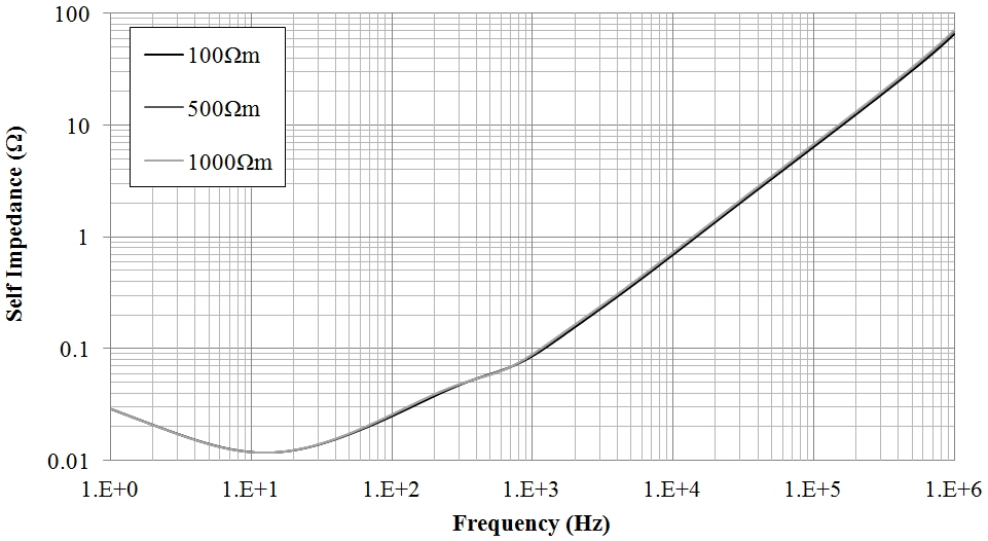

(a) Self Impedance (L)

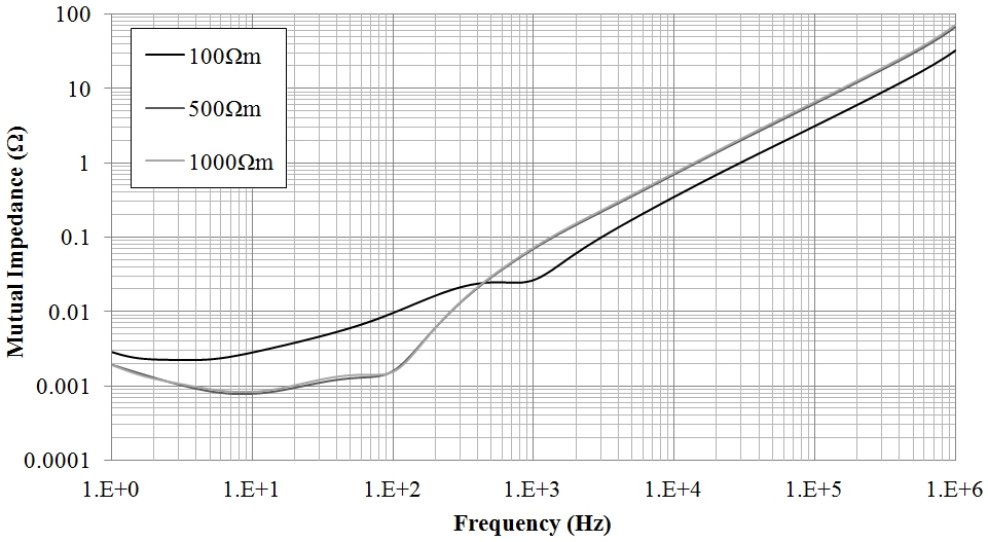

(b) Mutual Impedance (L-E)

Figure D.27: Domestic cable impedance variation with effective ρ (h=0m)

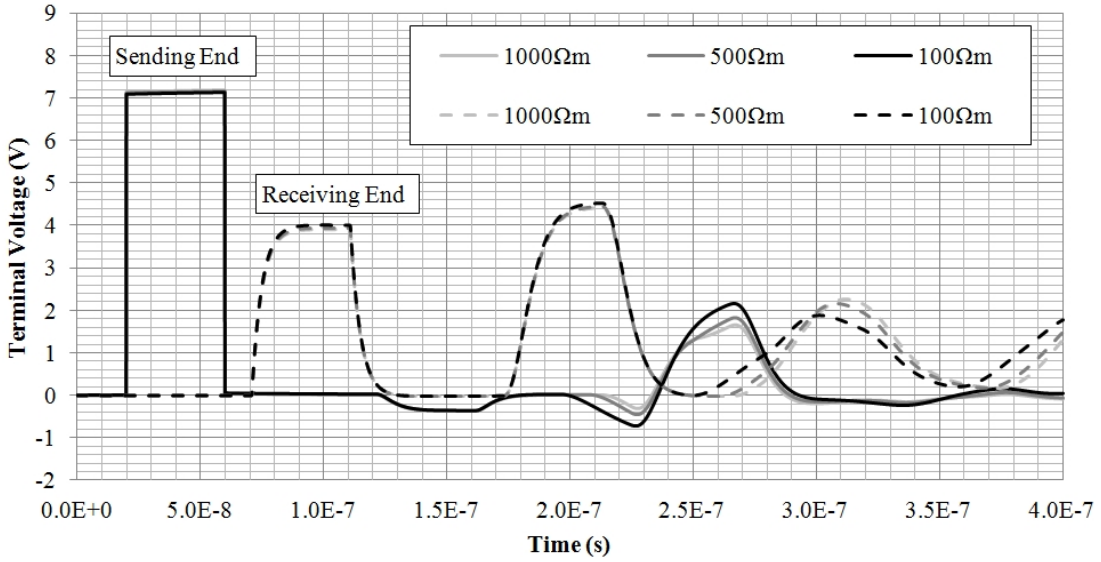

(a) Square Pulse

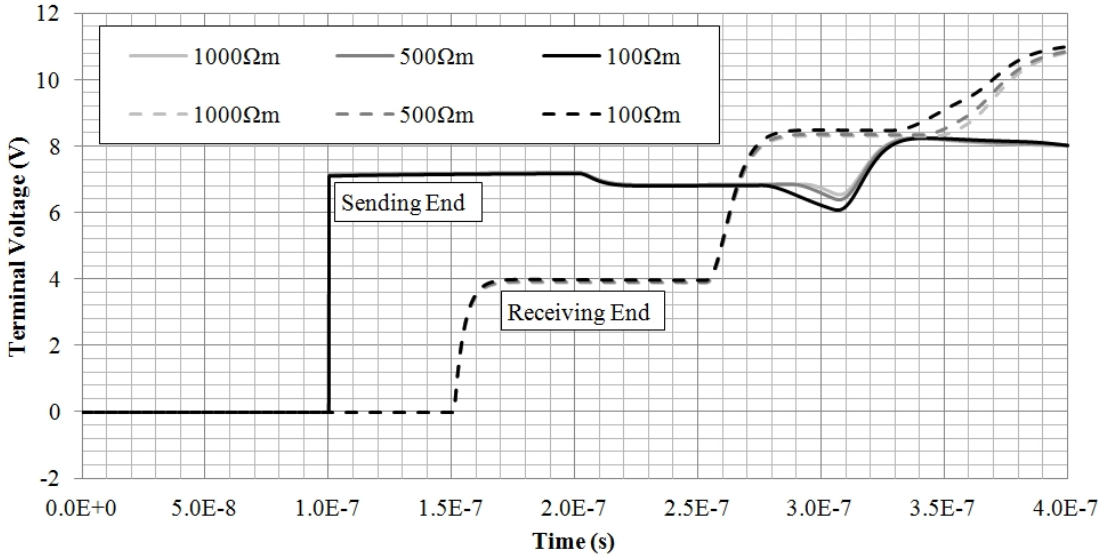

(b) Step

Figure D.28: Propagation tests with varying effective ρ (h=0m)

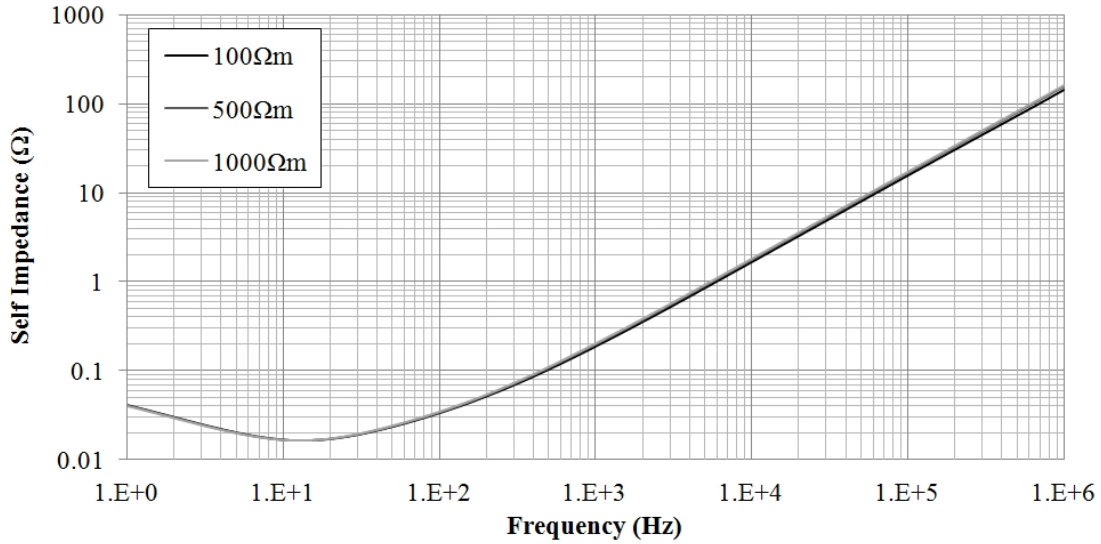

(a) Self Impedance (L)

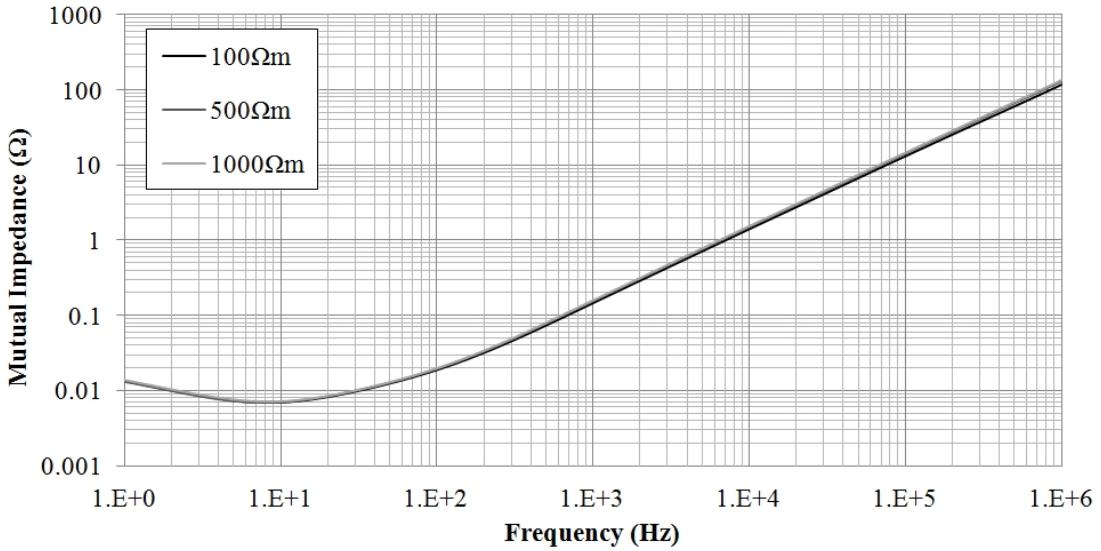

(b) Mutual Impedance (L-E)

Figure D.29: Domestic cable impedance variation with effective ρ (h=0.5m)

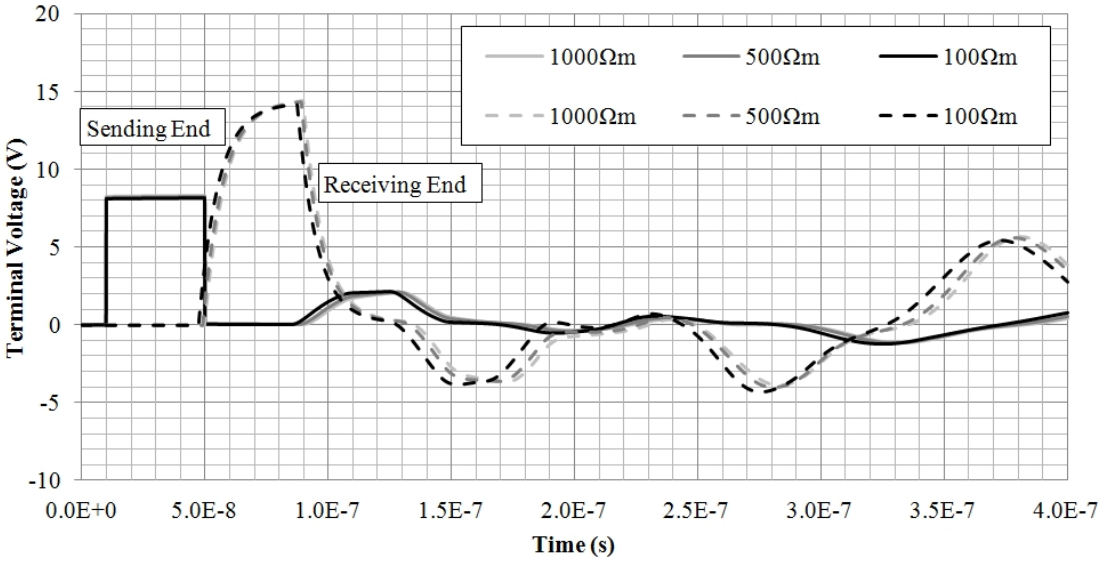

(a) Square Pulse

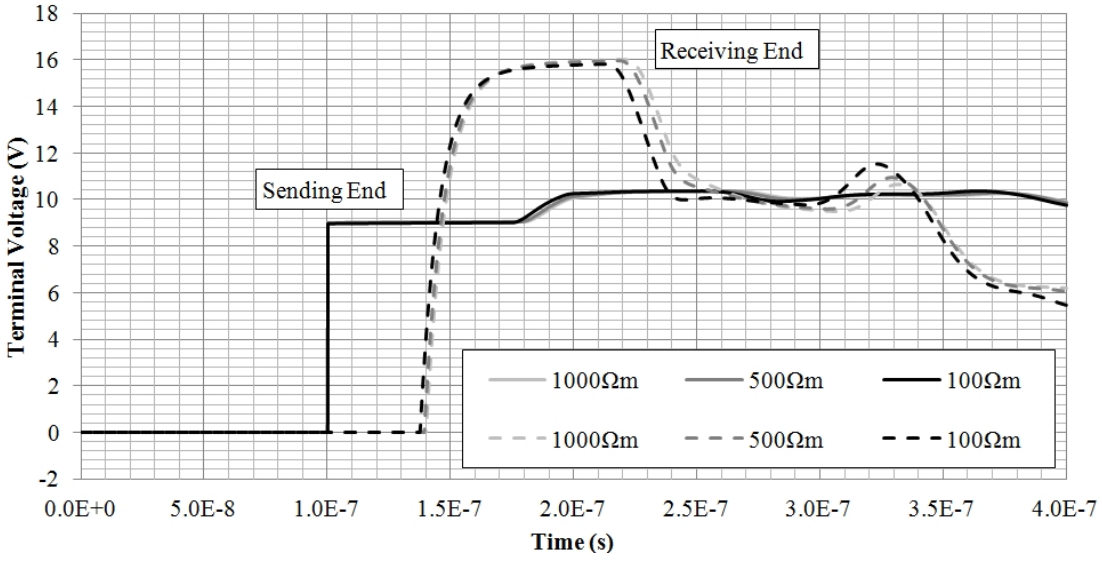

(b) Step

Figure D.30: Propagation tests with varying effective ρ (h=0.5m)

Principal observations:

- No discernible dependence of self-impedance on ground resistivity, regardless of position relative to the ground plane.
- Mutual impedance independent of ρ except in cases of very low resistivity where the conductor separation is of the same order of magnitude as cable position above ground (e.g. inside a metallic conduit).
- Minor decrease in phase velocity with increasing ρ.

D.5.1.2 Effect of Height Relative to Ground Plane

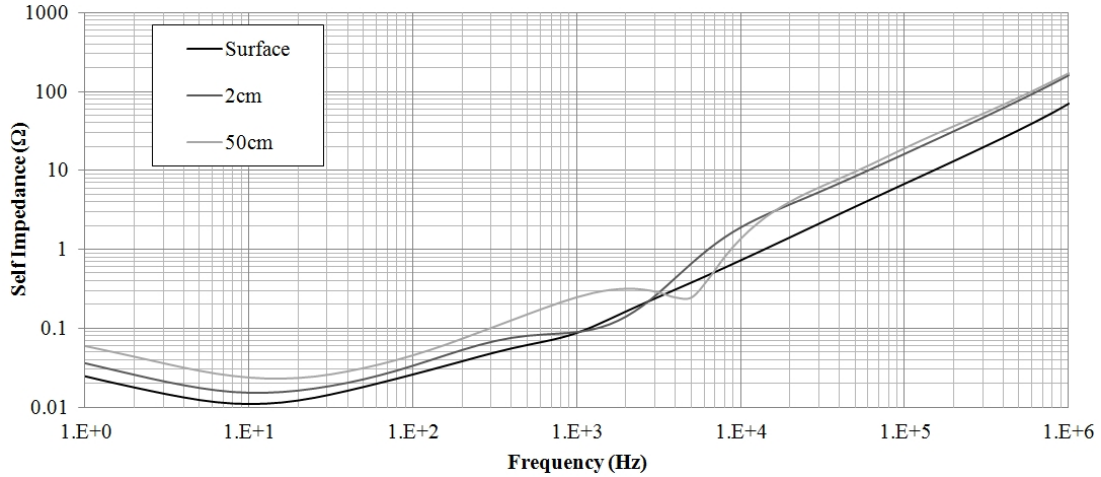

(a) Self Impedance (L)

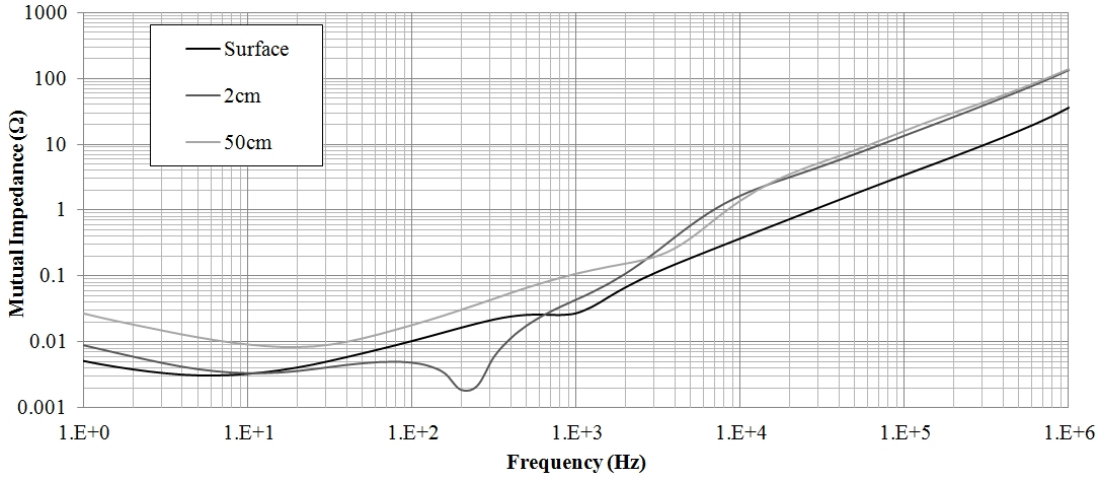

(b) Mutual Impedance (L-E)

Figure D.31: Domestic cable impedance variation with height (ρ=500Ωm)

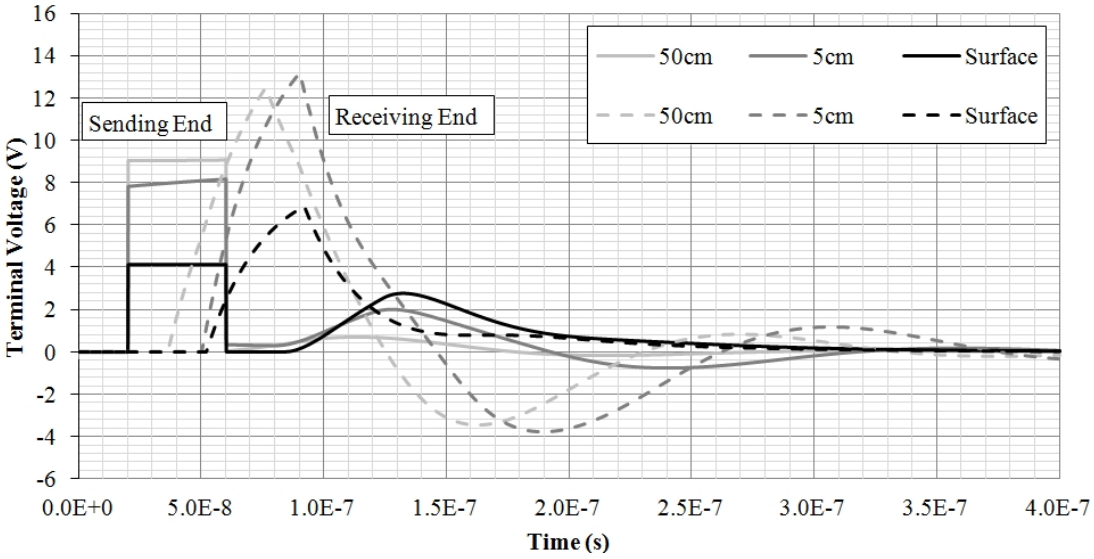

(a) Square Pulse

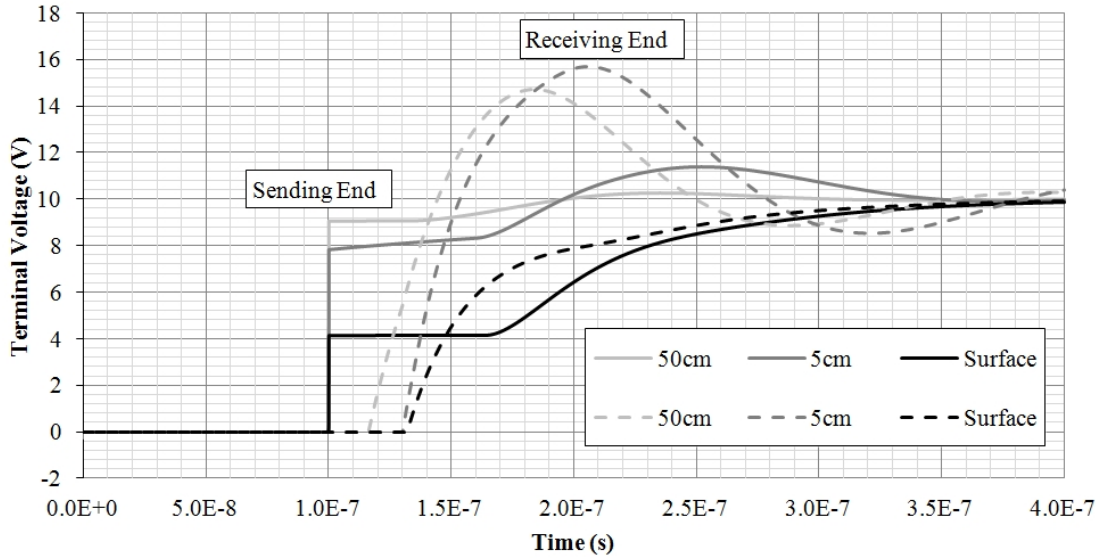

(b) Step

Figure D.32: Propagation tests with varying height (ρ=500Ωm)

Principal observations:

- Beyond h=2cm, self and mutual impedances are independent of proximity to ground at frequencies in excess of 10kHz.
- For cables at surface (h=0), both self and mutual impedances are significantly reduced at high frequency.
- Increased cable surge impedance with height (source impedance fixed: 50Ω)
- Increased propagation velocity with height

D.5.2 Urban 3-phase

The following test simulations were performed on a 75 metre long section of $95mm^2$ 3-phase Consac underground cable model (circular conductor equivalent) as specified in section D.3.

D.5.2.1 Effects of Earth Resistivity

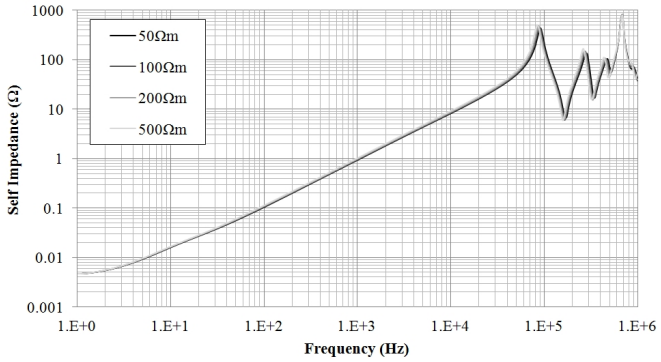

(a) Self Impedance

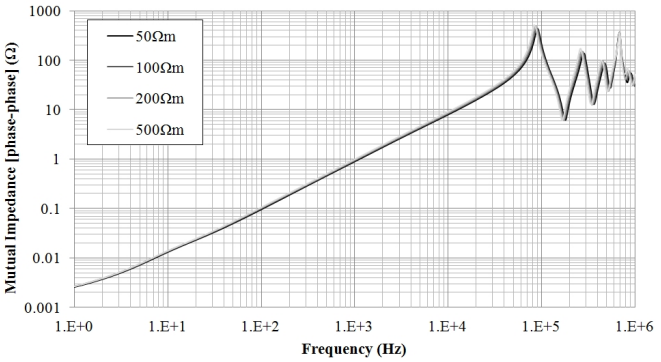

(b) Mutual Impedance: Phase-Phase

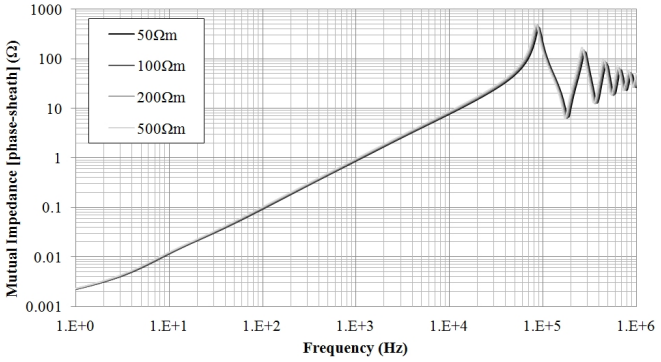

(c) Mutual Impedance: Phase-Phase

Figure D.33: Urban cable impedance variation with effective ρ (depth=0.5m)

D.5.2.2 Effect of Burial Depth

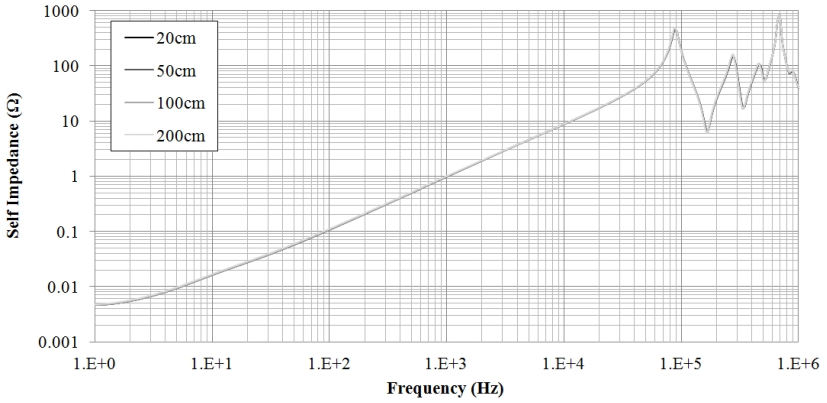

(a) Self Impedance

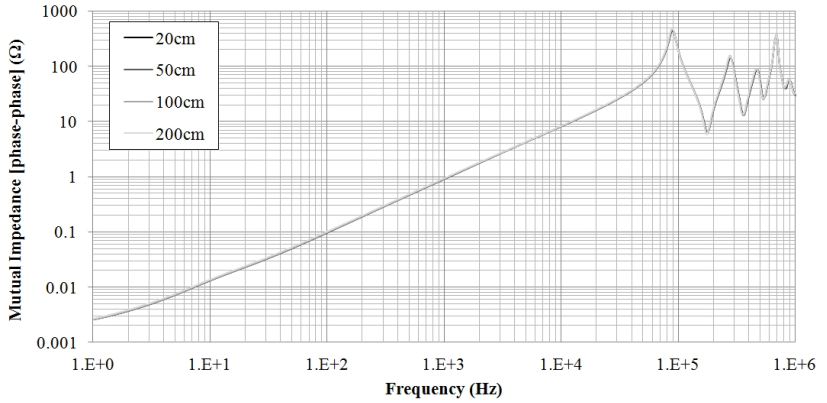

(b) Mutual Impedance: Phase-Phase

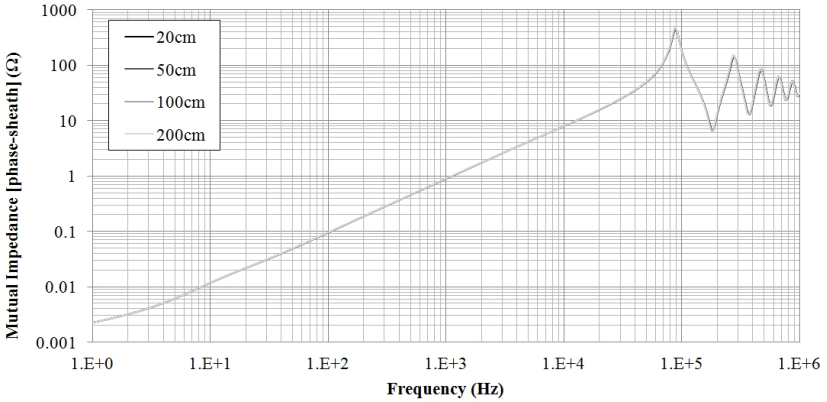

(c) Mutual Impedance: Phase-Phase

Figure D.34: Urban cable impedance variation with burial depth (ρ=100Ωm)

Principal observations:

- No discernible effect on impedance from either soil resistivity or burial depth due to the shielding effect of the concentric neutral return
- Pulse and Step test results (not shown) similarly invariant.

D.5.3 Rural 3-phase ABC

The following test simulations were performed on a 50 metre long section of $70mm^2$ 3-phase Aerial Bundled Conductor model as specified in section D.3.

D.5.3.1 Effects of Earth Resistivity

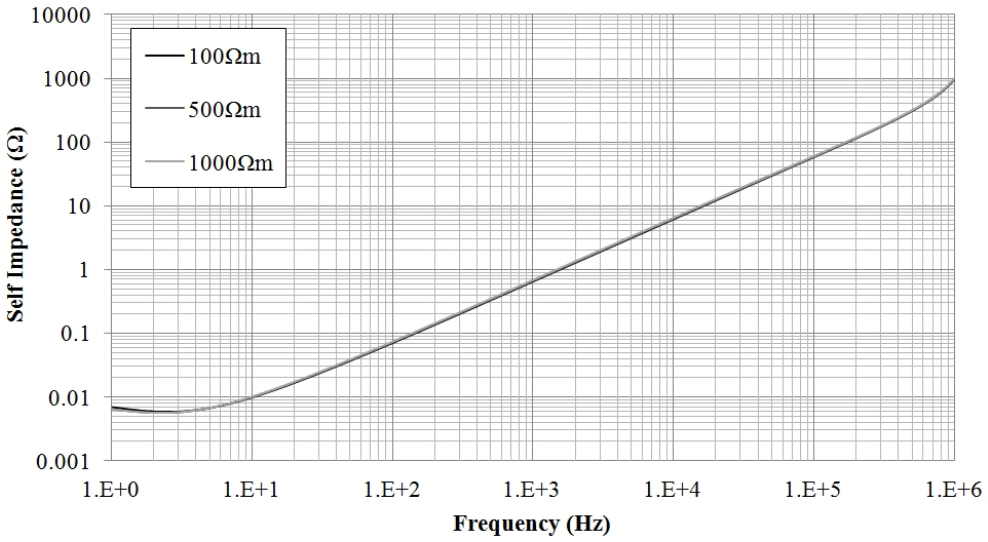

(a) Self Impedance

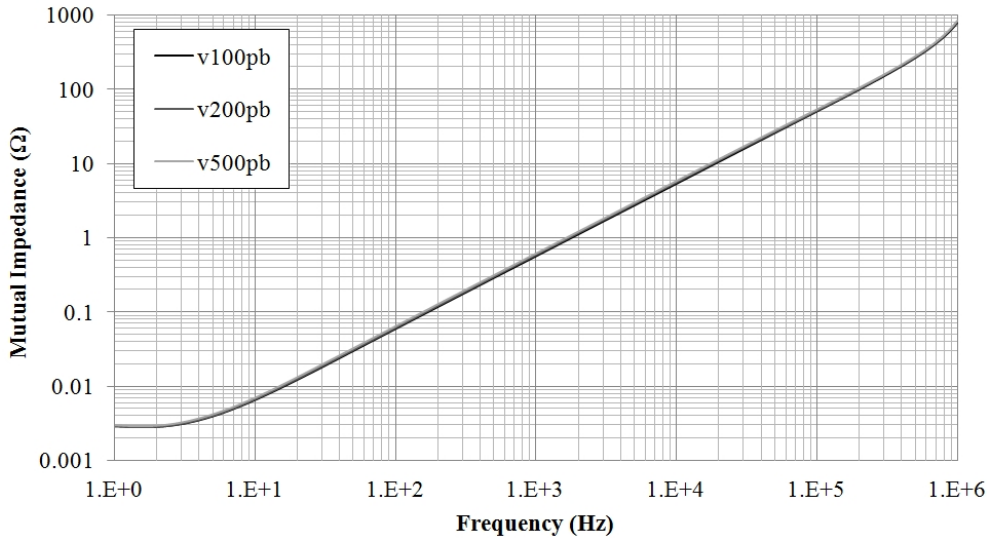

(b) Mutual Impedance: Phase-Phase

Figure D.35: ABC cable impedance variation with soil resistivity (height=10m)

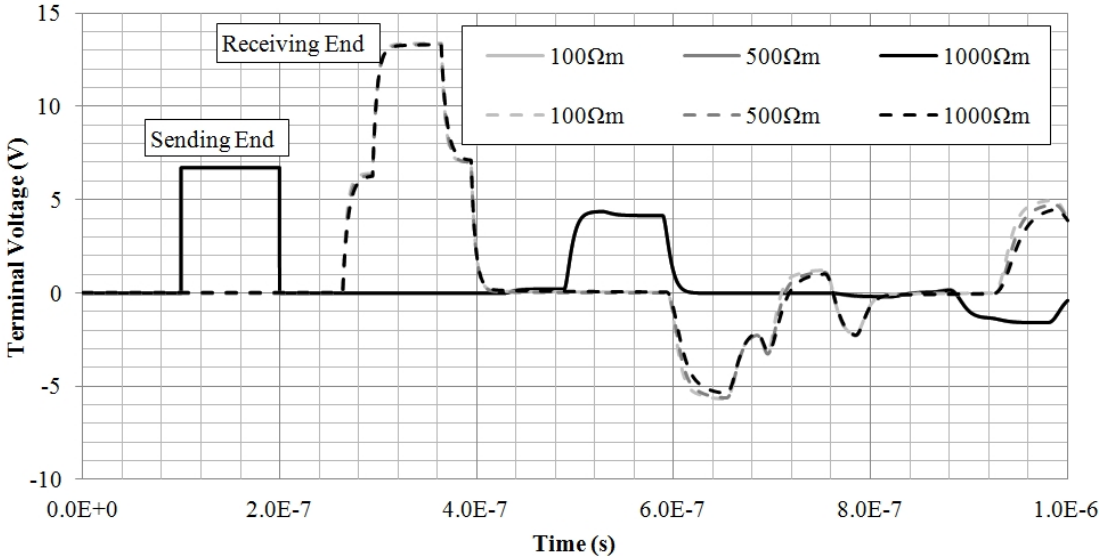

(a) Square Pulse

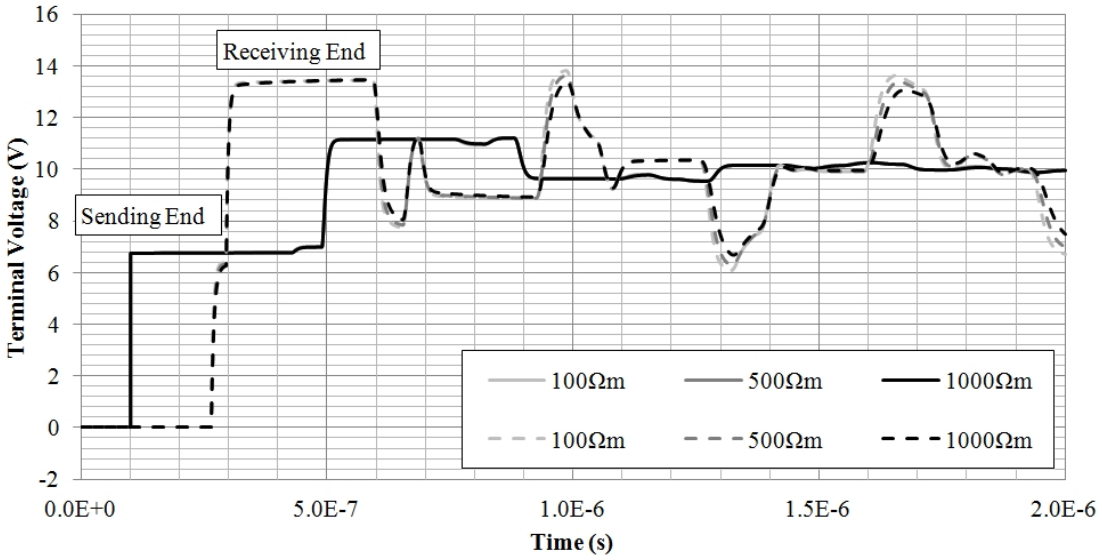

(b) Step

Figure D.36: Propagation tests (ABC) with varying soil resistivity (h=10m)

D.5.3.2 Effect of Pole Height

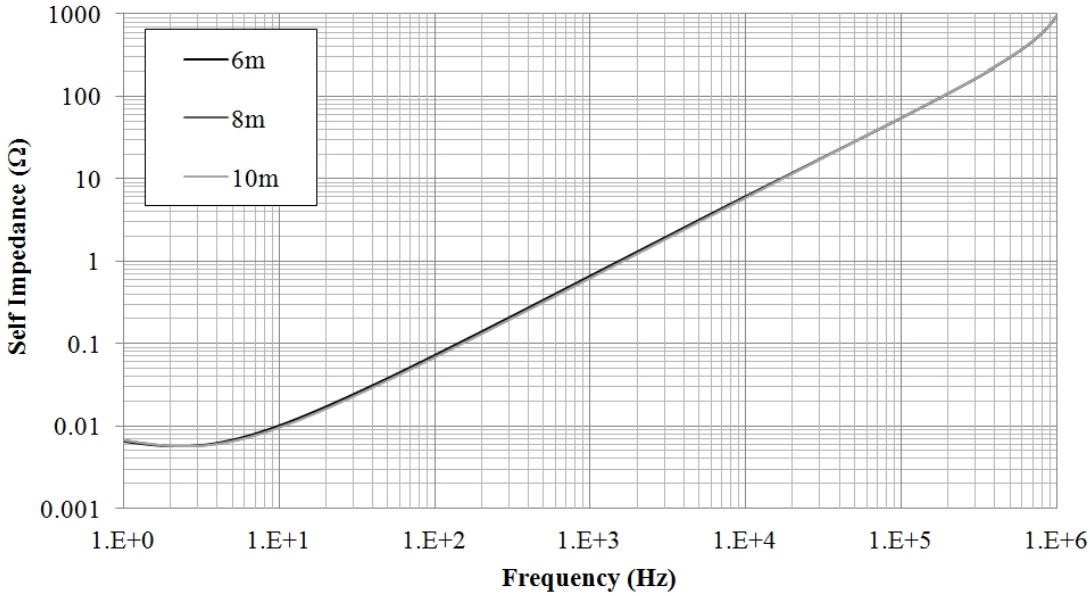

(a) Self Impedance

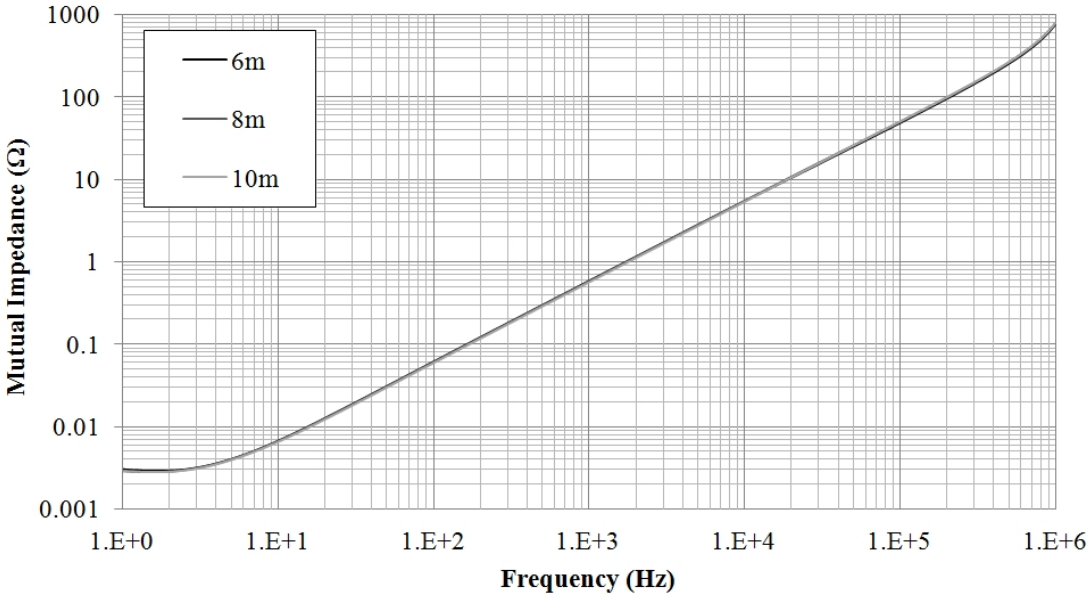

(b) Mutual Impedance: Phase-Phase

Figure D.37: ABC cable impedance variation with pole height ($\rho = 100\Omega m$)

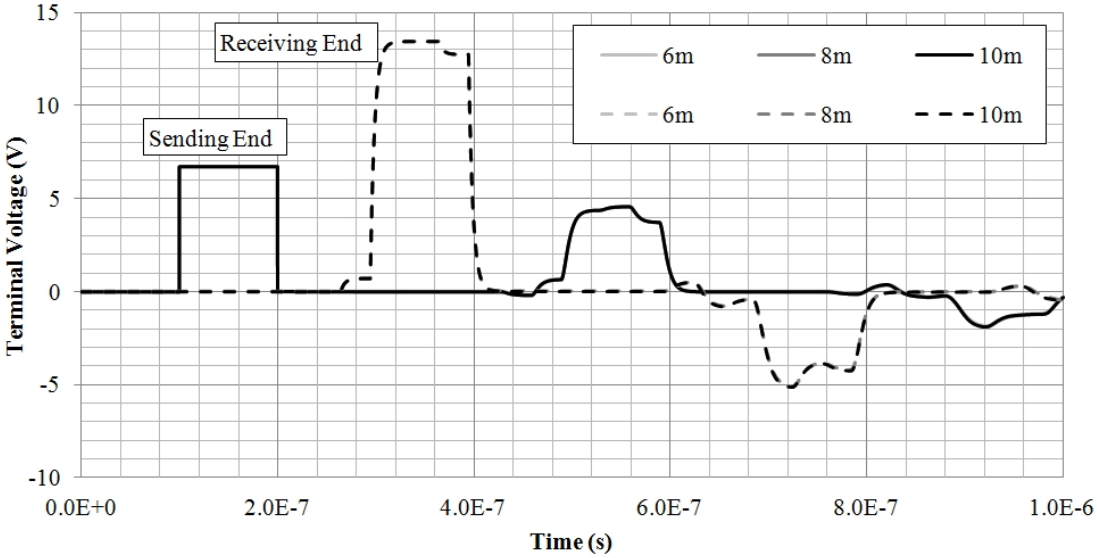

(a) Square Pulse

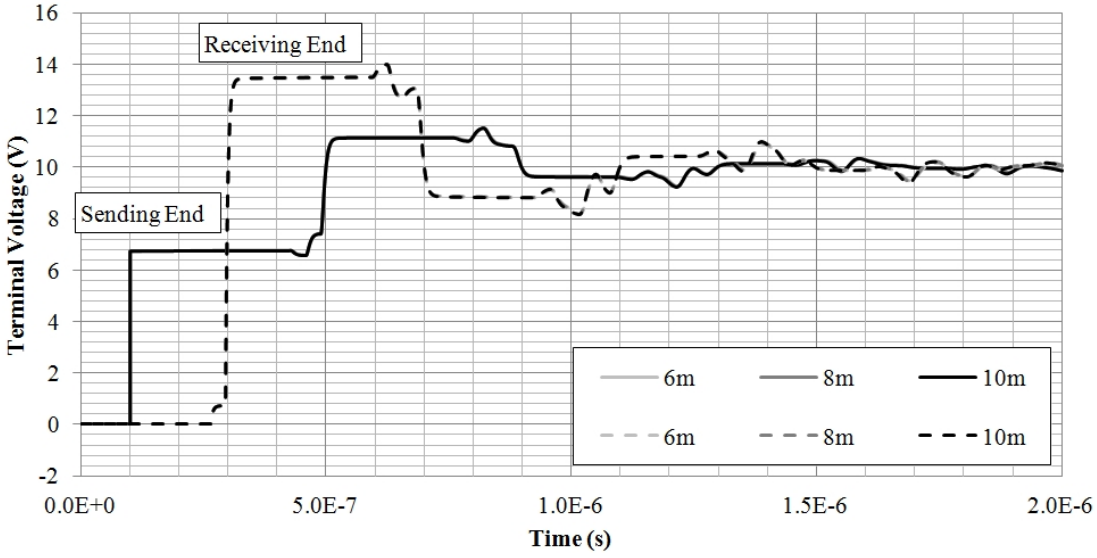

(b) Step

Figure D.38: Propagation tests (ABC) with varying pole height ($\rho = 100\Omega m$)

Principal observations:

- No discernible effect on impedance from either soil resistivity or pole height due to the relative proximity of protective earth/neutral conductor.
- No significant impact on propagation characteristics with variation in either parameter

D.6 Cable CSA Equivalence

In the absence of an established finite-element modelling preprocessor to the LCC routine in EMTP-ATP, a number of electrostatic simulations were performed in order to develop circular-conductor equivalents of sectored cables common to Urban underground networks. In making the transition between geometries, conductor cross-sectional areas are preserved but the use of circular conductors increases the overall cable diameter, and more significantly it reduces both inter-phase and phase-neutral capacitances (C_p,C_n) as depicted in Figure D.39.

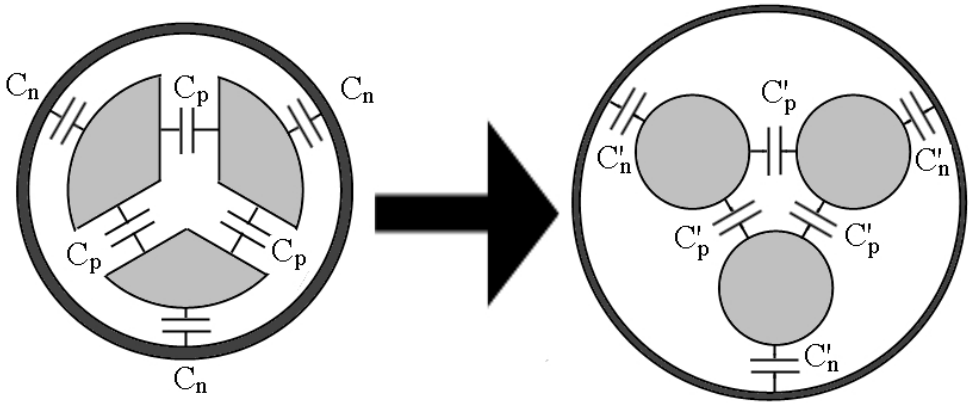

Figure D.39: Inter-phase and phase-neutral capacitances of Sectored and Circular cable models

This may be rectified by the introduction of a fictitious permittivity ε_r' for the insulation of the circular cable model which, assuming an homogeneous dielectric region has no impact on the series impedance of the cable. As shunt conductance is ignored in the model, there is no need to scale to account for dielectric loss. Capacitances C_p and C_n were determined by finite element analysis using the Electromagnetic Field package SLIM. Figure D.40 depicts the simulated sectored cross-section and its field and equipotential distributions in even and odd mode excitation.

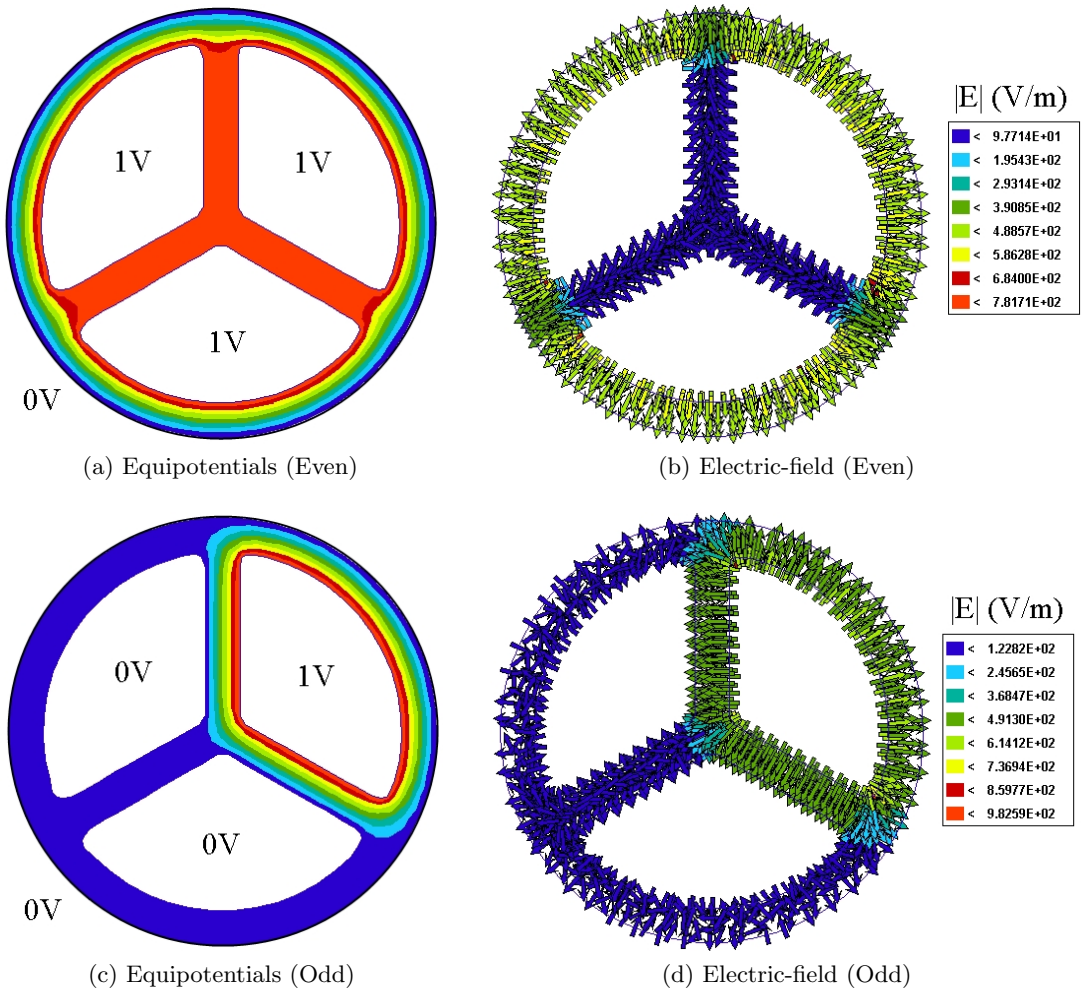

(a) Equipotentials (Even)

(b) Electric-field (Even)

(c) Equipotentials (Odd)

(d) Electric-field (Odd)

Figure D.40: Sectored Cable Geometry in SLIM

From odd- and even-mode excitation of the cables, capacitances can be calculated from the global electrostatic energies (U) output from the solver by the following equations:

$$C_n = \frac{2}{3} \cdot U_{even} \tag{D.1}$$

$$C_p = U_{odd} - \frac{1}{2} \cdot C_n \tag{D.2}$$

Figure D.41 depicts the equivalent cable geometry employing circular conductors, as modelled in SLIM. Minimum insulation thickness according to BS7870-3 is maintained.

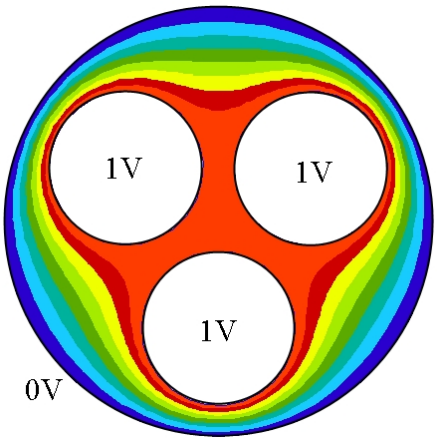

(a) Equipotentials (Even)

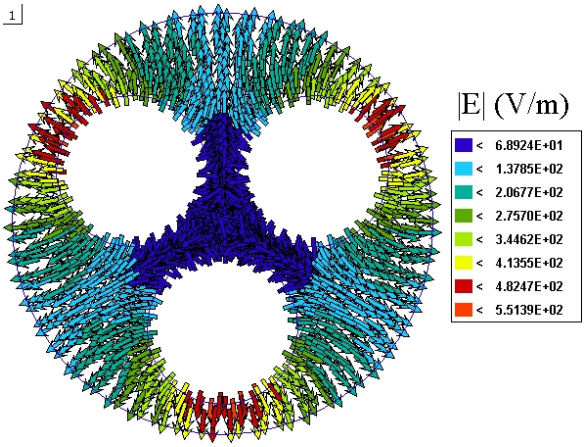

(b) Electric-field (Even)

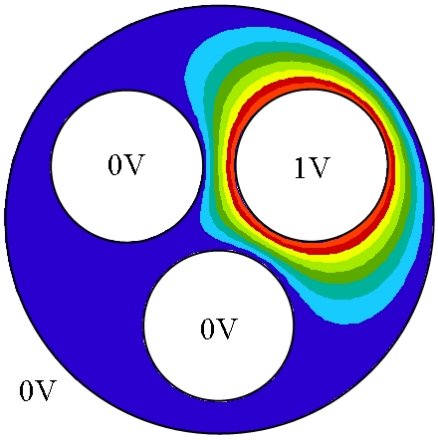

(c) Equipotentials (Odd)

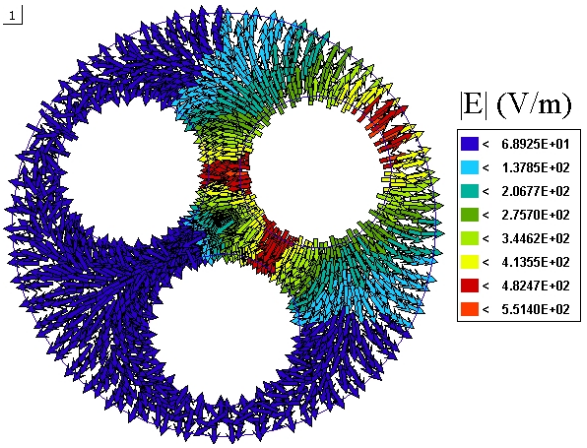

(d) Electric-field (Odd)

Figure D.41: Circular Cable Geometry in SLIM

Application of equations (D.1) and (D.2) to both cases gives the following capacitance ratios:

$$\frac{C_p}{C'_p} \approx \frac{C_n}{C'_n} \approx 1.6$$

A scaling of the insulation permittivity by this ratio yields inter-phase and phase-neutral capacitances corrected to within 10% of those of the original sectored geometry. This correction factor is used to specify the internal dielectric region of all 3-phase LV underground cable models used in this work.

Appendix E

Proposal for Update of the Solar Energy Laboratory (May 2010)

E.1 Introduction

The following document outlines a number of proposals for the modernisation of the School of Engineering's Solar Energy Laboratory, with a view to increasing its usefulness as a tool for teaching and research in electrical power and energy. An outline of the current equipment and laboratory configuration will be given, followed by proposals for purchases, upgrades and replacements. Where available, indicative cost estimates have been included in Section E.4.

E.2 Current Laboratory Configuration

The current setup is much the same as it was when the laboratory was originally commissioned, with the lamp array and power supplies remaining in place unchanged since the mid 1980s. As a result, much of the equipment is rather dated, and the running costs of the lab are considerably higher than modern counterparts. The laboratory is subject to a intensive maintenance regime, which due to access limitations means even minor jobs require considerable down-time and workshop intervention.

The lamp array in W/1.07 consists of 36 1000W mercury arc lamps, arranged in a 6x6 array. Power is supplied to the lamps from a 3-phase incomer, via a pair of voltage conditioning units, master variacs, and a bank of individual lamp ballast circuits with dimmer controls as shown in Figure E.1. A secondary supply is also wired to each lamp to feed the firing circuitry, though these circuits are controlled in groups of 3 from the wall-mounted push-button triggers.

The shortcomings of the current laboratory configuration may be broken down into the following key areas:

E.2.1 Lamps

The lamps currently in use are General Electric CID 1000W PAR 64 Mercury Halide Discharge. These lamps require a stable, finely controllable 250V ac supply, in order to maintain an on-load terminal voltage of 77V. In addition, a 9kV trigger circuit is required in order to initiate the arc across the lamp.

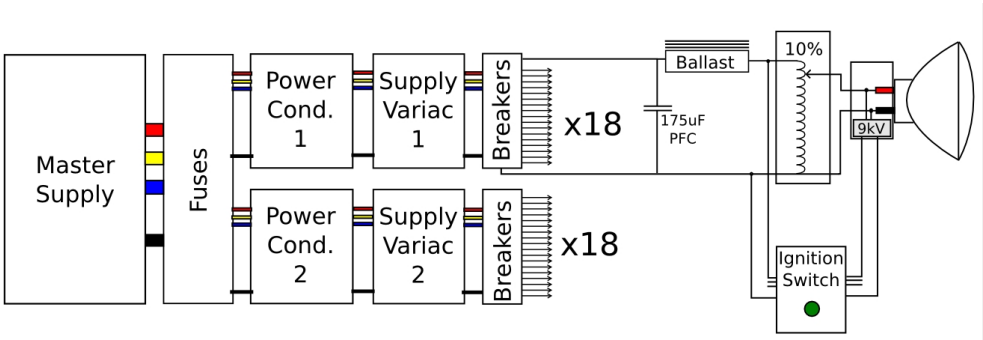

Figure E.1: Basic Lamp Supply Circuitry

Since harmonisation of the university supply to the European 230V standard, the lamps in the array have been running at below their rated voltage, a problem exacerbated by a number of faulty power factor correction capacitors. Discharge lamps of this type are by their nature highly sensitive to variations in voltage, and will typically not ignite if the supply drops below approximately 90% of the rated value. A small range of dimming may be achieved by varying the supply between 90-100% of the rated value, however the functionality of the control variacs has largely been lost since moving to 230V, such that at full supply the lamps are confined to the lower end of their operating range.

The reduced and varied terminal voltages mean that typical lamp brightness is considerably lower than in the original specification, lamp operating lifetimes are reduced, and certain lamps will often refuse to fire on the first attempt, requiring a 30-minute heat/cool cycle for those lamps which operate successfully before re-firing. At a replacement cost in eccess of £150 per lamp, the present system is economically unsustainable.

E.2.2 Ignition

Ignition for the lamps is provided by 12 normally-open 3-phase switches mounted on the wall of the laboratory. When a switch is held closed, power is supplied to the 9kV ignition circuits of three of the lamps. The ignition switches should only remain closed for maximum of 5 seconds, by which time all three lamps should ignite. As mentioned above however, ignition is not always successful and one of the lamps will require firing again.

This is the key problem with the current ignition scheme, in that individual control of the lamp igniters cannot be achieved if the lamps fire in groups of 3. It is also bad practice to re-fire lamps which are already lit, since this drastically reduces the life of both the lamp and igniter. A failed ignition therefore requires that the two operational lamps be cycled through a 10-minute warm-up period, and following extinguishing be allowed to cool for a further 20 minutes to allow the mercury vapor to deposit in the well of the lamp. Only then can the three lamps be successfully fired again. This makes failed ignition a major time-consuming factor in any testing regime.

E.2.3 Ballast and PFC

As with all forms of discharge lamp, the solar array requires a ballast in order to maintain a steady arc across the lamps. In addition, due to the low power factor of

such arcs, considerable correction is required in the form of large capacitors across the lamp terminals. Each lamp supply circuit is provided with a large ballast inductor and 175uF capacitor in order to maintain near unity power-factor, though this is somewhat compromised by running at a lower than specified supply voltage.

The ballast and PFC circuitry, although still functional, is no longer suitable for the job it is required to perform. A number of the ballast units require replacing as they produce excessive levels of noise when operational, and some of the PFC capacitors have failed resulting in drastically reduced lamp terminal voltage.

E.2.4 Dimming

In addition to the lamp ballast, a degree of dimming control was incorporated into the original design through the use of individual supply variacs. The 36 control variacs, mounted on the ballast panels running along the side of the laboratory, allow the supply volts to be dropped to approximately 90% of the rated value in order to reduce the arc intensity of individual lamps.

While the benefit of such a scheme in maximising the uniformity of emmitted radiation can easily be appreciated, the functionality has largely been lost since supply voltages were reduced to harmonised levels. Running at an upper voltage of 230V now means that lamps are confined to the lower end of their useful range, and any attempt to further reduce the supply volts will quench the arc. Any future scheme based on discharge lamps and requiring intensity control will need this issue addressing.

In addition to the operational limitations of the dimming circuitry, there is the practical issue of access and maintanance. Due to the physical size of the control panel, it is not actually possible to bring the lamp array down to ground level for maintenance as the crane is obstructed. It must therefore be suspended on 1m supports, making it very difficult to get access to the centre of the array to replace lamps and check the firing circuits.

E.2.5 General Circuitry and Labelling

Fault-finding and maintenance on the control and ballast circuitry is complicated by a general lack of color-coding and labelling. Faulty circuits need to be traced through by hand in order to know which ballast, dimmer control or PFC cap relates to which lamp, and half of the dimmer variacs are unlabelled. This makes it a complex and time-consuming process to determine the cause of faults on the system.

Since any change in lamp technology will require an overhaul of the supply, a fully-labelled, traceable system should be a priority in order to improve accessability and cut maintenance down-time.

E.3 Proposals

The following section outlines a number of proposals for upgrading or modernising the laboratory.

E.3.1 Lamp Array and Control Gear

Due to the range of lighting options available, there is no single ideal configuration that a new array should take. Each technology has its benefits and limitations, and the final decision will need to strike the best balance between functionality, flexibility and cost. There follows some examples of new configurations, with a breakdown of requirements in each case.

E.3.1.1 Option 1: Cold-Restrike Mercury Halide Discharge

The first option is to continue with cold-restrike mercury arc lamps, identical to those used in the present rig. This would allow continued use of the existing lamp housings, but the power supply, dimming and firing circuitry would require major overhaul. Firstly, the power supply to each lamp would need to be boosted back above 240V in order to bring the lamps back into a respectable operating range, though as already mentioned the dimmable range of the current lamps is small. The easiest way to achieve a correct operating voltage would be to adjust upper voltage limit of the master variacs, which should be simple enough as the units are rated for 470V 3 phase.

In addition, ageing PFC and ballast units would need servicing or replacing in order to balance out performance across the array, and the trigger circuits should also be replaced with modern high-voltage igniters, with individual firing control. In its current state, due to the limited functionality of the lamp dimming circuitry, the individual control variacs are of little or no use in any test regime. If dimming capability were deemed a requirement then the supply variacs would need to be maintained, however halogen lamps would be a far more suitable choice in this case due to their wide operating range.

Figure E.2 depicts the recommended GE setup for cold-restrike lamps. The drawback of this option, in addition to high replacement cost of faulty equipment and the need to maintain the bulky ballast and PFC banks, is the high lamp replacement cost. At approximately £125 + VAT each a full array replacement would cost approximately £5500, with a rated lifetime of 1500 hours. Through the use of individual ignition switches, much of the problem caused by the need to cycle lamps between firings is removed, but it does not negate the need to cycle array between tests. This drawback can be overcome by the use of hot-restrike lamps, as outlined in option 2. For a full cost breakdown of this option, see Section E.4.1.1.

E.3.1.2 Option 2: Hot-Restrike Mercury Halide Discharge

An alternative configuration using hot-restrike discharge lamps could also be implemented. This would eliminate the need to cycle the lamps after each operation, which would reduce testing time and also make the lab more suitable for short teaching demonstrations. As with option 1, this would allow us to keep the existing frame and lamp holders, and the requirements for ballast, PFC and firing switch replacement would be the same.

The main difference in this case would be the need for hot-restrike igniters. These are more expensive than their cold-restrike counterparts, with the recommended GE model costing about £450 each. Furnishing a complete lab with 36 hot-restrike igniters represents a major expense, and therefore makes this the most expensive option in terms of initial investment. In addition, running costs wuold remain high as hot-restrike lamps

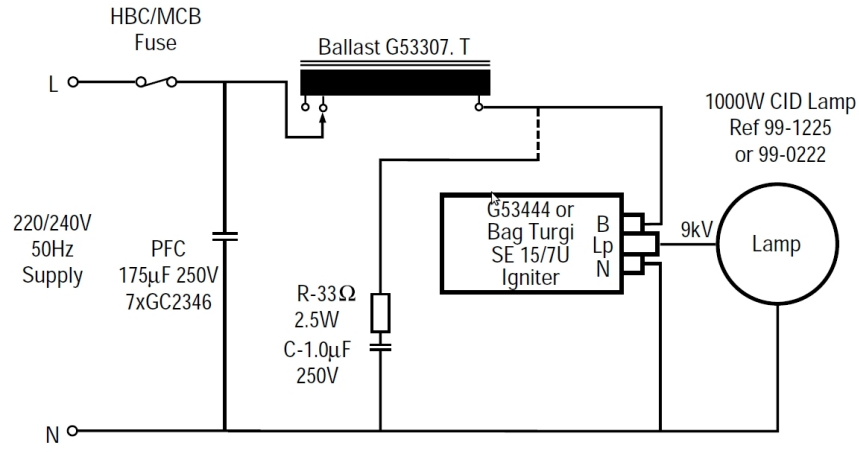

Figure E.2: Recommended Circuit for Cold-Restrike Mercury Halide Discharge Lamps

cost a little more than cold-restrike, and are rated for only 1000 hours. See Section E.4.1.2 for cost estimates.

Figure E.3 shows how a hot-restrike mercury halide array would be constructed

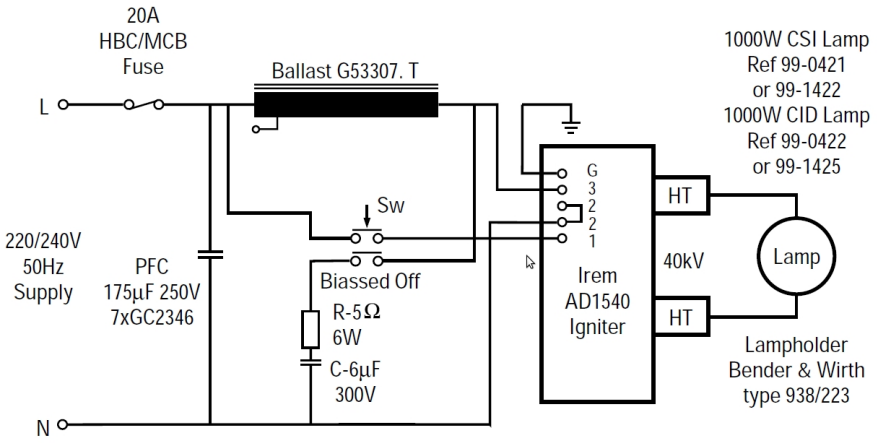

Figure E.3: Recommended Circuit for Hot-Restrike Mercury Halide Discharge Lamps

E.3.1.3 Option 3: Halogen Spot

As an alternative to the use of arc-lamps, it would be possible to design an array with comparable performance using parabolic halogen stage lights. These lamps present a number of advantages over the discharge lamps currently in use. A system based on halogens would be capable of a wider and more easily controllable range of dimming, would negate the need for ballast circuits altogether, and lamps would be easier and cheaper to replace than at present. Halogens also maintain a steadier brightness over their lifetime, and are easier to dispose of when failed

One drawback of halogens however is the significantly shorter lifetime of around 300

hours. Lamps will therefore need replacing about four times as often as at present, but at a cost of £20 + VAT per lamp, this still represents a much lower running cost than at present. There will also be the likely initial investment for 36 new lamp housings, as it is impossible to find PAR 64 halogens with G38 connectors. It may however be possible to retorofit the existing equipment with adapters, assuming that the current housings are capable of dissipating the eccess heat generated by halogen lamps

The most interesting opportunity presented by moving to halogen however is the option of using an off-the-shelf, robust stage lighting system. This would replace the existing bulky ballast, PFC and dimming circuitry, which could then be removed entirely, creating useful additional space for storage and maintenance. In its place would be a compact, wall-mounted 36-channel power-electronic dimmer, with a DMX connection to desk-mounted control board which could be located either in the laboratory itself, or in the 2nd floor control room.

This would allow the user to start up, dim, and shut down each lamp individually from a workstation, giving a degree of flexibility and control not possible with the current setup. A DMX controller could also be programmed to simulate the change in light intensity throughout the day if required. Such a system could be purchased for less than £2500, making this a more attractive initial investment than moving to hot-restrike discharge lamps. Figure E.4 provides an example of the equipment required to implement such a system. For cost estimates, see Section E.4.1.3.

(a) Halogen PAR (b) 18-Channel Dimmer Unit (c) DMX Control Panel

Figure E.4: Stage-Lighting System Components

E.3.1.4 Option 4: Halogen Flood

An alternative to spot lamps is to use halogen flood lights. The hardware requirements in this case would be identical to that outlined in option 3, as lamp ratings and connections would be the same. This highlights another degree of flexibility afforded by a halogen-based system in that it is possible to switch relatively quickly and cheaply between different lamps as the present test regime requires.

While spot lamps are useful for high intensity or small-area testing, a flood array would be ideal for maintaining a high degree of uniformity over large areas such as a militple-panel photovoltaic array. This capability would greatly reduce the effect of localised hot-spots which currently limits the test performance of PV cells. Halogen

floods have the same unit cost and rated lifetime as spots, with a full compliment of 36 costing less than £1000.

E.3.2 Access and Maintenance

A key contributor to laboratory downtime is the lack of dedicated equipment for the purpose of lamp replacement and general maintenance. At present, if a lamp is lost from the array the one-tonne rig must be transferred to a crane hoist, moved horizontally into position and lowered face-down onto four support structures at a height of about 1m from the ground. Since this arrangement only allows access to the lamps along the edges of the array, any central lamps must be replaced with the array in an upright postion where they can be reached from the floor. This allows the rig to swing dangerously on the crane hoist during maintenance which should be avoided.

To address these problems, the workshop recommendation is to purchase a dedicated lightweight scaffold tower of a suitable height to reach each of the 36 lamps in its upright position. Towers such as those shown in Figure E.5 are available for about £700, with a working height of 5.5m, or £1000 for working height of 7.15m.

(a) 3.5m Platform (b) 5.5m Platform

Figure E.5: Lightweight Mobile Scaffold Towers

Mr. Paul Farrugia has expressed concern, particularly from a safety perspective, over the continued use of the crane hoist for lifting and moving the lamp array. It is suggested that the current system be replaced with an X-Y drive system running either on a pair of fixed uprights or a rolling floor-mounted rig. This would give us the same if not a greater degree of manoeuvreability, allowing us to bring the array as close as required to the test object, wile completely eliminating the problem of the rig swinging and bouncing on the crane. Options for implementation will need to be discussed in greater detail with the mechanical workshop.

If the crane system can not be replaced, then to overcome the problem of the upright rig swinging during maintenance work, it is recommended that covered anchor points be sunk into the floor of the laboratory, allowing use of heavy-duty ratchet straps to tie the rig in place. This should be combined with a load-bearing cushion to protect the

rig and floor surface from impact with the ground. It is recommended that the crane units be fitted with variable speed drives in order to soften the lift/drop process, which at present causes the rig to jerk violently whenever the clutch is engaged. The present behaviour makes it difficult to lower the rig to the floor without rebounding, and also places excessive stress on the structure. The horizontal crane drives would also benefit from some additional control due to a slight speed imbalance between the right and left units. Over time this causes the rig to shift off-center, a problem which could be rectified either by matching the speeds or by providing a degree of individual control to each crane. Speed selectors and directional controls could be combined with the lamp control panel to provide a single control unit

In addition to crane lift control drives, the oscillation of the rig could also be reduced by fitting dampers between the inner and outer frames of the array. This would reduce the mechanical stress on the wiring, lamp housings and tilt control drives when the array is being manoeuvred into position.

Another important aspect to address is the tilt mecanism of the array. This is currently provided by a low-speed motor on a chain drive attatched to the tilt axis of the array. The problem here is due to the inertia of the rig, which when the tilt drive is activated causes its movement to lag the motor. The rotation is initially taken up by the chain, and the rig will then swing precariously into place to balance out. This is a difficult problem to address as the array is required to sit on the chain support when being manoeuvred, however a finer control of the motor position would be beneficial and help to reduce this effect.

E.3.3 Working Environment

Any laboratory test based on characterisation of devices or the collection of some form of statistical data requires the user to spend significant amounts of time working in the laboratory. The working environment should therefore be comfortable, and provide ample space for test equipment, tools and components.

The lab should be provided with desk space and chairs for at least two people to work for extended periods, and ideally a work table with clamps for building test equipment, soldering etc. Storage is currently provided by three metal cabinets and a cupboard/drawer unit at the back of the lab which is likely sufficient for current needs, but both need sorting, emptying and labelling in order to become useful. The laboratory also requires suitable regular and recycling waste disposal bins

It would also be beneficial to reinstate the 2nd floor control room, which would be used as a workspace and also to house any new control gear such as DMX dimmer boards. This woulg greatly reduce the time spent working under the lights, particularly for lengh characterisation or data-acquisition tests. It is also recommended that screening film be applied to the 2nd floor corridor windows to minimise distraction and avoid dazzling passers-by

Some thought will need to be given to heating of the laboratory, as winter temperatures indoors drop to around 10 °C without the lamps in operation, making it almost impossible to work. This is mostly due to poor insulation around the bay doors, but is also partly attributable to poor draught exclusion between W/1.07 and 1.08. The separator between the two labs currently consists of a vertical shutter door, with

the doorway blocked up with three large slabs of polystyrene foam. This does little to block draughts from next door, and the foam blocks consequentially move about which is noisy and distracting. It is recommended that the door be replaced with a more suitable alternative which provides a comparable degree of insulation between the rooms, while allowing access when necessary.

With regard to equipment specific to power-based measurememnt and testing, there are a number of tools which would be useful to have as permanent fixtures in the lab, such as a good quality oscilloscope, power analyser, a set of DC/high frequency voltage and current probes, and a range of high voltage leads, connectors, probes and commonly used components for quicky making up custom test equipment. More sophisticated equipment would need to be obtained on a project-specific basis.

One important addition from an electrical perspective however would be the provision of solid earthing points around the lab. These are currently not provided for, and the only option for earthing is to return to the supply earth which is unsuitable for any form of high voltage testing. Electrical connections to the laboratory metalwork or a dedicated earthing rod should be made available, together with a ready supply of earth-braid for the connection of individual pieces of equipment.

E.3.4 Health and Safety

On the subject of health and safety, there are a number of recommendations for improvement. First and foremost should be the provision of suitable safety eyewear for working under high-intensity lights. Though the risk of dangerous levels of UV exposure are minimal, the visible light intensity is high enough to cause serious eye damage. Filtered safety spectacles can be purchased cheaply and should be provided for all work in the laboratory, and also to visitors whenever the array is operational. It is also recommended that dedicated safety headwear and gloves be provided for whenever the array is brought down on the crane and lamps replaced.

Regarding the safety concerns of manoeuvring the solar array, the majority of concerns are summarised in Section E.3.2, and need not be repeated here. The addition of a lightweight scaffold tower will however require that correct training be undertaken for working at height, and suitable electrical safety provisions and guidelines will need to be available if the lab is to be used for ongoing work on photovoltaics.

E.4 Cost Esimates

The follwoing section summarises the material cost where possible of the proposals in section E.3. The majority of quotes are still pending as of 11/05/2010

E.4.1 Lamp Array and Control Gear

E.4.1.1 Option 1: Cold-restrike Discharge Lamps (maintaining current setup)

Table E.1: Initial Costs

Item	Unit Cost (£)	Qty	Subtotal (£)	VAT (£)	**Total (£)**	Supplier
Lamps: GE CID 1000W 99-1225 G38	126.00	36	4536.00	793.80	**5329.80**	A C lighting uk
Ignitors: G53444 THORN 1000W SE15/7W	40.00	36	1440.00	252.00	**1692.00**	slb breakers ltd
Replacement Ballasts	-	10	-	-	-	Unknown
Replacement PFC	-	10	-	-	-	Unknown
10A Single Phase Momentary Trigger Switches [1]	0.63	36	22.68	3.97	**26.65**	RS

Table E.2: Ongoing Costs

Item	Unit Cost (£)	Qty	Subtotal (£)	VAT (£)	**Total (£)**	Supplier
Lamps: GE CID 1000W 99-1225 G38	126.00	36	4536.00	793.80	**5329.80** [2]	A C lighting uk

[1] Existing trigger panels can be re-used

[2] Complete lamp replacement every 1200-1500 lamp-hours

E.4.1.2 Option 2: Hot-restrike Discharge Lamps

Table E.3: Initial Costs

Item	Unit Cost (£)	Qty	Subtotal (£)	VAT (£)	**Total (£)**	Supplier
Lamps: GE CID 1000W 99-1425 G38 HR	128.50	36	4626.00	809.55	**5435.55**	A C lighting uk
Ignitors: IREM AD 1540 igniter	400	36	14,400.00	2520.00	**16920.00**	unknown
Replacement Ballasts	-	10	-	-	-	Unknown
Replacement PFC	-	10	-	-	-	Unknown
10A Single Phase Momentary Trigger Switches [1]	0.63	36	22.68	3.97	**26.65**	RS
10A Single Phase Latching Trigger Switches	0.85	36	30.60	5.36	**35.96**	RS
Additional bias RC network	-	-	-	-	-	

Table E.4: Ongoing Costs

Item	Unit Cost (£)	Qty	Subtotal (£)	VAT (£)	**Total (£)**	Supplier
Lamps: GE CID 1000W 99-1425 G38 HR	128.50	36	4626.00	809.55	**5435.55** [2]	A C lighting uk

[1] Existing trigger panels can be re-used

[2] Complete lamp replacement every 1200-1500 lamp-hours

E.4.1.3 Options 3/4: Halogen Lamps

Table E.5: Initial Costs

Item	Unit Cost (£)	Qty	Subtotal (£)	VAT (£)	**Total (£)**	Supplier
Lamps: PAR 64 Halogen Reflector Lamp (Spot/Flood)	13.90	36	500.04	87.57	**587.61**	stagelighting.co.uk
18 Channel DMX Dimmer [1]	789.00	2	1578.00	276.15	**1854.15**	terralec uk
48 Channel DMX control board [1]	190.00	1	190.00	33.25	**223.25**	stagelighting uk
DMX cabling		50m	50.00	-	**50.00**	-

Table E.6: Ongoing Costs

Item	Unit Cost (£)	Qty	Subtotal (£)	VAT (£)	**Total (£)**	Supplier
Lamps: PAR 64 Halogen Reflector Lamp (Spot/Flood)	13.90	36	500.40	87.57	**587.61** [2]	stagelighting.co.uk

[1] Many options vailable with varying degrees of programmability - simplest option quoted
[2] Complete lamp replacement every 250-300 lamp-hours

E.4.2 Access and Maintenance

Item	Unit Cost (£)	Qty	Subtotal (£)	VAT (£)	**Total (£)**	Supplier
Scaffold Tower - Zarges 3.5m	589	1	589	103.08	**692.08**	machinemart
Scaffold Tower - Zarges 5.15m	779	1	779	136.33	**915.33**	machinemart
Ratchet Straps	5.95	4	23.80	4.16	**27.96**	-
Ground Anchor	46.72	4	170.21	29.79	**200.00**	Elite security supplies

E.4.3 Working Environment

awaiting quotes

E.4.4 Health and Safety

Item	Unit Cost (£)	Qty	Subtotal (£)	VAT (£)	**Total (£)**	Supplier
Eye Protection - bolle spider flash	6.92	10	69.20	12.11	**81.31**	sevsafe uk